Organic Phases in Microfluidic Systems: Enabling Real-Time Sensing of Small Molecules

by

Shannon Phelan Quevedo

A dissertation submitted in partial fulfillment
of the requirements for the degree of
Doctor of Philosophy
(Chemistry)
in the University of Michigan
2021

Doctoral Committee:

Professor Ryan C. Bailey, Chair
Professor Zhan Chen
Professor Jinsang Kim
Professor Mark Meyerhoff
Assistant Professor Ginger Shultz

Shannon P. Quevedo

swetzler@umich.edu

ORCID iD: 0000-0003-0614-9212

Dedication

In memory of Prof Bob Cave, who always made me feel like I could do anything, even a PhD

And

To my science, which kept me going when times were hard,

and to my eucalyptus tree, who kept me going when science couldn't.

Acknowledgments

I would first like to thank my advisor, Professor Ryan Bailey, for all of his support and help over my five years in his lab, as well as a summer at UIUC. His encouragement to try new areas of research, from polymers to optodes to chemistry education, have pushed me to become a more well-rounded chemist. I would also like to thank my committee members, Professor Zhan Chen, Professor Jinsang Kim, Professor Mark Meyerhoff and Assistant Professor Ginger Shultz, for all of the advice they have given me. I would like to give an extra special thank you to Professor Jinsang Kim, in whose Advanced Functional Polymers class I met my husband. I would also like to thank the NSF Graduate Research Fellowship Program for funding.

I would like to thank others who, while not on my committee, have served as key inspirations during my graduate school journey. Professor Paul Braun (UIUC), Professor Lydia Kisley, Dr. Kali Miller, Dr. Jennifer Reeves, and Professor Xuewei Wang (VCU) were integral in helping me to develop as a researcher and providing guidance throughout my graduate school career. Dr. Nancy Kerner and Dr. Carol Ann Castañeda, helped me rediscover my love of teaching, keeping me sane. I would also like to thank my professors from Harvey Mudd, who encouraged me throughout graduate school especially Professor Dave Vosburg, Professor Lelia Hawkins, and Professor Ron Grimm.

I have worked with some wonderful collaborators within the lab. Dr. Alex Stanton (Ninja) was an amazing mentor and introduction to the lab, and Dr. Heather Robison also provided a lot of support when I was striking it out on my own in my second year. I would also specifically like to thank my undergraduates, Robert Moeller and Michaela Barber, for working through some tough

projects like champs; as well as Nicholas Glenn and Keenan Wright, for struggling with me to get the microfluidic droptode project off the ground.

Moving from NY to CA and then to MI, it was nice to have a family established for me in the Bailey lab. I would particularly like to thank all leaders of the Sunshine committee (Jamy, Mari and Gloria) for helping to make the lab a happier and friendlier place, whether through cards, candy, or cake. I learned a lot from working with my fellow lab members, including Dr. Yi Xu, Dr. Steve Doonan, Dr. Maria Cruz Cardenosa Rubio, Dr. Emily Mordan, Dr. Sara Medfisch, Dr. Cole Chapman, Dr. John Orlet, Colleen Riordan, Gloria Diaz, Nico Mesyngier, Claire Cook, Nicholas Glenn, Marina Sarcinella and Krista Meserve, the experience of working with all of you has forever shaped me for the better. And, specifically to my fellow fifth years: we got through this without killing each other. Who would have guessed?

I would not have made it through graduate school without good supportive friends along the way, always willing to listen to me vent or distract me when I was stressing out too much including Ashley Doonan, Melissa, Dr. Phil, Dr. Pez, Tiff, Bobby, Claire, and Nevo. I would like to give an extra special shout-out to friends who have stuck with me through this PhD nonsense despite being in different careers and/or time zones including Dr. Allison Lim, Nicky Subler, Mikaela Kosich, Will Schneider, Tristan Fitch and Max Frenkel. Hans Zander, thanks for being the tallest person I know, as well as a great housemate, and of course, the countless hours of excellent food, drinks, video games, spam gifting, Marvel movies and advice.

I would also like to thank some particularly supportive lab members, including Steve, who taught me microfluidics when I was panicking, and then destroyed me at board games when I wasn't, Nico, for being an awesome Switzerland, and Dr. Cole, who put up with n+1 too many of my

crazy ideas. Colleen, thank you for being my ice cream buddy, my venting space, my closest friend and my maid of honor. I would have exploded by the end of second year without you. There would be nothing to acknowledge without the support of my family, both biological and new. A mis padres, hermano, y todos mis tios y primos nuevos, yo los quiero mucho. Luz and Miguel, thank you so much for welcoming me into your lives, supporting me through all of the tough times, and giving me the greatest gift of all, Danny. Grandma and Grandpa, thank you for all the encouraging phone calls, cards, love, and support. They made tough weeks better and the pocket money definitely supplied most of the lab's candy. I always appreciated your interest in the work I was doing, and I was so proud to have my abstract on your bedside table. Nana and Poppop, you were so proud of me starting my PhD journey, and though you aren't here to see the end of it, I know that you are sending me all of your love and support. I hope I have made you proud. Tara and Erin, thank you for being amazing sisters; always being willing to watch goofy videos with me, send me pictures of Lico when I wasn't home and listen to me talk about science stuff that I thought was really cool even though you couldn't have cared less. Mom and Dad, I would not have been able to get through anything in this life without your support: from the crossword puzzles to going to BNL Summer Sundays, from the rides home from after school activities to the walks at Sunken Meadow, you have made me into someone who is on her way to completing her PhD. I love you both so much and can never thank you enough.

Finally, to my best boy, my husband, the other Dr. Quevedo (until I become a Major), I am so lucky to have found you. You have been a port during the storm of grad school, taking care of and loving me when I couldn't do it myself. The words I have to thank you for how much you changed my life would be weird to see on paper, probably the first time *mrow* is written in a thesis, but I love you so very much. I am so happy to never have to imagine a life without you;

and I can’t wait to move to Lexington and start our new life together (with multiple cats and one dog).

Table of Contents

List of Tables

List of Figures

List of Appendices

List of Acronyms

AAS	Atomic Absorption Spectroscopy
ADP	Adenosine diphosphate
AFM	Atomic Force Microscopy
AMP	Adenosine monophosphate
AOB	Ammonia Oxidizing Bacteria
ATP	Adenosine triphosphate
ATRP	Atom Transfer Radical Polymerization
BPA	Bisphenol A
BPOTS	[11-(2-bromo-2-methyl) propionyloxy] undecyltrichlorosilane
BTEX	Benzene, toluene, ethylbenzene, xylene
CE	Capillary Electricity
Ch-MS	Chromatography-Mass Spectrometry
Chromoionophore I	3-Octadecanoylimino-7-(diethylamino)-1,2-benzophenoxazine, 9-(Diethylamino)-5-(octadecanoylimino)-5H-benzo[a]phenoxazine
Chromoionophore XI	Fluorescein octadecyl ester
Chromoionophore XV	4-(Dioctylamino)-4′-(trifluoroacetyl)azobenzene
COC	Cyclic olefin copolymer
COVID-19	Disease caused by SARS-CoV-2 (severe acute respiratory syndrome coronavirus 2)
CTC	Circulating tumor cells
DLLME	Dispersive Liquid-Liquid Microextraction

DMAEMA	2-(dimethylamino)ethyl methacrylate
DNA	Deoxyribonucleic acid
DOS	Dioctyl sebacate
ELISA	Enzyme-Linked Immunosorbent Assay
EPA	Environmental Protection Agency
FCS	Fluorescence Correlation Spectroscopy
FGFR	Fibroblast Growth Factor Receptor
FRAP	Fluorescence Recovery After Photobleaching
FRET	Förster Resonance Energy Transfer
FT-IR	Fourier Transform Infrared Spectroscopy
GC-MS	Gas Chromatography-Mass Spectrometry
GFP	Green Fluorescent Protein
H_2SO_4	Sulfuric Acid
HEMA	2-hydroxyethyl methacrylate
HEPES	(4-(2-hydroxyethyl)-1-piperazineethanesulfonic acid)
HF-LLE	Hollow-fiber Liquid-Liquid Extraction
HIV	Human Immunodeficiency Virus
HLLE	Homogeneous Liquid-Liquid Extraction
HMTETA	1,1,4,7,10,10-hexamethyltriethylenetetramine
ISE	Ion-Selective Electrodes
ISO	Ion-Selective Optode
KTFPB	Potassium tetrakis[3,5-bis(trifluoromethyl)phenyl] borate

LC-MS	Liquid Chromatography-Mass Spectrometry
LDH	Lactate dehydrogenase
LLE	Liquid Liquid Extraction
LLED	Liquid-Liquid Extraction Detection
LoD	Limit of Detection
LoQ	Limit of Quantitation
MES	2-(N-morpholino)ethanesulfonic acid
MIBK	Methyl isobutyl ketone
MIP	Molecularly Imprinted Polymers
MMA	Methyl methacrylate
MS	Mass Spectrometry
NADH	Nicotinamide adenine dinucleotide
NaTFPB	Sodium tetrakis[3,5-bis(trifluoromethyl)phenyl] borate
NB	Nitrobenzene
NIR	Near-infrared
NMR	Nuclear Magnetic Resonance Imaging
NOB	Nitrite Oxidizing Bacteria
NR	Neutron Reflectivity
PAAc	Poly(Acrylic Acid)
PBS	Phosphate-buffered Saline
PC	Polycarbonate
PDMAEMA	Poly[2(Dimethylamino)ethyl methacrylate]

PDMS	Poly(dimethyl siloxane)
PFAS	Perfluoroalkyl substances
$PFBS^-$	Perfluorobutanesulfonic acid
$PFOA^-$	Perfluorooctanoic acid
PFOH	1H, 1H, 2H, 2H-Perfluoro-1-octanol
$PFOS^-$	Perfluorooctanesulfonic acid
PHEMA	Poly(hydroxyethyl methacrylate)
PMMA	Poly(methyl methacrylate)
pNIPAm	Poly(N-isopropyl acrlyamide)
pNIPAM-co-AAc	Poly(N-isopropyl-acrylamide) co polymerized with acrylic acid
PTFE	Poly(tetrafluoroethylene); Teflon
PVC	Poly(vinyl chloride)
QCM	Quartz Crystal Microbalance
QCM-D	Dissipative Quartz Crystal Microbalance
RBOE	Rhodamine B octadecyl ester perchlorate
SD	Standard Deviation
SE	Spectral Ellipsometry
SH-SAW	Shear Horizontal Surface Acoustic Wave Sensor
SI-ATRP	Surface-Initiated Atom Transfer Radical Polymerization
SPE	Solid Phase Extraction
SPED	Solid Phase Extraction-Detection
SPR	Surface Plasmon Resonance

SPT	Single particle tracking
STEM	Science, Technology, Education and Math
$TDDANO_3$	Tetradodecylammonium nitrate
THF	Tetrahydrofuran
TMB	3,3',5,5'-Tetramethylbenzidine
XPS	X-ray Photoelectron Spectroscopy

List of Symbols

$<D>$	Average diffusion coefficient, molecular diffusivity
$1-\alpha$	Degree of protonation, Fluorescent signal normalized to 0.1M HCl and 0.1M NaOH
A	Fitted Parameter for Maximum Signal
A_m	Constant dependent on maximum shift at equilibrium
B	Fitted Parameter for Minimum Signal
C	Fitted Parameter for the Midpoint of the Linear Region
Ca^{2+}	Calcium
C_{amb}	Ambient concentration of the analyte
Cl^-	Chloride
$CuBr$	Copper (I) Bromide
$CuBr_2$	Copper (II) Bromide
d	Critical thickness of a polymer brush
D	Fitted Parameter for the Slope at the Midpoint of the Linear Region
F_{2M}	Fluorescent signal from 2M KCl
F_{Buffer}	Fluorescent signal from the buffer
F_{HCl}	Fluorescence of 0.1M hydrochloric acid
F_{Max}	Maximum fluorescent signal
F_{Min}	Minimum fluorescent signal
F_{NaOH}	Fluorescence of 0.1M sodium hydroxide

HCl	Hydrochloric acid
K^+	Potassium
KCl	Potassium Chloride
Na^+	Sodium
NaCl	Sodium chloride
NaOH	Sodium hydroxide
n_{eff}	Local Effective Refractive Index
$NH4^+$	Ammonium
NO_2^-	Nitrite
NO_3^-	Nitrate
Normalized Fluorescence	Fluorescent signal normalized to the response of the buffer and 2M of the analyte
P	Brush-solvent Partition Coefficient
p	Power parameter; steepness of the slope of the linear region
pH	Potential of hydrogen, $-\log[H^+]$
pK_a	$-\log(K_a)$, the negative log of the pH at which half of the analytes are charged
q	Constant dependent on the measurement, based on the angle of light going through the sensor
r	Radius of the microring
r_0	Ratio of the minimum and maximum shifts
Relative Fluorescence	Fluorescent signal normalized to the defined maximum and minimum fluorescence
Relative Shift	Change in resonant wavelength (pm)

$Shift_{Max}$	Maximum Shift
$Shift_{Min}$	Minimum Shift observed
t	Time
T	Response time for a given analyte-coating combinations
v	Droplet Speed
$V_{channel}$	Volume of the channel
x	Integer
$x0$	Dry brush thickness
Γ	Decay rate
λ	Resonant Wavelength
Ξ	Penetration of the evanescent field

Abstract

Small molecules play an important role in a variety of industrial and pharmaceutical processes. Many small molecules have important biological side effects, ranging from impacting blood pressure regulation to cancer. As such, it is important to be able to monitor the concentration of these molecules in both environmental and biological conditions. However, small molecule monitoring is challenging due to the low concentration, the low signal and the lack of specificity traditionally associated with small molecule detection. This thesis explores enhancing small molecule sensing by using organic phases in microfluidic systems, allowing pre-concentration of molecules and additional selectivity.

Chapter 1 explores the current detection methods used for small molecules, focusing on those that use organic phases for separative procedures. Organic phase separative procedures are divided into two categories: solid phase or liquid-liquid extraction. Advancements in separative technology, including molecularly imprinted polymers, nanoparticles, and dispersive liquid-liquid microextraction are explored. Separative/detection platforms are then explored, including methods based on stimuli responsive polymers, ion-selective optodes and microfluidic droptodes. When using organic phases for separative procedures, there is a need to characterize the interactions between the analyte and the organic phase. Chapter 2 demonstrates the novel use of silicon photonic microring resonators to characterize *in situ* polymer brush-small molecule interactions. By monitoring resonant wavelength shifts, brush-solvent-analyte interaction parameters, including partition and diffusion coefficients and pK_as, can be extracted from a

single set of data or from successive analyte introductions using a single brush-coated sensor. of polymer brushes with solvents and analytes, not easily accessed by other techniques.

Droplet microfluidic optodes, or “droptodes”, have also recently emerged as a powerful technology for rapid detection of small ions in complex matrices. Chapter 3 explores the influence of microfluidic parameters on droptode efficiency, including droplet flow rate, the presence of serpentine mixing channels and the ratio of the droplet to carrier volumes. Chapter 4 then demonstrates the creation of a novel multiplexed droptode system, by using a fluorinated oil phase to separate the analyte-sensitive phases. Five different biologically relevant ions, H^+, K^+, Na^+, Ca^{2+} and Cl^- were detected off of one sample, using only 20 µL of sample and 10 seconds of data collection. Finally, Chapter 5 expands the application of droptodes to detecting perfluoroalkyl substances (PFAS), carcinogenic precursors to non-stick materials. There is also preliminary exploration into characterizing novel fluorinated chromoionophores which will allow for better selectivity in our fluorinated oil phase.

In Chapter 6, I take a foray into chemical education research, by developing a novel lab for a Bioanalytical class. Relevance-focused teaching has been shown to improve student retention, especially for students with low success expectations. Thus, I developed a lab focused around the use of Enzyme Linked Immunosorbent Assays (ELISAs) in the context, originally, of developing Lupus Diagnostic Panels, but have since modified it to relate to the COVID-19 pandemic. Chapter 6 explores the implication of this lab for student learning.

Finally, Chapter 7 summarizes the work done during my PhD towards improving small molecule detection through the use of microfluidic organic phases. The future of the field of droptodes, in particular, is discussed, including potential microfluidic innovations such as Janus droplets, the expansion of droptode detection for other pollutants and matrices, the

miniaturization of the droptode system and a variety of other assays which could be performed using droptodes.

Chapter 1.

Uses of Organic Phases for Enhanced Small Molecule Detection: A Review

Small molecules, defined as molecules with a molecular weight below 900 Daltons that can impact human health, play an important role in industrial, environmental, and biological processes. Traditionally considered to consist of mostly organic molecules, small molecules can

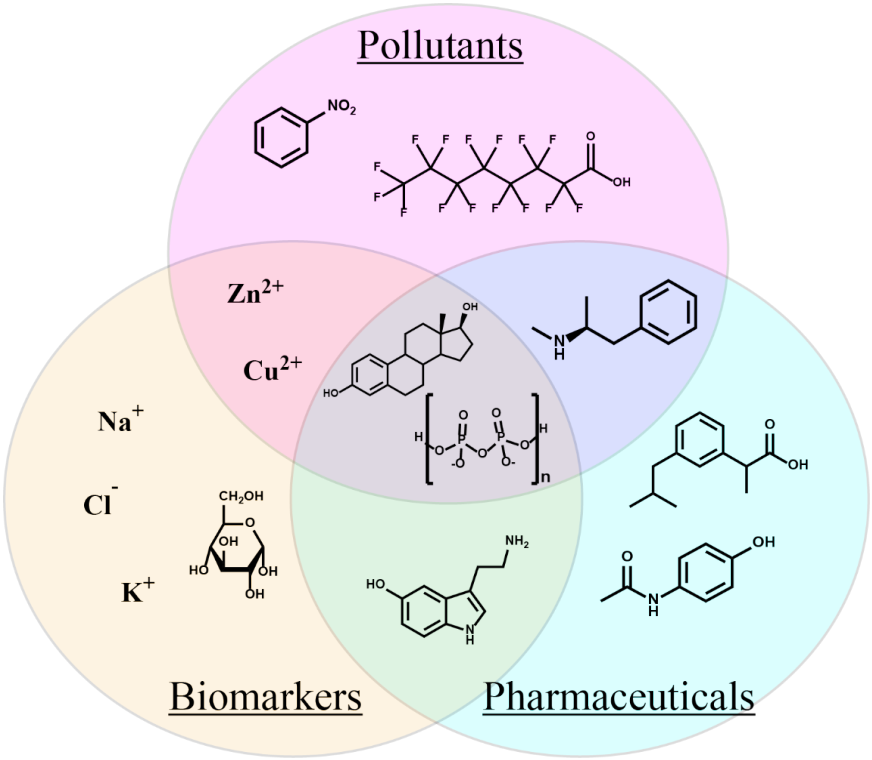

Figure 1.1. The various classes of commonly detected small molecules. These can range from pollutants like PFAS and nitrobenzene to pharmaceuticals like ibuprofen to biomarkers like potassium and glucose. Some small molecules fall under multiple categories, including methamphetamines which are both pharmaceuticals and pollutants, zinc and copper which are important to human health but also common pollutants, serotonin which is both made naturally and supplemented, and estradiol and polyphosphate which fall under all three categories.

include pharmaceuticals, opioids, toxins, and synthetic precursors (**Figure 1.1**). However, defining a small molecule solely by its molecular weight and potential impact on human biology means that low molecular weight ions should also be included in this category. Similar to organic small molecules, inorganic small molecules also have a range of roles in environmental and biological processes. For instance, perchlorate is a common pollutant in drinking water that has been linked to thyroid problems, [1,2] and zinc is considered one of the major environmental contaminants of drinking water.[3] Biologically, potassium, a monovalent ion, is central to the function of the cellular plasma membrane,[4,5] the regulation of blood pressure,[4] and the regulation of pH.[4,5] Other small inorganic molecules, such as polyphosphate, are polyionic in nature and play a major role in the blood coagulation cascade. Polyions such as these have been associated with angiogenesis, tumor metastasis and activation of the immune system,[6,7] as well as serving as indicators for the presence of bacteria in water supply.[8]

Because the range of small molecules is so large, there is a variety of different reasons to detect the small molecules' presence (**Figure 1.1**). In streams, small molecule detection can determine if the water contains carcinogenic pollutants such as nitrobenzene,[9] making the water unsafe to drink or bathe in. Testing water waste streams for opioid metabolites is also a common way for public health officials to monitor the extent of drug use within communities, and monitor the effectiveness of their anti-drug programs.[10] However, more complex matrices also need to be tested for small molecules, including testing if factory production lines contain trace levels of contaminants or determining if metal levels lead to unsafe work conditions in mines. Biologically, there is also need to test for small molecules, such as testing if ionic concentrations in the body are at the correct level via blood panels, monitoring for heavy metal poisoning, determining if someone has overdosed or measuring the extent of pollution within a person's

bloodstream. Many of these assays will not specifically be for one analyte: when testing water for pollution, the type of pollution can cover charged molecules, neutral molecules, organic molecules, inorganic molecules. Similarly, when monitoring levels of molecules in humans, there is often the desire to monitor different small molecules with minimal blood drawing (for instance both potassium and cocaine). Thus the range of applications for small molecules calls for a versatile assay, which is able to detect small molecules, whether inorganic or organic, in a variety of matrices.

Both the similarities and differences among small molecule analytes lead to challenges in establishing an ideal detection assay. For instance, many small molecules are in low concentrations (on the order of micromolar to nanomolar),[11] and do not cause large changes to physical properties such as mass or refractive index.[12] Additionally, the stability of organic samples is a challenge, as many pharmaceuticals will break down within the bloodstream or in water,[10] meaning that any detection system needs to be able to detect both the initial analyte and also its metabolites. Thus, an ideal assay would need to be able to detect uncharged organic molecules, highly charged metallic ions and any metabolites associated with their reactivity. Adding to the difficulty, within each of these broad subsets of molecules (uncharged organic, highly charged metallic) there are a variety of similarities making specificity challenging, such as functional group overlaps for organic molecules or similar charge densities for inorganic molecules.

Finally, the ubiquitous need for small molecule testing globally encourages the development of a point-of-analysis technique. Point-of-analysis, referred to in the biomedical field as point-of-care, is when measurements are made at the site from which the sample is taken. Thus there is less need to worry about sample contamination or degradation during transit.

Additionally, as point-of-analysis techniques need to be rapid and portable, many are developed with minimal instrumentation, making them ideal for low resource settings. Point-of-analysis technology would be ideal for various small molecule detection purposes, ranging from pollution, which occurs on a global scale, to healthcare which should be universal.

Thus, the ideal assay for small molecules should be versatile enough to detect both charged and uncharged analytes in a variety of sample matrices, be highly portable and use minimal technology. Multiplexability, to allow the measurement of metabolites of the analyte as well as the analyte itself, and real-time analysis would be a boon to the assay though not a requirement. Finally, the assay would need to have limits of detection in the nanomolar region or lower, and provide good specificity for the analyte of interest.

1.1 CONVENTIONAL SMALL MOLECULE DETECTION

One of the most common detection methods for small molecules is chromatography coupled to mass spectrometry (Ch-MS), including both liquid chromatography (LC-MS) and gas chromatography (GC-MS). Ch-MS can detect in complex matrices because of the separation created in the chromatographic stage. Because there has been significant research into different types of chromatography, it is possible to separate a variety of analytes, both charged and uncharged. As a detection platform, mass spectrometry (MS) has a high degree of specificity for a molecule of interest, because of fingerprint fragmentation patterns. MS also allows for the detection of many metabolites, though differentiation between a mixture of metabolites and the original analyte may be challenging. Finally, MS offers high sensitivity to low concentrations of molecules, down to femtograms/mL (depending on the ionization technique).[13] Ch-MS has been

used to detect a variety of small molecules including metabolites,[10,14,15] pollutants,[16,17] and pharmaceuticals.[10,18,19]

However, for broad global applications such as pollution detection or rapid medical testing, Ch-MS is less suitable. While Ch-MS has the potential for high-throughput methodology, separation time typically ranges from minutes to hours, depending on the sample complexity.[20] Commercial Ch-MS are currently not portable and do not offer real-time monitoring,[13] though environmental monitoring using portable MS has become more common.[21] In general, Ch-MS is also instrumentation heavy,[13] making it disadvantageous for low resource settings. Finally, while MS does offer good specificity, it requires fragmentation, that favors higher molecular weight species, making identification of small molecules more challenging.

Enzyme-based methods are also commonly used for small molecule detection. Enzyme reactivity is substrate-specific, lending high specificity to the detection platform. Breaking down a molecule of interest can result in the presence of a chromoionophore or a fluorophore, which can then be detected optically.[22] Some enzyme-based methods also detect based on electrochemical methods, if the enzymatic reaction involves a charge transfer, or produces an oxidative or reductive molecule.[23] Enzyme-based methods have the additional advantage of frequent turn-over, allowing very sensitive detection. However, one of the main limitations of the enzyme-based detection is the requirement to have an enzyme specific to the molecule of interest. Many pollutant molecules do not have specific known enzymes and instead have broader or off-target reactivities, Additionally many ions, such as potassium, are not modified by the presence of an enzyme.

An alternative method to detect small molecules is fluorescence detection, which can be performed in real-time with only a smartphone in a matter of seconds or minutes.[24–30] Depending

on the wavelength used for detection, fluorescence can be extremely robust against complex matrix environments such as serum.[31] However, the majority of small molecules do not have fluorophores, and tagging analytes with fluorophores can be difficult in complex samples.[32] Another concern is either high background or fluorescent quenching when analyzing low and high concentrations of analytes, respectively. An alternative to having to label the analyte is to create a system where there are specific interactions of the molecule of interest with a compound which can change fluorescence based upon analyte presence,[33] such as Förster Resonance Energy Transfer (FRET). However, FRET too has its downsides: low signal-to-noise ratios, making detection harder at low concentrations and the dependence of fluorophores upon environmental conditions like pH and temperature.[34]

1.2 USE OF ORGANIC PHASES FOR EXTRACTION TECHNOLOGIES

A potential means of expanding the application of small molecule detection is to rely on coupling detection methods to an extraction technology, such as the use of organic phases. Organic phases offer many benefits when quantifying small molecules in complex matrices. Most complex matrices studied for biological and environmental purposes are in the aqueous phase. Thus, extraction of the analyte of interest into the organic phase can remove most of the interfering compounds, expanding the possible detection methods available. Additionally, extraction offers the possibility of pre-concentrating the analyte, allowing use of less sensitive detection methods. Finally, partitioning into the organic phase is relatively easy to manipulate; whether by adding a hydrophobic tail to the analyte or by binding the analyte to an organic compound. This principle has been used to extract even small inorganic molecules into the organic phase, as will be discussed further below.

Generally, organic phase extraction can be classified into one of two categories: solid phase extraction (SPE) or liquid-liquid extraction (LLE). As suggested by their names, SPE and LLE work based on extraction of a molecule from the aqueous into a solid or liquid immiscible phase, respectively. Extensive reviews have been written recently on the advancements and limitations of both SPE [35–38]and LLE,[38–42] so here I will primarily explore trends in SPE and.

1.2.1 Solid Phase Extraction Technologies (SPE)

SPE has been adapted to minimize sample loss by using monoliths as the solid support. Porous monoliths are polymerized surfaces created with a porogen of a specific size to encourage the creation of high surface area to volume ratios which will generally adsorb analytes of interest similar to the size of the porogen. Monoliths have been used to extract both organic and inorganic species, depending on the formulation of monolith.[43,44] In order to improve efficiency of small molecule separation, many monoliths now are hybrid organic-silica monoliths, which incorporate the high surface areas and mesopores of silica monoliths with the low flow resistance and easy preparation of organic monoliths, contributing to their broader use in industrial processes.[43]

Combining microfluidics, where channel dimensions are at most microns across, with monoliths has minimized sample waste and can directly connect to the following separative or preparation step,[37] thus maximized separation efficiency. Monolith creation inside of small volumes is simple, and monoliths remain stable against a wide range of pHs, salt content, and solvents.[43] Monolith microfluidics has been used to extract many small molecules including phenolic compounds,[45] neonatal metabolites,[44] cocaine,[46] and pesticides,[47]and has been coupled to both MS,[45,46,48] and fluorescence detectors.[44] It should be noted however, that microfluidic

monoliths often perform general extraction, typically requiring an additional more specific separation procedure before performing detection for analytes of interest.[44,45]

Originally, the specificity of monoliths was rather broad due to their reliance on intermolecular forces, but in more recent years, monoliths have been modified in order to gain added specificity, such as through molecularly imprinted polymers (MIPs). A MIP is developed when a template molecule, a molecule with similar functional groups and structure to the analyte, is added to a mixture of monomer when forming the monolith (**Figure 1.2**). The monomer then polymerizes around the template, forming template-shaped holes in the polymer once the template is removed (**Figure 1.2**). When flowing a sample over the MIP, theoretically only the analyte of interest will be extracted into the template-shaped holes (**Figure 1.2**). The MIP is then washed by either a high concentration of the template molecule, to displace the analyte, or a solvent which causes the MIP to change shape and release the analyte for later analysis (**Figure 1.2**).[49] MIPs have been used extensively to capture small molecules, including chendeoxycholic acid,[50] organophosphates,[51] and aminoglycoside antibiotics,[52] and can be coupled to a variety of detection methods due to the removal of the complex matrix during extraction, including MS,[53,54] dye displacement,[55] fluorescence,[27,33,56] competitive radioassays,[57] and NMR.[58] However, multiplexing with MIPs has only recently been developed and thus is still rare,[54,59] typically requiring hour-long equilibration periods are to maximize extraction efficiency. MIPs also have a constant tension between strong enough intermolecular forces to capture the analyte but also weak enough that the analyte can ultimately be extracted from the MIP, making optimization for each analyte tedious.

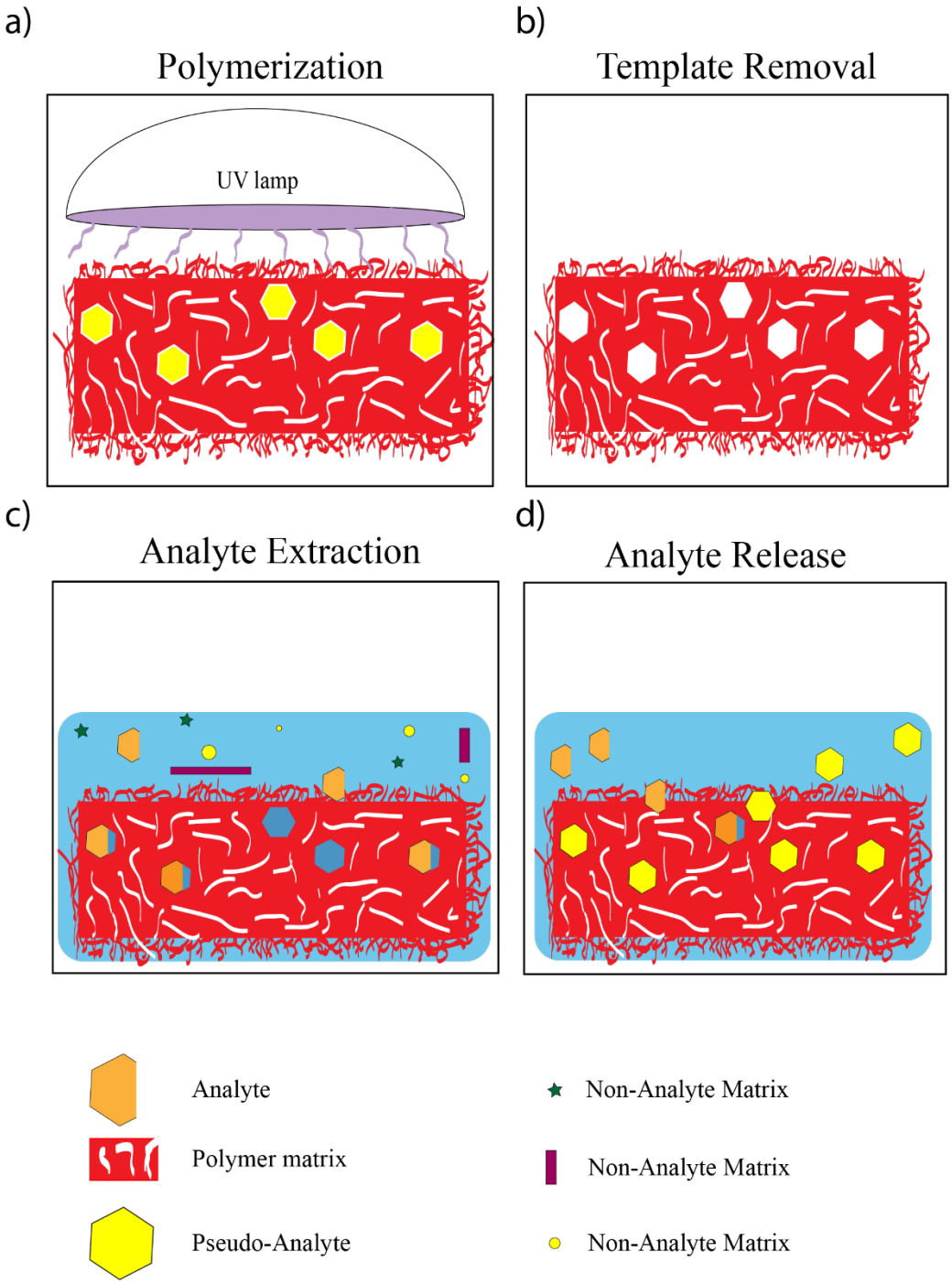

Figure 1.2.Process of Molecularly Imprinted Polymer Capture. (a) Monomer is polymerized around psuedo-analyte template molecules making template size holes (b). The pseudo-analyte template is washed out of the MIP leaving template sized holes(c) Anything shaped similar to the template in the sample partition into the holes while everything not does not. (d) The analyte is washed out using a special solvent or displacement with the template. Figures not drawn to scale.

Finally, organic frameworks coupled to magnetic materials in nanoparticles have become a novel form of SPE. Rather than extraction in a traditional column or surface flow-through format, extraction occurs in the form of magnetic nanoparticles with a surface composed of an organic framework that is monolithic or molecularly imprinted, suspended in the sample of interest. The nanoparticles are suspended in a sample of interest and after a short incubation period, on the order of minutes, the nanoparticles are then separated out from the solution magnetically, removing the analyte with them.[36] Thus, there is minimal solvent waste, no concerns about mass transfer and good analyte enrichment as the volume in which the analyte is resuspended is not pre-determined. Within the past year, magnetic-organic frameworks have been used to detect a variety of phthalate esters from beverages,[60] perfluorinated compounds from milk,[61] alkylphenols from water,[54] and blood lipid regulators, like bezafibrate, from water.[62] While currently used predominantly for the detection of single organic molecules, organic-metallic framework SPEs offers the opportunity for highly multiplexed detection of both organic and inorganic molecules, and could potentially even be combined with a detection technique based on selective nanoparticle enrichment.

1.2.2 Liquid-Liquid Extraction Technologies (LLE)

LLE is the most widely used sample preparation technique due to its generality as well as its high extraction efficiency.[41] Conventionally, LLE is based on transfer of molecules over an immiscible interface, such as one formed between organic and aqueous phases. LLE has been a standard in purification for organic chemistry, where it is often used to remove unwanted byproducts or isolate the molecule of interest based on the ability of only certain molecules to transfer over the interface. Traditional LLE, through separation funnels, can be used to extract

metal ions, in the presence of extractants which chelate the metal ion,[63,64] pharmaceuticals,[65] and many other small molecules, as has been discussed in depth in other reviews.[42]

LLE has also progressed to be further automated, with minimal sample and solvent waste. Continuous flow LLE, which encourages mixing in a pipeline followed by reseparation due to gravity or hydrophobicity, has become a mainstay in industrial processing. Other techniques in miniaturization have focused on minimizing the volume of solvent needed. For instance, hollow-fiber liquid-phase microextraction (HF-LLE) uses a porous capillary filled with organic solvent as the organic phase, minimizing the amount of solvent used.[40] Separations have also been performed using single organic droplet microextraction, exposing a single droplet suspended on a syringe tip to flowing aqueous sample.[39,40,42] Flow-based LLE has been coupled to detection techniques, including UV/visible spectroscopy, atomic absorption spectroscopy (AAS) and spectrofluorometry, for use in a variety of industrial scale processes.[42] Much like traditional LLE, both organic and inorganic molecules have been insolated using flow-based LLE, including rare earth metals by using phosphoric acid ligands,[63] and the antibiotic sulfamethoxazole.[65]

A recent focus for LLE has been the use of homogeneous phase separation techniques (HLLE). HLLE is based on the premise of solution miscibility changing as external conditions change. For instance, two solvents may be miscible at a high temperature but immiscible upon cooling. Other parameters commonly modified to change miscibility include pH, salt content and possible ion pair formations.[39,41] HLLE can be considered to have infinite interfacial surface area, due to the initial miscibility of the solvents, leading to equilibration times on the order of seconds and minimizing the solvent needed. While HLLE was originally used for metal ions, such as copper and uranium,[41] it has been developed further for organic and pharmaceutical

applications.[39] The broader adoption of HLLE has been impeded by solvent constraints, which directly limits what analytes can be extracted.

Dispersive liquid-liquid microextraction (DLLME) has also been a novel development in LLE processing. DLLME uses a ternary system of solvents for analyte extraction. Each solvent plays a different role in the extraction: the sample solvent, typically an aqueous phase, the extractive solvent, where the analyte should be isolated, and the dispersion solvent, which is miscible in both the sample and extractive solvent (**Figure 1.3**). The dispersion solvent encourages the extractive solvent to break into many fine droplets suspended in the sample solvent, maximizing interfacial surface area and thus minimizing equilibration time.[40,41] After equilibrium has been reached, centrifugation is used to separate the three-phase system. As of now, DLLME has mainly been tested on simple matrices, raising the question about if it will allow for high performance in more complex matrices. Additionally there has not been sufficient analysis of the purity of the sample or extractive phase after DLLME to determine the influence of the dispersive phase on separative ability.

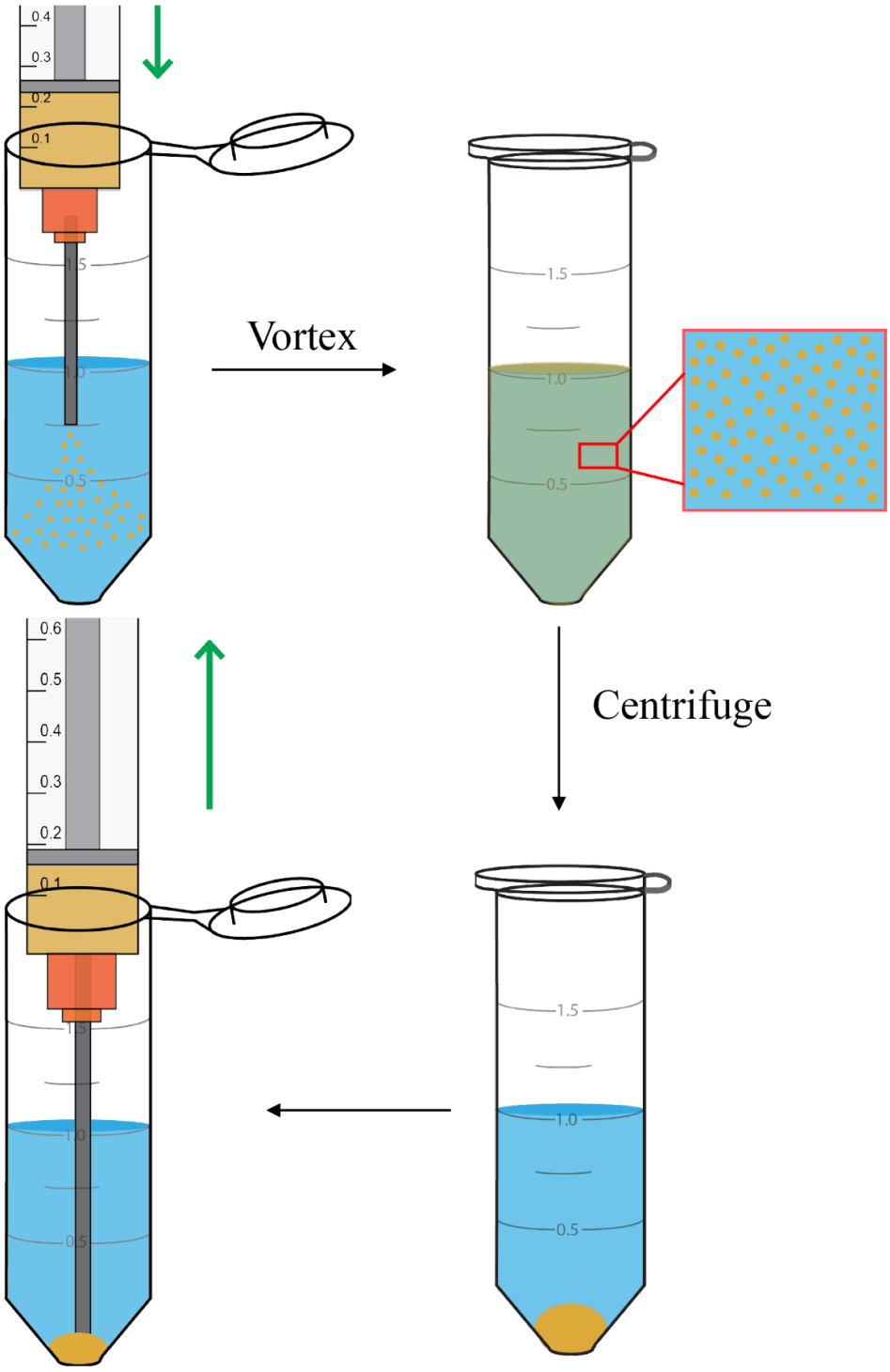

Figure 1.3. Dispersive Liquid-Liquid Microextraction (DLLME). A dispersive solvent and oil phase (yellow) are added to an aqueous sample (blue). This mixture is vortexed to form an emulsion, providing maximum surface area for partitioning. The sample solution is then spun down, separating out the oil phase from the aqueous phase. The oil phase, now containing the analyte of interest, can then be extracted. Figures not drawn to scale.

LLE and SPE methods generally perform extractions for later coupling into instrumentation for detection. Instead, it would be ideal to combine extraction and detection into one concurrent process. Doing so would allow the monitoring of the extraction process, providing both kinetic and thermodynamic information. A combined extraction-detection system would also use less resources, improving detection efficiency by minimizing sample loss, and have less chance of error due to contamination after separation occurs. Below I will review combined extraction and detection systems which capitalize off of the organic phase in both SPE and LLE systems (here referred to as SPED and LLED) for small molecule detection, as well as discuss potential advancements that could be made to enhance small molecule detection in the future.

1.3 USE OF SOLID ORGANIC PHASES FOR SMALL MOLECULE DETECTION

Using solid organic phases for small molecule detection can cover a variety of experimental techniques, including the use of polymeric matrices for improved extraction, polymeric nanoparticles, and polymers with measurable behaviors sensitive to the presence of an analyte. For the point of concision, this chapter will be focusing on polymers grafted to a surface, allowing for spatial multiplexing, and polymers whose identity is important to the role that they are serving (which is to say, changing a polymer identity would invalidate the detection method). Within these limitations, SPED can be divided into two general detection schemes: matrix-based detection schemes, where the polymer matrix is used to add specificity or preconcentration to a surface sensitive technique, and polymer-based detection schemes, which are based upon polymeric matrices changing properties upon exposures to analytes.

1.3.1 Matrix-Based Detection

Matrix-based detection is mainly used alongside surface-sensitive detection techniques where the organic phase can serve as an extractor, concentrator, and matrix for the ultimate measurement. Surface-sensitive techniques include electrochemical detection, which rely on electron transfer between the analyte and the surface, and optical detection, including surface plasmon resonance (SPR), quartz crystal microbalance (QCM), Fourier transformed infrared spectroscopy (FT-IR) and silicon photonic microring resonators. While each operate through different mechanisms, a similarity among all surface-sensitive techniques is the limitation of distance at which an analyte can be detected, governed by either the length over which an electron can transfer (for electrochemical methods) or the penetration of an evanescent field (for optical methods).

One role that polymers can play in matrix-based detection is imparting selectivity to surface-sensitive assays. Molecularly imprinted polymers (MIPs), as discussed earlier, can bind specific analytes to bring them within the range of the surface-sensitive detection method. Using MIP-based matrices, a variety of small molecules have been detected both electrochemically and optically, including carbohydrate antigens,[66] bilirubin,[67] amoxicillin,[68] and perfluoroalkyl compounds.[69] A variant of the MIP detection method was also recently published taking advantage of the bulk optical changes caused by analyte binding to MIP. Testosterone was extracted from a biological sample using MIPs, and the extraction was measured by the changing diffraction pattern as testosterone bound. The authors call this technique a MIP-based holographic imagining.[70] MIP-based holographic imaging detection is promising not only because of its specificity but also its minimal instrumentation, making this an ideal point-of-analysis technology.

An interesting alternative to using polymers as specificity agents is to take advantage of their lack of specificity to make complex measurements. Often referred to as electronic noses or electronic tongues, signals from less specific sensors can be analyzed using multi-variate data analysis to make a predictive model of concentration of a variety of analytes in a sample.[23,71] While originally used with enzymes and antibodies that lacked specificity, electronic tongue technology has expanded to include a variety of non-specific receptors, including polymers. A recent example of this technology used the signal from adsorption and desorption from a non-specific polymer film on a shear horizontal surface acoustic wave device (SH-SAW) to estimate the concentration benzene, toluene, xylene, heptane and naphthalene, and other pollutants in contaminated groundwater.[72] Detection limits for these BTEX pollutants were established as low as 10 ppb.[72] While this technique was extremely sensitive and specific in groundwater, with accuracies within 10% error,[72] it would be interesting to see how many analytes could be differentiated using only poly(epichlorohydrin) or poly(isobutylene), especially when expanding the analysis into other classes of compounds, such as pharmaceuticals, where metabolites also need to be measured.

Electronic tongue sensing has the potential to be expanded to other technologies, such as silicon photonic microring resonators. Used frequently in the Bailey lab, silicon photonic microring resonators are local refractive index detectors. Light is coupled from a linear waveguide into a ring-shaped optical cavity when the following condition is met (Eq 1):

$$m\lambda = 2\pi r n_{eff} \qquad [1]$$

where r is the radius of the ring, n_{eff} is the local effective refractive index and λ is the resonant wavelength. Changes in resonant wavelength can be measured as shifts in the dip in transmission, reported as Relative Shift in pm (**Figure 1.4**). Prior work by the Bailey lab has

shown the ability of microring resonators, 128 located and individually addressable on one 3x1 mm chip, to quantify small molecules such as acetaminophen and ibuprofen,[73] albeit at relatively high concentrations. To improve the limit of detection of small molecules, polymer brushes were grown off of the microring resonator surface, with the goal of concentrating the analyte near the surface of the microrings in order to use the most sensitive region of the evanescent field.[74] Polymer brushes are polymers grafted densely on the surface of the microrings such that they are forced to stand up and come into maximum contact with the solution (**Figure 1.4**).[75] We found that polymer brushes enhanced detection of small molecules by over a factor of 1000%, allowing detection of caffeine and acetaminophen into the micromolar concentration ranges. Additionally we found that the interactions between small molecules and polymer brushes were differentiable, likely due to their different intermolecular forces (**Figure 1.4**).[74] These results highlight the potential utility of a system with an electronic tongue format, where different polymer brushes would be grown on different microring resonators, all on one chip and then the signal from the different polymer films could be deconvoluted to get concentrations of a variety of analytes.

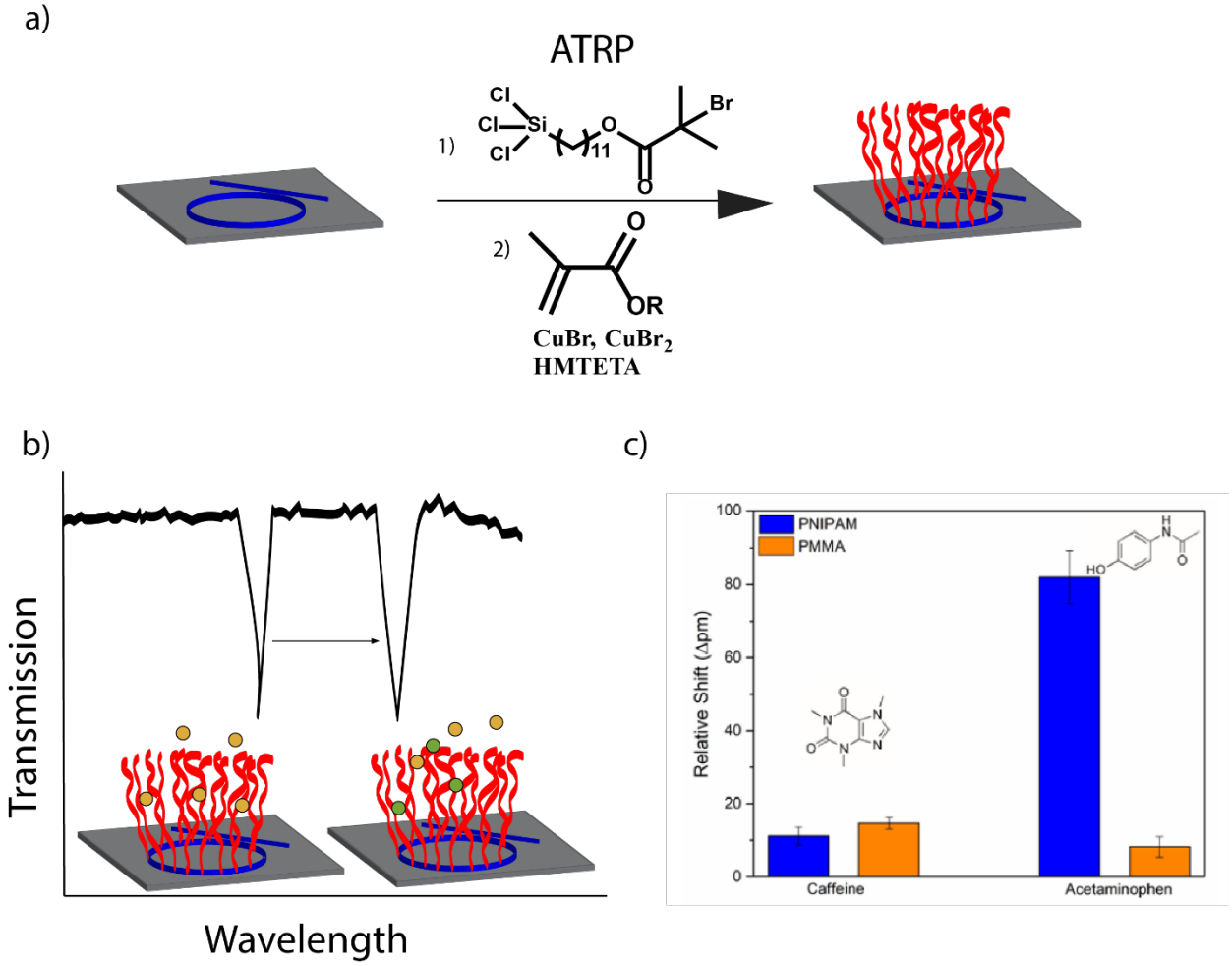

Figure 1.4. Polymer brushes' impact on microring resonators. (a) Polymer brushes were grown on microring resonators using ATRP. (b) As the local environment changes for the polymer brushes, by the green molecules partitioning in, there is a measurable change in the wavelength of the dip in transmission. (c) Two different polymer brushes (PMMA (poly(methyl methacrylate)) and PNIPAM (poly(N-isopropyl acrylamide)) have different responsiveness when exposed to acetaminophen, but similar responsiveness to caffeine. Data taken with permission from [72]. Figures not drawn to scale.

Despite advances in matrix-based detection, signals for small molecules still remain difficult to detect even when preconcentrated in a sensing region (bioassays using microring resonators typically have relative shifts of over 8000 pm as compared to the 100 pm shift here). A potential means around this is to take advantage of the polymer matrix rather than simply using it as an inert scaffold, so that the signal from the small molecule is amplified throughout the entire matrix area.

1.3.2 Polymer Based Detection

Stimuli-responsive, or "smart", polymers are defined as polymers which reversibly change their conformation based upon their local environment, including pH, temperature, salt content, and presence of particular analytes.[76] Using smart polymers, the presence of an analyte could be measured not only by the shift caused by the analyte itself, but its downstream effects on polymer conformation, causing further changes in signal.[1] There have been a plethora of

[1] Before discussing smart polymers, it is important to note that non-smart, or dumb, polymers also can change conformation in the presence of an analyte; the magnitude of these changes is simply not as large. For instance, in methanol, polymer matrices such as nafion[161] and poly(dimethyl siloxane) (PDMS)[162] are known to swell, a volumetric change which could be measured and correlated back to methanol concentration. Similarly, polymer systems such as poly(methyl methacrylate) (PMMA) are known to collapse in "bad" solvents (polymers prefer interactions with itself compared to interactions with the solvent) such as THF.[163] Though comparatively minor, these volumetric changes could still serve to enhance the detection of a small molecule and should not be discounted when designing polymer-based detection platforms.

reviews on connecting responsive polymers to medical diagnostics,[77,78] therefore this chapter will have a broader focus on the detection of general small molecules, not just medical applications.

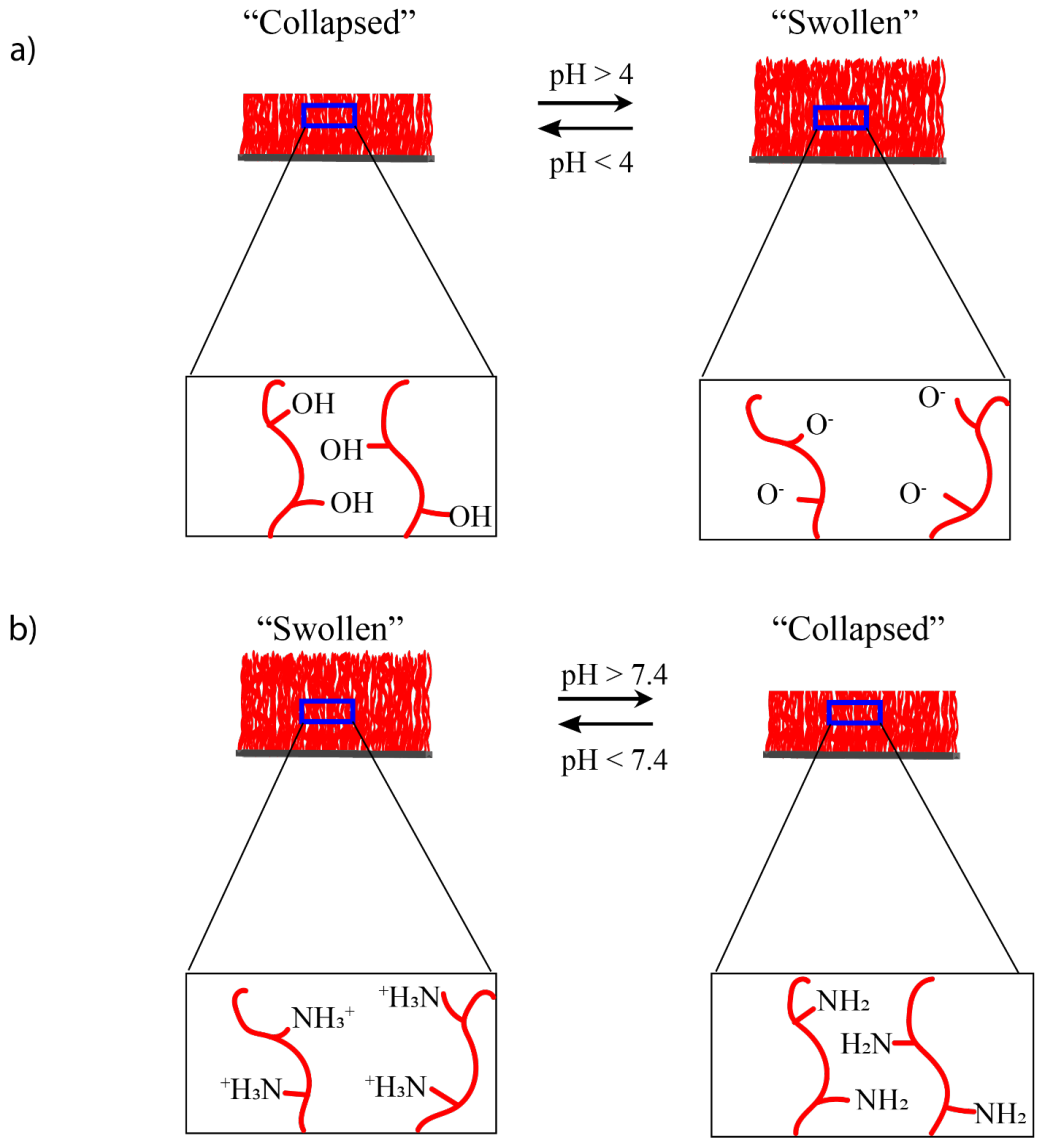

Figure 1.5. Examples of stimuli-responsive or "smart" polymer brushes (a) Poly(acrylic acid) (PAAc) collapses in acidic conditions due to protonated alcohols causing hydrophobicity, but swells in basic conditions because the deprotonated alcohols' negative charges repel each other. (b) Poly((dimethylamino)ethyl)methacrylate (PDMAEMA) shows inverted responses to those in PAA, swelling in acidic conditions, due to protonated amines, and collapsing in basic ones, due to hydrophobicity. Figures not to scale.

The swelling and collapsing of smart polymers is caused by the disruption of polymer-polymer and polymer-solvent intermolecular forces. The clearest example of smart polymers is the structural changes of acidic and basic polymers, such as poly(acrylic acid) (PAAc) and poly((dimethylamino)ethyl methacrylate) (PDMAEMA) (**Figure 1.5**), as the environmental pH changes. Briefly, underneath acidic conditions, PAAc is a neutral polymer brush, so it is collapses due to hydrophobic forces.[79] By contrast, PDMAEMA is positively charged from the tertiary amine, causing each individual polymer to repel from the others, leading to swelling (**Figure 1.5**).[76] The inverse happens at basic conditions, as PAAc, now negatively charged, begins repelling and swelling, while PDMAEMA, no longer charged, collapses. Ionic small molecules have also been shown to impact this reaction, by screening the charge repulsion of the polymer brushes.[79–82]

Figure 1.6. Generalized mechanism for the swelling or collapse of smart polymer brushes to amplify small molecule signals, based off of the experimental design in [92]. The analyte binds to the polymer brushes, causing signal as its charge gets near the surface. But because it is acidic, it also causes the polymer to swell. This not only allows more analyte close to the surface, increasing signal, but it also allows more charged molecules non-specifically to the surface causing signal amplification. When the analyte is not present, the collapsed polymer brush does not allow any non-analytes to the surface. Figures not drawn to scale.

There are a variety of ways to measure polymer brush swelling and collapsing. The most common way of measuring polymer brush volumetric change is via ellipsometry,[76,82,83] which measures the relative rotation of light as it passes through different materials and uses that data to model the materials' thicknesses.[80] Other methods for measuring polymer brush swelling include

surface-sensitive techniques like QCM-D,[79,84,85] AFM,[81,86,87] and FT-IR.[88,89] Some groups have developed novel technology based upon polymer brush swelling and collapse, by creating an optical sensor out of poly(N-isopropylacrylamide)-co-(acrylic acid) (pNIPAM-co-AAc) polymer brushes grafted to two Au coated glass surfaces.[90] The swelling or collapsing of the polymer brush causes a change in the resonance wavelength of the optical sensor, known as an etalon, indirectly allowing measurement of environmental conditions such as pH, temperature, and water content.[90]

Polymer brush swelling can be used for a variety of small molecule detection, if the small molecule itself causes changes in brush conformation. For instance, an electrochemical detector for sialic acid using a copolymer including the stimuli-responsive polymer poly(N-isopropylacrylamide) (PNIPAm) was developed such that sialic acid, upon binding to a boronic functional group, would cause PNIPAm to adopt a swollen conformation, which caused signal amplification by allowing more of the sialic acid analyte and other charged molecules to the surface (**Figure 1.6**).[91] It is important to note that on other platforms, the increase in polymer brush swelling could lead to more solvation of the brush, which is also measurable. To use polymer brushes' swelling and collapsing as a viable detection amplification method, it is necessary to fully characterize the brush interactions with a variety of common interferents, as well as under a variety of environmental conditions.

An alternative polymer matrix which could be used for small molecule detection is hydrogels, cross-linked polymers that swell in the presence of water. Hydrogels offer the benefit of high porosity, and thus a large interface between sample and sensing phase. They also provide a stabilizing liquid environment for proteins and antibodies, thus making them strong matrix candidates for biological analyses as has been discussed extensively in prior reviews.[92–96] Similar

to polymer brushes, hydrogels can also be stimuli-responsive, but their swelling or collapse is limited by the crosslinker used.[97,98]

Most techniques for small molecule detection using hydrogels will be either flow-based or colorimetric. Flow-based hydrogel detection has particularly found its stride in DNA-based hydrogels.[92,94,95] For instance, in a recent paper-based analytical device, the DNA from the hydrogels could either interact as a monomer, working to be part of the hydrogel, or interact as an aptamer to the small molecule, preventing hydrogel formation.[99] The presence of the small molecule of interest, defined by the aptamer used, allows for more flow which can be measured using distance traveled against a constant pressure, similar to a barometer. This method has been used to measure a variety of small molecule targets including cocaine, lead and adenosine, in high ionic strength matrices such as urine.[99] An alternative method, focused around hydrogels' encapsulating abilities, has been shown using pre-established DNA hydrogels. Typically, in the presence of the analyte, in this case aflatoxin B1, the aptamer would dissociate from the nanoparticle-laden hydrogel to interact with the analyte of interest. As the hydrogel structure would be broken, colored nanoparticles would be released and detected.[100] Other assays have similar methodology but release enzymes rather than nanoparticles, allowing downstream signal amplification.[101] A potential expansion for organic polymer hydrogels would be to take inspiration from these encapsulating methods and use labile linkers, such as an acid or base labile linker, in an organic hydrogel for detection of a small molecule which change pH (**Figure 1.7**). This core concept, of an analyte cleaving a polymer, has already been used for electrochemical detection of proteins using antibodies as a specificity agent,[102] but has not been used with hydrogel flow detection before. The hydrogel's dissociation could be measured either by the

release of nanoparticles, or by the change in measured flow rate when a certain pressure is applied.

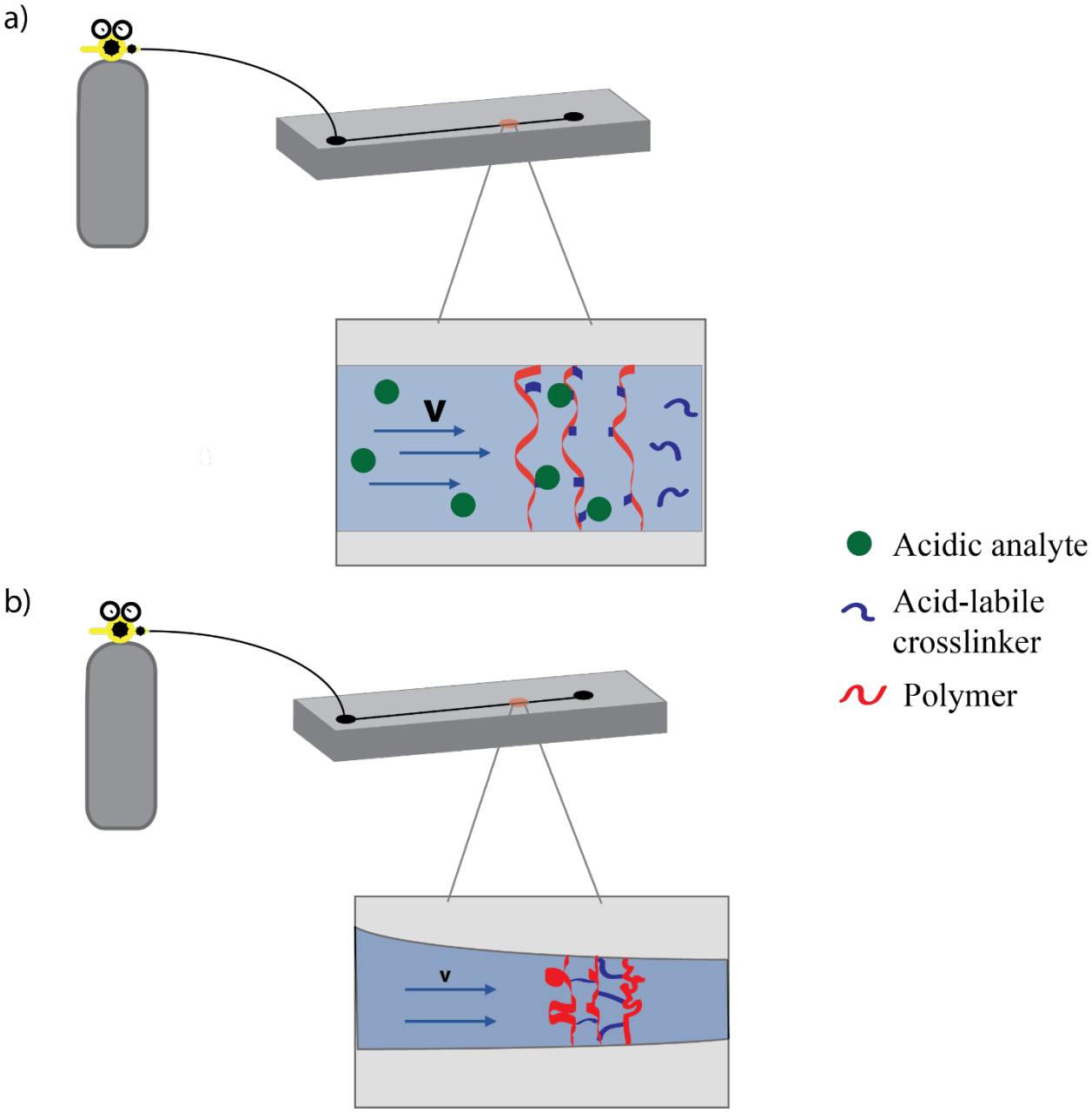

Figure 1.7. Detection scheme for acidic analyte with hydrogel with acid-labile crosslinker. (a) If the analyte is present, the acid-labile crosslinker is broken allowing the polymers to relax. This lowers internal resistance so the same pressure should provide a higher flowrate. (b) If the analyte is not present, the crosslinker stiffens the hydrogel and compresses the walls of the channel. The hydrogel has a higher fluidic resistance than just the polymers, leading to reduced flowrate with the same inlet pressure. Figures not drawn to scale.

Other assays use a change in hydrogel structure upon the presence of an analyte, compared to completely creating or destroying the hydrogel. For instance, hydrogels have been used to capture transition metals, like copper, as their crosslinkers, causing color changes by the transition metals presence which could be measured and be correlated to the ion concentration.[103] More interesting, in my opinion, is the recent article which used Bisphenol A (BPA) as an additional crosslinker for the pre-formed hydrogel. BPA interacted with cyclodextrin-modified hydrogel, leading to the BPA acting as a crosslinker and pulling the hydrogel tighter, which limited volumetric flow.[104] While the 120 μg/mL sample of BPA used is a higher concentration than the nanomolar concentration considered ideal for small molecule measurement, this format for small molecule detection relies on minimal instrumentation and could be improved by modulating the number of crosslinks per small molecule, causing a more intense volume change at low concentrations. Recent studies have also suggested that introducing more porosity, known as "voids," can increase the volume responsiveness of hydrogels,[105] potentially lowering detection limits further.

Another way of measuring hydrogel volume change due to analyte presence is colorimetric, via photonic crystals integration. Photonic crystals change their diffracted wavelength based upon their distance from each other. As the hydrogel changes volume so does the distance between the photonic crystals, changing the hydrogel's color.[106] Photonic crystal hydrogels, pioneered by the Asher group, have been used to detect a variety of small molecules by selective analyte polymer interactions including lectin-carbohydrate,[107] and human serum phenylpyruvate with oxyamine.[108] Other groups have continued to exploit photonic crystals with glucose detection using boronic acid[109] and humidity detection using acrylamide.[110] This novel relationship between distance and light could also be applied to other optical sensing schemes,

such as developing a hydrogel with FRET pairs. Hydrogels with aggregation induced emission or fluorescence quenching could also be developed for specific small molecules, potentially allowing better sensitivity in complex matrices.

Future work in the hydrogel space should focus on the integration of MIPs in hydrogels for volumetric changes in the presence of analytes, as this is a sensitive and selective technique that requires minimal instrumentation. Hydrogels have also been shown to funnel analytes through the formation of chemical gradients,[111] allowing the pre-concentration of analytes prior to measurement. These chemical gradients could be incorporated into more hydrogels for better limits of detection. Finally, a response relative to both polymer-based detection themes would be to incorporate more enzymes into design for amplified response. For instance, if an analyte interacts with an enzyme and causes the production of a proton, the local pH would change,[112,113] causing the polymer brush to change its conformation. This amplifies the local signal just from the single analyte, while also allowing enzymatic turnover for enhanced detection capabilities.

1.4 USE OF LIQUID-LIQUID EXTRACTION FOR SMALL MOLECULE DETECTION

While there are a variety of liquid-liquid extraction technologies, most extractions do not occur at the same time as detection. Those that do tend to rely on changes in optical properties due to the transfer of the analyte of interest from the aqueous to organic phases. I will be discussing LLED in two broad categories: ion-selective optodes (ISOs) (which technically have a solid interface but due to plasticizers the organic phase is modelled as a very viscous liquid) and microfluidic LLE, a major movement forward to minimize waste and sample loss.

1.4.1 Ion-Selective Optodes

Ion-selective optodes (ISOs) are materials which change color/fluorescence in the presence of an analyte of interest. An ionophore in a plasticized polymer matrix interacts with the analyte of interest and pulls it into the organic phase. The analyte's presence causes a charge imbalance, which is rectified by changing the charge state of the chromoionophore, which will change its fluorescent and colorimetric properties (**Figure 1.8**).[114–116] Lipophilic salt ion-exchangers are sometimes added to increase the speed of equilibration.[117] Unlike ion-selective electrodes, ISOs are bulk measurements rather than interfacial measurements, meaning that typical equilibration times can range from minutes to hours.

Optodes have been used to measure a variety of cations, anions, and neutral analytes, as has been discussed in many reviews.[114,118,119] More specifically, many common analytes have been measured using ISOs including potassium,[120–125] chloride,[123,126,127] heparin,[128–131] nitrite,[132] and protamine[130,133] among others. As is to be expected, there is currently a focus on expanding the analytes which optodes can be used to detect. These include transition metals such as silver and mercury[134] as well as developing miniature optodes for oxygen detection.[135] There is also a focus on expanding to more organic analytes of medical interest.

In order to detect an analyte for which there is no specific ionophore, like ibuprofen, a competitive assay was set up between an anionic surfactant and ibuprofen, which share similar charged characteristics. An increase in ibuprofen concentration lead to better pairing with the Rhodamine B octadecyl ester perchlorate (RBOE), encouraging RBOE to transfer into the lipophilic phase, disaggregate, and fluoresce.[136] In an attempt to expand the fields of analytes for detection, there has also been a renewed interest in using ionic liquids to solvate the polymer membrane. Ionic liquids have been shown to play different roles in optode chemistry, including

acting as ionophores for alkylamines[137] and serum albumin,[138] as well as a highly concentrated solvated dye, improving sensitivity and response time.[139,140] Ionic liquids also expand analytes by being a very polar phase immiscible with water, for instance, allowing the rapid measurement of the polyanion heparin, which has a large charge density.[140]

Another current focus in optodes research is changing the optodic matrix so it is cheaper, easier to synthesize or faster to equilibrate. A variety of alternative matrices to the traditional poly(vinyl chloride) (PVC) have been explored, including other polymers including polymethacrylate-poly(ethylene glycol) biphasic polymers and polycaprolactone. The variation in polymers used has been focused on environmentally friendliness, as polycaprolactone and PEG are both biodegradable, as well as the potential for implantable optodes.[141,142] Using biphasic polymers also allows better dye partitioning due to the more favorable local environment. There has also been a movement into using paper or other fiber-based optodes. Benefits of paper optodes include their low cost, hydrophilicity, small size, and environmental friendliness.[134] Paper and other fibers also have a high surface area to volume ratio and high porosity, leading to faster equilibration and measurements.

In order to improve extraction times, there has also been an emphasis in incorporating ISOs into nanoparticles, getting inspiration from DLLME (dispersive liquid-liquid microextraction). Nanoparticle based-ISOs have resulted in equilibration times as low as 10 minutes, much faster than the hours required for ISO equilibration.[31,136,141] Recent work has

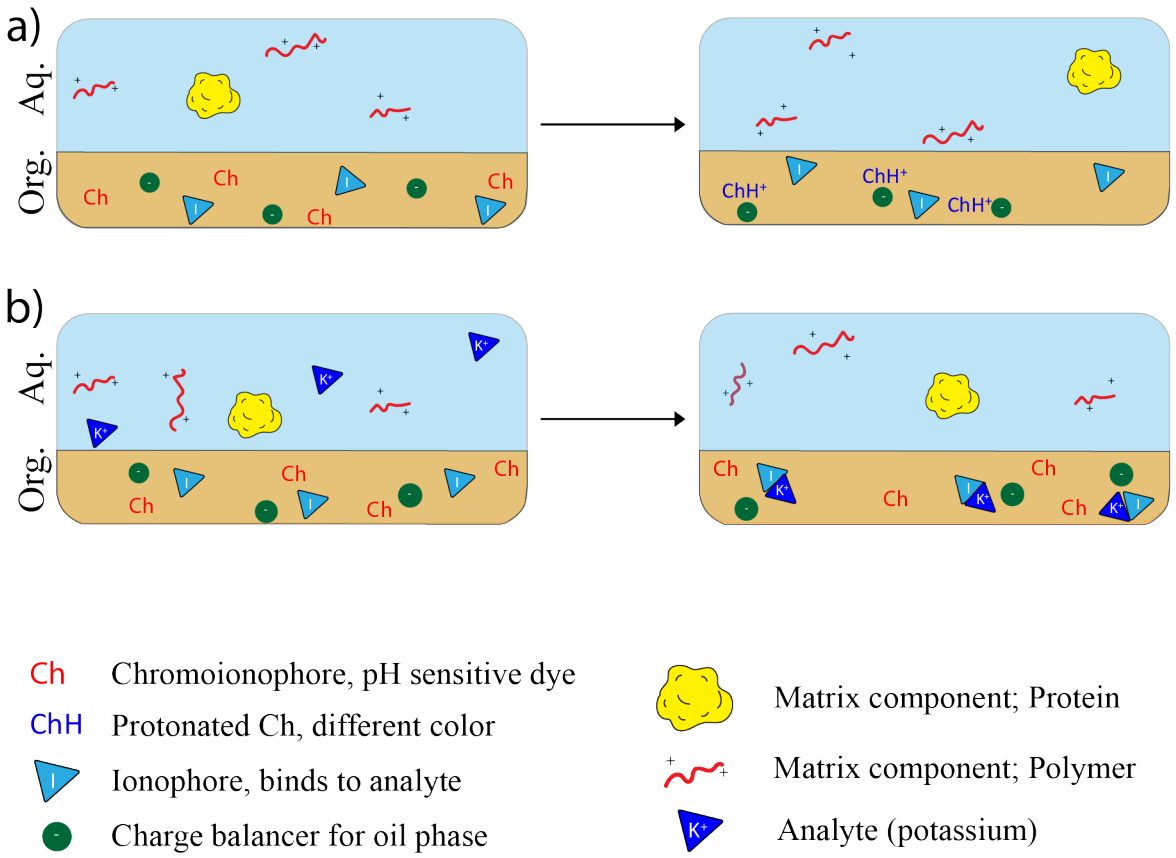

Figure 1.8. Mechanisms behind ion sensitive optodes. The organic phase for the ISO contains a pH-sensitive chromoionophore, an ionophore specific to the analyte of interest (in this case potassium ions), and a charge balancer to balance the charges in the oil phase. (a) When no potassium is present in the aqueous sample, hydrogen partitions from the aqueous phase to balance out the negative charge balancer, protonating the chromoionophore. The protonation of the chromoionophore causes it to change color and/or fluorescence. (b) When potassium is in the aqueous sample, the potassium binds to the ionophore and partitions into the oil phase. The positive charge from potassium acts as the counterion cation to the anionic charge balancer, so there is no need for hydrogen to protonate the chromoionophore. Figures not drawn to scale.

demonstrated that nanoparticles' optimization have less of a reliance on dye concentration than traditional ISOs, likely due to the larger interface with the sample.[143] Thus, nanoparticles could also lead to less reagent waste, as well as a potentially lower background, making them attractive alternatives to traditional ISOs. Preliminary results have demonstrated nanoparticle ISOs could

potentially use less concentrated dye,[143] but more studies in complex matrices need to be performed.

Aside from long equilibration time, ISOs are also limited in terms of sensitivity due to limits in concentrations of dye in the polymer phase. One means around this is to modify the polymer matrix to incorporate both hydrophobic and hydrophilic monomers in order to increase dye solubility.[142] Another study amplified the fluorescent signal using FRET. Specifically, the plasticizer chosen for the experiment was a fluorescent dye liquid and could serve as a donor in a FRET pair with the fluorescent sensing dye.[144] Using FRET pairs allowed a 22-fold increase in sensitivity with a lower sensing dye concentration,[144] but further studies in complex matrices should be performed to ensure selectivity of the ISO is not impacted.

A challenge with most chromoionophores currently is their pH sensitivity, which can cause challenges if working in a matrix with variable pH. A novel focus, based on work originally from the Bakker lab, is to use solvatochromatic, rather than pH sensitive, dyes. The presence of an analyte of interest will cause a charge transfer across the aqueous to organic interface, which then expels the dye into the aqueous phase causing a change in dye color or fluorescence. This has no reliance on pH; thus pH variation does not impact the sensitivity of the technique. Solvatochromatic dyes have been used in ISOs to determine calcium[145] and potassium concentrations.[143,146,147] Solvatochromatic dyes have also been shown to be both specific against common ionic interferants, like sodium,[146] and tunable by their lipophilicity.[147] Solvatochromatic dyes have allowed the creation of Nylon ISOs without plasticizers,[146] decreasing concerns over reagent leeching from the optode to the aqueous sample. So far, no studies have been published testing solvatochromatic dye behaviors in complex mixtures or biological samples, which would be necessary for this technique to be adopted in more ISOs moving forward.

An alternative to using solvatochromatic dyes has focused on modifying traditional fluorescence methods, including using ion-dependent dimerization of a dye Ion-dependent dimerization gave high sensitivity based on the change in fluorescence caused by the dimer for potassium, copper and lead.[31] As the dimerization cause near-infrared (NIR) fluorescence, the impact from blood on scattering and fluorescence was minimal, as demonstrated when potassium was detected in blood.[31] Ion-dependent dimerization was demonstrated to be pH independent across a wide pH range,[31] but more testing of the transition element ions in complex matrices should be performed.

Other work has been performed using aggregated emission/quenched dyes as part of ISOs. The basic premise of aggregated emission dyes is the ion-exchange, occurring due to analyte transfer, will concentrate the dyes within nanospheres of organic phases, causing them to either fluoresce (in the case of aggregated emission dyes) or stop fluorescing (when using aggregated quenched dyes).[136,148] While nanosensors using aggregated emission dyes were successfully used to detect potassium and sodium in buffered samples, when applied to complex samples there was interference caused by serum scattering and excitation.[148] The interference suggests the need for an additional extraction or purification before using the nanospheres. Potentially, changing the dye to have NIR fluorescence could also limit serum scattering and excitation, increasing sensitivity.

1.4.2 Microfluidic LLED

Some microfluidics LLEDs parallel the flow LLE discussed earlier in this chapter. For instance, a Y channel microfluidic chip has been developed which establishes a two-level flow between organic and aqueous phases. The ions are extracted into the organic phase using

ionophores and then detected using thermal lens microscopy. Both potassium and sodium were detected using less than 500 nL of solution, even when mixed together, down to a concentration of 10^{-4} M.[149] LLED has also been performed through a microporous membrane separating the aqueous and organic phases, adding a size selectivity to a more generalized extraction, utilizing fluorescence to detect the analyte.[150]

There are also many microfluidic systems that mimic single organic droplet microextractions. In these systems, organic phase droplets are trapped in recesses in the

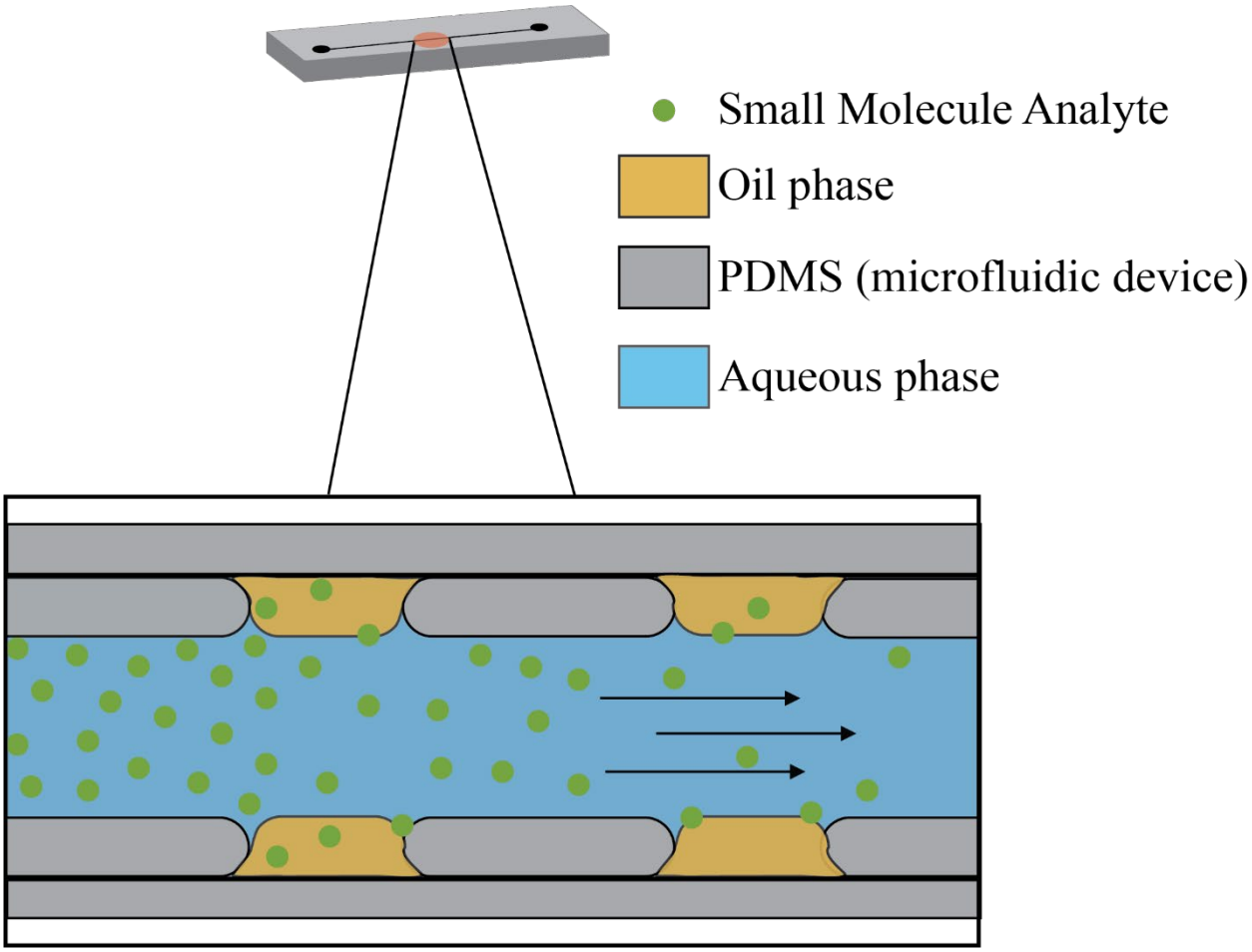

Figure 1.9. Microfluidic single organic droplet extraction. The oil phase (yellow) is trapped in wedges in the device. Aqueous phase with the analyte of interest (green) is then flowed through the device, allowing the analyte to partition into the oil phase. After the aqueous phase is done flowing, the oil phase can be expelled, and other manipulations can be performed on it. Figures not drawn to scale.

microfluidic device as aqueous phase continuously flows through the center of the device (**Figure 1.9**). Thus, the organic phase is exposed to many different aqueous interfaces, concentrating the analyte in the organic phase. Proof of concept studies demonstrated partitioning of butyl rhodamine B into 1-hexanol drops using laser induced fluorescence,[151] as well as performing droplet manipulation steps after the extraction to follow a chemiluminescent detection procedure, allowing multiplexing.[152] An alternative system has been created which uses a static droplet produced via a capillary, and detects the analyte using the capillary as a liquid core waveguide. [153] These techniques allow minimal solvent phase, thus less waste and

higher analyte concentration, as well as the use of small sample volumes, on the orders of nano- to microliters compared to the milliliters typically used in bulk.

Due to its excellent mixing capabilities, homogeneous LLE (HLLE) should be explored to see if it could provide more sensitivity or faster equilibration towards microfluidic LLEDs. There have been no studies attempting to performing homogeneous LLE on chip, despite the

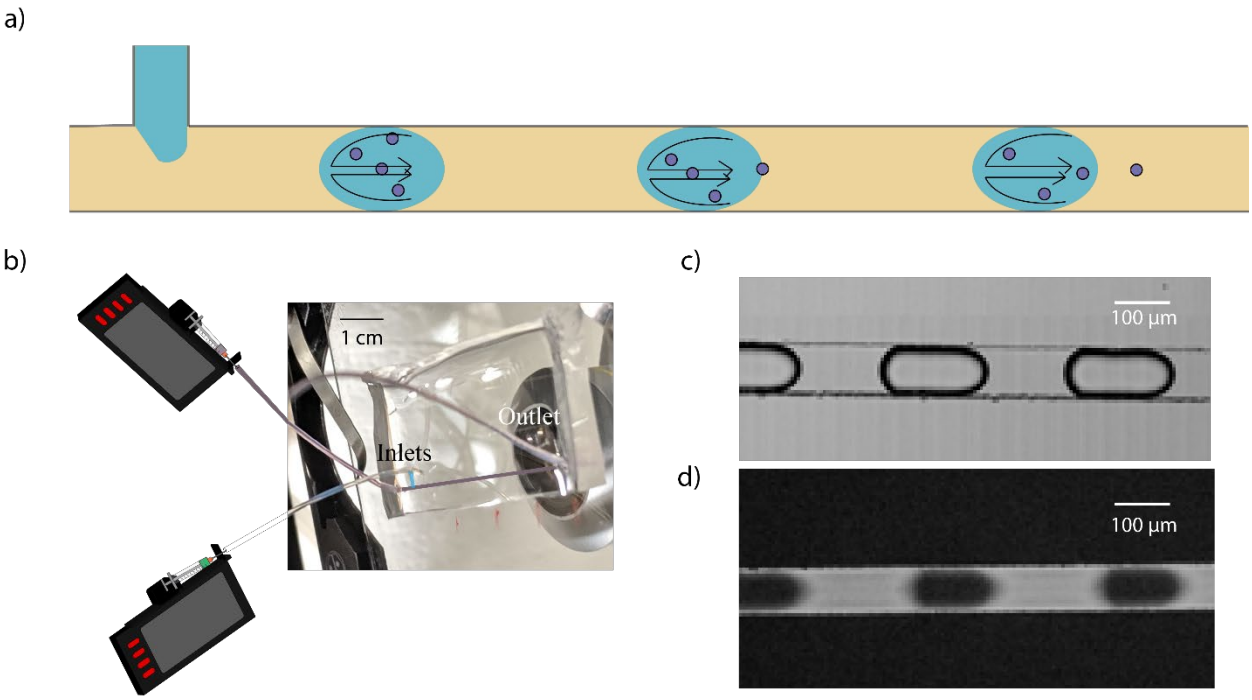

Figure 1.10. Droplet microfluidics. (a) Schematic of enhanced mixing caused by microfluidic droplet formation. Figure not drawn to scale. (b) Example of microfluidic chip being run using syringe pumps to control fluid flow. (c) Example of brightfield images of microfluidic droplets using a high-speed camera. (d) Example of fluorescent images of microfluidic droplets using a high-speed camera.

promise of its infinite interface. This is potentially because of the challenges of temperature and concentration changes on chip. However, adding salt and pH changes has been performed in microfluidic devices before.[154] There potentially could be challenges differential interaction

between one of the solvents with the channel walls v the middle of the channel, so that also would need to be further explored.

Further progress has been made to microfluidic LLEs by taking inspiration from DLLME and using droplet microfluidics rather than just microfluidic extraction. In droplet microfluidics, small droplets of an aqueous or oil phase are suspended and carried through the device by another immiscible phase (**Figure 1.10**). Droplet microfluidics offers the benefits of large surface area to volume ratios for the droplets, as well as improved mixing within the droplet themselves which improves extraction efficiency.[155] A variety of examples have used droplets as a means of improving extraction. One example developed slow nanoliter droplet extraction techniques by suspending adjacent aqueous and organic phases so that they interface.[155] In another case, nanoliter droplets were generated within an extractive carrier phase, resulting in fluorescent aluminum detection.[156] Microfluidic droplets have also been modeled and shown to perform well in immiscible organic-organic liquid extractions, such as the extraction of azobenzene from methanol into n-octane,[157] as well as for fluorescent extractions in both the droplet phase and carrier phase.[158]

A novel technique developed by the Meyerhoff group, in conjunction with the Bailey lab, has recently combined droplet microfluidic LLEs with ion-selective optodes to make microfluidic droptodes.[159] Each aqueous droplet acts as an isolated sample interacting with the carrier oil phase. The carrier oil phase contains the ionophore, ion-exchanger and chromoionophore typically found in optodes (**Figure 1.11**). When the analyte binds the ionophore and crosses the interface, there is a change in the charge state of the chromoionophore causing a change in both color and fluorescence. Effectively the carrier phase acts as an ISO for the droplet. Using microfluidic droptodes, a variety of ions were detected including potassium,

chloride and protamine, with limits of detection an order of magnitude below traditionally ISOs.[159] Microfluidic droptodes were also shown to detect potassium in 50% diluted whole blood, as the oil sensing phase was isolated from the blood contained in the droplet.[159] The microfluidic droptode system, by relying on fluorescence not inherent to the molecule, expands the range of analytes which can be detected, including some non-charged analytes like hydrogen peroxide.[159] The limitation of the droptode methodology, generally, is the need for a specific ionophore for an analyte of interest, which quickly becomes complicated as molecules become bigger.

The reliance on both droplet microfluidics and fluorescence measurement makes this an ideal point-of-analysis application. Microfluidics are known for being extremely portable and using minimal sample volume, which increases the amount of applications to which droptodes can bne applied. The fluorescence measurements, as stated before, are also portable and use minimal instrumentation, only a smartphone. Fluorescent measurements also require minimal data interpretation, allowing the droptode technology to be more accessible. Microfluidic droptodes so far have mainly been applied to biological analytes, but should hopefully soon be applied to a variety of charged pollutants and potentially extracts from solid matrices, to push the system to its limits.

There is still significant optimization required for microfluidic LLEDs. Very few studies have explored performing microfluidic LLE in complex biological matrices like blood, serum, plasma or urine. Also there has been minimal demonstratable optimization of channel design and droplet size for optimal extraction-detection capabilities.[158,160] It is also still necessary to analyze the impact of differential parameters, like viscosity, on microfluidic LLED, which would be important for certain applications, such as moving into human samples where characteristics like

blood viscosity can differ drastically. Microfluidics also offers the opportunity to couple multiple devices together, potentially allowing sequential extractions which has not yet been observed with microfluidic LLEs or LLEDs.

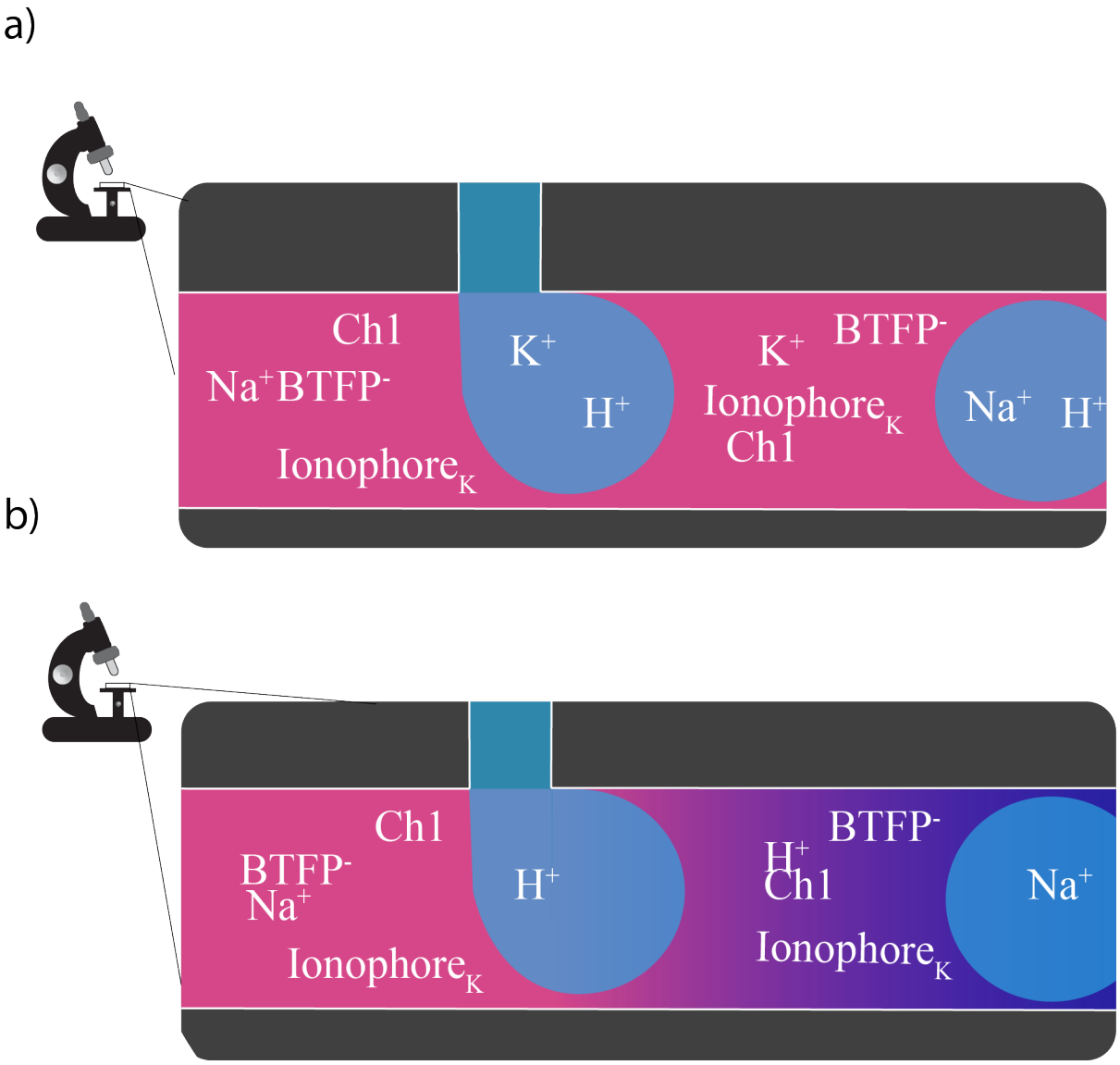

Figure 1.11. Droptode mechanism. (a) When the analyte, in this case potassium, is not present, the protonation of the chromoionophore is used to balance the charge exchanger, leading to a color change. This is the same mechanism as in ISOs, but the oil phase is liquid rather than plasticized polymer. (b) When potassium is present, it serves to balance the charge exchanger after it is extracted to the oil phase by the ionophore, again paralleling ISOs. Figure adapted with permission from [160]. Figures not drawn to scale.

1.5 CONCLUSIONS

In this chapter, I have described a variety of extraction and detection methodologies to use for small molecule detection, focusing on both solid and liquid phase extraction. While some techniques, such as molecularly imprinted polymers, are extremely specific for the molecule of interest, others, such as polymer brushes, provide much less specificity but a better general measurement of the total small molecule content of the solution. Combining solid phase and liquid-liquid extraction with detection capabilities typically rely on either surface-sensitive techniques, upon which concentration of the analyte of interest can occur, or on fluorescent or colorimetric detection in the organic phase, as is seen with ISOs and a majority of LLEDs. Both SPED and LLED are pushing towards greener chemistries with less solvent waste, as well as creative techniques to ensure faster equilibration.

This chapter has highlighted the scarcity of small molecule detection technologies that can work rapidly in complex matrices, especially when the sample is limited. Therefore, this dissertation will focus on developing novel SPED and LLED technologies to detect small molecules, using less than 1 mL of sample and less than 10 minutes of time. Microfluidic technology will be combined with organic extractions on different detection platforms to detect a variety of organic and inorganic small molecules. In Chapter 2, a SPED technology was developed by growing a variety of polymer brushes on silicon photonic microring resonators, allowing the determination of small molecules' partition coefficients, diffusion coefficients and depths of partitioning. The changing behavior of polymer brushes under different pH conditions was also highlighted as a means of altering polymer brush-analyte interactions. Using polymer brushes on silicon photonic microring resonators could allow for the rapid screening of polymer brushes for protective coatings against small molecules under different buffering conditions, as it

uses only 200 µL of sample, nanometers of polymer brush and less than 10 minutes of runtime per condition. However, while useful for industrial applications, the global accessibility of silicon photonic microring resonators' instrumentation is limiting. Therefore, in Chapters 3 through 5, I explored a more universal point-of-analysis LLED technology, microfluidic droptodes. As discussed above, microfluidic droptodes have demonstrated promise for the quantification of small charged species, such as ions like potassium and chloride, even in complex matrices. The novelty of the technology, however, left much room for improvement and exploration. Thus, in Chapter 3, I analyzed the impact of changing droplet speed and size on microfluidic droptode behavior. By tuning the droplet size and the amount of in-channel mixing, I was able to move the limit of detection for the microfluidic droptode by over one order of magnitude, demonstrating the versatility of the microfluidic droptode device for a variety of applications. In Chapter 4, I continued to expand the microfluidic droptode toolbox by developing a multiplexable microfluidic droptode, using fluorinated oil to separate the analyte-sensitive phases. The new multiplexability allows applications, such as whole blood electrolyte analysis, to be explored, as demonstrated in Chapter 4. Using microfluidic droptodes for blood electrolyte analysis would minimize blood draws needed in emergencies, as it can use as little blood as a finger prick. In Chapter 5 I….Finally, in Chapter 6, I took a foray into chemical education research, developing a relevance motivated ELISA lab for a Bioanalytical Chemistry course. Overall, this dissertation demonstrates…

1.6 REFERENCES

1. Todd, E. Perchlorate as an Environmental Contaminant. *Environ. Sci. Pollut. Res.* **9**, 187–192 (2002).

2. García, S., Albero, I., Ortuño, J. A., Sánchez-Pedreño, C. & Expósito, R. Flow-Through Bulk Optode for the Spectrophotometric Determination of Perchlorate. *Microchim. Acta* **143**, 59–63 (2003).

3. Zinc - Health Professional Fact Sheet. https://ods.od.nih.gov/factsheets/Zinc-HealthProfessional/.

4. Schwartz, A. B. Potassium-Related Cardiac Arrhythmias and Their Treatment. *Angiology* **29**, 194–205 (1978).

5. Walz, W. Role of Astrocytes in the Clearance of Excess Extracellular Potassium. *Neurochem. Int.* **36**, 291–300 (2000).

6. Morrissey, J. H., Choi, S. H. & Smith, S. A. Polyphosphate: An Ancient Molecule that Links Platelets, Coagulation, and Inflammation. *Blood* **119**, 5972–5979 (2012).

7. Smith, S. A. *et al.* Inhibition of Polyphosphate as a Novel Strategy for Preventing Thrombosis and Inflammation. *Blood* **120**, 5103–5110 (2012).

8. Roewe, J. *et al.* Bacterial Polyphosphates Interfere with the Innate Host Defense to Infection. *Nat. Commun.* **11**, 1–12 (2020).

9. U.A. Safety Data Sheet . NB Safety Data Sheet. *Mater. Saf. Data Sheet* **4(2)**, 8–10 (2012).

10. Sulej-Suchomska, A. M. *et al.* Urban Wastewater Analysis as an Effective Tool for Monitoring Illegal Drugs, Including New Psychoactive Substances, in the Eastern European region. *Sci. Rep.* **10**, 81–87 (2020).

11. US EPA. *Drinking Water Health Advisories for PFOA and PFOS*. https://www.epa.gov/ground-water-and-drinking-water/drinking-water-health-advisories-pfoa-and-pfos (2019).

12. Peltomaa, R., Glahn-Martínez, B., Benito-Peña, E. & Moreno-Bondi, M. C. Optical Biosensors for Label-Free Detection of Small Molecules. *Sensors.* **18**, (2018).

13. Committee, R. A. M. *Guide to achieving reliable quantitative LC-MS measurements*. *Committee, RSC Analytical Methods* vol. 1 (2015).

14. Zhang, A., Sun, H., Wang, P., Han, Y. & Wang, X. Modern Analytical Techniques in Metabolomics Analysis. *Analyst* **137**, 293–300 (2012).

15. Li, B. *et al.* Performance Evaluation and Online Realization of Data-Driven Normalization

Methods used in LC/MS Based Untargeted Metabolomics Analysis. *Sci. Rep.* **6**, 1–13 (2016).

16. Barceló, D. & Petrovic, M. Challenges and achievements of LC-MS in Environmental Analysis: 25 Years On. *TrAC - Trends Anal. Chem.* **26**, 2–11 (2007).

17. Lucci, P., Saurina, J. & Núñez, O. Trends in LC-MS and LC-HRMS Analysis and Characterization of Polyphenols in Food. *TrAC - Trends Anal. Chem.* **88**, 1–24 (2017).

18. Lim, C. K. & Lord, G. Current Developments in LC-MS for Pharmaceutical Analysis. *Biol. Pharm. Bull.* **25**, 547–557 (2002).

19. Dahal, U. P., Jones, J. P., Davis, J. A. & Rock, D. A. Small Molecule Quantification by Liquid Chromatography-Mass Spectrometry for Metabolites of Drugs and Drug Candidates. *Drug Metab. Dispos.* **39**, 2355–2360 (2011).

20. Kinghorn, R., Milner, C. & Zweigenbaum, J. Analysis of Trace Residues of Explosive Materials by Time-of-Flight LC/MS. *Agil. Technol. Appl. Note* 1–18 (2006).

21. Davey, N. G., Bell, R. J., Gill, C. G. & Krogh, E. T. Mapping the Geospatial Distribution of Atmospheric BTEX Compounds Using Portable Mass Spectrometry and Adaptive Whole Air Sampling. *Atmos. Pollut. Res.* **11**, 545–553 (2020).

22. Viveros, L., Paliwal, S., McCrae, D., Wild, J. & Simonian, A. A Fluorescence-based Biosensor for the Detection of Organophosphate Pesticides and Chemical Warfare Agents. *Sensors Actuators, B Chem.* **115**, 150–157 (2006).

23. Cetó, X., González-Calabuig, A., Capdevila, J., Puig-Pujol, A. & Del Valle, M. Instrumental Measurement of Wine Sensory Descriptors Using a Voltammetric Electronic Tongue. *Sensors Actuators, B Chem.* **207**, 1053–1059 (2015).

24. Ray, A. *et al.* Measurement of Serum Phosphate Levels Using a Mobile Sensor. *Analyst* **145**, 1841–1848 (2020).

25. Wang, H. *et al.* Semiquantitative Visual Detection of Lead Ions with a Smartphone via a Colorimetric Paper-Based Analytical Device. *Anal. Chem.* **91**, 9292–9299 (2019).

26. Ayres, L. B., Lopes, F. S., Garcia, C. D. & Gutz, I. G. R. Integrated Instrumental Analysis Teaching Platform with Smartphone-Operated Fluorometer. *Anal. Methods* **12**, 4103–4174 (2020).

27. Al Amin, M., Sobhani, Z., Chadalavada, S., Naidu, R. & Fang, C. Smartphone-based / Fluoro-SPE for Selective Detection of PFAS at ppb Level. *Environ. Technol. Innov.* **18**, 100778 (2020).

28. Hossain, A., Member, S., Canning, J., Ast, S. & Peter, J. Lab - in - a - phone : Smartphone - based Portable Fluorometer for pH Field Measurements of Environmental Water. *IEEE*

Sensors. **15**, 5095 (2014).

29. Bueno, D., Muñoz, R. & Marty, J. L. Fluorescence Analyzer Based on Smartphone Camera and Wireless for Detection of Ochratoxin A. *Sensors Actuators, B Chem.* **232**, 462–468 (2016).

30. Cao, Z., Tseng, H. Y., Salvante, K., Nepomnaschy, P. & Parameswaran, M. A. High Sensitivity Fluorescence Detection Using Smart Phone Cameras. *Proceedings of IEEE Sensors* (2017). doi:10.1109/ICSENS.2016.7808864.

31. Deng, L., Zhai, J., Du, X. & Xie, X. Ionophore-Based Ion-Selective Nanospheres Based on Monomer–Dimer Conversion in the Near-Infrared Region. *ACS Sensors* (2021) doi:10.1021/acssensors.0c02577.

32. Malone, B. R., Humphrey, C. W., Romer, T. R. & Richard, J. L. Determination of Aflatoxins in Grains and Raw Peanuts by a Rapid Procedure with Fluorometric Analysis. *JOURNAL OF AOAC INTERNATIONAL*. **83** (2000).

33. Jenkins, A. L., Yin, R. & Jensen, J. L. Molecularly Imprinted Polymer Sensors for Pesticide and Insecticide Detection in Water. *Analyst* **126**, 798–802 (2001).

34. Leavesley, S. J. & Rich, T. C. Overcoming Limitations of FRET Measurements. *Cytom. Part A* **89**, 325–327 (2016).

35. Andrade-Eiroa, A., Canle, M., Leroy-Cancellieri, V. & Cerdà, V. Solid-Phase Extraction of Organic Compounds: A Critical review. Part II. *TrAC - Trends Anal. Chem.* **80**, 655–667 (2016).

36. Andrade-Eiroa, A., Canle, M., Leroy-Cancellieri, V. & Cerdà, V. Solid-Phase Extraction of Organic Compounds: A Critical Review (Part I). *TrAC - Trends Anal. Chem.* **80**, 641–654 (2016).

37. Buszewski, B. & Szultka, M. Past, Present, and Future of Solid Phase Extraction: A Review. *Crit. Rev. Anal. Chem.* **42**, 198–213 (2012).

38. Hansen, F. A. & Pedersen-Bjergaard, S. Emerging Extraction Strategies in Analytical Chemistry. *Anal. Chem.* **92**, 2–15 (2019).

39. Poole, C. F. *Milestones in the development of liquid-phase extraction techniques*. *Liquid-Phase Extraction* (2020). doi:10.1016/B978-0-12-816911-7.00001-3.

40. Pena-Pereira, F., Lavilla, I. & Bendicho, C. Miniaturized Preconcentration Methods Based on Liquid-Liquid Extraction and Their Application in Inorganic Ultratrace Analysis and Speciation: A Review. *Spectrochim. Acta - Part B At. Spectrosc.* **64**, 1–15 (2009).

41. Anthemidis, A. N. & Ioannou, K. I. G. Recent Developments in Homogeneous and Dispersive Liquid-Liquid Extraction for Inorganic Elements Determination. A Review.

Talanta **80**, 413–421 (2009).

42. Silvestre, C. I. C., Santos, J. L. M., Lima, J. L. F. C. & Zagatto, E. A. G. Liquid-liquid Extraction in Flow Analysis: A Critical Review. *Anal. Chim. Acta* **652**, 54–65 (2009).

43. Masini, J. C. & Svec, F. Porous Monoliths for On-line Sample Preparation: A Review. *Anal. Chim. Acta* **964**, 24–44 (2017).

44. Sahore, V. *et al.* Automated Microfluidic Devices Integrating Solid-Phase Extraction, Fluorescent Labeling, and Microchip Electrophoresis for Preterm Birth Biomarker Analysis. *Anal. Bioanal. Chem.* **410**, 933–941 (2018).

45. Carrasco-Correa, E. J., Cocovi-Solberg, D. J., Herrero-Martínez, J. M., Simó-Alfonso, E. F. & Miró, M. 3D Printed Fluidic Platform with In-Situ Covalently Immobilized Polymer Monolithic Column for Automatic Solid-Phase Extraction. *Anal. Chim. Acta* **1111**, 40–48 (2020).

46. Bouvarel, T., Delaunay, N. & Pichon, V. Selective Extraction of Cocaine from Biological Samples with a Miniaturized Monolithic Molecularly Imprinted Polymer and On-line Analysis in Nano-liquid Chromatography. *Anal. Chim. Acta* **1096**, 89–99 (2020).

47. Chen, L., Wang, Z., Pei, J. & Huang, X. Highly Permeable Monolith-based Multichannel In-Tip Microextraction Apparatus for Simultaneous Field Sample Preparation of Pesticides and Heavy Metal Ions in Environmental Waters. *Anal. Chem.* **92**, 2251–2257 (2020).

48. Svec, F. Preparation and HPLC Applications of Rigid Macroporous Organic Polymer Monoliths. *Journal of Separation Science.* **27**, 747–766 (2004).

49. Turiel, E. & Martín-Esteban, A. Molecularly Imprinted Polymers-Based Microextraction Techniques. *TrAC - Trends in Analytical Chemistry*. **118**, 574–586 (2019).

50. Yu, X., Zeng, H., Wan, J. & Cao, X. Computational Design of a Molecularly Imprinted Polymer Compatible with an Aqueous Environment for Solid Phase Extraction of Chenodeoxycholic Acid. *J. Chromatogr. A* **1609**, 460490 (2020).

51. Arias, P. G. *et al.* Selective Solid-Phase Extraction of Organophosphorus Pesticides and their Oxon-Derivatives from Water Samples using Molecularly Imprinted Polymer followed by High-Performance Liquid Chromatography with UV Detection. *J. Chromatogr. A* **1626**, 461346 (2020).

52. Zhang, Z. *et al.* Synthesis of Dummy-Template Molecularly Imprinted Polymer Adsorbents for Solid Phase Extraction of Aminoglycosides Antibiotics from Environmental Water Samples. *Talanta* **208**, 120385 (2020).

53. Arabi, M. *et al.* Strategies of Molecular Imprinting-based Solid-Phase Extraction Prior to Chromatographic Analysis. *TrAC - Trends Anal. Chem.* **128**, 115923 (2020).

54. Xie, X. *et al.* Novel Magnetic Multi-Templates Molecularly Imprinted Polymer for Selective and Rapid Removal and Detection of Alkylphenols in Water. *Chem. Eng. J.* **357**, 56–65 (2019).

55. Karube, I. Optical Detection of Chloramphenicol using Molecularly Imprinted Polymers. *Anal. Chem.* **69**, 2017–2021 (1997).

56. Wagner, S., Bell, J., Biyikal, M., Gawlitza, K. & Rurack, K. Integrating Fluorescent Molecularly Imprinted Polymer (MIP) Sensor Particles with a Modular Microfluidic Platform for Nanomolar Small-Molecule Detection Directly in Aqueous Samples. *Biosens. Bioelectron.* **99**, 244–250 (2018).

57. Lavignac, N., Allender, C. J. & Brain, K. R. Current Status of Molecularly Imprinted Polymers as Alternatives to Antibodies in Sorbent Assays. *Anal. Chim. Acta* **510**, 139–145 (2004).

58. Shinde, S. *et al.* Urea-Based Imprinted Polymer Hosts with Switchable Anion Preference. *J. Am. Chem. Soc.* **142**, 11404–11416 (2020).

59. De Rycke, E. *et al.* Novel Multiplex Capacitive Sensor Based on Molecularly Imprinted Polymers: A Promising Tool for Tracing Specific Amphetamine Synthesis Markers in Sewage Water. *Biosens. Bioelectron.* **178**, (2021).

60. Pang, Y. H., Yue, Q., Huang, Y. Ying Yang, C. & Shen, X. F. Facile Magnetization of Covalent Organic Framework for Solid-Phase Extraction of 15 Phthalate Esters in Beverage Samples. *Talanta* **206**, 120194 (2020).

61. Zhang, M. *et al.* In-Situ Synthesis of Fluorinated Magnetic Covalent Organic Frameworks for Fluorinated Magnetic Solid-Phase Extraction of Ultratrace Perfluorinated Compounds from Milk. *J. Chromatogr. A* **1615**, 460773 (2020).

62. Peña-Méndez, E. M. *et al.* Metal Organic Framework Composite, nano-Fe3O4@Fe-(benzene-1,3,5-tricarboxylic acid), for Solid Phase Extraction of Blood Lipid Regulators from Water. *Talanta* **207**, 120275 (2020).

63. Dwadasi, B. S., Goverapet Srinivasan, S. & Rai, B. Interfacial Structure in the Liquid-Liquid Extraction of Rare Earth Elements by Phosphoric Acid Ligands: A Molecular Dynamics Study. *Phys. Chem. Chem. Phys.* **22**, 4177–4192 (2020).

64. Bourgeois, D., El Maangar, A. & Dourdain, S. Importance of Weak Interactions in the Formulation of Organic Phases for Efficient Liquid/Liquid Extraction of Metals. *Curr. Opin. Colloid Interface Sci.* **46**, 36–51 (2020).

65. Markina, N. E., Markin, A. V., Weber, K., Popp, J. & Cialla-May, D. Liquid-liquid Extraction-Assisted SERS-Based Determination of Sulfamethoxazole in Spiked Human Urine. *Anal. Chim. Acta* **1109**, 61–68 (2020).

66. Rebelo, T. S. C. R. *et al.* Molecularly Imprinted Polymer SPE Sensor for Analysis of CA-125 on Serum. *Anal. Chim. Acta* **1082**, 126–135 (2019).

67. Akhoundian, M., Alizadeh, T. & Pan, G. Fabrication of the Enzyme-less Voltammetric Bilirubin Sensor Based on Sol-gel Imprinted Polymer. *Electroanalysis* **32**, 479–488 (2020).

68. Ayankojo, A. G., Reut, J., Öpik, A., Furchner, A. & Syritski, V. Hybrid Molecularly Imprinted Polymer for Amoxicillin Detection. *Biosens. Bioelectron.* **118**, 102–107 (2018).

69. Kazemi, R., Potts, E. I. & Dick, J. E. Quantifying Interferent Effects on Molecularly Imprinted Polymer PFAS Sensors. *Anal. Chem.* **92**, (2020).

70. Fuchs, Y., Soppera, O., Mayes, A. G. & Haupt, K. Holographic Molecularly Imprinted Polymers for Label-Free Chemical Sensing. *Adv. Mater.* **25**, 566–570 (2013).

71. Heras, J. Y., Pallarola, D. & Battaglini, F. Electronic Tongue for Simultaneous Detection of Endotoxins and Other Contaminants of Microbiological origin. *Biosens. Bioelectron.* **25**, 2470–2476 (2010).

72. Sothivelr, K., Bender, F., Josse, F., Yaz, E. E. & Ricco, A. J. Obtaining Chemical Selectivity from a Single, Nonselective Sensing Film: Two-Stage Adaptive Estimation Scheme with Multiparameter Measurement to Quantify Mixture Components and Interferents. *ACS Sensors* **3**, 1656–1665 (2018).

73. Wade, J. H. & Bailey, R. C. Refractive Index-Based Detection of Gradient Elution Liquid Chromatography Using Chip-Integrated Microring Resonator Arrays. *Anal. Chem.* **86**, 913–919 (2014).

74. Stanton, A. L. D., Serrano, K. A., Braun, P. V. & Bailey, R. C. Polymer Brush-Modified Microring Resonators for Partition-Enhanced Small Molecule Chemical Detection. *ChemistrySelect* **2**, 1521–1524 (2017).

75. Barbey, R. *et al.* Polymer **B**rushes via Surface-Initiated Controlled Radical Polymerization: Synthesis, Characterization, Properties, and Applications. *Chem. Rev.* **109**, 5437–5527 (2009).

76. Willott, J. D. *et al.* Hydrophobic Effects Within the Dynamic pH-Response of Polybasic Tertiary Amine Methacrylate Brushes. *Phys. Chem. Chem. Phys.* **17**, 3880–3890 (2015).

77. Shu, T. *et al.* Stimuli-Responsive Polymer-Based Systems for Diagnostic Applications. *J. Mater. Chem. B* **8**, 7042–7061 (2020).

78. Appavoo, D., Park, S. Y. & Zhai, L. Responsive Polymers for Medical Diagnostics. *J. Mater. Chem. B* **8**, 6217 (2020).

79. Hollingsworth, N. R., Wilkanowicz, S. I. & Larson, R. G. Salt- and pH-Induced Swelling

of a Poly(acrylic acid) Brush: Via Quartz Crystal Microbalance w/Dissipation (QCM-D). *Soft Matter* **15**, 7838–7851 (2019).

80. Chudoba, R., Heyda, J. & Dzubiella, J. Tuning the Collapse Transition of Weakly Charged Polymers by Ion-Specific Screening and Adsorption. *Soft Matter* **14**, 9631–9642 (2018).

81. Lego, B., Skene, W. G. & Giasson, S. Swelling Study of Responsive Polyelectrolyte Brushes Grafted from Mica Substrates: Effect of pH, Salt, and Grafting Density. *Macromolecules* **43**, 4384–4393 (2010).

82. Zhang, H. & Ruhe, J. Swelling of Poly(methyacrlic acid) Brushes: Influence of Monovalent Salts in the Environment. *Macromolecules* **38**, 4855–4860 (2005).

83. Fielding, L. A., Edmondson, S. & Armes, S. P. Synthesis of pH-Responsive Tertiary Amine Methacrylate Polymer Brushes and their Response to Acidic Vapour. *J. Mater. Chem.* **21**, 11773–11780 (2011).

84. He, J. *et al.* Study and Application of a Linear Frequency - Thickness Relation for Surface-Initiated Atom Transfer Radical Polymerization in a Quartz Crystal Microbalance. *Macromolecules* **40**, 3090–3096 (2007).

85. Du, Y. *et al.* Understanding the Oxidative Stability of Antifouling Polymer Brushes. *Langmuir* **33**, 7298–7304 (2017).

86. Parnell, A. J. *et al.* Direct Visualization of the Real Time Swelling and Collapse of a Poly(methacrylic acid) Brush Using Atomic Force Microscopy. *Soft Matter* **5**, 296–299 (2009).

87. Valiaev, A., Abu-Lail, N. I., Dong, W. L., Chilkoti, A. & Zauscher, S. Microcantilever Sensing and Actuation with End-Grafted Stimulus-Responsive Elastin-Like Polypeptides. *Langmuir* **23**, 339–344 (2007).

88. Schuh, C. & Rühe, J. Penetration of Polymer Brushes by Chemical Nonidentical Free Polymers. *Macromolecules* **44**, 3502–3510 (2011).

89. Dong, R., Lindau, M. & Ober, C. K. Dissociation Behavior of Weak Polyelectrolyte Brushes on a Planar Surface. *Langmuir* **25**, 4774–4779 (2009).

90. Wei, M., Gao, Y. & Serpe, M. J. Polymer Brush-Based Optical Device with Multiple Responsivities. *J. Mater. Chem. B* **3**, 744–747 (2015).

91. Ding, S. *et al.* Rational Design of a Stimuli-Responsive Polymer Electrode Interface Coupled with in Vivo Microdialysis for Measurement of Sialic Acid in Live Mouse Brain in Alzheimer's Disease. *ACS Sensors* **2**, 394–400 (2017).

92. Vázquez-González, M. & Willner, I. Stimuli-Responsive Biomolecule-Based Hydrogels

and Their Applications. *Angew. Chemie - Int. Ed.* 2–38 (2019) doi:10.1002/anie.201907670.

93. Dhanjai *et al.* Polymer Hydrogel Interfaces in Electrochemical Sensing Strategies: A Review. *TrAC - Trends Anal. Chem.* **118**, 488–501 (2019).

94. Mondal, S., Das, S. & Nandi, A. K. A Review on Recent Advances in Polymer and Peptide Hydrogels. *Soft Matter* **16**, 1404–1454 (2020).

95. Pinelli, F., Magagnin, L. & Rossi, F. Progress in Hydrogels for Sensing Applications: A Review. *Mater. Today Chem.* **17**, 100317 (2020).

96. Yetisen, A. K. *et al.* Photonic hydrogel sensors. *Biotechnology Advances* **34**, 250–271 (2016).

97. Turan, E. & Çaykara, T. Swelling and Network Parameters of pH-Sensitive Poly(acrylamide-co-acrylic acid) Hydrogels. *J. Appl. Polym. Sci.* **106**, 2000–2007 (2007).

98. Dong, L. & Jiang, H. Autonomous Microfluidics with Stimuli-Responsive Hydrogels. *Soft Matter* **3**, 1223–1230 (2007).

99. Wei, X. *et al.* Target-Responsive DNA Hydrogel Mediated Stop-Flow Microfluidic Paper-Based Analytic Device for Rapid, Portable and Visual Detection of Multiple Targets. *Anal. Chem.* **87**, 4275–4282 (2015).

100. Ma, Y. *et al.* Portable Visual Quantitative Detection of Aflatoxin B1 Using a Target-Responsive Hydrogel and a Distance-Readout Microfluidic Chip. *Lab Chip* **16**, 3097–3104 (2016).

101. Wei, X. *et al.* Microfluidic Distance Readout Sweet Hydrogel Integrated Paper-Based Analytical Device (μDiSH-PAD) for Visual Quantitative Point-of-Care Testing. *Anal. Chem.* **88**, 2345–2352 (2016).

102. Dailey, J., Fichera, M., Silbergeld, E. & Katz, H. E. Impedance Spectroscopic Detection of Binding and Reactions in Acid-Labile Dielectric Polymers for Biosensor Applications. *J. Mater. Chem. B* **6**, 2972–2981 (2018).

103. Fan, K. *et al.* Semiquantitative Naked-Eye Detection of Cu(II) with a Standard Colorimetric Card: Via a Hydrogel-Coated Paper Sensor. *Anal. Methods* **12**, 1561–1566 (2020).

104. Shiraki, Y. *et al.* Preparation of Molecule-Responsive Microsized Hydrogels via Photopolymerization for Smart Microchannel Microvalves. *Macromol. Rapid Commun.* **36**, 515–519 (2015).

105. Coukouma, A. E. & Asher, S. A. Increased Volume Responsiveness of Macroporous Hydrogels. *Sensors Actuators, B Chem.* **255**, 2900–2903 (2018).

106. Holtz, J. H. & Asher, S. A. Polymerized colloidal crystal hydrogel films as intelligent chemical sensing materials. *Nature* **389**, 829–832 (1997).

107. Cai, Z., Sasmal, A., Liu, X. & Asher, S. A. Responsive Photonic Crystal Carbohydrate Hydrogel Sensor Materials for Selective and Sensitive Lectin Protein Detection. *ACS Sensors* **2**, 1474–1481 (2017).

108. Jang, K., Horne, W. S. & Asher, S. A. Human Serum Phenylpyruvate Quantification Using Responsive 2D Photonic Crystal Hydrogels via Chemoselective Oxime Ligation: Progress toward Developing Phenylalanine-Sensing Elements. *ACS Appl. Mater. Interfaces* **12**, 39612–39619 (2020).

109. Zhang, C., Cano, G. G. & Braun, P. V. Linear and Fast Hydrogel Glucose Sensor Materials Enabled by Volume Resetting Agents. *Adv. Mater.* **26**, 5678–5683 (2014).

110. Tian, E. *et al.* Colorful Humidity Sensitive Photonic Crystal Hydrogel. *J. Mater. Chem.* **18**, 1116–1122 (2008).

111. Zhang, S. *et al.* Selective Autonomous Molecular Transport and Collection by Hydrogel-Embedded Supramolecular Chemical Gradients. *Angew. Chemie - Int. Ed.* **58**, 18165–18170 (2019).

112. JM, G., Alvaro, G., CM, R. & Fernandez-Lafuente, R. Industrial Design of Enzymic Processes Catalysed by Very Active Immobilized Derivatives: Utilization of Diffusional Limitations (Gradients of pH) as a Profitable Tool in Enzyme Engineering. *Biotechnol. Appl. Biochem.* **20**, 357–369 (1994).

113. Shrestha, P., Cui, Y., Wei, J., Jonchhe, S. & Mao, H. Single-Molecule Mechanochemical pH Sensing Revealing the Proximity Effect of Hydroniums Generated by an Alkaline Phosphatase. *Anal. Chem.* **90**, 1718–1724 (2018).

114. Xie, X. & Bakker, E. Ion-Selective Optodes: From the Bulk to the Nanoscale. *Anal. Bioanal. Chem.* **407**, 3899–3910 (2017).

115. Bakker, E., Bühlmann, P. & Pretsch, E. Carrier-Based Ion-Selective Electrodes and Bulk Optodes. 1. General Characteristics. *Chem. Rev.* **97**, 3083–3132 (1997).

116. Fu, B., Bakker, E., Yun, J. H., Yang, V. C. & Meyerhoff, M. E. Response Mechanism of Polymer Membrane-Based Potentiometric Polyion Sensors. *Anal. Chem.* **66**, 2250–2259 (1994).

117. Schaller, U., Bakker, E., Spichiger, U. E. & Pretsch, E. Ionic Additives for Ion-Selective Electrodes Based on Electrically Charged Carriers. *Anal. Chem.* **66**, 391–398 (1994).

118. Spichiger, U. E., Freiner, D., Bakker, E., Rosatzin, T. & Simon, W. Optodes in Clinical Chemistry: Potential and Limitations. *Sensors Actuators B. Chem.* **11**, 263–271 (1993).

119. Spichiger-Keller, U. E. Ion- and Substrate-Selective Optode Membranes and Optical Detection Modes. *Sensors Actuators, B Chem.* **38**, 68–77 (1997).

120. Wang, L. *et al.* Simplified Fabrication for Ion-Selective Optical Emulsion Sensor with Hydrophobic Solvatochromic Dye Transducer: A Cautionary Tale. *Anal. Chem.* **91**, 8973–8978 (2019).

121. Soda, Y., Citterio, D. & Bakker, E. Equipment-Free Detection of K + on Microfluidic Paper-Based Analytical Devices Based on Exhaustive Replacement with Ionic Dye in Ion-Selective Capillary Sensors. *ACS Sensors* **4**, 670–677 (2019).

122. Jansod, S. & Bakker, E. Tunable Optical Sensing with PVC-Membrane-Based Ion-Selective Bipolar Electrodes. *ACS Sensors* **4**, 1008–1016 (2019).

123. Lee, J. *et al.* An Integrated Ion-Selective Optode Sensor Cartridge for Directly Detecting Electrolyte Ions in Blood Plasma Without Pretreatment to Adjust pH. *Sensors Actuators, B Chem.* **280**, 256–262 (2019).

124. Du, X. & Xie, X. Non-Equilibrium Diffusion Controlled Ion-Selective Optical Sensor for Blood Potassium Determination. *ACS Sensors* **2**, 1410–1414 (2017).

125. Wang, K. *et al.* Characterization of Potassium-Selective Optode Membranes Based on Neutral Ionophores and Application in Human Blood Plasma. *Anal. Sci.* **6**, 715–720 (1990).

126. Ceresa, A., Qin, Y., Peper, S. & Bakker, E. Mechanistic Insights into the Development of Optical Chloride Sensors Based on the [9]Mercuracarborand-3 Ionophore. *Anal. Chem.* **75**, 133–140 (2003).

127. Cha, M. J. *et al.* Asymmetric Cellulose Acetate Membrane-Based Carbonate- and Chloride-Selective Electrodes. *Anal. Chim. Acta* **315**, 311–319 (1995).

128. Wang, E., Meyerhoff, M. E. & Yang, V. C. Optical Detection of Macromolecular Heparin Via Selective Coextraction into Thin Polymeric Films. *Anal. Chem.* **67**, 522–527 (1995).

129. Dürüst, N., Meyerhoff, M. E., Ünal, N. & Naç, S. Spectrophotometric Determination of Various Polyanions with Polymeric Film Optodes using Microtiter Plate Reader. *Anal. Chim. Acta* **699**, 107–112 (2011).

130. Chen, Q. *et al.* Rapid Equilibrated Colorimetric Detection of Protamine and Heparin: Recognition at the Nanoscale Liquid-Liquid Interface. *Anal. Chem.* **91**, 10390–10394 (2019).

131. Kim, S. B., Kang, T. Y., Cha, G. S. & Nam, H. Quantitative Determination of Heparin Levels in Serum with Microtiter Plate-Format Optode. *Anal. Chim. Acta* **557**, 117–122 (2006).

132. Yang, S., Wo, Y. & Meyerhoff, M. E. Polymeric Optical Sensors for Selective and Sensitive Nitrite Detection Using Cobalt(III) Corrole and Rhodium(III) Porphyrin as Ionophores. *Anal. Chim. Acta* **843**, 89–96 (2014).

133. Kim, S. B. *et al.* Determination of Protamine Using Microtiter Plate-Format Optodes. *Anal. Chim. Acta* **439**, 47–53 (2001).

134. Phichi, M., Imyim, A., Tuntulani, T. & Aeungmaitrepirom, W. Paper-Based Cation-Selective Optode Sensor Containing Benzothiazole Calix[4]arene for Dual Colorimetric Ag^{+} and Hg^{2+} Detection. *Anal. Chim. Acta* **1104**, 147–155 (2020).

135. Bondyale-Juez, D. R., Packard, T. T., Viera-Rodríguez, M. A. & Gómez, M. Respiration: Comparison of the Winkler Technique, O_2 Electrodes, O_2 Optodes and the Respiratory Electron Transport System Assay. *Mar. Biol.* **164**, 1–11 (2017).

136. Kaczmarczyk, B., Kisiel, A., Piątek, P., Maksymiuk, K. & Michalska, A. Induced Ion-Pair Formation/ De-aggregation of Rhodamine B Octadecyl Ester for Anion Optical Sensing: Towards Ibuprofen Selective Optical Sensors. *Talanta* **227**, 122147 (2021).

137. Yung, K. Y., Hewitt, A. J. S., Hunter, N. P., Bright, F. V. & Baker, G. A. 'Liquid litmus': Chemosensory pH-Responsive Photonic Ionic Liquids. *Chem. Commun.* **47**, 4775–4777 (2011).

138. Galpothdeniya, W. I. S. *et al.* Fluorescein-based Ionic Liquid Sensor for Label-Free Detection of Serum Albumins. *RSC Adv.* **4**, 17533–17540 (2014).

139. Mizuta, T., Sueyoshi, K., Endo, T. & Hisamoto, H. Ionic Liquid-Based Dye: A "Dyed plasticizer" for Rapid and Highly Sensitive Anion Optodes Based on a Plasticized PVC Membrane. *Sensors Actuators, B Chem.* **258**, 1125–1130 (2018).

140. Mizuta, T. *et al.* A Lipophilic Ionic Liquid-Based Dye for Anion Optodes: Importance of Dye Lipophilicity and Application to Heparin Measurement. *Analyst* **145**, 5430–5437 (2020).

141. Yan, R. *et al.* Biodegradable Ion-Selective Nanosensors with p-Diethylaminophenol Functionalized Rhodamine as Chromoionophore for Metal Ions Measurements. *Sensors Actuators B. Chem.* 129672 (2021).

142. Saranchina, N. V. *et al.* Smartphone-Based Colorimetric Determination of Fluoride Anions Using Polymethacrylate Optode. *Talanta* **226**, 122103 (2021).

143. Xie, X., Szilagyi, I., Zhai, J., Wang, L. & Bakker, E. Ion-Selective Optical Nanosensors Based on Solvatochromic Dyes of Different Lipophilicity: From Bulk Partitioning to Interfacial Accumulation. *ACS Sensors* **1**, 516–520 (2016).

144. Mizuta, T., Sueyoshi, K., Endo, T. & Hisamoto, H. Lipophilic Fluorescent Dye Liquids: Förster Resonance Energy Transfer-Based Fluorescence Amplification for Ion-selective

Optical Sensors Based on a Solvent Polymeric Membrane. *Anal. Chem.* 0–5 (2021).

145. Zhai, J., Xie, X. & Bakker, E. Solvatochromic Dyes as pH-Independent Indicators for Ionophore Nanosphere-Based Complexometric Titrations. *Anal. Chem.* **87**, 12318–12323 (2015).

146. Wang, X. *et al.* Plasticizer-Free and pH-Independent Ion-Selective Optode Films Based on a Solvatochromic Dye. *Anal. Methods* **12**, 2547–2550 (2020).

147. Wang, L. & Bakker, E. A Tunable Detection Range of Ion-Selective Nano-Optodes By Controlling Solvatochromic Dye Transducer Lipophilicity. *Chem. Commun.* **55**, 12539–12542 (2019).

148. Wang, R., Du, X., Ma, X., Zhai, J. & Xie, X. Ionophore-Based pH Independent Detection of Ions Utilizing Aggregation-Induced Effects. *Analyst* **145**, 3846–3850 (2020).

149. Hisamoto, H., Horiuchi, T., Tokeshi, M., Hibara, A. & Kitamori, T. On-Chip Integration of Neutral Ionophore-Based Ion Pair Extraction Reaction. *Anal. Chem.* **73**, 1382–1386 (2001).

150. Cai, Z. X., Fang, Q., Chen, H. W. & Fang, Z. L. A Microfluidic Chip Based Liquid-Liquid Extraction System with Microporous Membrane. *Anal. Chim. Acta* **556**, 151–156 (2006).

151. Chen, H., Fang, Q., Yin, X. F. & Fang, Z. L. Microfluidic Chip-Based Liquid-Liquid Extraction and Preconcentration Using a Subnanoliter-Droplet Trapping Technique. *Lab Chip* **5**, 719–725 (2005).

152. Shen, H., Fang, Q. & Fang, Z. L. A Microfluidic Chip Based Sequential Injection System with Trapped Droplet Liquid-Liquid Extraction and Chemiluminescence Detection. *Lab Chip* **6**, 1387–1389 (2006).

153. Sun, M., Du, W. Bin & Fang, Q. Microfluidic Liquid-Liquid Extraction System Based on Stopped-Flow Technique and Liquid Core Waveguide Capillary. *Talanta* **70**, 392–396 (2006).

154. Xu, Y. *et al.* A Droplet Microfluidic Platform for Efficient Enzymatic Chromatin Digestion Enables Robust Determination of Nucleosome Positioning. *Lab Chip* **18**, 2583–2592 (2018).

155. Wells, S. S. & Kennedy, R. T. High-Throughput Liquid-Liquid Extractions with Nanoliter Volumes. *Anal. Chem.* **92**, 3189–3197 (2020).

156. Kumemura, M. & Korenaga, T. Quantitative Extraction Using Flowing Nano-Liter Droplet in Microfluidic System. *Anal. Chim. Acta* **558**, 75–79 (2006).

157. Lubej, M. *et al.* Microfluidic Droplet-Based Liquid-Liquid extraction: Online Model Validation. *Lab Chip* **15**, 2233–2239 (2015).

158. Mary, P., Studer, V. & Tabeling, P. Microfluidic Droplet-Based Liquid-Liquid Extraction. *Anal. Chem.* **80**, 2680–2687 (2008).

159. Wang, X. *et al.* Ionophore-Based Biphasic Chemical Sensing in Droplet Microfluidics. *Angew. Chemie Int. Ed.* **58**, 8092–8096 (2019).

160. Wetzler-Quevedo, S. P. Meyerhoff, M.E. & Bailey, R. C. Characterization of the Impact of Mixing and Volumes on the Behavior of Microfluidic Droptodes. *Submitted*. (2021).

161. Soniat, M. & Houle, F. A. Swelling and Diffusion During Methanol Sorption into Hydrated Nafion. *J. Phys. Chem. B* **122**, 8255–8268 (2018).

162. Lee, J. N., Park, C. & Whitesides, G. M. Solvent Compatibility of Poly(dimethylsiloxane)-Based Microfluidic Devices. *Anal. Chem.* **75**, 6544–6554 (2003).

163. Zhou, X. D., Zhang, S. C., Huebner, W., Ownby, P. D. & Gu, H. Effect of the Solvent on the Particle Morphology of Spray Dried PMMA. *J. Mater. Sci.* **36**, 3759–3768 (2001).

Chapter 2.

Real-time Measurement of Polymer Brush Dynamics Using Silicon Photonic Microring Resonators: Analyte Partitioning and Interior Brush Kinetics

This work was adapted from Wetzler, S. P. et al. *Real-Time Measurement of Polymer Brush Dynamics Using Silicon Photonic Microring Resonators: Analyte Partitioning and Interior Brush Kinetics.* Langmuir ***36****, 10351–10360 (2020). This work was done alongside Dr Kali Miller (UIUC under Prof Paul V. Braun) who grew some of the polymer brushes and contributed to discussions about data analysis. Dr Lydia Kisley (Case Western) gave helpful discussion about the modelling aspects of the project. Dr. Alexandra L.D. Stanton originally conceived of the idea for growing polymer brushes on microring resonators and exposing them to plasticizers.*

2.1 INTRODUCTION

Polymer brushes are widely applied to impart surfaces with properties vastly different from either the native surface or the analogous bulk polymer,[1,2] and have been used in biomedical[3,4] and membrane[5] applications due to their ability to provide protective and antibiofouling properties.[6,7] The confined nature imposed by the high graft density common in surface-initiated polymer brushes can lead to differences in properties relative to the bulk equivalent, including refractive index,[8] glass transition temperature,[9–11] and hydrophobicity,[11–17] properties which can even change with brush thicknesses and as a function of depth within a brush.

A facile method to extract important analyte-specific brush characteristics, including diffusion and partition coefficients, as well as the chemical response of polymer brushes to changes in solvent (e.g., the brush pK_a) would advance the field's ability to optimize brush properties for specific applications. For instance, brush pK_a can control the ability of a system to swell and collapse, which is particularly important when developing membranes for drug delivery applications.[1] Additionally, proton exchange membrane fuel cells, such as those used for

direct methanol fuel cells, rely on partitioning and diffusion to directly control the speed and amount of fuel stored, making the knowledge of the related constants crucial.[18]

For these and other applications, there is a need to develop generalizable technologies that can rapidly characterize analyte-brush dynamics for a variety of chemical systems. However, direct measurement of analyte-brush equilibria and kinetics remains a challenge. Analysis of target molecule-brush dynamics requires localization and spatial differentiation, as brush properties can differ between the brush's interface and the brush interior. Real-time measurement is necessary as polymer brushes can swell or collapse as a result of analyte partitioning,[19] resulting in temporally changing target molecule-brush dynamics. Real-time measurement also provides measurement of real-time kinetics, allowing for extraction of diffusion constants. A multiplexable technique could provide additional advantages, allowing for quick screening of dynamics across a variety of brushes with a single analyte sample.

Most techniques currently used to analyze analyte-brush dynamics focus on brush conformational response to analyte introduction. Atomic force microscopy (AFM) is a common brush analysis technique,[20–22] but has limited access to probing beyond the brush surface. X-ray photoelectron spectroscopy (XPS),[23] neutron reflectivity (NR),[24,25] and, most common of all, *in situ* spectral ellipsometry (SE)[26–28] have been used as analysis techniques to determine the structural impact of analyte binding to the brushes, as they offer spatial resolution. However, each of these systems has their own limitations: XPS operates in vacuum and only probes to a depth of ~10 nm,[23] NR requires a neutron source, as well as deuteration of analytes or brushes that can potentially change interactions, and SE is susceptible to overfitting data during the required course of response modelling.[29] Additionally, these techniques cannot provide real-time information about dynamics on the order of seconds, as required for many kinetic studies. Quartz

crystal microbalance (QCM) studies can also provide real-time information regarding solvent swelling, based upon mass changes on the quartz surface, but does not provide analyte localization information.[30,31] Fourier transform infrared spectroscopy (FTIR) has been used to indirectly measure analyte diffusion in the brush interior by detecting the changes in brush protonation states upon analyte introduction;[12,32] however, FTIR can only detect a chemical change to the brush as a result of analyte partitioning or an analyte which has a unique IR signature in a very thick polymer brush, which are limited cases at best.

A new method of applying polymer brush-modified silicon photonic microring chips to monitor analyte-brush interactions was recently developed in the Bailey lab.[33] Specifically, using microring resonators, refractive index changes due to changes in the local environment of the microring, e.g., caused by analyte partitioning, or brush swelling or collapse, can be identified. As such, microring resonators provide a versatile platform for analyzing a variety of analyte-brush dynamics. In previous work, brush-functionalized silicon photonic microring resonator array technology has been used for combinatorial screening of polymerization conditions,[34] and partition-enhanced small molecule detection.[33] Partitioning of analytes into polymer brushes has been utilized to enhance the concentration-dependent signal of small organic molecules as a method for quantitative detection.[33] However, using this technology for polymer brush characterization is largely unexplored[35] and has the potential to optimize the design of polymer brushes for particular applications, based upon permeability and diffusion requirements. The high sensitivity of the platform to changes occurring within 100 nm of the ring surface and the ability to measure environmental changes in real-time[36] provides both localization information as well as temporal resolution, allowing determination of analyte-brush dynamics. Additionally, the silicon-on-insulator technology provides a low-cost platform on account of well-established

semiconductor processing, and the presence of multiple rings allows for multiplexing. Finally, the microring resonator system offers a means of monitoring both brush conformational changes and analyte presence using a single, label-free platform.

Here we demonstrate the utility of silicon photonic microring resonators for *in situ* characterization of analyte-polymer brush dynamics. Microring surfaces were modified using surface-initiated atom transfer radical polymerization (SI-ATRP), enabling the construction of well-defined polymer brushes hydrophilic or hydrophobic in nature. Diffusion and partitioning of small molecules into the polymer brush were observed in real-time and conformational changes were quantified by measuring and fitting shifts in the resonance wavelength. Real-time measurement allowed for the extraction of the partition coefficients, diffusion coefficients, and pK_as, for both hydrophobic and hydrophilic polymer brushes, and ionic and organic analytes, over a variety of polymer brush thicknesses. Polymer-brush coated microring resonators open the door for rapid determination of optimal polymer brush-analyte combinations for a variety of applications, including antifouling coatings and analyte release mechanisms.

2.2 EXPERIMENTAL SECTION

2.2.1 Materials

2-hydroxethyl methacrylate (HEMA), 2-(dimethylamino)ethyl methacrylate (DMAEMA), methyl methacrylate (MMA), copper (II) bromide, copper (I) bromide, 1,1,4,7,10,10-hexamethyltriethylenetetramine (HMTETA), nitrobenzene (NB), methyl isobutyl ketone (MIBK), tetrahydrofuran (THF), and inhibitor removers were purchased from Sigma-Aldrich. Inhibitor was removed from each monomer by passing it through a column of inhibitor removers. The initiator [11-(2-bromo-2-methyl) propionyloxy] undecyltrichlorosilane (BPOTS)

was purchased from Gelest. A pH 9 buffer solution was made from sodium bicarbonate and sodium carbonate. Buffer solutions at pH 8 and pH 7 were made from sodium phosphate monobasic and sodium phosphate dibasic. Buffer solutions at pH 4 and pH 3 were made from acetic acid and sodium acetate. Adjustments to pH were made using 1 M NaOH and 1 M HCl until the pH measured of the solution was within 0.1 of the reported pH. The total ionic strength of all pH buffer solutions was adjusted to 0.18 M using sodium chloride. All other chemicals were obtained from Sigma-Aldrich and were used as received.

2.2.2 Monolayer self-assembly

Initiator monolayers were formed using silane self-assembly onto both microring resonator chips and blank silicon wafers (cut in pieces of 2 cm x 1 cm, used for ellipsometric measurements) simultaneously. Substrates were cleaned using acetone and isopropanol, activated using oxygen plasma for 3 minutes (150 W, March Plasmod GCM-200) and then exposed to a 1 mM solution of BPOTS initiator in anhydrous hexanes at room temperature under argon. After 24 hours, the substrates were removed from the reaction mixture and sonicated sequentially in hexanes, ethanol, and water. They were then dried in a nitrogen stream and used immediately.

2.2.3 Surface-initiated atom transfer radical polymerization (SI-ATRP)

Following procedures similar to those developed by the Matyjaszewski group,[3] substrates, including both the silicon wafer and microring resonator chip, were placed in a reaction vessel and purged with argon. Monomer (500 mmol, 300 equiv) was diluted with solvent to make a 5 M solution and degassed for 15 min in a separate Schlenk flask. HMTETA (544 μL, 2 mmol, 1.2 equiv), CuBr (240 mg, 1.67 mmol, 1 equiv), and $CuBr_2$ (75 mg, 0.33 mmol, 0.2 equiv) were then added to the monomer solution under positive argon flow. The flask was then sealed and the

mixture transferred to the reaction vessel containing the substrates. After the reaction period, substrates were removed and sonicated sequentially in tetrahydrofuran, ethanol, and water, and then dried in a nitrogen stream.

2.2.4 Ellipsometry

Control silicon wafer film thickness was determined using spectroscopic ellipsometry (VASE, J.A. Woollam Co.) and analyzed by WVASE software using a three-layer model. The ellipsometric parameters (Ψ, Δ) were measured at three angles of incidence (65°, 70°, 75°) and from 400 nm to 800 nm. Software-supplied refractive indices were used for silicon (substrate) and silicon dioxide (empirically determined to be 2.3 nm thick). Three separate measurements with a beam spot size of approximately 1 mm were taken based upon the extremes of the dimensions of the chip. Data was fit to a Cauchy layer model, with fixed (A_n, B_n) values of (1.45, 00.1) and no optical absorption to determine dry polymer brush thickness.

2.2.5 Silicon photonic microring resonators

Design of the microring resonator array chips and operation of the instrumentation has been previously described.[37,57] Microring resonator sensor chips and the Maverick M1 optical scanning instrumentation were purchased from Genalyte, Inc. (San Diego, CA). The chip was functionalized (see above) and then covered with a Mylar gasket and Teflon lid to direct solution into two flow channels (Figure S1). Solutions were flowed over the chip using peristaltic pumps at 20 μL/min for various lengths of time while the chip was interrogated using a wavelength-tunable laser centered at 1550 nm, sweeping over a 12 nm spectral range. The change in resonant wavelength (Δpm) was measured in real-time. The evanescent field from the microring resonator

falls-off exponentially from the microring surface, providing an active sensing range within 100 nm of the resonator surface.[36]

2.2.6 Data analysis

Data analysis was performed using R and software provided by Genalyte, Inc. Sensor traces were corrected for temperature fluctuations and response was averaged over clusters, or groups of 4 microrings. One cluster of rings, with a response representative of the entire array of 128 rings, was chosen for further analysis to minimize standard deviation potentially caused by brush defects. Resonance shifts were measured at consistent time points, ~3/4 of the way into the analyte step, in order to provide time for equilibration for the majority of the brushes. Differences in shift were determined by subtracting the analyte step and the preceding solvent step, unless otherwise noted. All curve fittings were performed in R using a non-linear least squares fitting.

2.3 RESULTS AND DISCUSSION

2.3.1 Microring Resonators

The silicon-on-insulator sensor chips each have 30 μm diameter active microrings in 32 individual addressable groups of four as well as four temperature controls.[37] Each silicon microring can be selectively functionalized as the rest of the surface is covered by a protective fluoropolymer cladding. Light travels down waveguides by total internal reflection and couples into microrings at discrete wavelengths according to the interferometric-based condition:

$$m\lambda = 2\pi r n_{eff}, \qquad [2.1]$$

where m is an integer, λ is the resonant wavelength, r is the radius of the microring and n_{eff} is the local effective refractive index (Equation 2.1, **Figure 2.1**).

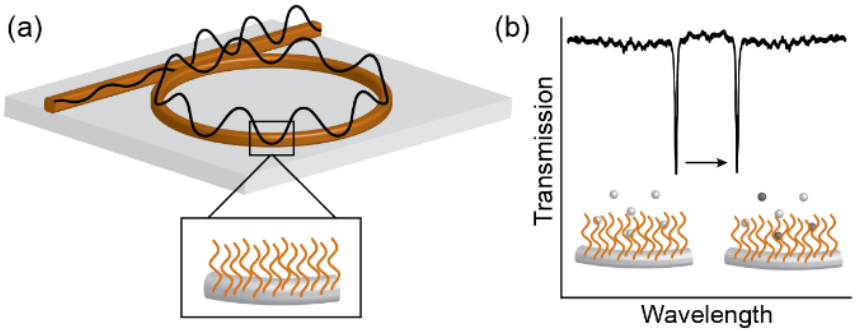

Figure 2.1. (a) Light is coupled into polymer-functionalized silicon photonic microring resonators at discrete wavelengths defined by the local refractive index. (b) Resonant optical modes are visualized by a dip in transmission intensity. Shifts in the resonant wavelength are observed in real time as changing analyte solutions are passed over the microring surface.

At the beginning of each assay, an initial resonant wavelength measurement is used as a baseline. As various analyte solutions are flowed over the microring, the change in the effective refractive index can then be observed by a shift in the resonant wavelength, measured as a change in the dip in the transmission (**Figure 2.1**).

2.3.2 Surface functionalization

Microring resonator arrays were modified by growing polymer brushes directly from the silicon surface. An initiator monolayer was formed by self-assembly of [11-(2-bromo-2-methyl) propionyloxy] undecyltrichlorosilane (BPOTS). The monolayer thickness was measured using ellipsometry on a silicon wafer in the same reaction vessel as the microring resonators, and was found on average to be 17 ± 2 Å, which compares well to prior studies.[38] The polymer brush was subsequently synthesized by SI-ATRP using methyl methacrylate (MMA), 2-hydroxyethyl

methacrylate (HEMA), or 2-(dimethylamino)ethyl methacrylate (DMAEMA) monomers. The reaction was stopped at various times to obtain desired thicknesses, all of which are reported in terms of dry thicknesses found by taking ellipsometry measurements from a brush-functionalized silica wafer grown concurrently with the microring resonator chip (**Table 2.1**).

Table 2.1. Table of dry brush thicknesses and errors with time of ATRP

Brush Type	**Dry Brush Thickness (nm)**	**Thickness Error (nm)**	Growth Time (hr)
PDMAEMA	12.4	0.2	0.5
PDMAEMA	29	1	2
PDMAEMA	58	0.1	4
PDMAEMA	83	4	4.5
PDMAEMA	202	3	5
PDMAEMA	269	3	5.5
PMMA	18.0	0.3	4
PMMA	35	1	6
PMMA	47.0	0.6	12
PMMA	112	2	8*
PMMA	158	2	9*
PHEMA	13	8	0.07
PHEMA	28.0	0.6	0.03
PHEMA	45	7	0.25
PHEMA	60.0	0.4	0.17
PHEMA	143	2	0.33

PHEMA	174	1	0.33

* Including ascorbic acid references using an ARGET ATRP system for the brush growth, where the reactive radicals are constantly regenerated, and excess oxygen is scavenged, by the ascorbic acid. This results in thicker brushes but can also lead to increased dispersity.

2.3.3 Data Analysis from Microring Resonators

All rings were worked up to determine the average ring response, after which a cluster of 4 rings most closely following the average ring response was used for the rest of the analysis. Shifts were calculated by difference in relative wavelength shift between ¾ into the step and ¾ into the prior rinse step, after subtracting out (from each ring) the response due to thermal fluctuations (based on the thermal control). Data was outputted in the form of a CSV file which was then worked up using an R code provided (Appendix 1). Fits were performed using the provided code as well.

2.3.4 Analyte partitioning between solvent and polymer brush.

The partition coefficient and diffusion coefficient can be extracted from the resonant wavelength shift as an analyte partitions into the polymer brush from the bulk solvent. The partition coefficient (the ratio of the analyte concentration in the brush and bulk solvent) is a standard description of coatings and allows for more quantifiable comparisons between analyte-brush systems. The responses of sensors modified with hydrophobic (PMMA), hydrophilic (PHEMA), and pH-responsive brushes (PDMAEMA) were monitored in real-time upon exposure to three common organic analytes, which are also known to be plasticizers, methyl isobutyl ketone (MIBK), nitrobenzene (NB) and tetrahydrofuran (THF). The resonance wavelengths of the brush-coated microrings were tracked as the solution was changed from water to the specific analyte (**Figure 2.2**). The shifts in resonance wavelength as a function of

time measured during this partitioning were fit to a Langmuir binding isotherm derived by Sothivelr et al. for analyzing molecular partitioning into a thin film:[39]

$$Relative\ Shift = -A(e^{-\frac{t}{T}} + C_{amb}P) \qquad [2]$$

where *Relative Shift* is the given shift (Δpm) at any time point *t*, *A* is a constant dependent on the maximum observed shift at equilibrium, *T* is the response time for a given analyte-coating combination (the time required to reach half of the maximum value), C_{amb} is the ambient concentration of the analyte, and *P* is the brush-solvent partition coefficient. Note that in using

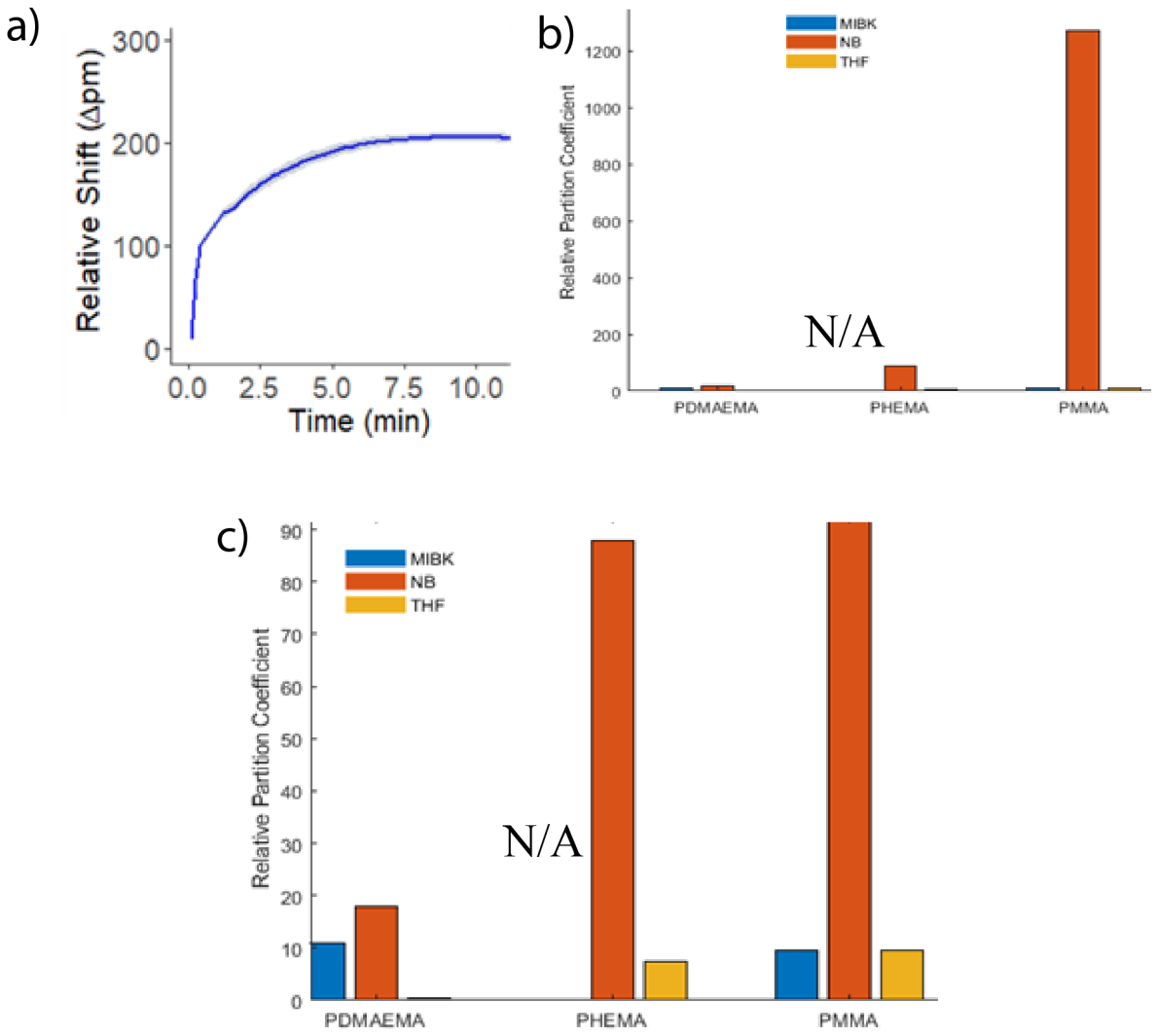

Figure 2.2. (a) The real-time curve of 4 rings of 40 nm PMMA-coated microring as the analyte is changed from water to 100 mM THF in water. The data was fit to Equation 2 (a Langmuir binding isotherm) to extract partitioning coefficients. (b) A graph of the relative partition coefficients of 100 mM of analyte in each brush type (with the exception of NB which only showed solubility up to 1 mM in water). N/A represents an inability to observe partitioning. (c) A zoom in of the partitioning graph in (b) to better show trends.

this equation, it is assumed that there is a constant value for the analyte concentration in the bulk, due to constant flow of fresh analyte-containing solution, and that the only cause of the change being measured is due to single analyte partitioning. The values of the partition coefficient were

obtained by fitting the relative shift of the system from water to the analyte of interest as a function of time to the above equation, leaving *P* and *T* as variable parameters (**Figure 2.2**).

Solubility calculations were used to orthogonally compare the results of the microring resonators' partition coefficient determination to how soluble in theory an analyte should be in the brush. Solubility was calculated using the difference in the Hildebrand solubility parameters of the polymers and solvents, determined in prior literature. When the solubility differences are close to zero, we would expect higher solubility and thus higher partitioning. This trend is observed in **Table 2.2**, where PMMA, which showed the highest overall partitioning, has Hildebrand solubility parameters differences closest to zero while PHEMA, which showed the smallest overall partitioning has among the highest differences in the Hildebrand solubility parameters.

Table 2.2. Change in Hildebrand Solubility Parameters for Tested Brush-Plasticizer Pairs.

Brush Type	**THF Δδ ($MPa^{1/2}$)**	**NB Δδ ($MPa^{1/2}$)**	**MIBK Δδ ($MPa^{1/2}$)**
PMMA	0.4	3.1	2.1
PHEMA	8.1	5.4	10.6
PDMAEMA	4.4	7.1	1.9

It is important to note that the Hildebrand solubility parameter does not take into account electrostatic interactions or the collapse/swelling that may occur upon small molecule partitioning. This is particularly problematic for PDMAEMA, as PDMAEMA can undergo deprotonation depending on changes in conditions. Additionally, the difference in the Hansen solubility parameters is considered better for polar solvents or polymers, but PDMAEMA has no reported

Hansen solubility parameters that we could find. This could account for the variability between the calculated solubility parameter and the found partition coefficient.

Calculated partition coefficients ranged between 0.4 and 1300 (**Table 2.3**). Recall that the greater the partition coefficient, the greater fraction of analyte is localized in the brush compared to in solution. Most partition coefficients were much greater than 1, affirming that these analytes have more favorable interactions in the semi-organic polymer brush than in the aqueous phase, as expected. Two predominant exceptions were noted. An exception was found with MIBK in PHEMA which showed no partitioning. However, this is explained by the large difference in Hildebrand solubility parameters, and thus solubility, between MIBK and PHEMA. There was also an exception of THF in PDMAEMA, which consistently had partition coefficients less than 1 regardless of the brush length (**Table 2.4**).

Table 2.3. Fits to Partition Coefficient Determination Equation for Plasticizer-Brush Combos

	MIBK			**NB**			**THF**		
	A	**T**	**P**	**A**	**T**	**P**	**A**	**T**	**P**
PDMAEMA	196	4.4	11	684	1.77	17.9	-340	2.51	0.39
PHEMA	No fit	No fit	No fit	-5.0	1.36	87.56	18.26	5.68	7.32
PMMA	29	1.422	9.553	42	9.62	1271	217.21	1.48	9.46

This was unexpected given that the Hildebrand solubility parameters while different, were not as extreme a difference as other pairs (such as THF with PHEMA) (**Table 2.2**). Potentially this is because the Hildebrand solubility parameter does not do provide a comparison between a polymeric environment and an aqueous environment, which is more competitive in nature. The

challenge of differential solubility in water could also be a potential complication, as nitrobenzene, which showed far lower solubility in water than either MIBK or THF, also demonstrated extraordinary partitioning compared to its two counterpart analytes. However, with the exception of nitrobenzene, the solubility of PMMA, PHEMA and PDMAEMA, as determined by the Hildebrand parameters, generally tracked with the calculated partition coefficients, especially when comparing analytes between brush systems, confirming the validity of this approach (**Table 2.2**).

2.3.5 Impact of Dry Brush Thickness on Partition Coefficient

The relationship between brush thickness and partition coefficient appears to vary based on the brush type. For instance, in PMMA, the quintessential hydrophobic brush, brush thickness increases causes partition coefficient increases. This would generally make sense because a thicker brush would have more volume over which an analyte could be distributed, meaning that the relative analyte concentration would be higher. It is interesting to note that PHEMA and PDMAEMA, both more hydrophilic brushes, do not follow this trend. This could be due to a change in brush conformation at thicker brushes, potentially leading to a gradient in relative hydrophobicity. As stated above, we also have not found Hansen solubility parameters for PDMAEMA or PHEMA, which could provide better estimations of their behaviors compared to the Hildebrand solubility parameters. This preliminary data, including the variations in the rise time and equilibrium shifts changing sign frequently for the same brush type, suggests much more needs to be explored about intra- and inter-brush interactions (**Table 2.4**, **Table 2.5**, **Table 2.6**).

Table 2.4. Fits for Partition Coefficient Determination by Dry Brush Thickness on PDMAEMA

PDMAEMA	MIBK			NB			THF		
Dry Brush Thickness (nm)	**A**	**T**	**P**	**A**	**T**	**P**	**A**	**T**	**P**
20	196	0.33	0.41	-338*	30*	1067*	-685	1.14	0.320
40	574	4.41	10.9	684	1.78	17.9	-359	2.51	0.39
200	-643	2.10	0.07	-539	1.68	92.4	-734	2.95	0.19

*Fit questionable based on T-value being same as maximum allowed by the fit

Table 2.5. Fits for Partition Coefficient Determination by Dry Brush Thickness on PMMA

PMMA	MIBK			NB			THF		
Dry Brush Thickness (nm)	**A**	**T**	**P**	**A**	**T**	**P**	**A**	**T**	**P**
10	22	12.1	2.60	9.5	15.7	399	23	4.52	1.36
20	18	1.41	15.5	71	0.93	883	26	3.70	0.91
40	28	1.42	9.56	42	9.62	1270	217	1.48	9.46
114	31	4.80	16.5	47	7.32	1160	45	5.35	9.96

Table 2.6. Fits for Partition Coefficient Determination Based On Dry Brush Thickness for PHEMA

PHEMA	MIBK			NB			THF		
Dry Brush Thickness (nm)	**A**	**T**	**P**	**A**	**T**	**P**	**A**	**T**	**P**
30	No fit	No fit	No fit	-6.1*	27.4*	597*	17	3.88	7.32
60	No fit	No fit	No fit	-5.0	1.4	87.6	18	5.68	7.32
135	-7.5	6.80	0.154	-3.0	5.98	44.5	-8	1.14	0.203

*Fit questionable based on T-value being same as maximum allowed in the fit

2.3.6 Diffusion coefficient dependence on dry brush thickness

Diffusion coefficients quantify mobility of analytes within a matrix. In polymer systems, diffusion coefficients are commonly calculated via fluorescence techniques such as fluorescence recovery after photobleaching (FRAP)[40,41] and fluorescence correlation spectroscopy (FCS).[42,43] Diffusion coefficients can also be calculated by single particle tracking (SPT) which calculates trajectories from the visualization of individual fluorescent molecules, providing highly quantitative information on diffusion constants.[40,44] Equations derived from Fick's law can be used to quantify diffusion in thin films as long as the boundary conditions (e.g. constant source) are known and the diffusion constant of the probe within the film does not vary spatially.[45–47] Although these established methods provide an accurate means for measuring diffusion coefficients, our platform can determine both partition and diffusion coefficients from a single sample measurement, thus greatly increasing the information that can be gained from one experiment. Additionally, brush-modified microring resonators do not require fluorescent probes

or chemical modifications, allowing for the direct analysis of the system of interest without perturbations from labeling.

In our system, we monitored the relative shift of 10, 50, and 200 nm thick PDMAEMA brushes in real-time upon changing a pH 9 carbonate buffer to a pH 8 phosphate buffer (**Figure 2.3**). Note that at this pH change, no structural changes are expected within the brush, and we would not expect salting out as the salt concentrations are lower than reported in prior work to change the brush regime.[25] The real-time resonance shifts were first normalized to the highest value ($Shift_{Max}$) to correctly compare systems which have differential partitioning (and thus different relative shift values at equilibrium). It was observed that thin brushes equilibrate

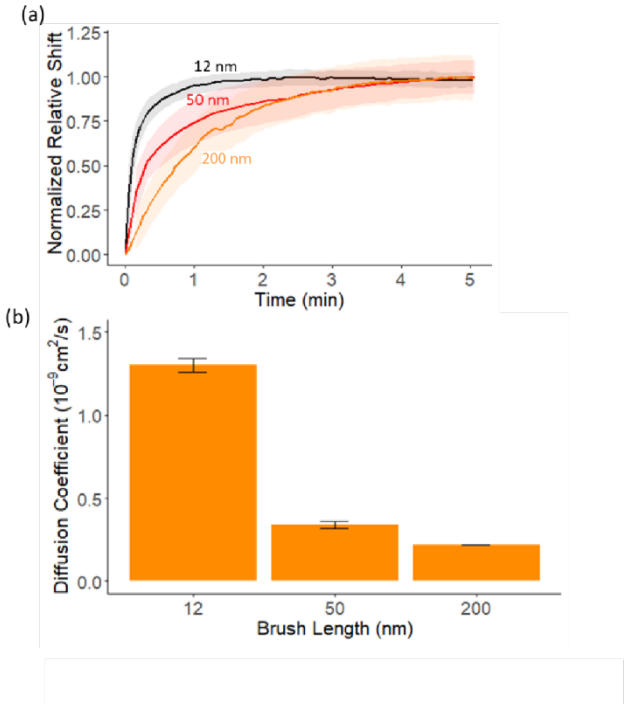

Figure 2.3. (a) The relative shift of PDMAEMA coated microrings at 12 nm (black), 50 nm (red) and 200 nm (orange) thicknesses as the buffer is changed from 0.18 M carbonate buffer (pH 9) to 0.18 M phosphate buffer (pH 8). Data is represented as solid lines with standard deviation between the rings represented as shading. (b) A summary of the extracted diffusion coefficients showing that diffusion becomes slower with increasing polymer brush thickness. Error bars are the standard error in calculated diffusion coefficient.

quickly (~1 min) while thicker brushes take much longer (~5 min). The normalized shift was fit to a negative exponential decay expression, based off of a Langmuir binding isotherm:[48]

$$\frac{Relative\ Shift}{Shift_{Max}} = 1 - e^{-\Gamma t} \qquad [3]$$

which allowed the real-time data to be determined by fitting the decay rate Γ. A diffusivity equation used in evanescent wave light scattering studies was adapted to allow the determination of the diffusivity from the decay rate:[48]

$$< D > = \frac{\Gamma}{q^2 + \Xi^2} \qquad [4]$$

where <*D*> is the average diffusion coefficient (molecular diffusivity), Γ is the decay rate from Equation 3, q is dependent on the measurement and Ξ is the penetration of the evanescent field.

Note that the exponential fall-off in sensitivity as a function of distance from the sensor is similar to that for evanescent wave light scattering studies, allowing the same equation to be adapted for our microrings. Ξ is the length of the evanescent field penetration depth. This was defined previously for the microring resonators to be approximately 64 nm and is a constant of the system. q is the scattering wave vector, defined by the magnitude of change in the evanescent field, which can be interpreted as the change in signal. q can be broken up into a parallel and perpendicular component, of which the perpendicular component is irrelevant to our system.[6] As Eq. 1 in the main text indicates a relationship between the wavelength of light used and the refractive index determined, we get that

$$q = \frac{m}{r} \qquad [2]$$

where m is the number of times that light circles the microring resonator, defining the resulting evanescent field, and r is the radius of the ring. Again, both of these are system constants for our measurement system. Previous work has shown m to be 60.77 and r to be 30 μm,[5] and thus q is 0.004052.

From the decay rate, diffusion coefficients of phosphate into PDMAEMA were found to vary from 0.22 to 1.3 x 10^{-9}cm^2/s depending on the brush thickness (**Figure 2.3**, **Table 2.7**).

Table 2.7. Diffusion Values for Plasticizer in PDMAEMA of Varying Thicknesses

Dry Brush Thickness (nm)	**Diffusion Coefficient (10^{-9} cm^2/s)**
12	1.30 $\pm$ 0.04
50	0.30 $\pm$ 0.02
200	0.200000 $\pm$ 0.00005

The results show a clear dependence on dry polymer brush thickness, with thicker polymer brushes having smaller diffusion coefficients. Thicker brushes are less likely to have conformational flexibility, hindering the motion of the phosphate buffer. Note that this is independent of the partition coefficient changing due to brush thickness variation. The observed difference in diffusion coefficient suggests brush formation variation with brush thickness. If the brushes maintained a consistent density, we would not expect diffusion coefficients to change as the brush length was increased, as this seems to indicate that as brushes get thicker, analyte is forced to move slower through them, suggesting thicker brushes have a higher density. This could potentially suggest a bi-layer formation of the brush, a diffuse outer layer with a dense inner layer, but further studies on systems which provide resolution closer to the brush-aqueous interface would be needed to confirm this.

The observed magnitudes are consistent with fluorescence correlation spectroscopy studies and single molecule tracking experiments, which have typically found diffusion coefficients of ionic probes in polyelectrolyte brushes to vary between 0.5-10 x 10^{-9} cm^2/s.[41,49] The diffusional difference is likely due to a probe size difference as well as differential ionic interactions between the probe and the polyelectrolyte brush. It is important to note that the measurements presented in this chapter are ensemble diffusivity measurements. Individual diffusivity measurements in polymer brushes have been shown to cluster around a slow and a fast diffusion, something not observable using our system.[50]

2.3.7 Effect of dry brush thickness on critical thickness of permeable brushes

Permeability refers to the ability of an analyte to diffuse through a material. Quantifying and comparing permeability is important for developing polymer systems with optimal physical properties for applications including coatings, controlled drug release, plastics packaging,

membranes, and composite materials.[51] To probe differences in permeability through dense brushes, we consider transport from the brush/solvent interface axially down to the microring sensor surface as a function of the thickness of separate brush samples. When PMMA is exposed to an analyte from baseline solvent, we observe that the relative shift approaches zero as the thickness of a polymer brush increases (**Figure 2.4**). This suggests that there is a certain thickness at which the analyte can no longer access the sensing region, as the resonant wavelength does not change upon analyte introduction. We define this brush thickness at which the analyte is no longer permeable to the sensor surface as the critical thickness.[52,53] It can be assumed that these effects are not due solely to the evanescent decay from the instrument system because the trends of brush penetrability vary depending on analyte and brush type and thus are not simply instrumental artifacts (**Figure 2.4**). Thus, comparative permeability judgments can be made between brushes and analytes. Note that the existence of a critical thickness, like the diffusion coefficient variations, also supports the presence of a diffuse outer layer of the brush followed by a dense inner layer. How this distribution varies is likely to be determined by brush composition and analyte type.

To verify the effect of brush thickness on permeability across a variety of brush functionalities, PDMAEMA, PHEMA and PMMA polymer brushes were tested when exposed to THF and NaCl. The shifts of the sample organic analyte were defined by the shift between 5% THF in water and 5% THF-d_8 in water, as this changes the refractive index of the analyte of interest without changing any crucial intermolecular forces such as hydrogen bonding. For the same reasoning, ionic measurements were defined by the shift between water and 100 mM NaCl such that the only pertinent force would be ionic strength. Additionally, PDMAEMA was tested with these analytes in pH 9 or 3 buffer such that the brush would only be measured in either completely

collapsed or swollen form.[25] All measurements were found to follow the same trend as THF in PMMA (**Figure 2.4**). As the response types have different magnitudes, it is clear that the system is predominantly responding to the analyte partitioning into the brush and not an increase/decrease in evanescent field strength due to the brush's presence.

Critical thicknesses were calculated based on an equation originally used to define the penetration of the evanescent field in the microring resonator[35] which was adapted to determine the critical thickness from the decreasing exponential curve:

$$Relative\ Shift = \ Shift_{Max} e^{-\frac{x}{d}\ln(r)} - Shift_{Min} \quad [5]$$

where x is the dry brush thickness, r is the ratio of the minimum and maximum shifts, and d is the critical thickness (**Table 2.8**).

Table 2.8. Critical Thickness of Brushes in Various Solutions.

Brush	THF Critical Thickness (nm)	NaCl Critical Thickness (nm)
PMMA	73	59.5
PHEMA	196.2	48.4
PDMAEMA Acidic	192.6	20.8
PDMAEMA Basic	271.2	0.95

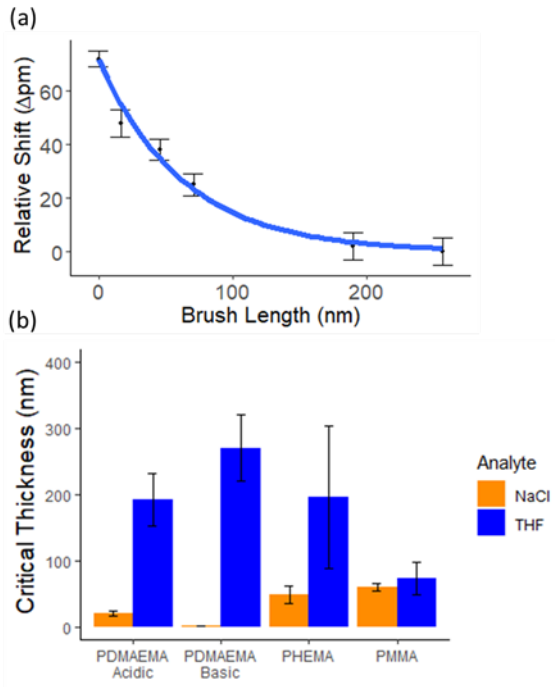

Figure 2.4. (a) Relative shift of a PMMA-coated microring from 5% THF in water to 5% THF-d_8 in water in response to changing dry polymer brush thickness fit to Equation 7 (b) A summary of the critical thicknesses from various polymer/analyte combinations. THF permeability was calculated from difference in the shift between 5% THF and 5% THF-d_8 in water, whereas NaCl permeability was calculated from a difference in the shift between aqueous and 100 mM NaCl. PMMA and PHEMA's aqueous phase was water, while PDMAEMA's aqueous phase was basic, pH 9 (0.18 M carbonate buffer) or acidic, pH 3 (0.18 M acetate buffer). Errors were calculated based from the errors in the parameters by the R curve fitting program.

Critical thickness provides a means of quantifying the favorability of brush-analyte interactions. For THF, acidic PDMAEMA brushes have a critical thickness of 193 $\pm$ 40 nm while the more basic PDMAEMA brushes have critical thicknesses of 271 $\pm$ 51 nm. This suggests that THF transport begins to be restricted at thinner brush thicknesses in acidic conditions for PDMAEMA, likely due to the more unfavorable solubility of the organic THF within the charged acidic state of PDMAEMA, compared to the non-charged state of PDMAEMA (**Figure 2.4**). Conversely, acidic PDMAEMA critical thickness for NaCl is twenty times as large as that for basic PDMAEMA by similar reasoning.

However, some trends do not follow bulk polymer expectations. For instance, PMMA has 0.37 times the critical thickness when exposed to THF compared to PDMAEMA and PHEMA, despite its solubility in bulk polymer and its high partition coefficient found earlier in this chapter. Additionally, the relative permeability of NaCl in PDMAEMA, even in its swollen form, is 0.43 times that of the relative permeability of NaCl in PMMA and PHEMA despite the charged state of NaCl. It is possible that these inconsistencies result from differences in the behavior and properties as dense films when compared to their bulk polymer counterparts. For example, the PMMA brushes near the sensor surface could adopt morphologies that restrict analyte permeability.[54] Additionally, internal brush densities can vary between various polymer brushes, impacting the ability of analytes to penetrate. It is important to note, however, that the penetration ability into a brush varies by analyte, which suggests some form of analyte specific interaction rather than just primarily brush density impacts on our measurements. Overall the interplay of these competing factors of intra- and inter-brush interactions, along with potential changes from a salted to osmotic brush regime,[19] are difficult to predict, thus demonstrating the importance of techniques that directly observe molecular partitioning in a way that is sensitive to all effects within the evanescent field.

2.3.8 Polymer brush swelling and collapsing behavior

Our previous analyte conditions all showed exponential fall-off of signal with increasing dry brush thickness (**Figure 2.4**). However, all analytes tested in those experiments were not expected to significantly swell or collapse the brush, as they did not have saturating concentrations or significantly change pH, and thus all that was observed was partition and diffusion efficiency variations across brush-analyte combinations. However, changing analytes that lead to major brush conformational changes could also impact the signals observed on the

brush-coated microring resonators. In order to characterize these types of analytes, we found the pK_as of a variety of dry thicknesses of a pH-responsive brush on the microring resonators.

It is well known that the pK_a of thin polymer brush films can be highly dependent on the dry polymer brush thickness and solution conditions.[19–28] These variations suggest that both brush thickness and the solution conditions, including ionic strength, are important determinants of pH-based swelling or collapse in polymer brush systems. The pK_a of a brush was also shown previously to depend upon the point of measurement. That is, pK_as measured close to the brush initiator for acidic brushes were found to be higher than pK_as measured at the top of the brush.[32] The multiple factors involved in brush pH response lead to challenges in quickly and specifically determining pK_a for brushes and thus their potential for swelling or collapse in different conditions.

Shifts in the resonance wavelength can be used to quantify characteristic values, such as pK_a, for the brush system grafted to the microring resonators. As an example, PDMAEMA is pH responsive with a pK_a of about 7.3 in water.[55] The brush undergoes a transition from collapsed to swollen conformation as the pH of the buffer solution is decreased and the side chains are protonated (**Figure 2.5**). By monitoring the real-time resonance shifts upon exposing the PDMAEMA brush surface to increasingly basic buffer solution cycles, we observe a differential pH responsiveness, where at pHs prone to swelling (pHs 3-6) a bulk shift followed by a long plateau can be observed, whereas those closer to the brush pK_a (pH 7 and pH 8) appear to plateau quickly (**Figure 2.5**). Similarly, resonant wavelength shifts at lower pH ranges have larger deviations than at higher pH ranges because lower pH ranges cause brush conformational change and thus more measurement variation (**Figure 2.5**). The change in resonant wavelength as a function of pH was fit to the logistic curve:

$$\Delta Shift = \frac{Shift_{Min} - Shift_{Max}}{1 + (\frac{\Delta pH}{pK_a})^p} \quad [6]$$

where Δ*Shift* is the change in resonant wavelength between a pH 9 carbonate buffer and various other buffer solutions at a pre-determined time point, p is the power parameter (the steepness of the slope of the linear region of the curve), and the pK_a of the polymer brush near the ring surface is the midpoint of the curve. It is crucial to note that by keeping time intervals consistent, the difference in permeability of the differing brush thicknesses can be highlighted (**Table 2.8**).

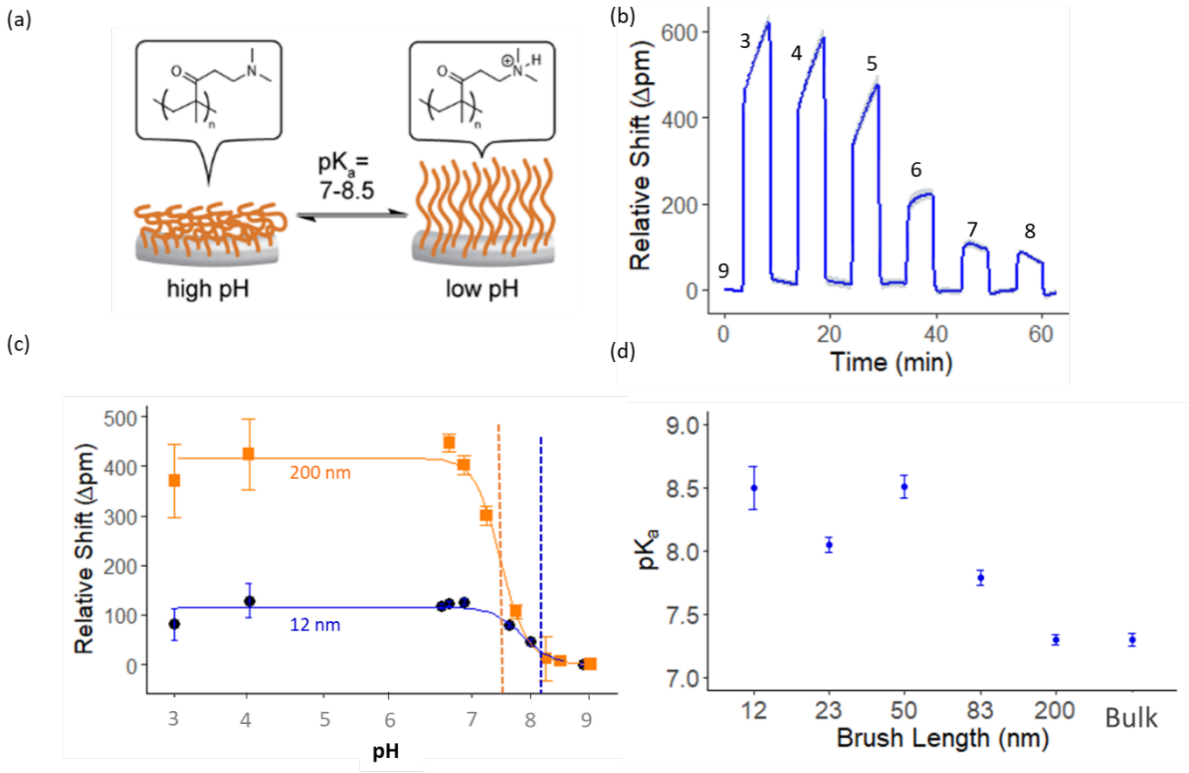

Figure 2.5 (a) Schematic of PDMAEMA polymer brush collapse and swelling. (b) Real-time response of 40 nm PDMAEMA-coated microrings to carbonate (pH 9), phosphate (pH 6-8), and acetate buffers (pH 3-5). The line is the real time data and the shading is the error between rings. (c) Relative shift of 200 nm (orange squares) and 12 nm (blue circles) PDMAEMA-coated microrings in response to changing pH conditions. The sigmoidal curves are a fit of the data to Equation 7. Dashed vertical lines are shown to mark the extracted pK_a values. Error bars are the rings' standard deviation. (d) Dependence of pK_a on polymer brush thickness shows pK_a decreases with increasing dry brush thickness. Error bars are the standard error in the calculated pK_a. Dry brush thicknesses of 12 nm and 50 nm were found to have a statistically significant difference in pK_a compared to the bulk (α=0.1).

We used the described method to calculate the pK_a close to the substrate surface of five PDMAEMA brush thicknesses by fitting the relative wavelength shift to Equation 7 (**Table 2.9**). Clear differences in brush pK_a can be seen with a change in brush thickness (**Figure 2.5**). Upon plotting the pK_a as a function of dry brush thickness, our results demonstrate that as brush thickness increases the pK_a of the brush more closely approaches that of the free bulk polymer.

Table 2.9. Fits for pK_a Determination for Various PDMAEMA Brush Thicknesses.

Dry Brush Thickness (nm)	$Shift_{Max}$	$Shift_{Min}$	pK_a	p
12	116 ± 9	-3 ± 26	8.5 ± 0.1	-25 ± 21
23	347 ± 9	-5 ± 16	8.05 ± 0.06	-15 ± 2
50	342 ± 12	5 ± 19	8.51 ± 0.09	-11 ± 2
83	416 ± 16	0 ± 19	7.79 ± 0.06	-24 ± 6
200	694 ± 22	-3 ± 23	7.30 ± 0.04	-24 ± 5

The approaching bulk behavior of the brush polymer PDMAEMA is consistent with prior results demonstrating that measuring close to the substrate/brush interface gave pK_as larger than the pK_a for bulk polymer.[25,32] However, whether this effect is consistent for different brush thicknesses has not been explored and was only explored acidic brushes, which swell upon deprotonation. We can also clearly see that brush thickness does have an effect on the apparent pK_a value as predicted, where thinner brushes have a higher pK_a than thicker brushes.[32] The difference in surface pK_a, as calculated by goniometry, compared to interior brush pK_a, also lends credence to the theory that brushes could support a spatial charge gradient in certain pH conditions, as previously suggested.[32]

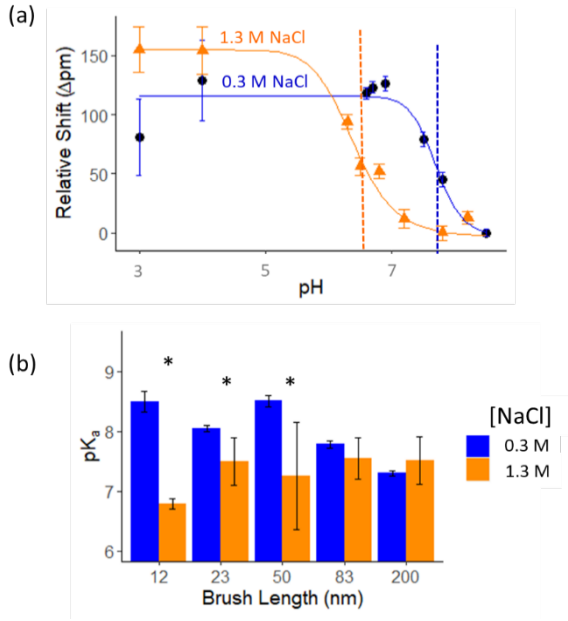

Figure 2.6 (a) Relative shift of 12 nm PDMAEMA-coated microrings in response to changing pH in low (0.3 M, blue circle) and high (1.3 M, orange triangle) salt conditions. The sigmoidal curves are a fit of the data to Equation 7. Error bars are standard deviation in the rings. (b) Thin brushes are observed to have a large pK_a sensitivity to salt concentration while thick brushes show less dependence. Low salt concentration (0.3 M) is blue while high salt concentration (1.3 M) is in orange. Error bars are the standard error in the pK_a. * represents a statistical difference with an alpha less than 0.1.

Microring resonators can be used to analyze the impact of different solution conditions on swelling and collapse behaviors. By measuring relative shift resulting from brush collapse (caused by pH changes) in different NaCl concentrations, we observed that there is a large difference in both the maximum shift and pK_a for thin brushes, changing as much as 1.75 pK_a units for the thinnest brush (**Figure 2.6**). However, there seems to be minimal sensitivity to salt concentration changes in thicker brushes (**Table 2.10**). Upon extracting pK_a values, we observe that this trend holds upon screening five different brush thicknesses (**Figure 2.6**). This is likely because a thicker brush has the potential for more areas of water isolated from the bulk solvent, meaning less permeability.[56] The impact of salt content on polymer brush pK_a, and thus polymer

brush swelling/collapse, only reinforces the importance of ionic strength controlled experiments when relying on pH-based performance.

Table 2.10. Fits for pKa Determination in High Salt Buffers for Various PDMAEMA Brush Thicknesses.

Dry Brush Thickness (nm)	$Shift_{Max}$	$Shift_{Min}$	pK_a	p
12	155 ± 8	3 ± 10	7.7 ± 0.1	-10 ± 4
23	251 ± 20	-5 ± 81	7.5 ± 0.4	-8 ± 5
50	169 ± 26	-5 ± 107	7.3 ± 0.9	-7 ± 8
83	366 ± 25	-5 ± 97	7.6 ± 0.4	-9 ± 4
200	345 ± 31	-5 ± 108	7.5 ± 0.4	-9 ± 5

2.3.9 pK_a Fitting: Extent of Equilibration Effect on Found pK_a

The speed of the assay was also greatly increased, requiring only 1.5 hours of analysis compared to the six hours required if letting the brush fully equilibrate, while showing the same trends in pK_a (**Figure 2.S 3**). While the numerical value of the pKa measurement differs based on the time point at which the resonant wavelength shift is measured, the pKa trend remains the same regardless of whether the brush is at equilibrium or not (Figure S4). This demonstrates that for the microring resonator-polymer brush system, equilibrium is not required in order to establish trends for pKa values under changing conditions. Additionally, the microring resonator system easily allows time modifications to fit the exposure time of the membrane, meaning that the

tested conditions can very closely mimic the conditions the membrane is exposed to, and thus the

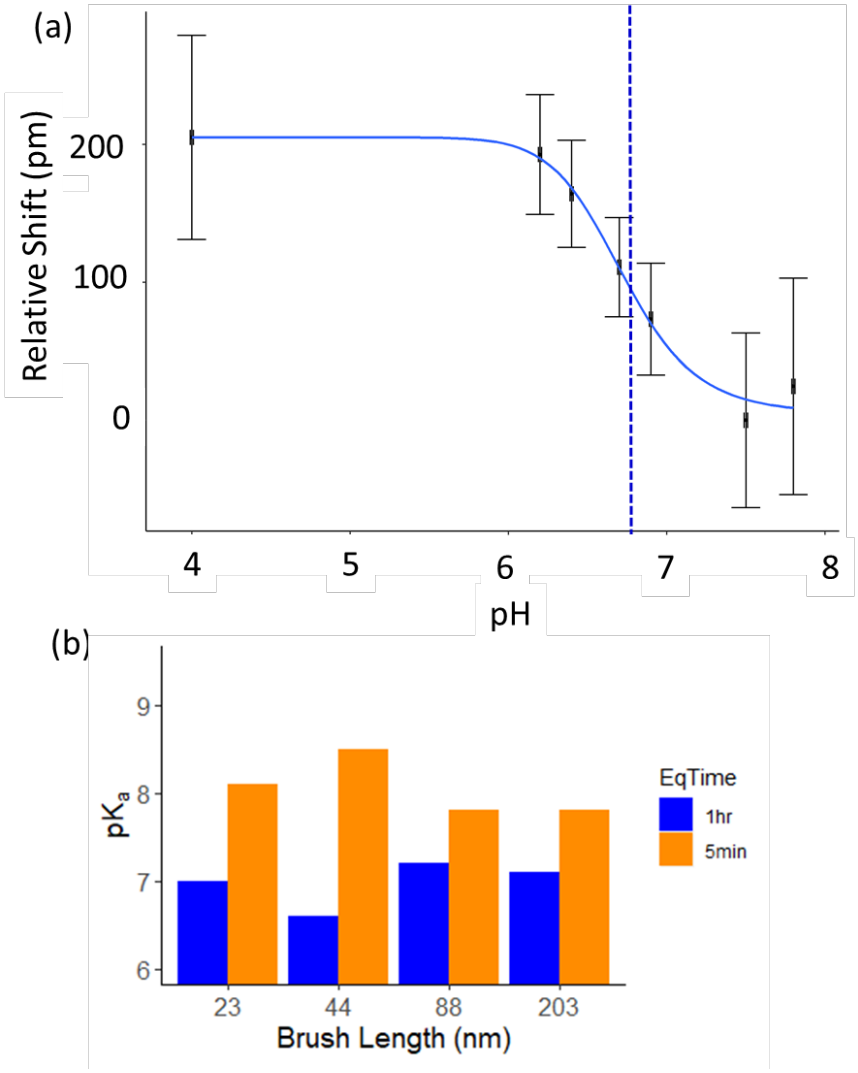

Figure 2.7. pK_a determination fit for 6 hour time point along with trend observed across brushes. (a) Relative shift of 40 nm PDMAEMA coated microrings in response to changing pH conditions. The sigmoidal curve is a fit of the data to Equation 2. A dashed vertical line is shown to mark the extracted pK_a value. Error bars are the rings' standard deviation. (b) Comparing the extracted pK_a for equilibration compared to kinetic shorter measurements. 1 hr equilibration time is in blue and resembles the bulk polymer while the kinetic 5 min equilibration time demonstrates more thickness dependence.

results of the assay should mimic the results of the membrane in the condition of interest.

2.3.10 Probing changes in polymer brush properties

Upon observing the pK_a dependence on dry brush thickness, we were interested in the effects of thickness on brush swelling and collapse. Thus the change in signal as pH of systems were varied was recorded for both a pH-responsive brush, PDMAEMA, and a pH-inert brush, PMMA (**Figure 2.8**).

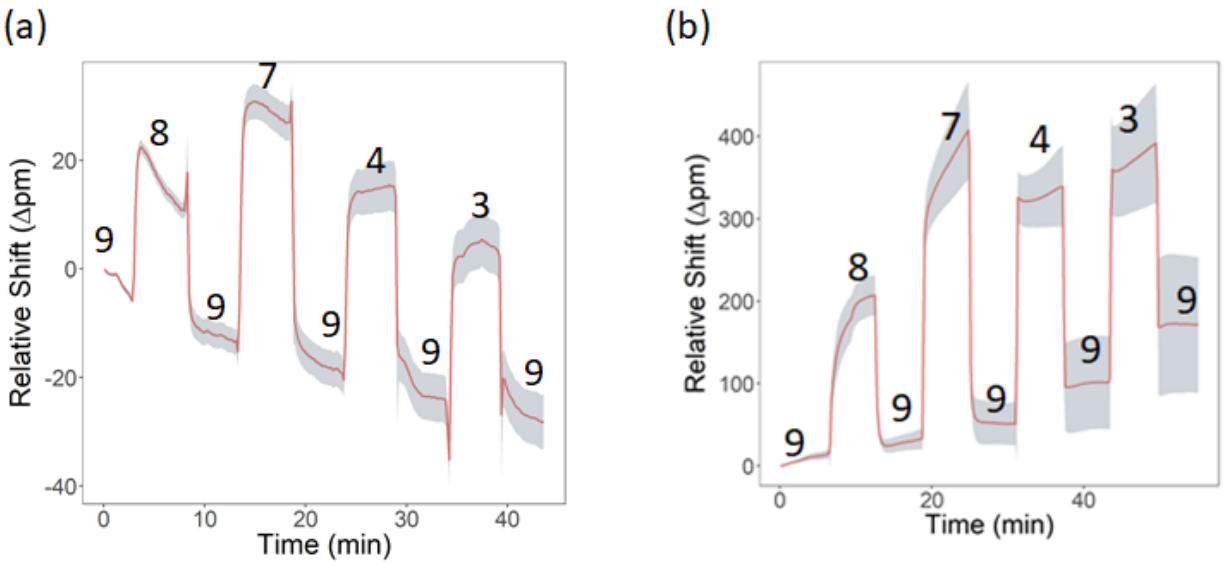

Figure 2.8. Exposing polymer brushes to a variety of pH steps. (a) PMMA polymer brush. (b) PDMAEMA polymer brush.

Upon exposing PMMA brush-coated chips, originally in pH 9 carbonate buffers, to a variety of pH buffers, the signal curves with respect to thickness still show consistent behaviors of exponential fall-off (**Figure 2.9**). This can be rationalized by considering how the hydrophobic nature of the brush does not change in response to pH, thus all that is being observed is partitioning and diffusion, exactly the same as observed with THF and NaCl (**Figure 2.4**). The amplitude and the exponent of the fit change slightly, due to both changes in the relative attraction between the brush and individual buffer components, and the differential refractive index for each buffer component (**Table 2.11**). But the extracted critical thickness values remain

similar (**Table 2.12**). This reaffirms that PMMA is pH-inert, showing that our system can accurately represent the hydrophobic state of brushes based upon signal response curves.

Table 2.11. PMMA pH Response

pH	Exponential Fits
8	$Shift = 48.12522e^{-0.02782x} - 0.41565$
7	$Shift = 89.72521e^{-0.02690x} - 0.86417$
3	$Shift = 55.91950e^{-0.01886x} - 2.87798$

Table 2.12. Critical Thickness of Different Brushes in Different pH Buffers

Polymer Brush	CT pH8 (nm)	CT pH7 (nm)	CT pH3 (nm)
PMMA	170	173	157
PDMAEMA	127	N/A	N/A

However, PDMAEMA showed radically different behaviors upon exposure to different pH buffers (**Figure 2.8**). The response to pH 8 buffer decreases exponentially with brush thickness and thus shows critical thickness behavior, consistent with PMMA's response to pH changes as well as all of the brush responses to THF and NaCl (**Table 2.13**). This is consistent with the hydrophobicity of PDMAEMA at pH 8. However, the response to pH 7 buffer increases logarithmically and the response to pH 3 buffer is linear. Note, it is likely that the response to the pH 3 buffer is indeed logarithmic, we just have measured it in the linear range. The deviation from the expected exponential fall-off can be rationalized by these transitions of PDMAEMA to

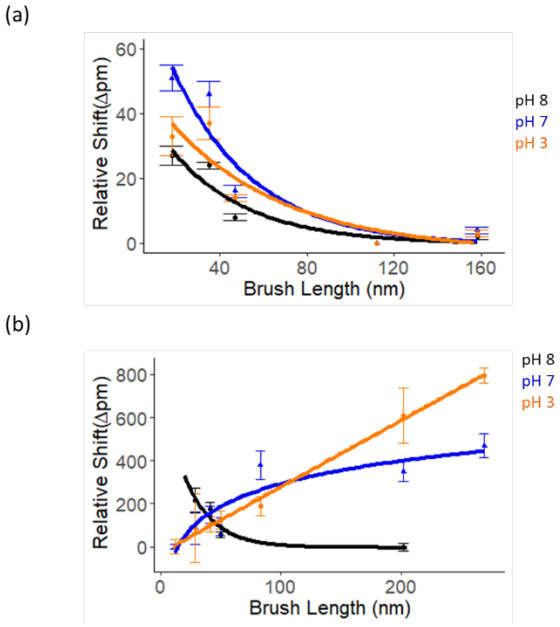

Figure 2.9 Relationship of dry brush thickness to relative shift when transitioning from pH9 to pH8 (black), pH7 (blue), and pH3 (orange) buffers. (a) PMMA brushes show similar exponential fall off regardless of pH. (b) PDMAEMA brushes show differing signal curve relationships as pH change.

a semi-hydrophilic and hydrophilic brushes at these pHs, respectively. The increase in hydrophilicity is accompanied by polymer brush swelling, which means that there are likely multiple competing factors influencing the found response profiles (**Figure 2.9**). Changes in

brush conformation will influence both the refractive index near the substrate surface, where the evanescent field intensity is the highest, as well as the partition coefficient of the analyte in the brush. The amount of solvent dissolved in the brush at a given time is also going to change with the changing hydrophilicity. Using other data off of the microring resonators indicates the consistency of our data.

Table 2.13. PDMAEMA Fits for pH Response

pH	Fits
8	$Shift = 765.96323e^{-0.04177x} - 3.83987$
7	$Shift = 151.82log(x) - 406.17$
3	$Shift = 3.08x - 28.95$

The shape of the curves observed for pH 7 and pH 3 themselves are consistent with our previous experiments. As the PDMAEMA brush thickness increases, the local pK_a is reduced. The same pH change at a thinner brush would cause more swelling than at a thicker brush around the pK_a of the brush in question. Near the pK_a of PDMAEMA, thicker brushes show reduced relative swelling and less change in the amount of analyte in the brush, as revealed by the logarithmic profile. This is similar to the behavior with the pH 8 buffer, except that the change in signal is positive. This is likely because of the brush swelling which will allow more analyte and solvent, rather than less, to be present with pH changes. Comparatively, pH 3 buffer is far from the pK_a of all of the PDMAEMA brushes tested, and thus we would expect the swelling for the pH 3 brush to continue regardless of dry brush thickness. This would result in always have a

more swollen brush, over the thickness regime tested leading to continual positive change, as observed with the linear fit, assuming that the brush is pH-sensitive. Thus, data collected by exposing brushes to various pH changes is shown to be internally consistent with the data collected in regards to brush diffusion, brush pK_a and brush partitioning coefficient.

2.4 CONCLUSIONS

We have demonstrated the utility of silicon photonic microring resonators as a platform for the *in-situ* characterization of polymer brush surfaces. Well-defined hydrophilic, hydrophobic, and stimuli-responsive polymer brushes were grown from the resonator surface. This allowed for the direct observation and quantification of the characteristics of specific brush-solvent-analyte systems, such as: diffusion and partitioning coefficients, critical thickness, hydrophobicity, and pK_a. Many of these constants can be extracted from the same set of data, which increases the amount of information gained during each individual experiment. Additionally, the surface sensitive nature of our detection platform provides a good complement to brush-liquid interface sensitive techniques, such as goniometry. Microring resonators' spatial independence allows for spatial multiplexing of brush types, and in future work, should allow for fast combinatorial screening of analyte-brush systems in a multiplexed fashion.

While microring resonators provide a sensitive high-throughput platform for polymer brush study, it would be ideal to have a system which is more portable in order to study small molecules, such that pollution analysis can be at point of collection rather than some time afterwards. Thus, the rest of this thesis will explore the use of a smaller and cheaper technology as a means of analyzing small molecule concentrations, microfluidic droptodes.

2.5 ACKNOWLEDGMENTS

This work was supported in part by the National Science Foundation (CHE-1508656), the Defense Threat Reduction Agency (HDTRA 1-12-1-0035), and the Department of Defense/US Army (W911NF-17-1-0351). K.A.M. (DGE-1746047), S.P.W. (DGE-1256260), and A.L.D.S. (DGE-1144245) acknowledge the National Science Foundation for support and L.K. acknowledges the Arnold O. and Mabel M. Beckman Foundation Beckman-Brown Interdisciplinary Postdoctoral Fellowship. We thank Nathan Reed for assistance in developing polymer brush synthesis methodology. We also thank members of the Braun and Bailey groups for insightful discussions and Professor Christopher Evans for technical advice. This work was carried out in part in the Materials Research Laboratory Central Research Facilities at the University of Illinois and at the Lurie Nanofabrication Facility at the University of Michigan.

2.6 REFERENCES

1. Zoppe, J. O. *et al.* Surface-Initiated Controlled Radical Polymerization: State-of-the-Art, Opportunities, and Challenges in Surface and Interface Engineering with Polymer Brushes. *Chem. Rev.* **117**, 1105–1318 (2017).

2. Chen, W. L., Cordero, R., Tran, H. & Ober, C. K. 50th Anniversary Perspective: Polymer Brushes: Novel Surfaces for Future Materials. *Macromolecules* **50**, 4089–4113 (2017).

3. Ayres, N. Polymer Brushes: Applications in Biomaterials and Nanotechnology. *Polym. Chem.* **1**, 769–777 (2010).

4. Krishnamoorthy, M., Hakobyan, S., Ramstedt, M. & Gautrot, J. E. Surface-Initiated Polymer Brushes in the Biomedical Field: Applications in Membrane Science, Biosensing, Cell Culture, Regenerative Medicine and Antibacterial Coatings. *Chemical Reviews* vol. 114 10976–11026 (2014).

5. Keating, J. J., Imbrogno, J. & Belfort, G. Polymer Brushes for Membrane Separations: A Review. *ACS Applied Materials and Interfaces* vol. 8 28383–28399 (2016).

6. Chen, H. *et al.* Molecular Understanding and Structural-Based Design of Polyacrylamides and Polyacrylates as Antifouling Materials. *Langmuir* **32**, 3315–3330 (2016).

7. Stuart, M. A. C. *et al.* Emerging Applications of Stimuli-Responsive Polymer Materials. *Nature Materials* **9**, 101–113 (2010).

8. Matyjaszewski, K. Atom Transfer Radical Polymerization (ATRP): Current Status and Future Perspectives. *Macromolecules* **45**, 4015–4039 (2012).

9. Tate, R. S. *et al.* Extraordinary Elevation of the Glass Transition Temperature of thin Polymer Films Grafted to Silicon Oxide Substrates. *J. Chem. Phys.* **115**, 9982–9990 (2001).

10. Yamamoto, S., Tsujii, Y. & Fukuda, T. Glass Transition Temperatures of High-Density Poly(methyl methacrylate)Brushes. *Macromolecules* **35**, 6077–6079 (2002).

11. Cheng, N., Brown, A. A., Azzaroni, O. & Huck, W. T. S. Thickness-Dependent Properties of Polyzwitterionic Brushes. *Macromolecules* **41**, 6317–6321 (2008).

12. Schuh, C. & Rühe, J. Penetration of Polymer Brushes by Chemical Nonidentical Free Polymers. *Macromolecules* **44**, 3502–3510 (2011).

13. Adiga, S. P. & Brenner, D. W. Stimuli-Responsive Polymer Brushes for Flow Control through Nanopores. *J. Funct. Biomater.* **3**, 239–256 (2012).

14. Park, Y. S., Ito, Y. & Imanishi, Y. Permeation Control through Porous Membranes Immobilized with Thermosensitive Polymer. *Langmuir* **14**, 910–914 (1998).

15. Lanotte, L., Guido, S., Misbah, C., Peyla, P. & Bureau, L. Flow Reduction in Microchannels Coated with a Polymer Brush. *Langmuir* **28**, 13758–13764 (2012).

16. Dhinojwala, A. & Granick, S. Surface Forces in the Tapping Mode: Solvent Permeability and Hydrodynamic Thickness of Adsorbed Polymer Brushes. *Macromolecules* **30**, 1079–1085 (1997).

17. Ivkov, R., Butler, P. D., Satija, S. K. & Fetters, L. J. Effect of Solvent Flow on a Polymer Brush: A Neutron Reflectivity Study of the Brush Height and Chain Density Profile. *Langmuir* **17**, 2999–3005 (2001).

18. Yang, T. *et al.* A Graphene Oxide Polymer Brush Based Cross-Linked Nanocomposite Proton Exchange Membrane for Direct Methanol Fuel Cells. *RSC Adv.* **8**, 15740–15753 (2018).

19. Barbey, R. *et al.* Polymer Brushes Via Surface-Initiated Controlled Radical Polymerization: Synthesis, Characterization, Properties, and Applications. *Chem. Rev.* **109**, 5437–5527 (2009).

20. Lego, B., Skene, W. G. & Giasson, S. Swelling Study of Responsive Polyelectrolyte Brushes Grafted from Mica Substrates: Effect of pH, Salt, and Grafting Density. *Macromolecules* **43**, 4384–4393 (2010).

21. Parnell, A. J. *et al.* Direct Visualization of the Real Time Swelling and Collapse of a Poly(methacrylic acid) Brush Using Atomic Force Microscopy. *Soft Matter* **5**, 296–299 (2009).

22. Valiaev, A., Abu-Lail, N. I., Dong, W. L., Chilkoti, A. & Zauscher, S. Microcantilever Sensing and Actuation with End-Grafted Stimulus-Responsive Elastin-Like Polypeptides. *Langmuir* **23**, 339–344 (2007).

23. Barbey, R., Laporte, V., Alnabulsi, S. & Klok, H. A. Postpolymerization Modification of Poly(glycidyl methacrylate) Brushes: An XPS Depth-Profiling Study. *Macromolecules* **46**, 6151–6158 (2013).

24. Schüwer, N., Geue, T., Hinestrosa, J. P. & Klok, H. A. Neutron Reflectivity Study on the Postpolymerization Modification of Poly(2-hydroxyethyl methacrylate) Brushes. *Macromolecules* **44**, 6868–6874 (2011).

25. Sanjuan, S., Perrin, P., Pantoustier, N. & Tran, Y. Synthesis and Swelling Behavior of pH-Responsive Polybase Brushes. *Langmuir* **23**, 5769–5778 (2007).

26. Fielding, L. A., Edmondson, S. & Armes, S. P. Synthesis of pH-Responsive Tertiary Amine Methacrylate Polymer Brushes and Their Response to Acidic Vapour. *J. Mater.*

Chem. **21**, 11773–11780 (2011).

27. Willott, J. D. *et al.* Hydrophobic Effects Within the Dynamic pH-Response of Polybasic Tertiary Amine Methacrylate Brushes. *Phys. Chem. Chem. Phys.* **17**, 3880–3890 (2015).

28. Zhang, H. & Ruhe, J. Swelling of Poly(methyacrlic acid) Brushes: Influence of Monovalent Salts in the Environment. *Macromolecules* **38**, 4855–4860 (2005).

29. Yim, H. *et al.* Evidence for Vertical Phase Separation in Densely Grafted, High-Molecular-Weight Poly(N-isopropylacrylamide) Brushes in Water. *Phys. Rev. E - Stat. Nonlinear, Soft Matter Phys.* **72**, (2005).

30. He, J. *et al.* Study and Application of a Linear Frequency-Thickness Relation for Surface-Initiated Atom Transfer Radical Polymerization in a Quartz Crystal Microbalance. *Macromolecules* **40**, 3090–3096 (2007).

31. Du, Y. *et al.* Understanding the Oxidative Stability of Antifouling Polymer Brushes. *Langmuir* **33**, 7298–7304 (2017).

32. Dong, R., Lindau, M. & Ober, C. K. Dissociation Behavior of Weak Polyelectrolyte Brushes on a Planar Surface. *Langmuir* **25**, 4774–4779 (2009).

33. Stanton, A. L. D., Serrano, K. A., Braun, P. V. & Bailey, R. C. Polymer Brush-Modified Microring Resonators for Partition-Enhanced Small Molecule Chemical Detection. *ChemistrySelect* **2**, 1521–1524 (2017).

34. Limpoco, F. T. & Bailey, R. C. Real-Time Monitoring of Surface-Initiated Atom Transfer Radical Polymerization Using Silicon Photonic Microring Resonators: Implications for Combinatorial Screening of Polymer Brush Growth Conditions. *J. Am. Chem. Soc.* **133**, 14864–14867 (2011).

35. Wade, J. H. & Bailey, R. C. Applications of Optical Microcavity Resonators in Analytical Chemistry. *Annu. Rev. Anal. Chem.* **9**, 1–25 (2016).

36. Luchansky, M. S. *et al.* Characterization of the Evanescent Field Profile and Bound Mass Sensitivity of a Label-Free Silicon Photonic Microring Resonator Biosensing Platform. *Biosens. Bioelectron.* **26**, 1283–1291 (2010).

37. Iqbal, M. *et al.* Label-Free Biosensor Arrays Based on Silicon Ring Resonators and High-Speed Optical Scanning Instrumentation. *IEEE J. Sel. Top. Quantum Electron.* **16**, 654–661 (2010).

38. Xue, C. *et al.* Protein Adsorption on Poly(N -isopropylacrylamide) Brushes: Dependence on Grafting Density and Chain Collapse. *Langmuir* **27**, 8810–8818 (2011).

39. Sothivelr, K., Bender, F., Josse, F., Yaz, E. E. & Ricco, A. J. Obtaining Chemical Selectivity from a Single, Nonselective Sensing Film: Two-Stage Adaptive Estimation

Scheme with Multiparameter Measurement to Quantify Mixture Components and Interferents. *ACS Sensors* **3**, 1656–1665 (2018).

40. Braeckmans, K., Deschout, H., Demeester, J. & De Smedt, S. C. Measuring Molecular Dynamics by FRAP, FCS, and SPT. in *Optical Fluorescence Microscopy: From the Spectral to the Nano Dimension* vol. 9783642151750 153–163 (Springer-Verlag Berlin Heidelberg, 2011).

41. Heitzman, C. E., Tu, H. & Braun, P. V. Two-Dimensional Diffusion of Prodan on Self-Assembled Monolayers Studied by Fluorescence Recovery After Photobleaching. *J. Phys. Chem. B* **108**, 13764–13770 (2004).

42. Reznik, C., Estillore, N., Advincula, R. C. & Landes, C. F. Single Molecule Spectroscopy Reveals Heterogeneous Transport Mechanisms for Molecular Ions in a Polyelectrolyte Polymer Brush. *J. Phys. Chem. B* **113**, 14611–14618 (2009).

43. Reznik, C. *et al.* Single Ion Diffusive Transport Within a Poly(styrene sulfonate) Polymer Brush Matrix Probed by Fluorescence Correlation Spectroscopy. *J. Phys. Chem. B* **112**, 10890–10897 (2008).

44. Tauzin, L. J. *et al.* Charge-Dependent Transport Switching of Single Molecular Ions in a Weak Polyelectrolyte Multilayer. *Langmuir* **30**, 8391–8399 (2014).

45. Xu, Q., Zhang, K. & Jiang, J. Molecular Simulation and Analysis of Sorption Process toward Theoretical Prediction for Liquid Permeation through Membranes. *J. Phys. Chem. B* **122**, 12211–12218 (2018).

46. Tsai, T. H., Ali, M. A., Jiang, Z. & Braun, P. V. Dynamic Gradient Directed Molecular Transport and Concentration in Hydrogel Films. *Angew. Chemie - Int. Ed.* **56**, 5001–5006 (2017).

47. Ali, M. A., Tsai, T. H. & Braun, P. V. Amplified Detection of Chemical Warfare Agents Using Two-Dimensional Chemical Potential Gradients. *ACS Omega* **3**, 14665–14670 (2018).

48. Filippidi, E., Michailidou, V., Loppinet, B., Rühe, J. & Fytas, G. Brownian Diffusion Close to a Polymer Brush. *Langmuir* **23**, 5139–5142 (2007).

49. Zhang, C., Chu, X., Zheng, Z., Jia, P. & Zhao, J. Diffusion of Ionic Fluorescent Probes Atop Polyelectrolyte Brushes. *J. Phys. Chem. B* **115**, 15167–15173 (2011).

50. Elliott, L. C. C., Barhoum, M., Harris, J. M. & Bohn, P. W. Trajectory Analysis of Single Molecules Exhibiting non-Brownian Motion. *Phys. Chem. Chem. Phys.* **13**, 4326–4334 (2011).

51. Comyn, J. Introduction to Polymer Permeability and the Mathematics of Diffusion. in *Polymer Permeability* 1–10 (Springer Netherlands, 1985).

52. Mahalik, J. P., Sumpter, B. G. & Kumar, R. Vertical Phase Segregation Induced by Dipolar Interactions in Planar Polymer Brushes. *Macromolecules* **49**, 7096–7107 (2016).

53. Hwang, S. T. & Kammermeyer, K. Effect of Thickness on Permeability. *Polym Sci and Technol.* **6**, 197–205 (1974).

54. Zhou, X. D., Zhang, S. C., Huebner, W., Ownby, P. D. & Gu, H. Effect of the Solvent on the Particle Morphology of Spray Dried PMMA. *J. Mater. Sci.* **36**, 3759–3768 (2001).

55. Zhang, C. & Maric, M. Synthesis of Stimuli-responsive, Water-soluble Poly[2-(dimethylamino)ethyl methacrylate/styrene] Statistical Copolymers by Nitroxide Mediated Polymerization. *Polymers (Basel).* **3**, 1398–1422 (2011).

56. Nagai, K. *et al.* Solubility and Diffusivity of Sodium Chloride in Phase-Separated Block Copolymers of Poly(2-dimethylaminoethyl methacrylate), Poly(1,1′-dihydroperfluorooctyl methacrylate) and Poly(1,1,2,2-tetrahydroperfluorooctyl acrylate). *Polymer (Guildf).* **42**, 09941–09948 (2001).

57. Washburn, A. L., Gunn, L. C. & Bailey, R. C. Label-Free Quantitation of a Cancer Biomarker in Complex Media Using Silicon Photonic Microring Resonators. *Anal. Chem.* **81**, 9499–9506 (2009).

Chapter 3.

Characterization of the Impact of Mixing and Volumes on the Behavior of Microfluidic Droptodes

This work was adapted from Wetzler-Quevedo, S.; Meyerhoff, M.E. and Bailey R.C. Characterization of the Impact of Mixing and Droplet Volumes on the Behavior of Microfluidic Droptodes. Analyst. 2021.

3.1 INTRODUCTION

The rapid and sensitive detection of ions in a variety of matrices is critical not only for monitoring reaction processing and contamination, but also for disease diagnostics and clinical practice. Traditionally, ions are measured using ion-selective electrodes (ISEs) or ion-selective optodes (ISOs): technologies that exhibit a change in voltage or color/fluorescence, respectively, depending on the presence of an ion of interest.[1,2] ISOs offer the additional benefit of minimal instrumentation, leading to a high potential for ISOs as low-cost point-of-care devices.[2] Additionally, changes in organic phase composition and the ratio of organic and aqueous phases have been shown to affect optodic sensitivity.[3] However, ISOs suffer from the need for milliliters of sample, equilibration times on the orders of minutes, and the possibility of leaching reagents into the sample. These limitations, along with swelling of the PVC or other polymeric matrices that typically comprise the optodes, greatly decrease ISOs' long term usage and reliability for clinical practice.[2,4,5]

In response to these drawbacks, we have developed a droplet microfluidic optode system, which we have termed as "droptodes."[6] In a droptode system, the aqueous phase is segmented into individual micro to nano-liter sized droplets separated by an immiscible carrier

oil phase containing a chromoionophore, an ionophore with selectivity for the analyte of interest and an ion-exchanger. Ion-exchange takes place across the aqueous/oil boundary, leading to an ion-dependent change in the charge state of the chromoionophore causing a colorimetric and/or fluorometric signal change (**Figure 3.1**).

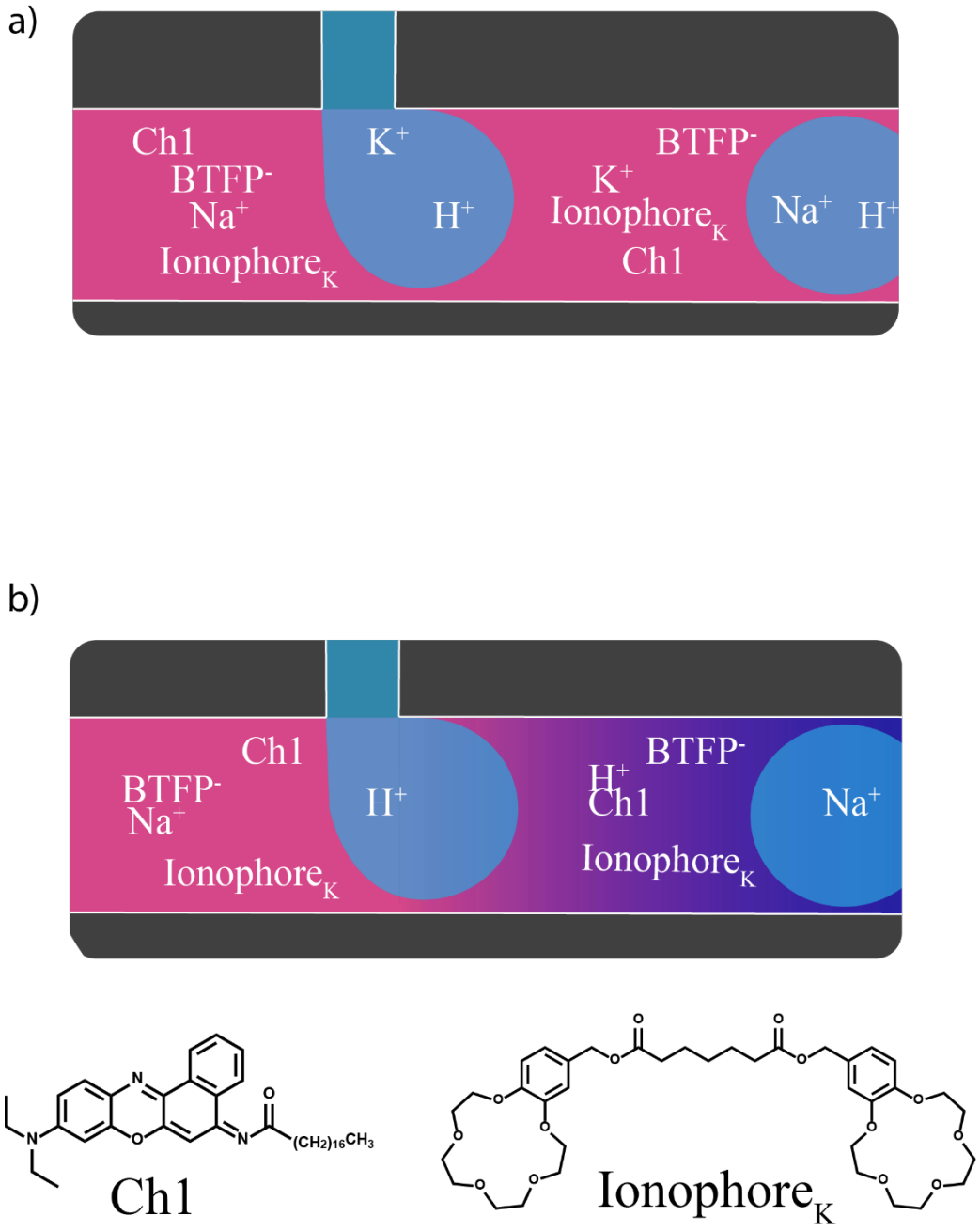

Figure 3.1. Mechanism for potassium detection in droptode. (a) When no potassium is present, a proton is used to balance the charge caused by the ion-exchanger (NaBTFP), leading to a change in the chromophoric properties of the chromoionophore (Ch1). (b) When potassium is present, it bonds with the specific ionophore and transfers into the oil phase. The positive charge from potassium balances the negative charge from the ion exchager, meaning no proton transfer is needed and there is no change in color and/or fluorescence.

Droptode measurements are performed in only seconds, do not suffer from leeching of reagents, and use very small (nL-μL) sample sizes. Additionally, droptode channels are fabricated in poly(dimethyl siloxane) (PDMS) devices, which allow for low cost and rapid prototyping.[7] Droptode technology has been shown to be compatible with detection of cations, anions and polycations, and can operate with complex sample matrices, such as whole blood, owing to the fact that the optical signal measurement is made in the oil phase.[6]

While droptodes have opened up a novel means of analyzing ions using microfluidics, the benefits of droplet microfluidics on the droptode system have not yet been fully exploited. Droplet microfluidics allows for real-time analysis, modulation of droplet size and composition, and the varying of droplet speeds.[8,9,10] Thus, the flexibility of droplet microfluidics could allow for one droptode device to be used for measurement over a variety of concentration ranges by simply changing fluidic parameters.

Herein the impacts of experimental parameters on droptode sensitivity using a potassium droptode system are explored. Specifically, we analyzed the impact of droplet speed and position of measurement relative to droplet generation on droptode sensitivity. We found that, despite spending the same amount of time on device, changing droplet speed and the position of measurement on device do not lead to the same changes in sensitivity. However, we confirmed that channel-induced mixing led to droptodes with increased sensitivity at low concentrations by almost an order of magnitude. We also analyzed the impact of changing droplet volume compared to carrier volume, finding that a higher aqueous volume led to a more sensitive linear region, but reduces the dynamic range at lower concentrations. Taken together, these studies support the fact that droptodes can be tuned to optimize analytical performance for diverse measurement applications.

3.2 EXPERIMENTAL SECTION

3.2.1 Chemicals and Materials

Unless otherwise stated, all chemicals were purchased from Sigma Aldrich. SU-8 2025 negative epoxy photoresist was a product of MicroChem Corp. Silicon wafers were purchased from University Wafer. Tridecafluoro-1,1,2,2-tetrahydrooctyl silane was from Gelest Inc. Poly(dimethyl siloxane) (PDMS) was purchased as separate base and curing agents from Momentive Performance Materials. 24-gauge needles and plastic syringes were obtained from Thermo Fisher Scientific. 24-gauge PTFE tubing was from Cole-Parmer. The syringe pumps used were Pump 11 Pico Plus Elite models from Harvard Apparatus.

3.2.2 Device Fabrication

Devices were fabricated using standard soft lithography techniques.[7] SU-8 2025 negative epoxy photoresist was applied to a clean Silicon wafer to a thickness of 40 μm via spin-coating. Masks were designed in AutoCAD software (Autodesk, Inc.) and were printed as transparencies (CAD/Art Services, Inc) for use in photolithography. After wafer baking and development, tridecafluoro-1,1,2,2-tetrahydrooctyl trichlorosilane was deposited on the resulting master molds using vacuum assisted chemical vapor deposition. Devices were made from their respective masters using a 10:1 degassed mixture of RTV615 base: curing agent ratio. Holes for the inlet and outlet were punched using a 24-gauge needle and then devices were adhered to a glass slide using oxygen plasma bonding. All channels were 40 μm in depth and 80 μm in width, except for the aqueous inlet which was 40 μm in width (**Figure 3.2**). The standard measurement point was 3 cm from the T-junction unless otherwise noted.

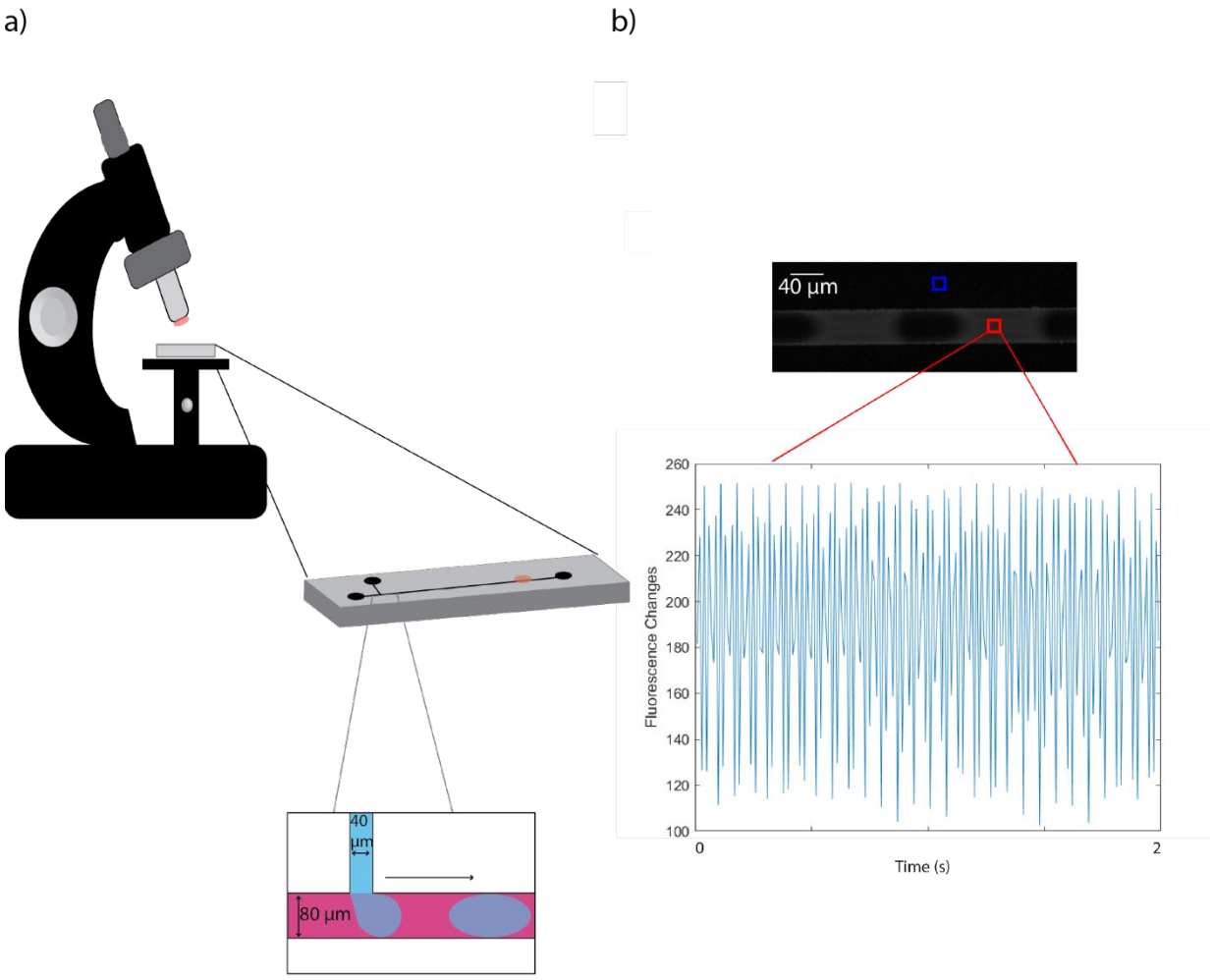

Figure 3.2. Method of droptode measurement. (a) Droplets were formed using a PDMS microfluidic device and their fluorescence was measured using a fluorescent microscope. (b) In order to track fluorescence, a set area within the channel as analyzed for its fluorescence changes. The background (blue box) from outside the channel was subtracted frame by frame. The resulting peaks were then averaged.

3.2.3 Droptode Experiments

Samples were serially diluted from a 1 M potassium chloride (KCl) solution in pH 7.4 HEPES buffer. Stock solutions of 400 µM Chromoionophore I in dioctyl sebacate (DOS), 1 mM potassium Ionophore II in DOS and 1 mM sodium tetrakis[3,5-bis(trifluoromethyl)phenyl] borate (NaTFPB) in DOS were aliquoted and stored at -20°C for up to three months. Stocks were

used to make an oil phase with the final concentrations of 100 μM Chromoionophore 1, 300 μM potassium ionophore II and 200 μM NaTFPB. Both the sample and oil solutions were loaded into plastic 3 mL syringes and flowed through 24-gauge PTFE tubing into the device using syringe pumps to generate droplets. Unless otherwise noted, the solution delivery rate was 2 μL/min. The intensity of fluorescence at various points was determined using a Nile Red filter cube (Leica Microsystems), and a VEO 640L high speed camera (Vision Research Inc.) connected to a DMi8 light microscope (Leica Microsystems).

3.2.4 Data Analysis

The relationship between total flow rate on the device (that is the sum of both the aqueous and oil flow rates), and the time spent on the device was calculated by dividing the volume traveled on the device by the total flow rate, or (Equation 3.1)

$$t = \frac{V_{channel}}{v} = \frac{0.096\ \mu L}{v} \qquad [3.1]$$

All images from a single calibration curve were combined in ImageJ (NIH). Droplet size, spacing and frequency was determined from brightfield images. For fluorescent images, the combined images were enhanced in their contrast to 0.3% saturation, and normalized using ImageJ software, for easier visualization. The fluorescence intensity within a 30 x 30-pixel spot in the middle of the channel was determined using ImageJ for each frame of the combined video samples, averaging about 40 measurements from oil segments (code in Appendix 2). A separate measurement of the background was taken and subtracted from the in-channel fluorescence intensity on a frame-by-frame basis. The resulting measurements were then analyzed for peaks using MATLAB (**Figure 3.2**, code in Appendix 3). To account for variations in light source and oil concentration, data were normalized (Equation 3.2):

$$Normalized\ Fluorescence = 1 - \frac{F - F_{Max}}{F_{Max} - F_{Min}} = 1 - \frac{F - F_{Buffer}}{F_{Buffer} - F_{2M}} \quad [3.2]$$

Where F is the fluorescence caused by the sample, F_{2M} is the fluorescence caused by 2M KCl in pH 7.4 0.1M Tric-HCl as the aqueous phase and F_{Buffer} is the fluorescence caused by the Tris buffer only as the aqueous phase.

The results of the measurements were then fit to a logistic curve against the log of the concentration of potassium to determine the limit of detection, the linear range, and the sensitivity of the various droptode conditions (**Figure 3.3**, Equation 3.1, code in Appendix 4). The limit of detection (LoD) was calculated as the concentration at 3 times the noise in the baseline response and the sensitivity was determined based on the slope found in the linear range.

3.3 RESULTS AND DISCUSSION

Initially time on device was varied by changing the speed of droplets on the device. The ratio between the aqueous and oil flow rate remained equal, thereby keeping the size and spacing of the droplets consistent (SD: 4.3%), while the total flow rate varied between 1 µL/min and 32 µL/min. The resulting fluorescence curves (**Figure 3.3**) demonstrate that a slower overall flow rate, and therefore more time on device, leads to greater fluorescence difference between the buffer and the 1M potassium sample.

Once the curves were normalized using Equation 1 (**Figure 3.3**), the curves appear to be similar in shape. The fastest moving droptode has a limit of detection of 2×10^{-4} M, about three times higher than all other speeds of droptodes tested, which converged around $6 \times 10^{-5} \pm 2 \times 10^{-5}$ M. The convergence of limits of detection suggests that the majority of the droptode conditions

tested here achieved equilibrium between two phases, with the exception of the fastest droplet generation rate.

Selectivity was minimally impacted by the droptode speed across a range of concentrations of the interfering ion (in this case sodium ions). The exception for this is when moving at the fastest droptode speed studied, where each droplet takes 0.2 s to traverse the length

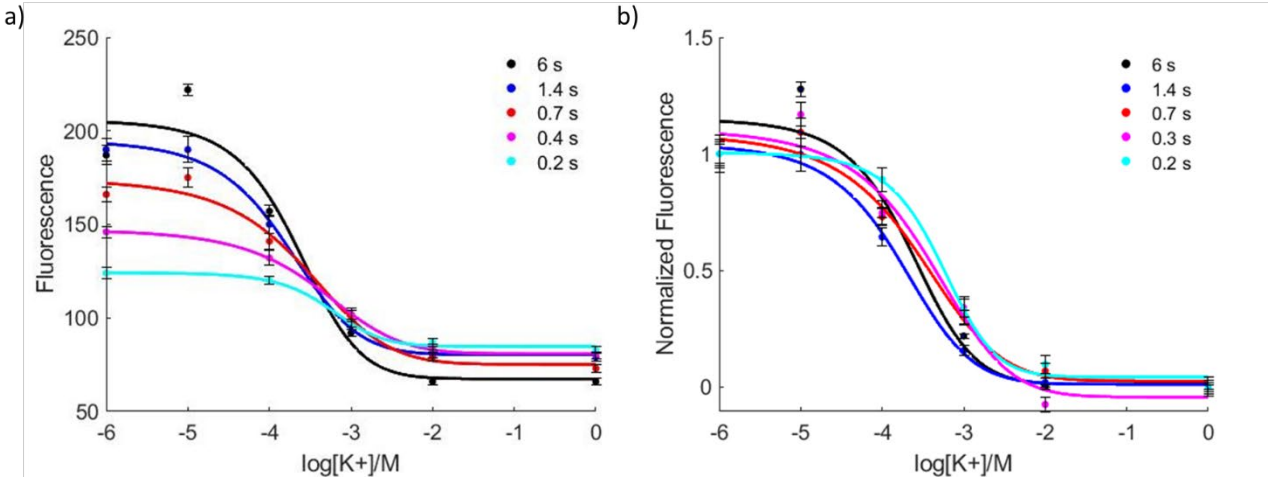

Figure 3.3. Fluorescence Measurements of potassium droptodes at various flow rates. (a) The original fluorescent measurements. Note that the maximum and minimum fluorescence is impacted by time on device. (b) The fluorescence normalized to the maximum and minimum fluorescence, defined by the buffer response and the response to 2M KCl, respectively. All except the fastest droptode, 0.2 s on device, have limits of detection within approximately 1 x 10^{-5} M of each other. Error bars represent the standard deviation between measurements (n=3).

of the device. At that point, we see a decline in selectivity against both 0.1M and 1M NaCl, but not a selectivity decline against 1 x 10^{-3} M NaCl (**Figure 3.4**). By comparison, in ion-selective electrodes the selectivity coefficient against sodium for the same ionophore was found to be 6 x 10^{-4} compared to a constant background of 1 x 10^{-4} M potassium.[11]

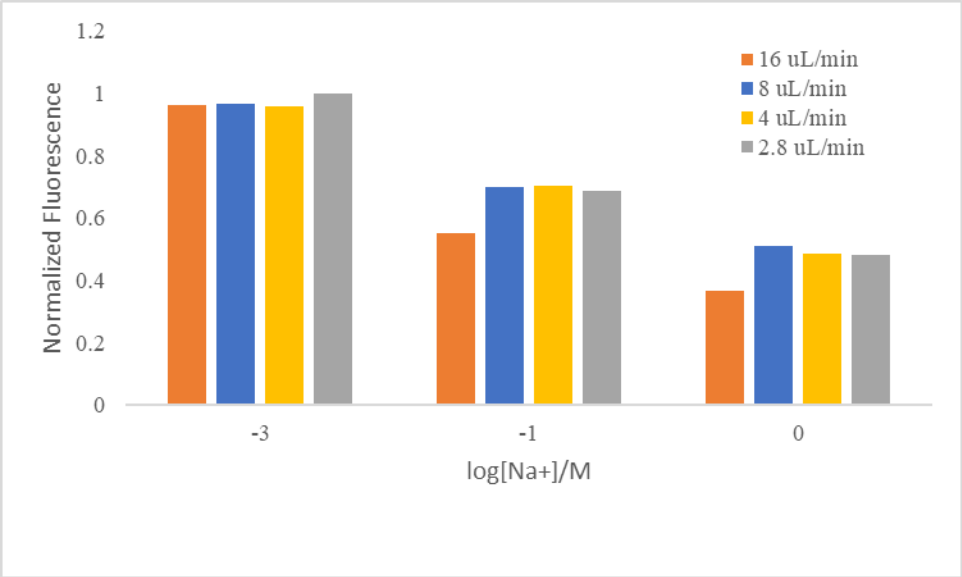

Figure 3.4. Na^+ Selectivity in a K^+ Selective Oil as Change Flow Rate. In a 1:1 flow ratio, at various total flow rates, aqueous droplets were flown in an oil carrier phase. The ideal value for a selective oil would be for 1-α to be 1 for all concentrations of Na^+. We see the first divergence from this when looking at 10^{-1} M Na^+. Note that the deviation from 1 is similar for the three lower flow rates, but greater for the highest one. This trend continues when looking at 1M Na^+.

However, there is some potential that changing the speed of the droplets, rather than just varying the time on device, also altered the speed of mixing by changing the velocity of local flow fields.[12] In order to test this, we analyzed the response of droptodes at different distances from the droplet generation T junction. If the only thing impacting the calibration curves was equilibration time, we would expect changing the droptode measurement position to result in similar calibration curves to those in **Figure 3.3**. However, as **Figure 3.5** demonstrates, the calibration curves do not all converge. Specifically, the less time on device, based on measurement position, the lower limit of detection for the testing application. By spending half the amount of time on device, the limit of detection decreased from 5 x 10^{-5} M to 1.7 x 10^{-7} M. This decrease in limit of detection came alongside a lessening of sensitivity in the linear region, by a factor of 1.3. The dynamic range was expanded, but sensitivity within the dynamic range

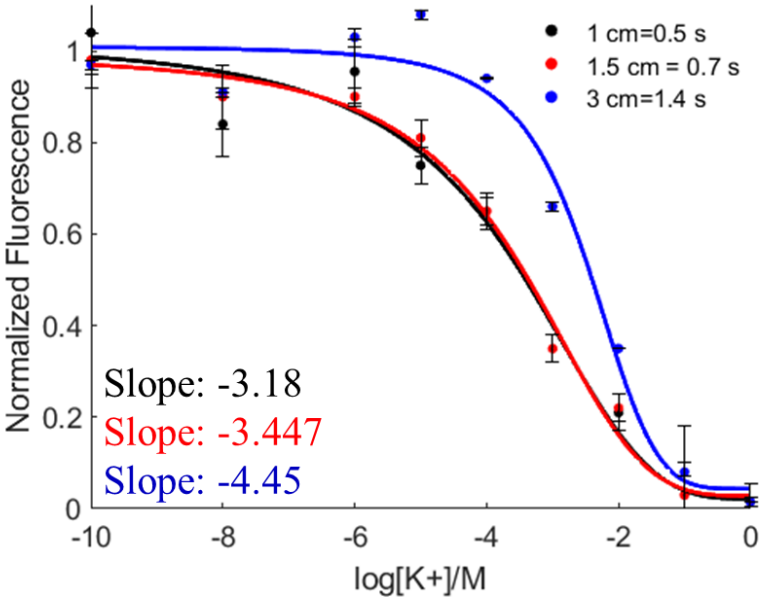

Figure 3.5. The impact of time on device by changing the measurement point on droptode behavior. The error bars are the standard deviation between measurements (n=3). As the droptode measurement point moved further from the T junction, the steeper and narrower the linear response range.

was decreased by 33%. While these results seem counterintuitive, as more time on device should allow more time for equilibration, they were observed over three replicates and three different devices. Potential causes for this observed lower detection limit, such as PDMS leeching or competition between pH and potassium equilibration, should be explored further.

It is also important to note that the change in position of measurement on device also impacted the selectivity of the device against sodium ions, but in this case the impact of the selectivity was more universal. The selectivity at an earlier point of detection was decreased for sodium concentrations ranging from 1 x 10^{-3} M to 1M NaCl, which is an expanded range compared to that seen for changing total flow rate on device (**Figure 3.6**).

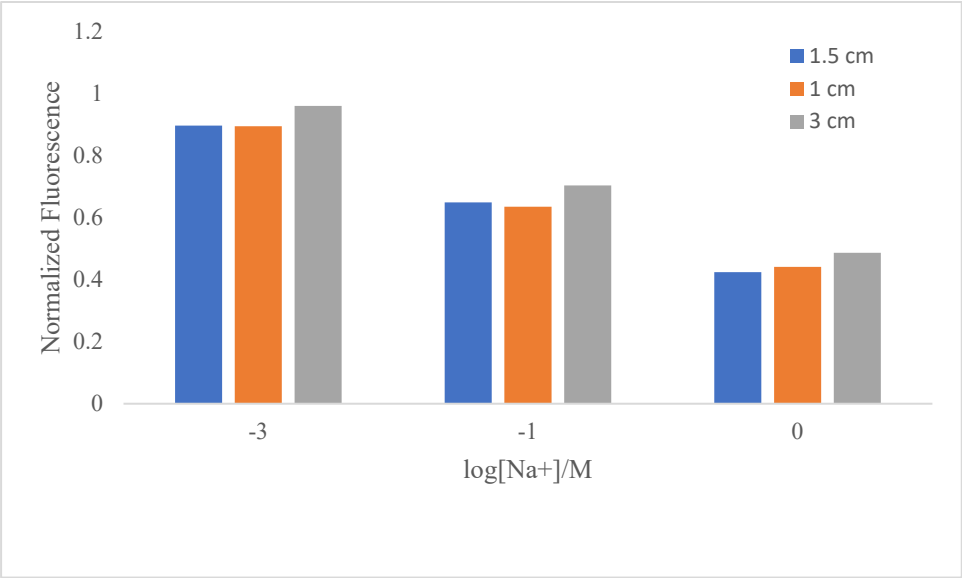

Figure 3.6. Na^+ Selectivity in a K^+ Selective Oil as Change Position. In a 1:1 flow ratio, at a 4 µL/min total flow rate, aqueous droplets were flown in an oil carrier phase. The ideal value for a selective oil would be for 1-α to be 1 for all concentrations of Na^+. We see the first divergence from this when looking at 10^{-3} M Na^+ when measuring at 1 and 1.5 cm. This is surprising as when looking at flow rate on device we do not see divergence until higher Na^+ concentrations. Note that the deviation continues when looking at higher Na^+ concentrations, where the 3 cm mark consistently has the closest to the ideal value of 1.

It is interesting to note that the calibration curves in **Figure 3.4** do not exactly resemble those in **Figure 3.3**. This suggests that time for equilibration is not the only factor when it comes to defining the magnitude of analyte response. Since all other conditions (such as droplet size, oil size and device pattern) were held constant, the differences between **Figure 3.3** and **Figure 3.4** suggest that mixing, which has been shown to change with changing flow rates,[12] could be one of the causes of this difference.

3.3.1 Impact of Mixing Devices

To determine if mixing would lead to improved sensitivity, we analyzed the behavior of potassium droptodes on a traditional mixing device. The serpentine curves in the mixing device are known to cause changes in the internal vortices within a droplet, allowing analytes previously stuck at the center of the droplets to come to the surface and have the potential to transfer more efficiently into the oil phase (**Figure 3.7**).[12,13,14,15] In order to do a proper comparison between mixing and non-mixing channels, the position of measurement was kept consistent on both devices for calibration (1.5 cm and 3 cm from the junction, **Figure 3.7**).

For the serpentine device, it is important to clarify that the 3 cm point was mid-way through the device (**Figure 3.7**) rather than being an endpoint of the device. The location was chosen to ensure that the same time was spent on both the mixing and straight devices.

At the 1.5 cm post-droplet generation, the non-mixing device appears to maintain a wider linear range and lower limit of detection. However, the response at 1.5 cm on the mixing device, looks extremely similar to the 3 cm on the non-mixing device, with a limit of detection differing by 0.01 log units or 1×10^{-6} M (**Figure 3.8**). This suggests that the droptodes at the 1.5 cm mark on the mixing device have achieved the same level of equilibrium as the droptodes at the 3 cm on the non-mixing device.

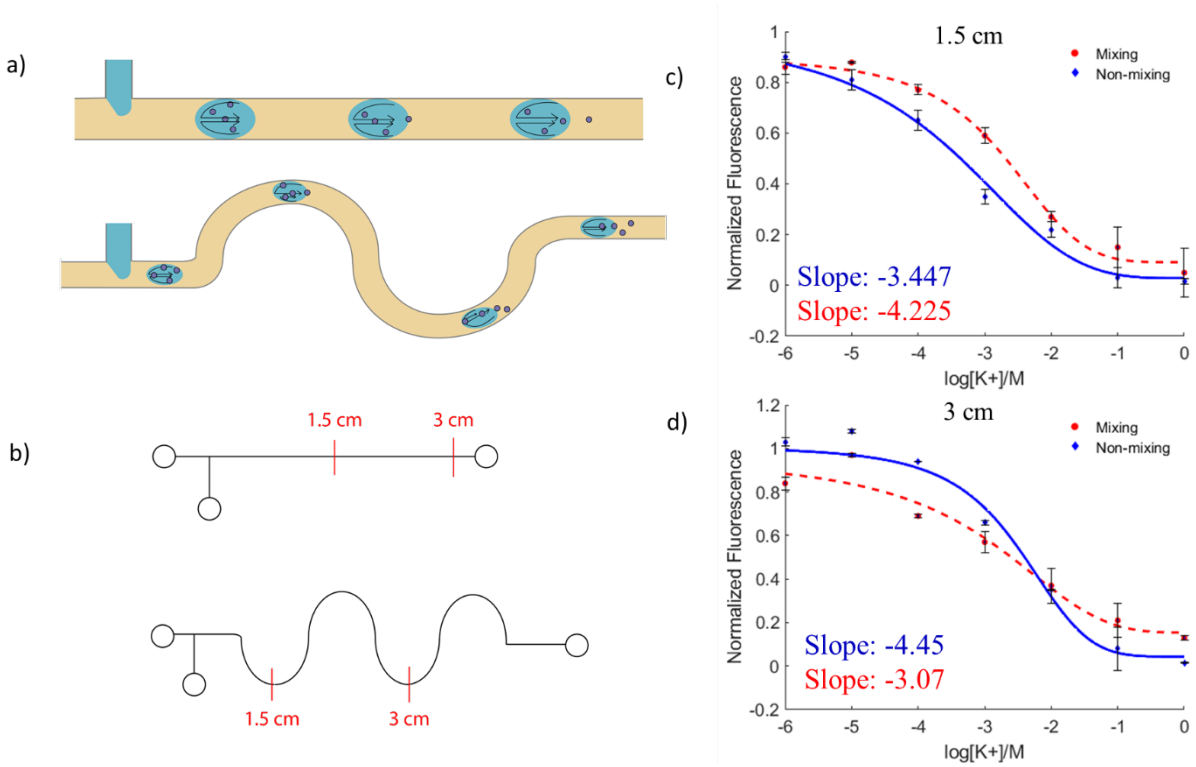

Figure 3.7. Testing mixing microfluidic devices. (a) Adding serpentine channels promotes mixing within the droplet compared to straight channels. (b) Image of the T channel and serpentine device used for analysis with measurement locations marked.(c)Comparing droptode response between mixing and non-mixing device at 1.5 cm from the T junction. Notice that the non-mixing and mixing devices have different droptode responses, where the mixing device has a response very similar to the 3 cm response of the non-mixing device. (c) Droptode response between mixing and non-mixing device at 3 cm from the T junction. Notice that the mixing device, while less sensitive in the linear range, has an expanded linear range and a lower limit of detection. The error bars for all are based on standard deviation in measurements (n=3)

Thus, mixing appears to increase the speed to reach equilibrium between the oil and aqueous phases, and thus the overall kinetics of K+ response. While recording fluorescence at the 3 cm mark on the mixing device, by comparison, the LoD of the device is about an order of magnitude lower compared to the non-mixing device (9.5×10^{-6} M vs 4.4×10^{-5} M). From **Figure 3.7**, it appears that the non-mixing device equilibrates at these flow rates, while potentially the mixing device has entered into the exhaustive sensing regime, further lowering limits of detection.

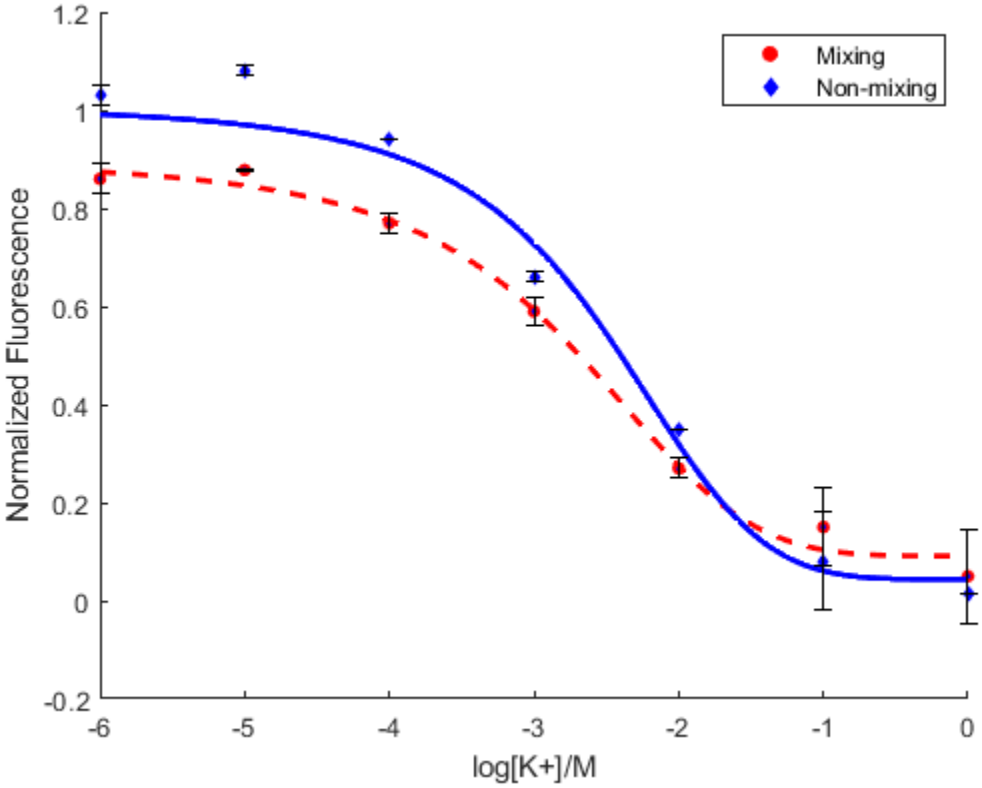

Figure 3.8. Comparing the 1.5 cm measurement on mixing device to the 3 cm measurement on linear device. The slopes and midpoints are similar to one another, but more interestingly the limits of detection are within 0.01 log units of one another. This potentially suggests that the 1.5 cm mixing device is able to equilibrate to the same point as the 3 cm linear device, in half the time.

3.3.2 Droplet volume changes

One of the major advantages of using microfluidic droptodes is the fluidity of the oil phase. Rather than plasticizing a solid polymer to make it fluid-like, the liquid oil phase used in droptodes allows rapid transition in composition and size. Droplet microfluidics are known for their ability to form droplets of various sizes and spacing. Because optodes are known to have varying responses based on the ratios of their aqueous and organic phases,[2] we hypothesized that droplet size and spacing would similarly impact on droptode calibration.

An important caveat to note is the lack of surfactants in the droptode system. Surfactants, most commonly used in microfluidics to stabilize droplets along their interfaces, have been shown to interfere with the operation of ion-selective electrodes.[16] Though no study has yet been performed for surfactants' impact on droptode behavior, surfactants were not used in our droptode system. Notably, the lack of surfactants does, at this stage, impact droplet size stability.

Using syringe pumps to control flow, the size and spacing of the droplets were inversely related. In order to keep the same total flow rate, as the aqueous flow rate was increased, the oil flow rate was decreased. For clarity, all flow conditions are reported in terms of the ratio of the oil phase flow rate to the overall flow rate. A ratio of < 0.5 is therefore a condition where the oil phase flow rate is less than the aqueous phase flow rate, and a ratio of >0.5 is where the oil phase flow rate is greater than the aqueous phase flow rate. A ratio of 0.5 means the oil phase flow rate and aqueous phase flow rate are equivalent. It was observed that as the aqueous flow rate increased, at the expense of the oil flow rate, the droplet size increased and the droplet spacing decreased. Similarly, a decrease in the aqueous flow rate, and increase in the oil flow rate, led to smaller droplets and larger droplet spacing (**Figure 3.9**).

Three different flow rate ratios were used to study the impact of droplet sizing and spacing on the potassium calibration curve, with a total overall flow rate of 4 μL/min maintained throughout these experiments (**Figure 3.9**). The higher error in these experiments is likely due to lack of droplet size stabilization when not using a 1:1 ratio of flows. As the size of the aqueous droplets increase and the size of the oil spacing decreases, the sensitivity of the droptode in the linear region also increases. Between the highest and lowest aqueous flow rates, we see an increase in the sensitivity by a factor of 10, from 3×10^{-5} M to 4×10^{-6} M. We hypothesize that

the smaller oil phase leads to faster saturation of the chromoionophore in the oil phase, which leads to higher sensitivity.

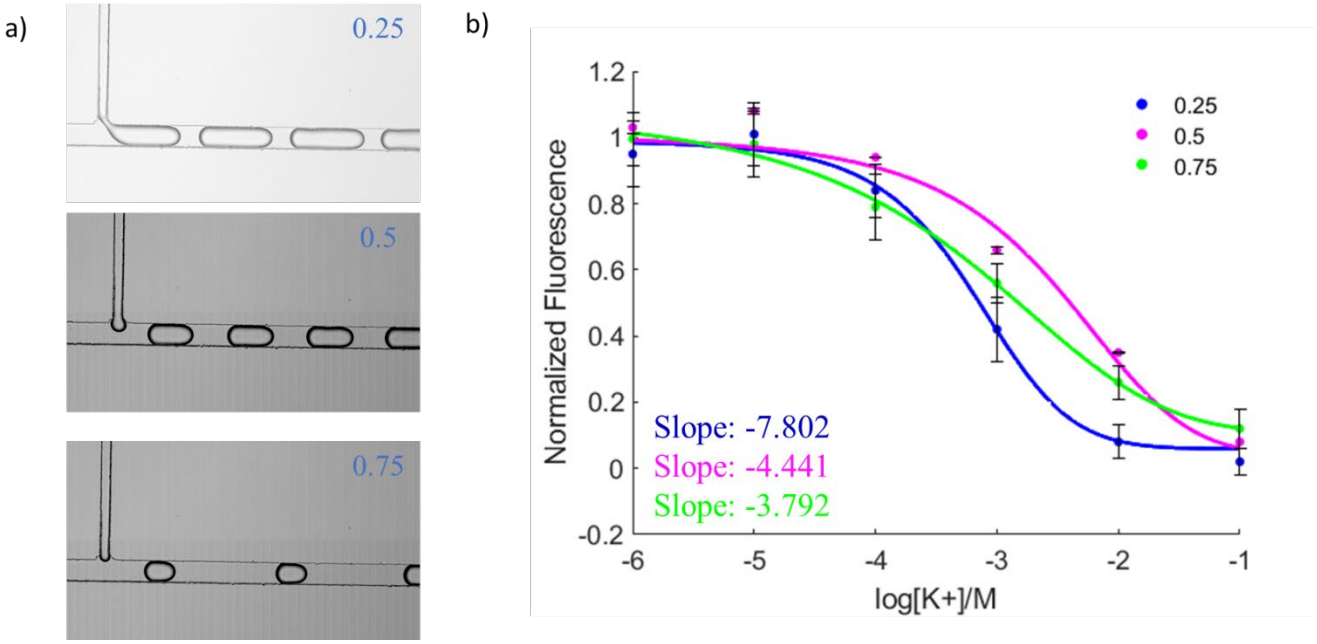

Figure 3.9. Droptode Performance with Changing Droplet Size. (a) The three different droplet conditions: 0.25 is 1 µL/min oil, 3 µL/min aqueous; 0.5 is 2 µL/min oil and 2 µL/min aqueous; 0.75 is 3 µL/min oil, 1 µL/min aqueous. (b) The results of running the potassium droptode under these conditions. The error bars are the standard deviation between measurements (n=3).

However, that increase in sensitivity at high aqueous flow rates comes at the cost of the linear range. The linear range at high aqueous flow rates is a full order of magnitude smaller than at low aqueous flow rates (**Figure 3.9**). Specifically, the linear range was expanded to include lower concentrations of potassium, all the way to 1 x 10^{-5} M K^+, compared to when the droplets were at their biggest. There was about half an order of magnitude expansion of the linear range to higher concentrations of potassium as well as in the largest oil spacing/smaller droplet size experiments. By tuning the droplet size and spacing, the same droptode device can be used for a variety of applications, demonstrating high versatility.

3.4 CONCLUSIONS

In this chapter, we have demonstrated the importance of mixing efficiency and droplet size to droplet efficiency for selective ion sensing. Time on device was shown to not significantly change the droptode behavior, except in the most extreme cases. However, by increasing mixing, droptodes were shown to have an increased linear range by 1.5 orders of magnitude, as well as a lower limit of detection by an order of magnitude. Increasing the size of the aqueous droplet, compared to the oil phase spacing, was also shown to impact droptode behavior, by increasing the sensitivity of the linear region of the droptode fluorescence response curve. This study suggests that dynamically manipulating fluid conditions (aqueous and oil phases) on a single device can result in tunable sensitivities and linear dynamic ranges for ion-selective sensing. Hence, using these approaches may be beneficial in optimizing droptode responses for a diverse range of analytical measurements of various ionic species via use of different ionophores in the organic phases.

3.5 ACKNOWLEDGMENTS

S.P.W.Q (DGE-1256260) acknowledges the National Science Foundation for support. The authors would also like to acknowledge Nicolas Mesyngier, of the University of Michigan for providing the basis for the MATLAB analysis code.

3.6 REFERENCES

1. Bakker, E., Buhlmann, P. & Pretsch, E. Carrier-Based Ion-selective Electrodes and Bulk Optodes. 1. General Characteristics. *Chem. Rev.* **97**, 3083–3132 (1997).

2. Xie, X. & Bakker, E. Ion-selective Optodes: From the Bulk to the Nanoscale. *Anal. Bioanal. Chem.* **407**, 3899–3910 (2017).

3. Bychkova, V. & Shvarev, A. Surface Area Effects on the Response Mechanism of Ion Optodes: A Preliminary Study. *Anal. Chem.* **81**, 7416–7419 (2009).

4. Zhang, Q., Wang, X., Decker, V. & Meyerhoff, M. E. Plasticizer-Free Thin-Film Sodium-Selective Optodes Inkjet-Printed on Transparent Plastic for Sweat Analysis. *ACS Appl. Mater. Interfaces* **12**, 25616–25624 (2020).

5. Qin, Y. & Bakker, E. A Copolymerized Dodecacarborane Anion as Covalently Attached Cation-Exchanger in Ion-Selective Sensors. *Anal. Chem.* **75**, 6002–6010 (2003).

6. Wang, X. *et al.* Ionophore-Based Biphasic Chemical Sensing in Droplet Microfluidics. *Angew. Chemie - Int. Ed.* **58**, 8092–8096 (2019).

7. Xia, Y. & Whitesides, G. M. Soft Lithography. *Angew. Chemie - Int. Ed.* **37**, 550–575 (1998).

8. Ding, Y., Howes, P. D. & Demello, A. J. Recent Advances in Droplet Microfluidics. *Anal. Chem.* **92**, 132–149 (2020).

9. Doonan, S. R., Lin, M. & Bailey, R. C. Droplet CAR-Wash: Continuous Picoliter-Scale Immunocapture and Washing. *Lab Chip* **19**, 1589–1598 (2019).

10. Xu, Y. *et al.* A Droplet Microfluidic Platform for Efficient Enzymatic Chromatin Digestion Enables Robust Determination of Nucleosome Positioning. *Lab Chip* **18**, 2583–2592 (2018).

11. Kimura, K., Maeda, T., Tamura, H. & Shono, T. Potassium-Selective PVC Membrane Electrodes Based on Bis- and Poly(Crown Ethers). *J. Electroanal. Chem* **95**, 91–101 (1979).

12. Yang, L., Li, S., Liu, J. & Cheng, J. Fluid Mixing in Droplet-Based Microfluidics with T Junction and Convergent–Divergent Sinusoidal Microchannels. *Electrophoresis* **39**, 512–520 (2018).

13. Wang, J., Wang, J., Feng, L. & Lin, T. Fluid Mixing in Droplet-Based Microfluidics with a Serpentine Microchannel. *RSC Adv.* **5**, 104138–104144 (2015).

14. Mengeaud, V., Josserand, J. & Girault, H. H. Mixing Processes in a Zigzag Microchannel: Finite Element Simulations and Optical Study. *Anal. Chem.* **74**, 4279–4286 (2002).

15. Lee, C. Y., Wang, W. T., Liu, C. C. & Fu, L. M. Passive Mixers in Microfluidic Systems: A Review. *Chem. Eng. J.* **288**, 146–160 (2016).

16. Malinowska, E. & Meyerhoff, M. E. Influence of Nonionic Surfactants on the Potentiometric Response of Ion-Selective Polymeric Membrane Electrodes Designed for Blood Electrolyte Measurements. *Anal. Chem.* **70**, 1477–1488 (1998).

Chapter 4.

Multiplexed Detection of Serum Electrolyte Panel Ions Using Microfluidic Droptodes

4.1 INTRODUCTION:

Serum electrolyte panels, also known as blood ion panels or electrolyte testing, are standard tests for annual physicals, as well as hospital admissions. Typically, serum electrolyte panels test for the concentrations of a variety of ions including potassium, sodium, chloride and calcium. These ions have been shown to be crucial in the function of the plasma membrane,[1,2] human bone strength,[3] in addition to the regulation of blood pressure,[1] and pH.[1] Both hypo- and hyper-concentrations of these ions have been correlated with a variety of ailments, including alcoholism,[1] diabetes,[1,4] cancer,[5] osteoporosis,[3] and heart disease.[1] There has also been interest in using serum electrolyte panels as biomarkers for acute myocardial infarction,[6] as well as for macrovascular complications for diabetic patients.[4] It has also been suggested that serum electrolyte panels are useful for monitoring children rehydrating using IVs.[7] Blood ion panels are typically measured using a blood-gas analyzer, which consists of automated ion-selective electrodes (ISEs).[8]

However, serum electrolyte panels do have their drawbacks. Not only do serum electrolyte panels require a full blood draw, which can be problematic in patients experiencing blood loss, but they also are statically determined by the analytes that the blood gas analyzer can test, So additional blood samples are needed to test for an ion not in the blood gas analyzer protocol. Additionally, there is concern in the medical community about overtesting people for ion changes, especially in children, as testing is expensive and frequent blood draws could be

harmful.[9,10] It is also difficult to run serum electrolyte panels in low resource settings, due to the high cost of blood gas analyzers, creating a gap in medical care due to socioeconomic status.

An ideal serum electrolyte panel assay should thus be rapid and use minimal sample. Each individual detection platform within the panel should be sensitive in the physiological region for each of the analytes and be specific for the analytes of interest. An ideal panel would also be low cost and require minimal resources, with a high potential for automation. It would also be ideal for a serum electrolyte panel to have flexible ion targeting, where if a clinician needed to detect an ion not normally tested for, it could be substituted on the same platform.

A potential alternative to a traditional blood-gas analyzer is to use a technology working on the same premise as a competing technology, ion-selective optodes (ISOs). A chromoionophore, which changes color with protonation, an ionophore selective to the ion of interest and an ion-exchanger, to speed up the charge transfer, are suspended in a plasticized polymer matrix. The analyte binds to the ionophore and is extracted into the polymer matrix, causing a charge transfer across the interface. In order to maintain the neutrality of the polymer matrix, the chromoionophore either protonates or deprotonates, leading to a measurable change in color. Optodes are ideal for point-of-analysis applications, generally requiring minimal instrumentation. However, as ISOs require bulk changes, equilibration times are on the order of minutes and hours, and there are concerns about reagent leeching into samples. Additionally, ISOs are not typically automated.

A novel advancement in ISOs pioneered by the Meyerhoff group, in conjunction with the Bailey lab, has been the development of microfluidic droptodes; a combination of droplet microfluidic and ISO technology.[11] Concisely, aqueous droplets with volumes ranging from nanoliters to picoliters are suspended and flowed down a channel in a carrier oil phase. The

carrier oil phase contains all of the reagents necessary for ISO detection: a chromoionophore (which changes fluorescent state with protonation), an ionophore selective to the ion of interest and an ion-exchanger, to speed up the charge transfer (**Figure 4.1**). Droptode technology has been used to measure the concentration of various ions, including potassium, sodium, chloride and protamine.[11] Droptodes have also demonstrated the ability to measure in complex matrices, including measuring the concentration of potassium in 50% diluted whole blood.[11] Droptodes can use as little as 10 μL of sample, and measurements take less than 0.5 seconds.[11] Thus, droptodes are an ideal technology to adapt to measure serum electrolyte panels. However, droptodes have only measured one analyte at a time, requiring a different device for each analyte, which could potentially hinder droptode automation.

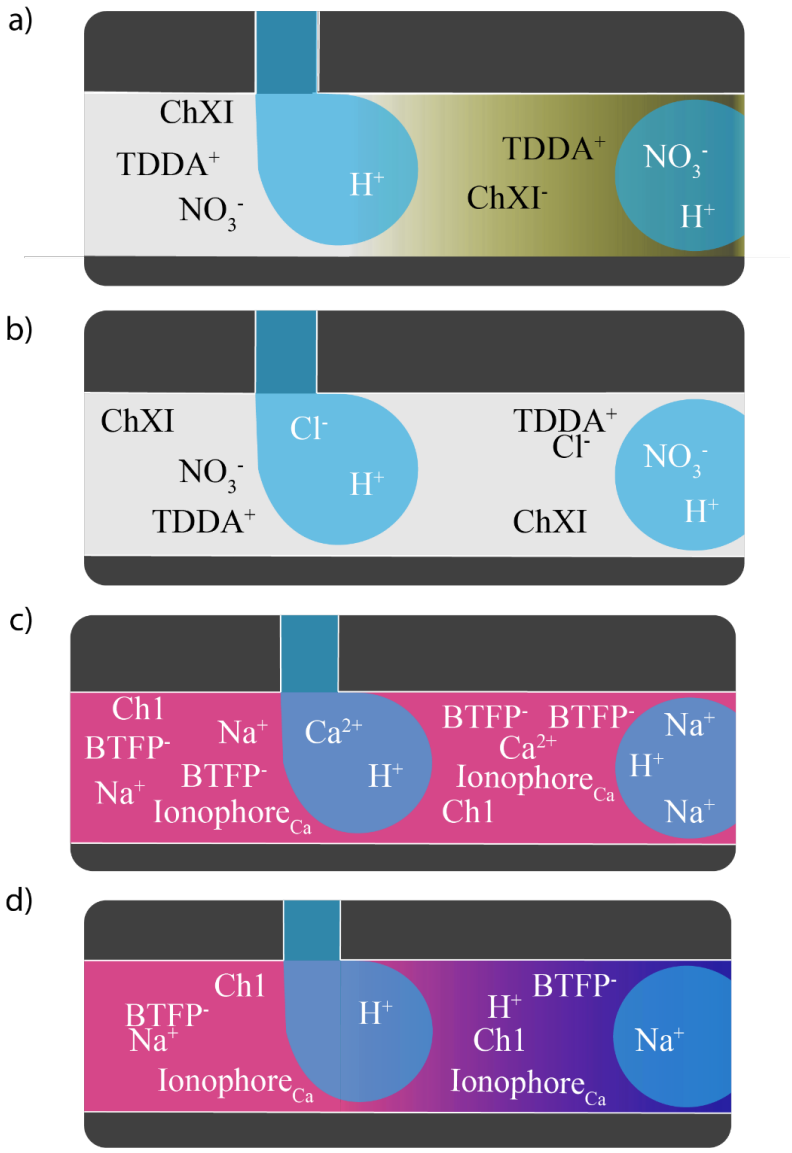

Figure 4.1. Sample droptode devices. Chloride detection is (a) and (b). Calcium detection is (c) and (d). (a) When no chloride is present, the chromoionophore needs to deprotonate to preserve charge balance, causing a change in color. (b) When chloride is present, it binds to the ionophore and is extracted into the organic phase where it serves as the counterion to $TDDA^+$. Thus the chromoionophore does not change its charge state. (c) When calcium is present, the calcium binds to the ionophore counterbalancing the $BTFP^-$. (d) When calcium is not present, the chromoionophore has to protonate to counter-balance $BTFP^-$. Thus the chromoionophore changes its color.

In this chapter, we will demonstrate the ability to temporally multiplex droptodes, through the use of Fluorinert FC-40 spacers to separate the analyte-sensitive oil phases. We will then use these temporally multiplexed droptodes to measure the ions present in serum electrolyte panels and calibrate the multiplexed droptodes to be physiologically relevant. These multiplexed droptodes will ultimately be used to detect serum electrolyte concentration in serum, plasma or human whole blood.

4.2 EXPERIMENTAL

4.2.1 Chemicals and Materials

Unless otherwise stated, all chemicals were purchased from Sigma Aldrich. This includes Chromoionophore I, Sodium tetrakis[3,5-bis(trifluoromethyl)phenyl]borate (NaTFPB), Potassium tetrakis[3,5-bis(trifluoromethyl)phenyl]borate (KTFPB), Chromoionophore X, tetradodecylammonium nitrate ($TDDANO_3$) and all of the ionophores. SU-8 2025 negative epoxy photoresist was purchased from MicroChem Corp. Silicon wafers were purchased from University Wafer. Tridecafluoro-1,1,2,2-tetrahydrooctyl silane was purchased from Gelest Inc. Poly(dimethyl siloxane) (PDMS) was purchased as separate base and curing agents from Momentive Performance Materials. 24-gauge needles and plastic syringes were purchased from Thermo Fisher Scientific. 24-gauge PTFE tubing was purchased from Cole-Parmer. The syringe pumps used were Pump 11 Pico Plus Elite from Harvard Apparatus. Fluorinert FC-40 was purchased from 3M. All samples were dissolved in a 0.1 M Tris-H_2SO_4 buffer (pH 7.4) and all oil phases were dissolved in dioctyl sebacate (DOS). To get the proper sodium concentration, sodium chloride, sodium bicarbonate and sodium sulfate were used, to get proper calcium

concentration calcium chloride was used, and to get proper potassium concentration potassium sulfate was used. The total chloride concentration was based on zinc chloride, sodium chloride and calcium chloride.

4.2.2 Microfluidic device preparation

Devices were made using a microfabrication process consisting of standard photolithography and soft lithography.[12,13] Masks were designed in AutoCAD software (Autodesk, Inc.) and were printed as transparencies (CAD/Art Services, Inc) for photolithography. SU-8 2025 negative epoxy photoresist was spun-coat to a height of 40 μm onto a clean Silicon wafer. The wafer was developed and then, tridecafluoro-1,1,2,2-tetrahydrooctyl trichlorosilane was deposited via vacuum assisted chemical vapor deposition. Devices were made using a 10:1 degassed mixture of base: curing agent ratio to create PDMS (RTV615). The inlet and outlets were punched using a 24-gauge needle. Devices were bonded to a glass slide using oxygen plasma bonding. All channels were 40 μm in depth and 80 μm in width, except for the aqueous inlet which was only 40 μm in width.

4.2.3 Droptode Experiments

For the oil phase: 3 mL plastic syringe were filled with 1 mL of DOS and all trapped air was removed. Syringes were then attached to 24 gauge PTFE tubing and placed on the syringe pumps. Syringes were first run in infusion mode for 1 minute at 100 μL/min, to make sure all trapped air escaped. Syringes were then run in extraction mode in a vial of DOS for 2 minutes at 100 μL/min to ensure flow. After the extraction period was over, the tubing was left in the vial for 30 seconds to allow the pressure to stabilize, ensuring no air would be trapped. The tubing

was then transferred to a vial of Fluorinert FC-40, and a total volume of 4 μL at 100 μL/min was pulled up into the tubing.

For pilot experiments, after waiting 30 seconds the tubing was placed in a vial of Na^+ sensitive oil (100 μM chromoionophore I, 200 μM KTFPB, 400 μM Sodium ionophore X) for a total of 4 μL extraction at 10 μL/min. After 30 seconds the tubing was transferred to the FC-40 vial and a total volume of 2 μL at 10 μL/min was pulled into the tubing. The tubing was then placed in a K^+ sensitive oil (100 μM Chromoionophore I, 200 μM NaTFPB, 300 μM Potassium ionophore II) and a total of 4 μL was extracted at 10 μL/min. This process was repeated 10 times, with the tube end being wiped off with a cleanroom wipe each time, and finally capped off with 4 μL of DOS, to stabilize flow before measurements.

For the full multiplexing experiments; after waiting 30 seconds, the tubing was then placed in a vial of calcium sensitive oil (100 μM Chromoionophore I, 100 μM NaTFPB, 400 μM Calcium ionophore I), and a total volume of 4 μL at 100 μL/min was pulled into the tubing. After 30 seconds the tubing was transferred to the FC-40 vial and a total volume of 2 μL at 100 μL/min was pulled into the tubing. This pattern (4 μL of analyte-sensitive oil, 2 μL of FC-40) continued through the Cl^- sensitive oil (300 μM Chromoionophore XI, 450 μM $TDDANO_3$), Na^+ sensitive oil (100 μM Chromoionophore I, 100 μM KTFPB, 100 μM Sodium ionophore X), pH sensitive oil (300 μM Chromoionophore XI), K^+ sensitive oil (100 μM Chromoionophore I, 200 μM NaTFPB, 300 μM Potassium ionophore II), a Chromoionophore XI oil, for spacing (300 μM Chromoionophore XI, 300 μM $TDDANO_3$, 400 μM ***N,N***-Dioctyl-3α,12α-bis(4-trifluoroacetylbenzoyloxy)-5β-cholan-24-amide) and another pH sensitive oil (100 μM Chromoionophore I) which was let run for 6 μL to ensure good flow occurred before the measurements started.

The aqueous solution was simply loaded into plastic 3 mL syringes and then flowed through 24-gauge PTFE tubing into the device using syringe pumps. The solutions were each pumped at a speed of 2 μL/min. The amount of fluorescence at 3 cm from the T-junction was determined using a Nile Red filter cube (Leica Microsystems), for K^+, Na^+, and Ca^{2+}, and a GFP filter cube (Leica Microsystems) for pH, Cl^- and CO_3^{2-}, and a VEO 640L high speed camera (Vision Research Inc.) connected to a DMi8 light microscope (Leica Microsystems).

4.2.4 Droptode Data Analysis

Standard data analyses was carried out, as discussed in prior chapters.[13] Briefly, all videos were combined in ImageJ with an enhanced contrast (NIH). The fluorescence of a 30 x 30-pixel spot in the middle of the channel was calculated for each frame, averaging about 40 droplets per total measurement. The fluorescence response of outside of the channel was subtracted, to account for light variations. Peaks were determined from the resulting measurements using MATLAB (Appendix 2 and 3). To account for variations in oil concentration, data was normalized by setting

$$Relative\ Fluorescence = 1 - \frac{F - F_{Max}}{F_{Max} - F_{Min}} \quad [1]$$

Where F is the fluorescence of the sample, F_{Max} and F_{Min} were defined as the fluorescences at one order of magnitude below and above the typical physiological concentration of the analyte, respectively (**Table 4.1**). The results of the measurements were then fit to a logistic curve against the log of the concentration of the analyte of interest (Appendix 2).

Table 4.1. F_{Min} and F_{Max} for each analyte multiplexed as part of the whole blood electrolyte analysis.

Analyte	**F_{Max} Concentration/M**	**F_{Min} Concentration/M**
K^+	10^{-4}	10^{-2}
Na^+	10^{-2}	10^{0}
Ca^{2+}	10^{-4}	10^{-2}
Cl^-	10^{-3}	10^{0}

4.3 RESULTS AND DISCUSSION:

4.3.1 Theory Behind Multiplexing

As long as the oil phases remain independent of one another, there should be no cross-over from one oil phase on the other. This is partially because of the sample flow, meaning that each analyte-sensitive oil will be exposed to a new sample from the aqueous phase. Thus, keeping the oil phases separated from one another is a major priority. We propose using an immiscible oil, in this case Fluorinert FC-40, as a spacer in between the analyte-sensitive oils, preventing them from touching one another and thus allowing independent detection (**Figure 4.2**).

4.3.2 2-plex multiplexing

Before performing multiplexing on a full blood panel, we wanted to ensure that we could multiplex two oil phases which otherwise would interfere with each other: sodium and potassium. Each sensing phase contains a counterion which is the same composition as what the

other is detecting, thus if there was any crosstalk between the oil phases, it should be measurable in the fluorescent response of the droptodes (**Figure 4.2**). However, as both sodium and potassium calibrated similar to how they calibrated in a non-multiplexed system,[11] this indicates the success at using FC-40 spacers to separate the two oil phases and keep their measurements independent of one another (**Figure 4.2**). Larger errors were seen at lower concentrations of the analyte of interest, in the case of potassium, but if there was cross-talk between the oils we would have expected the 10^{-6}M to be suppressed in signal rather than enhanced. This suggests that the errors seen here are more systemic within the droptode system, as will be discussed at the end of the chapter.

a)

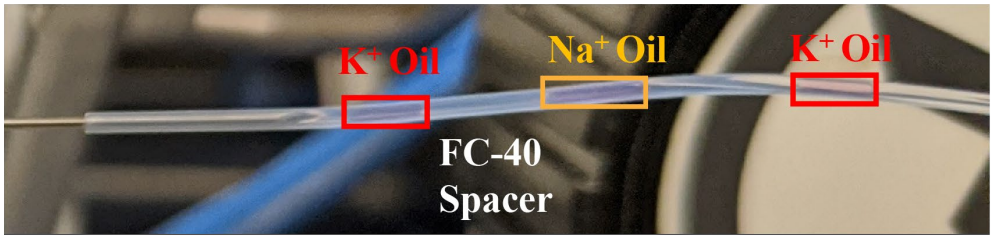

b)

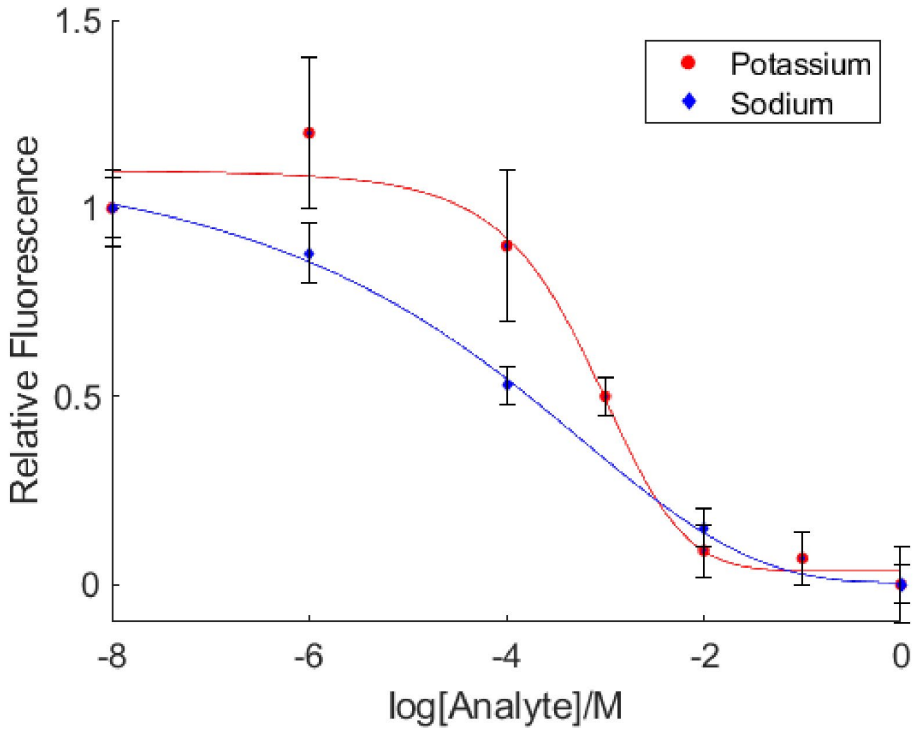

Figure 4.2. 2-plex calibration of potassium and sodium on microfluidic droptodes. (a) (Top) Colored image of the droplets spaced by FC-40 in the oil inlet tube. (bottom) A brightfield image of the oil phases separated by FC-40 (the square droplets). (b) The results of 2-plex calibration of potassium and sodium on droptodes. Note that both follow the same trend as seen when performing singleplex experiments. In these experiments, relative fluorescence was normalized to the buffer condition for F_{Max} and 1M for $F_{Min.}$ Data here was averaged over n=6 trials, n=3 trials over two separate days.

4.3.3 Optimization of Oil Phases for Physiological Conditions

From prior experiments, the potassium calibration curve was already sensitive in the physiologically range of potassium (3.2-5.6 mM)[14], so no further modification of the potassium sensitive oil was necessary. However, the sodium calibration used in the pilot study was not sensitive in the 135-145 mM range needed for physiological sodium detection.[15] Calibrations also had to be made for calcium (with sensitivity over 1.05-1.3 mM),[16] and chloride (with sensitivity over 96-106 mM).[17] Because of the difference in charge between chloride compared to sodium/potassium/calcium, for chloride detection chromoionophore XI was used while for sodium/potassium/calcium chromoionophore I was used.

An added challenge for working with chromoionophore XI was the propensity for chromoionophore XI to partition into the aqueous phase in basic enough conditions. Thus, data analysis for chloride detection had to be modified manually to indicate whether the fluorescence was in the oil or aqueous phase. In the aqueous phase, the fluorescence was given a negative value (showing the lack of fluorescence in the oil phase) compared to the positive value in the oil phase. The same procedure, for consistency, was carried out on all of the analytes, but Chromoionophore I only showed fluorescence in the oil phase, so there was no change in sign. The normalization using Equation 1 was performed on this modified data set. All analyte-sensitive oils were developed to be sensitive to the analytes in their physiological ranges by tuning the concentrations of chromoionophore, ionophore and ion-exchanger (**Figure 4.3**). It is important to note that both the calcium and chloride ions appear as if they would fit better using a sigmoidal fit, but there were not enough points collected to perform that fitting for calcium. As the purpose of this analysis was to ensure there was oil reactivity across the physiological

concentration ranges, the goodness of fit was not pursued further, leaving that for when actually multiplexing the analytes.

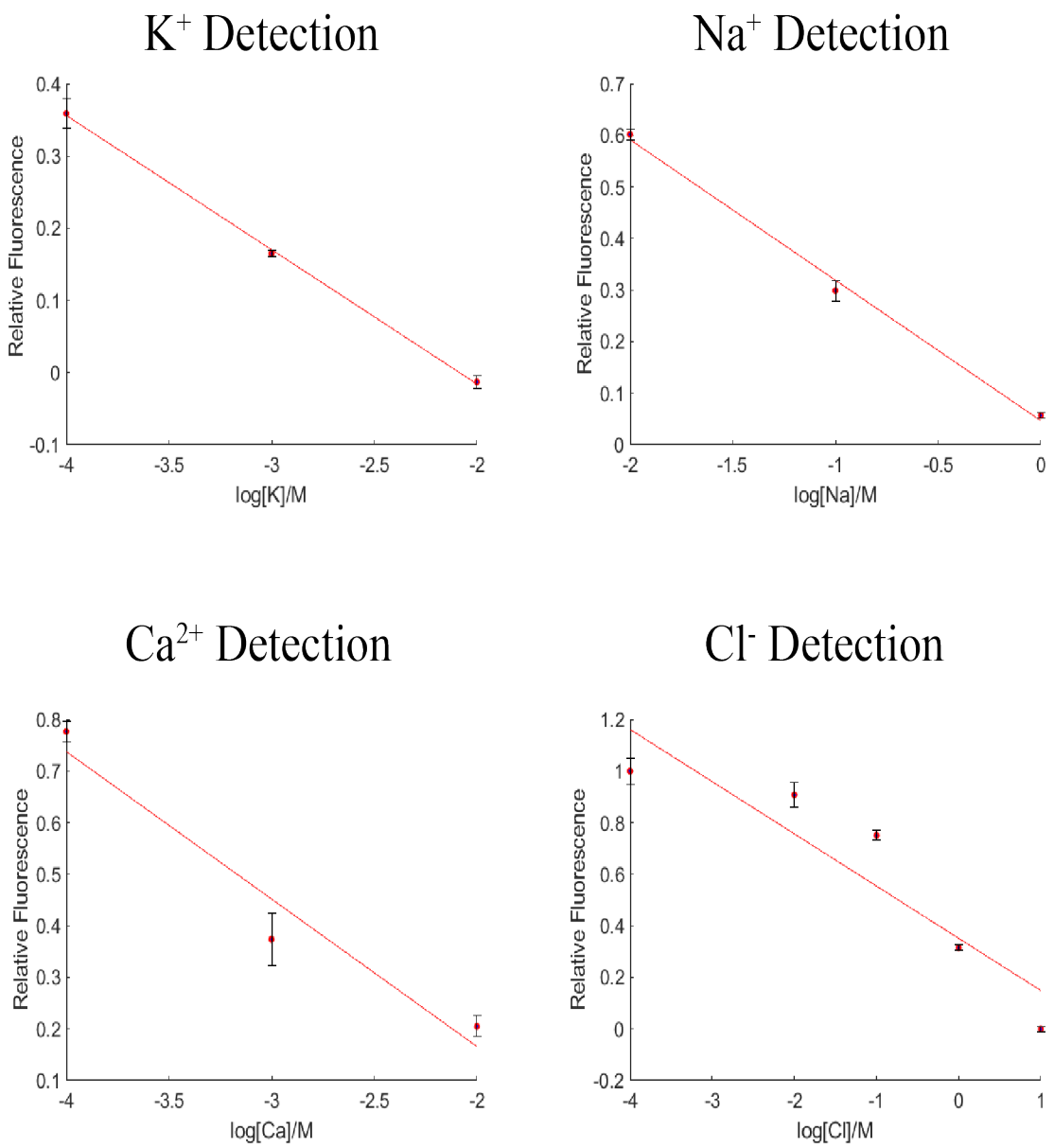

Figure 4.3. Calibration curves of various analytes in serum electrolyte panel, including potassium, sodium, calcium and chloride. These were single-plex calibrations taken to make sure that there was oil responsiveness in the physiological range. These responses (for sodium,and potassium) are consistent with previously published responses, and all oil phases shown here showed responsiveness in the physiological range. Data points are an average of n=2 trials, as this was preliminary work to establish sensitivity of the oil phase. Both calcium and chloride ions look like they would have fit better sigmoidally, but there were not enough points to perform that fitting. Since the purpose of this analysis was to ensure oil reactivity across the physiological range, the calibrations were not pursued further.

4.3.4 Multiplexing

pH-sensitive oils were interspersed to ensure that all samples maintained a pH of 7.4. The multiplexing of the system had slight impacts on the calibration curves for each analyte, mostly due changes in the droplet system upon changing between the analyte-sensitive and fluorinated oil phases. Chloride detection suffered the worst. But even without an ionophore, chloride calibration and selectivity was achieved over other anions such as sulfate and carbonate. Additionally, chloride detection was using a different chromoionophore, whose impact on PDMS has not yet been fully characterized. However, overall calibration in physiological ranges of the analytes was maintained (**Figure 4.4**), suggesting that multiplexed droptodes could, after further optimization, be a good low-resource alternative to blood gas analyzers.

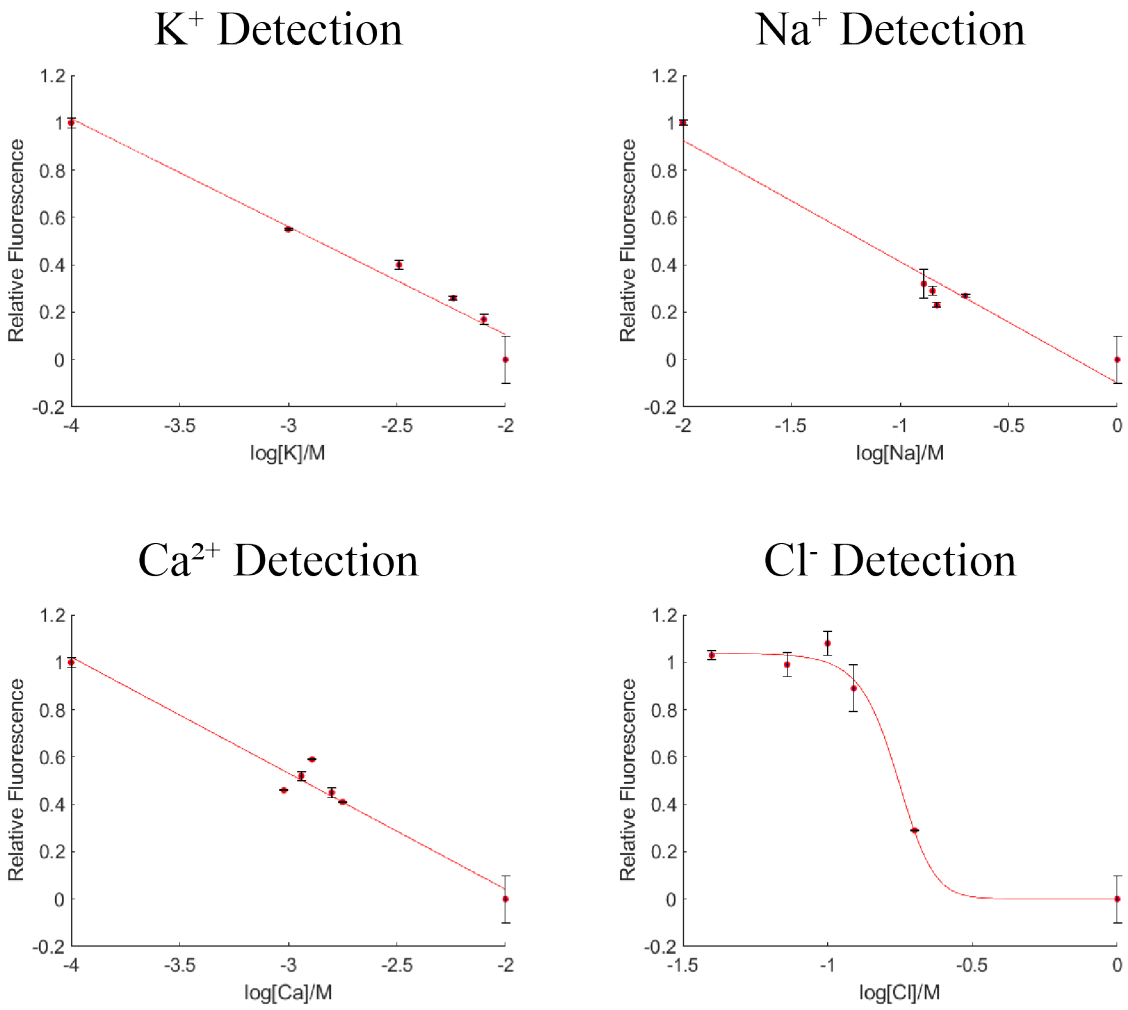

Figure 4.4. Multiplexed calibrations of serum electrolyte panel ions. These measurements were taken using the multiplexed droptode method as well as with potassium, sodium, chloride and calcium in all of the samples. Data here is an average of n=2 trials.

4.4 CONCLUSIONS AND FUTURE WORK

4.4.1 Conclusions

In this work we have demonstrated the ability of droptodes to temporally multiplex by taking advantage of the immiscibility of the analyte-sensitive oils with FC-40, keeping the oils

separated and independent of one another. Multiplexing on one device would allow for a less complicated and wasteful system, using only one device, easing automation. We were able to calibrate for sodium, potassium, calcium and chloride at physiological conditions, mimicking a traditional serum electrolyte panel, within a five minute time period and using minimal sample. This chapter demonstrates the ability to perform multiplexed electrolyte detection on chip, which could ultimately improve accessibility of rapid serum electrolyte detection in low resource areas.

4.4.2 Future Work

While the multiplexing ability of the droptode system has been demonstrated, this is an ongoing project, so optimization should be performed on the experiments performed in this chapter. Specifically, the chloride ion should be tuned to have it be linearly responsive across the whole physiological range. Tuning the chloride-selective oil could involve decreasing the concentration of the chromoionophore or increasing the concentration of the $TDDANO_3$. There also should be more replicates run on the multiplexed calibration in order to better fill out the full linear range, especially for sodium and calcium. Finally, further characterization should be done on the flow in the multiplexed droptode system to determine the variations in droplet size and speed each time flow is reestablished between the aqueous phase and oil phase, after the FC-40 passes.

In the future, the multiplexed droptode system should be performed in a complex matrix in order to ensure its accuracy for use as a blood panel. More experiments should also be performed across the possible range of pHs in the human body, to ensure that the mild pH fluctuations do not impact measurement. Finally, before commercial use, the system should be

optimized to run the oil for the minimum time possibly needed for the measurement as well as create a system to automate taking the images for fluorescent imaging.

4.5 ACKNOWLEDGMENTS

S.P.W.Q (DGE-1256260) acknowledges the National Science Foundation for support. The authors would also like to acknowledge Nicolas Mesyngier, of the University of Michigan for providing the basis for the MATLAB analysis code.

4.6 REFERENCES

1. Schwartz, A. B. Potassium-Related Cardiac Arrhythmias and Their Treatment. *Angiology* **29**, 194–205 (1978).

2. Walz, W. Role of Astrocytes in the Clearance of Excess Extracellular Potassium. *Neurochem. Int.* **36**, 291–300 (2000).

3. Dalemo, S., Eggertsen, R., Hjerpe, P., Almqvist, E. G. & Boström, K. B. Bone Mineral Density in Primary Care Patients Related to Serum Calcium Concentrations: a Longitudinal Cohort Study from Sweden. *Scand. J. Prim. Health Care* **36**, 198–206 (2018).

4. Wang, S. *et al.* Serum Electrolyte Levels in Relation to Macrovascular Complications in Chinese Patients with Diabetes Mellitus. *Cardiovasc. Diabetol.* **12**, 146 (2013).

5. Vodnala, S. K. *et al.* T Cell Stemness and Dysfunction in Tumors are Triggered by a Common Mechanism. *Science.* **363**, 80, (2019).

6. Ramasamy, R., Murugaiyan, S. B., Gopal, N. & Shalini, R. The Prospect of Serum Magnesium and an Electrolyte Panel as an Adjuvant Cardiac Biomarker in the Management of Acute Myocardial Infarction. *J. Clin. Diagnostic Res.* **7**, 817–820 (2013).

7. Wathen, J. E., MacKenzie, T. & Bothner, J. P. Usefulness of the Serum Electrolyte Panel in the Management of Pediatric Dehydration Treated with Intravenously Administered Fluids. *Pediatrics* **114**, 1227–1234 (2004).

8. Blood Gas / pH / Chemistry Point of Care Analyzer Core Medical Equipment - Information. 18853 (2011).

9. Rothrock, S. G., Green, S. M., McArthur, C. L. & DelDuca, K. Detection of Electrolyte Abnormalities in Children Presenting to the Emergency Department: A Multicenter, Prospective Analysis. *Acad. Emerg. Med.* **4**, 1025–1031 (1997).

10. Tchou, M. J. *et al.* Reducing Electrolyte Testing inHospitalized Children by using Quality Improvement Methods. *Pediatrics* **141**, (2018).

11. Wang, X. *et al.* Ionophore-Based Biphasic Chemical Sensing in Droplet Microfluidics. *Angew. Chemie - Int. Ed.* **58**, 8092–8096 (2019).

12. Xia, Y. & Whitesides, G. M. Soft Lithography. *Angew. Chemie - Int. Ed.* **37**, 550–575 (1998).

13. Wetzler-Quevedo, S. P. & Bailey, R. C. Characterization of the Impact of Mixing and Volumes on the Behavior of Microfluidic Droptodes. *Submitted*. (2021).

14. Harris, R. Serum Potassium. *BMJ.* **2**, 1341–1342 (1951).

15. Rowett, D. & Yaftali, S. Serum Sodium. *Med. Comput. J.* **1**, 13–17 (1980).

16. Goldstein, D. A. *Clinical Methods: The History, Physical, and Laboratory Examinations Chapter 143: Serum Calcium*. *THE JOURNAL OF INFECTIOUS DISEASES* • vol. 130 (Butterworths, 1990).

17. Morrison, G. *Serum Chloride*. *Clinical Methods: The History, Physical, and Laboratory Examinations* (Butterworths, 1990).

Chapter 5.

Development of Microfluidic Droptodes For Detection of PFAS

This work was performed with Dr Jennifer Reeves, Joshua Wolfe, and Keenan Wright, under the direction of Prof Mark Meyerhoff and Prof Ryan C. Bailey. J. Reeves synthesized the fluorinated chromoionophores. J. Wolfe performed bulk experiments with varying proportions of oil to aqueous phase. K. Wright performed experiments on droptode devices investigated the impact of volumetric ratios on PFAS detection.

5.1 INTRODUCTION

As the desire for non-stick materials, including cooking utensils and storage containers, grows, so does the use of fluorocarbon precursors in industrial processes. These fluorinated alkyl chains are generally referred to as perfluoroalkyl substances (PFAS) and include a variety of compounds including $PFOS^-$ (perfluorooctanesulfonate), PFOA (perfluorooctane), PFBS (perfluorobutane sulfonic acid) and GenX (a commercial PFOS alternative).[1] The basic structure of PFAS is generally the same, a fluorocarbon tail attached to an acidic head group such as a sulfonate or carboxylate group. PFAS can vary based on their length of their tails as well as the branching structure used.

A variety of industrial processes incorporate PFAS leading to concerns over PFAS pollution. PFAS is used for food packaging as well as for fabric protection and stain resistant clothing. It is also commonly used as a component in firefighting foam and film-forming foams used by airstrips.[1,2] Thus, PFAS pollution is not just a result of wastewater from PFAS producing/using industries, but also leeching from food storage containers or run-off from disaster mitigation strategies. PFAS additionally has been shown to be bioaccumulative, with 99% of Americans believed to have detectable levels of PFAS in their bloodstream.[1] As PFAS is

a suspected carcinogen and has been shown to be related to immune system effects *in utero* and low birth weights, the ubiquitous presence of PFAS is concerning.[3–5] The EPA suggests that PFAS levels in drinking water should be no higher than 70 ppt or 70 ng/L, around 0.17 nM.[6] Thus, it would be ideal to have a highly sensitive and versatile method to detect PFAS in a variety of environments.

Initial PFAS detection techniques relied on mass spectrometry coupled to a separation technology, such as chromatography or solid state extraction.[2,7–10] While these gold standards have the ability to measure very low concentrations of PFAS, matrix complexity can quickly obscure measurements in the background. These measurements have generally been performed in wastewater streams. However, there is current interest in detecting PFAS in human blood,[1] which would be extremely challenging without a pre-extraction technique. Additionally, mass spectrometry does not offer a point-of-analysis capability for PFAS detection, instead requiring sampling and storage. While this is excellent for academic studies, the process is cumbersome for real time monitoring all over the world.

Current PFAS detection techniques have expanded their capabilities to improve portability. PFAS is now commonly detected using electrochemical techniques, as these techniques typically offer automation and require minimal instrumentation. In order to use electrochemical detection, PFAS first needs to be extracted from the solution of interest which has been done using molecularly imprinted polymers,[11] metal organic frameworks,[12] or pre-concentration using electric pulses between two immiscible electrolyte solutions.[13] The relevant PFAS concentration could then be measured based off of a reporter oxidizer molecule[11] or based on PFAS crossing over an interface.[13] However, electrochemical reporting often still uses complicated technology that is not widely available.

Thus, an alternative method for PFAS detection focuses on optical detection, using little more than a smartphone. These methods, too, tend to rely on extraction procedures, generally via solid phase extraction (SPE), followed by use of a dye that changes color or fluorescence based on PFAS presence.[14,15] Optical methods have the advantage of minimal instrumentation or infrastructure requirements, making detection easier to perform at the point of analysis. Unfortunately, these optical methods have limits of detection in the parts per billion range,[14,15] which is several order of magnitudes below the parts per trillion range necessary to detect PFAS in water. Additionally, as with any extraction procedure, increasing the complexity of the matrix increases the chance of interfering signals, especially for optical methods.

The Meyerhoff lab (University of Michigan) in conjunction with our lab, has recently created an optical detection method which excels in detecting small molecules in complex matrices: microfluidic droptodes. Droptodes work on the principle of generating aqueous droplets in carrier oil phases, effectively constructing thousands of tiny optode environments, all on the order of nanoliters in volume. The carrier oil phase acts as the sensor of a traditional optode and contains the color changing chromoionophore, the ion-exchanger for charge balance and the ionophore. The carrier phase then interacts with the aqueous sample phase as it carries the droplets down the channel, on the order of 0.5 s per measurement. Droptodes have previously been used to make measurements of small ions in whole blood, including potassium, chloride and protamine, with limits of detection over an order of magnitude lower than using colorimetric optode systems.[16]

Therefore, in this chapter,we have proposed and implemented a pilot droptode system for PFAS detection in aqueous solutions, using chromoionophore I in perfluorooctanol as the sensing phase. The droptode buffer system was optimized for maximum response to PFAS and

detected down to 1 μM PFAS in aqueous samples. However, the perfluorooctanol sensing phase was not selective enough for PFAS detection, and thus we also worked to explore other fluorinated chromoionophores for use in our droptode system. Finally, we demonstrated the first use of Teflon as an optodic matrix by using it for both pH and PFAS detection.

5.2 METHODS

5.2.1 Theory

PFAS are small charged molecules, which suggests that they can be detected using a droptode system. However, there are no known PFAS ionophores, which suggests another method of extraction into the oil phase will be necessary. We propose to rely on the fact that PFAS, as a fluorinated compound, will have better solubility in a fluorinated matrix than a nonfluorinated one. Thus, PFAS will be selectively extracted into perfluorooctanol from water, while all non-fluorinated compounds will remain in the aqueous phase. As the PFAS is extracted, its charged head group will cause a proton to be coextracted with it, to maintain charge balance (**Figure 5.1**). The coextracted proton will bond to Chromoionophore I, causing it to shift in color and fluorescence.

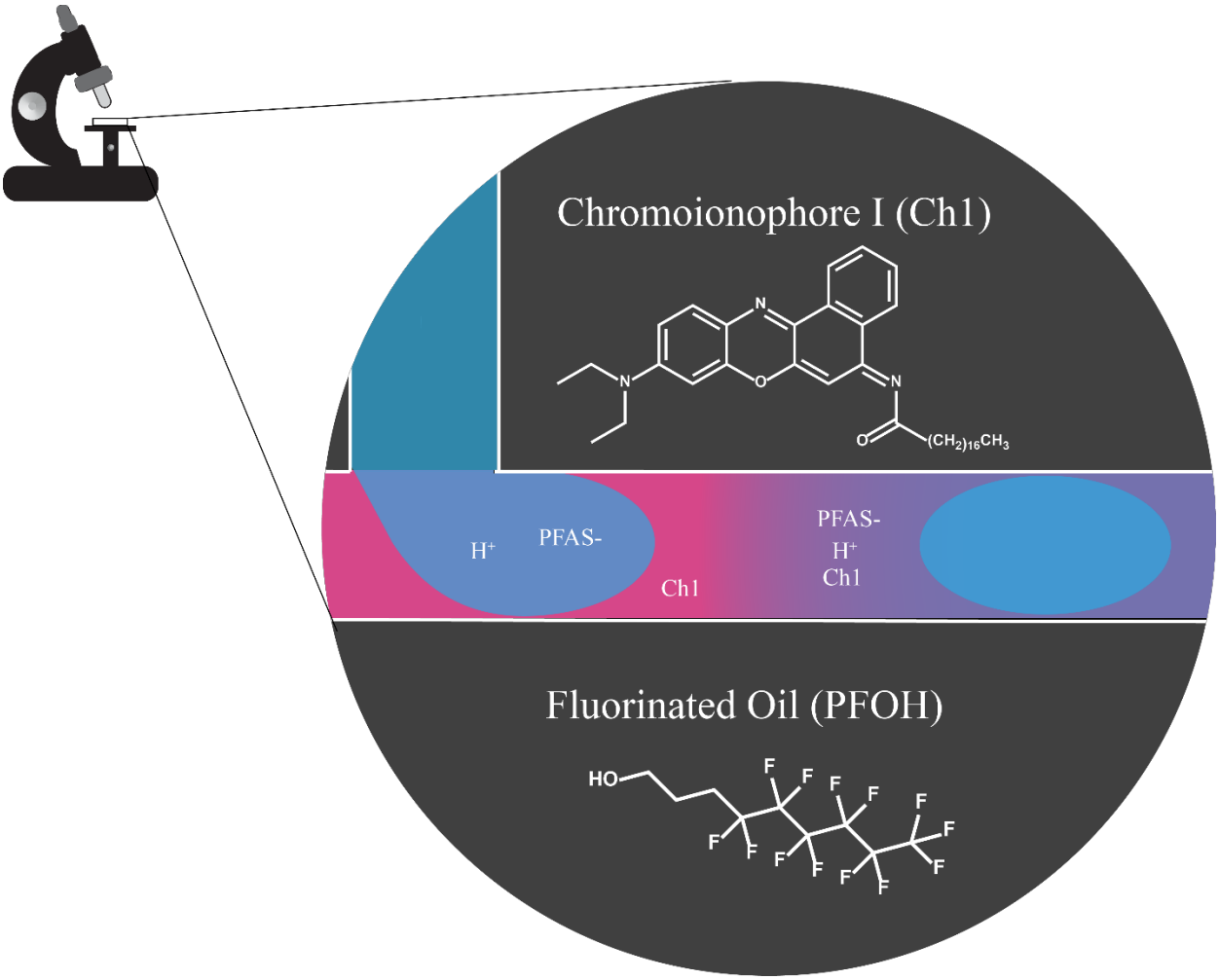

Figure 5.1. Mechanism of Droptode Detection of PFAS. PFAS in the sample phase partitions into the fluorinated sensing phase. This causes a proton co-extraction, leading to a change in Chromoionophore I charge and color/fluorescence.

5.2.2 Chemicals and Materials

Unless otherwise stated, all chemicals were purchased from Sigma Aldrich. SU-8 2025 negative epoxy photoresist was purchased from MicroChem Corp. Silicon wafers were purchased from University Wafer. Tridecafluoro-1,1,2,2-tetrahydrooctyl silane was purchased from Gelest Inc. Poly(dimethyl siloxane) (PDMS) was purchased as separate base and curing agents from Momentive Performance Materials. 24-gauge needles and plastic syringes were

purchased from Thermo Fisher Scientific. 24-gauge PTFE tubing was purchased from Cole-Parmer. The syringe pumps used were Pump 11 Pico Plus Elite from Harvard Apparatus. Unless otherwise stated, samples were serially diluted from a 10^{-3} M PFAS solution in 0.1 M carbonate buffer (pH 9.8). Oil solutions were created by dissolving chromoionophore I in perfluorooctanol at various concentrations. Teflon sheets and porous Teflon sheets of various thicknesses were bought from VWR.

5.2.3 Bulk Experiments

$PFOS^-$ was dissolved in 0.1 M solutions of various buffers to a final concentration of 10^{-3}M. Buffers used included 0.1M glycine (pH 2.2), 0.1M acetate (pH 4.2), 0.1M 2-(N-morpholino)ethanesulfonic acid (MES) (pH 5.2), 0.1 M Tris(hydroxymethyl) aminomethane (Tris) (pH 6.8), 0.1 M 4-(2-Hydroxyethyl)-1-piperazine ethanesulfonic acid (HEPES) (pH 7.4), 0.1M phosphate (pH 7.4) and 0.1M carbonate buffer (pH 9.8). 100 µL of oil phase and 100 µL of aqueous phase were added to a microcentrifuge tube and vortexed for 10 seconds at maximum speed. They were then briefly centrifuged to allow for the separation between the oil and aqueous phases. The response of the oil phase was monitored colorimetrically. Images were analyzed in ImageJ for their blue hue.

5.2.4 Fabricating Droptode Devices

Devices were fabricated using standard soft lithography techniques.[17,18] Masks were designed in AutoCAD software (Autodesk, Inc.) and were printed as transparencies (CAD/Art Services, Inc) for use in photolithography. SU-8 2025 negative epoxy photoresist was spun-coat onto a clean Silicon wafer to a thickness of 40 µm. After photolithography and wafer

development, tridecafluoro-1,1,2,2-tetrahydrooctyl trichlorosilane was deposited on the master via vacuum assisted chemical vapor deposition. Devices were made from masters using a 10:1 degassed mixture of base: curing agent ratio to create PDMS (RTV615). Holes for the inlet and outlet were punched using a 24-gauge needle. Devices were bonded to a glass slide using oxygen plasma bonding. All channels were 40 μm in depth and 80 μm in width, except for the aqueous inlet which was only 40 μm in width.

5.2.5 Droptode Experiments

Solutions were individually loaded into plastic 3 mL syringes and then flowed through 24-gauge PTFE tubing into the device using syringe pumps. Unless otherwise noted, the solutions were each pumped at a speed of 1 μL/min. The magnitude of fluorescence at various points was determined using a Nile Red filter cube (Leica Microsystems), and a VEO 640L high speed camera (Vision Research Inc.) connected to a DMi8 light microscope (Leica Microsystems). Measurements were taken 3 cm from the T junction unless otherwise noted.

5.2.6 Droptode Data Analysis

Standard data analyses was carried out, as discussed previously.[18] Briefly, all videos were combined to form a single file in ImageJ (NIH). Contrast was normalized and enhanced to 0.3% saturation. The fluorescence of a 30 x 30-pixel spot in the middle of the channel was calculated for each frame of the combined video samples, averaging about 200 time points each, or 40 oil segments (code in Appendix 2). The resulting measurements were then analyzed for peaks using

MATLAB (Appendix 2-3). To account for variations in light source and oil concentration, data was normalized to terms of 1-α (Equation 5.1),

$$1 - \alpha = 1 - \frac{F - F_{Max}}{F_{Max} - F_{Min}} = 1 - \frac{F - F_{HCl}}{F_{HCl} - F_{NaOH}} \quad [5.1]$$

Where 1-α is the degree of protonation, F is the fluorescence of the sample, F_{HCl} is the fluorescence of 0.1M HCl and F_{NaOH} is the fluorescence of 0.1M NaOH. The results of the measurements were then fit to a logistic curve against the log of the concentration of $PFOS^-$ (code in Appendix 4).

5.2.7 Making $PFOS^-$ Optode

Optodes for $PFOS^-$ were made by depositing 0.5 mL of the oil phase from droptodes on paper and Teflon sheets of various porosity. After letting the solution dry for 2 hours, 10 μL aqueous droplets of buffer, 10^{-3}M $PFOS^-$, 0.1M HCl and 0.1M NaOH were applied and imaged using a smartphone. Droplets were then allowed to dry and the optode was imaged again. Images were analyzed in ImageJ.

5.3 RESULTS AND DISCUSSION

Initial experiments demonstrated the solubility of chromoionophore I in a fluorinated oil, perfluorooctanol, but not in Fluorinert FC-40 or Novec 7500. Thus, all experiments were initially performed with chromoionophore I while waiting for novel fluorinated chromoionophores to be synthesized, as discussed later in this chapter.

5.3.1 Determining Optimal pH Ranges for Detection

Experiments were first performed in bulk to determine the optimal buffer composition for $PFOS^-$ detection. The basis of $PFOS^-$ detection in all of the mechanisms below is the same.

Optimal buffer composition was determined by the buffer with the maximal colorimetric difference in the response of the sensing phase (200 μM Chromoionophore I in perfluorooctanol)

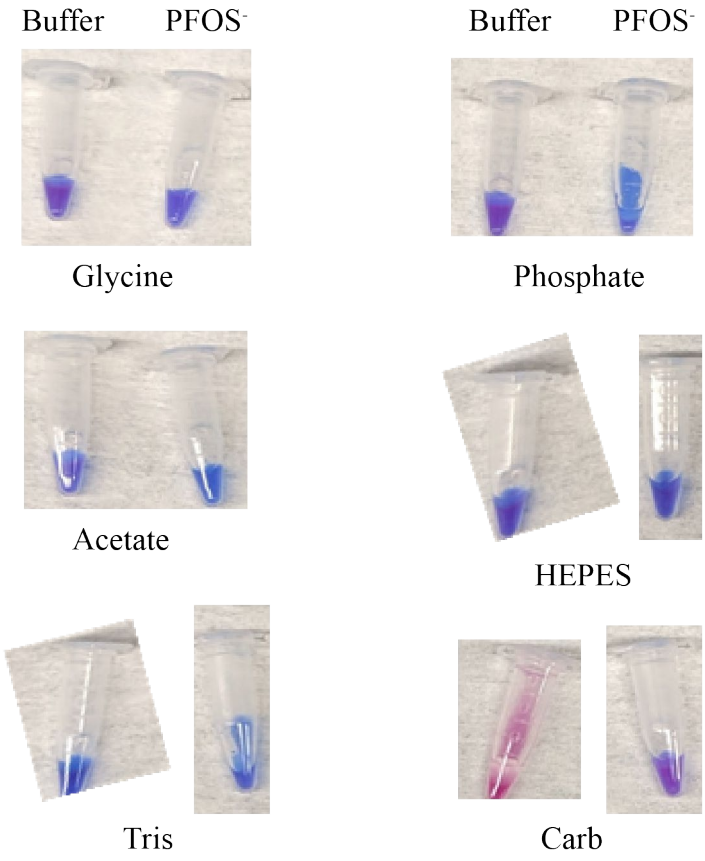

Figure 5.2. Colorimetric responses of 200 μM Chromoionophore I in perfluorooctanol to various buffers and 10^{-3} M $PFOS^-$. The pH 10 carbonate buffer showed the largest difference between the buffer and 1 mM $PFOS^-$.

between the buffer and 10^{-3} M $PFOS^-$. Both buffer composition and pH were tested (**Figure 5.2**). The inorganic versus organic composition of the buffer did not seem to elicit as much variation

as the pH changes, with the optimal detection being at a basic pH (~pH 10) (**Figure 5.3**). The limit of detection when using a carbonate buffer is around 10^{-5}M based on ImageJ analysis (**Figure 5.3**). Prior research has demonstrated the improved detection limits in droptodes compared to bulk optode systems,[19] due to better mixing, increased surface area to volume ratios, and the use of fluorescence detection. Thus, droptode detection of $PFOS^-$ was carried out on the carbonate diluted system, with the hope of improved sensitivity in the droptode experiments.

5.3.2 Droptode Detection

Initial droptode detection was performed using the same oil phase as the bulk experiments, 200 μM chromoionophore I in perfluorooctanol, in standard conditions for droptode experiments.[18,16] High sensitivity was seen in the region of 10^{-4}-10^{-3} M $PFOS^-$ (**Figure 5.4**), with a limit of detection calculated to be around 10^{-5} M $PFOS^-$. While the high sensitivity was encouraging, the droptode was still a million-fold away from the ideal limit of detection defined by the EPA (~10^{-11} M).[6]

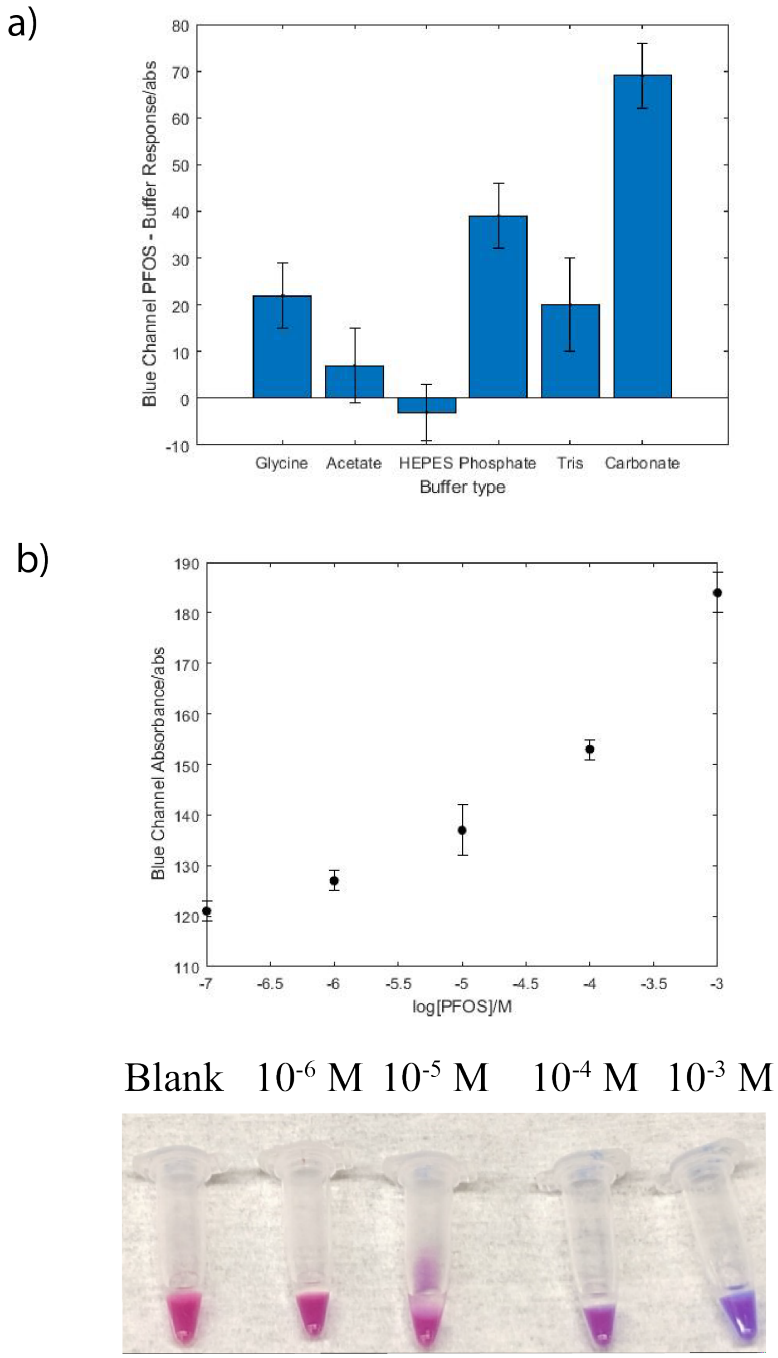

Figure 5.3. Optimization of $PFOS^-$ detection optically. (a) The difference between 200 µM chromoionophore I response to buffer vs 10^{-3} M $PFOS^-$ was tested in various buffers (Figure S2). The samples' oil phases were then imaged in a blue responsive channel using ImageJ and the difference between the response of $PFOS^-$ and the buffer were determined. (b) The buffer with the widest range for colorimetric response, carbonate, was tested for the 200 µM chromoionophore I response at different $PFOS^-$ concentrations. Top shows the results of the blue channel absorbance test were and bottom shows the colorimetric response.

5.3.3 Manipulations Towards Optimizing Droptode Detection

5.3.3.1 Volumetric Manipulations

One of the first manipulations attempted in the bulk phase was changing the ratio of aqueous and oil phases, which has been previously shown to alter limits of detection.[18] Attempting to mimic the conditions of the droptode system, the oil and aqueous phase ratios were not varied dramatically, 1 part oil to 3 parts aqueous or 3 parts oil to 1 part aqueous. Neither showed extreme improvement over the equal parts oil and aqueous phase (**Figure 5.4**). Unpublished work done by the Meyerhoff lab has suggested that volumetric manipulations that are more extreme could optimize droptode response. This has not yet been adapted into a droptode system though, where the large differences in the interfacial structure could complicate the benefits of this system.

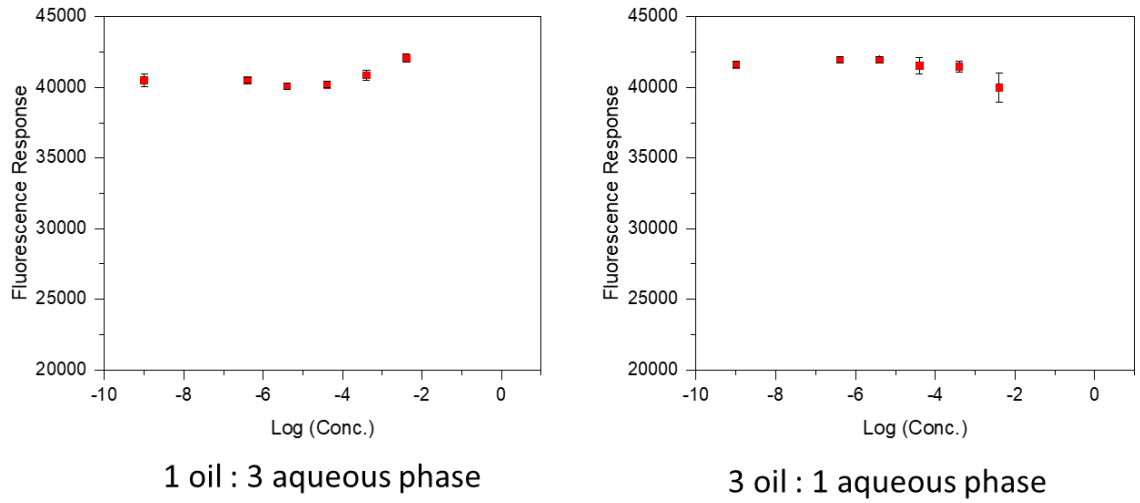

Figure 5.4. Impact of Aqueous and Oil Phase Volumes on $PFOS^-$ Droptode Response. Especially at low concentrations, changing the volumetric ratio of the oil phase and aqueous phase causes minimal signal differentiation.

5.3.3.2 Dye Concentrations

Another option for lowering limits of detection was included changing the concentration of chromoionophore I in perfluorooctanol. Too high of a chromoionophore concentration could lead to background preventing observation of color changes. Thus, 20 µM chromoionophore I was also tested in droptodes. 20 µM chromoionophore allowed the differentiation between 10^{-5} M and 10^{-6} M, over an order of magnitude lower than 200 µM allowed (**Figure 5.5**). There is potential that using even lower chromoionophore concentrations would further improve the limit

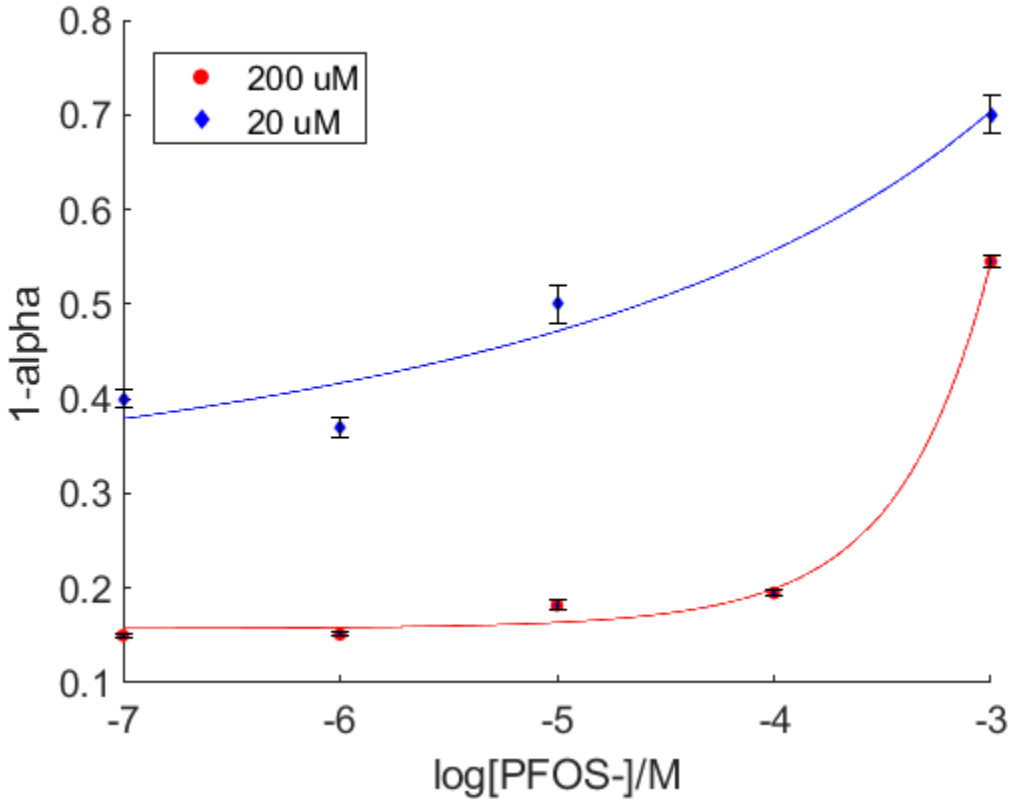

Figure 5.5. Testing $PFOS^-$ Detections in Droptodes. Using 200 µM chromoionophore I provides maximum sensitivity around 5 x 10^{-4} M $PFOS^-$ and a LoD around 10^{-5}M. By decreasing the chromoionophore concentration by a factor of 10, we gain over an order of magnitude better concentration differentiation. Fits are drawn to help the eye (n=1)

of detection, however there is concern that a chromoionophore concentration at 2 µM would be too low for the fluorescent microscope to measure. Further work should be performed to optimize the droptode chromoionophore concentration for maximum sensitivity at the lowest concentrations.

5.3.3.3 Flow Rate Changes

Prior work has explored the impact of flow rate on droptodes and found minimal correlation between droptode speed and sensitivity.[18] However, as that work was focused predominantly around monovalent cation detection using an ionophore, flow rate was also tested as a potential variable for $PFOS^-$ detection. Changing the overall flow rate from 4 µL/min to 6 µL/min caused minimal differences in droptode behavior for both 200 µM chromoionophore I and 20 µM chromoionophore I sensing phases, validating the results from prior experiments (**Figure 5.6**).

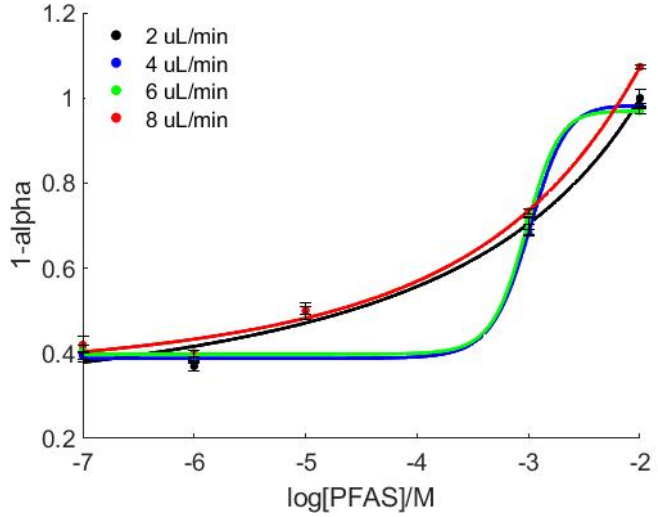

Figure 5.6. Impact of Flow Rates on $PFOS^-$ droptode response. Increasing the flow rate above 6 µL/min or decreasing it below 2 µL/min caused loss of the sigmoidal behavior.

5.3.4 Towards the Impact of Fluorinated Chromoionophores on Sensitivity

The solubility of chromoionophore I could potentially cause issues with this assay's development for selective $PFOS^-$ detection. Specifically, chromoionophore I is not a fluorinated molecule, yet was still able to be solubilized in perfluorooctanol. This suggests that other organic molecules which are not fluorinated could have similar properties. Thus, it would be more ideal to have a sensing phase that is more fluoroselective and does not have chromoionophore I solubility, such as Fluorinert FC-40 or Novec 7500.

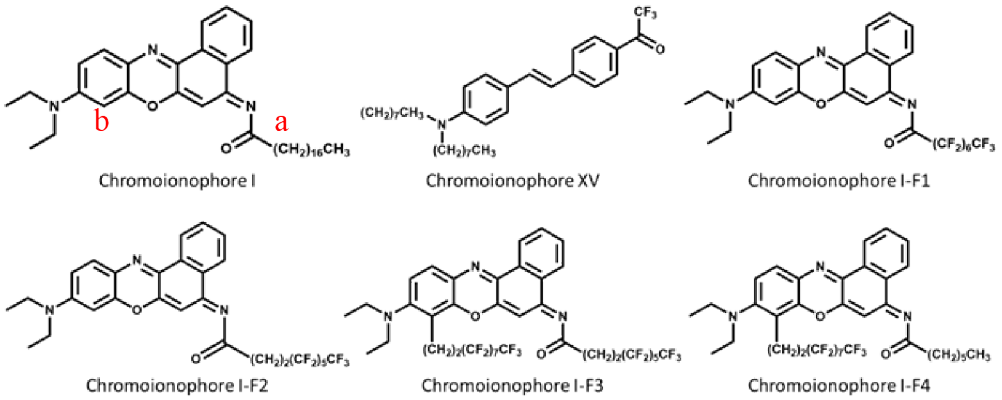

Figure 5.7. Different chromoionophore options for $PFOS^-$ detection. Chromoionophore I and Chromoionophore XV are commercially available. All others were/will be made in-house by Dr Jennifer Reeves.

In order to find a chromoionophore which could be solubilized in Fluorinert FC-40 or Novec 7500, our lab has been collaborating with Dr Jennifer Reeves of the Meyerhoff lab. Fluorination of chromoionophore I offered a good starting point for creating a chromoionophore with good solubility and $PFOS^-$ responsiveness. We have also looked at chromoionophore XV, which has a fluorocarbon tail and thus could be a good starting point for any further fluorinations. There are two prime synthetic fluorination spots on Chromoionophore I. The first is in place of the hydrocarbon tail on Chromoionophore I, (represented by position a on

Chromoionophore I in **Figure 5.7**) which synthetically should be relatively straight forward to create. By making the tail a fluorocarbon instead, the stability of the chromoionophore in fluorinated oils should be improved, though the question remains if the chromoionophore will be predominantly interfacial and act as a surfactant. This is unlikely due to the high hydrophobicity of the aromatic core group but could pose a problem if the fluorinated oil was interfaced with another oil phase such as dioctyl sebacate. If there was concern over the core not being fluorinated enough, there is also the possibility to add a fluorocarbon tail off the benzene ring in the molecule, ortho to the bonded secondary amine group, as represented by position b on Chromoionophore I (**Figure 5.7**). While stability in this position should be strong, there is concern that the electrophilicity of the fluorocarbon could change the pK_a of the chromoionophore, which would need to be accounted for during testing. Adding hydrocarbon spacers before the fluorocarbon chain should hopefully mitigate the instability.

Once the chromoionophores were synthesized, they were characterized for their solubility in three fluorinated oils (perfluorooctanol, Fluorinert FC-40, Novec 7500) as well as their pH responsiveness/stability. All tested chromoionophores so far (Ch XV and Ch1-F1) have had no solubility in Fluorinert FC-40 but good solubility in Novec 7500 and perfluorooctanol. Thus, pH experiments were performed with Novec 7500 as the sensing oil phase (**Figure 5.8**). For Chromoionophore I-F1, the chromoionophore was stable when exposed to acidic pHs. But upon exposure to basic pHs, Chromoionophore I-F1 forms a colored precipitate in the aqueous phase, suggesting a breakdown in the chromoionophore where it loses its fluorinated tail (**Figure 5.8**).

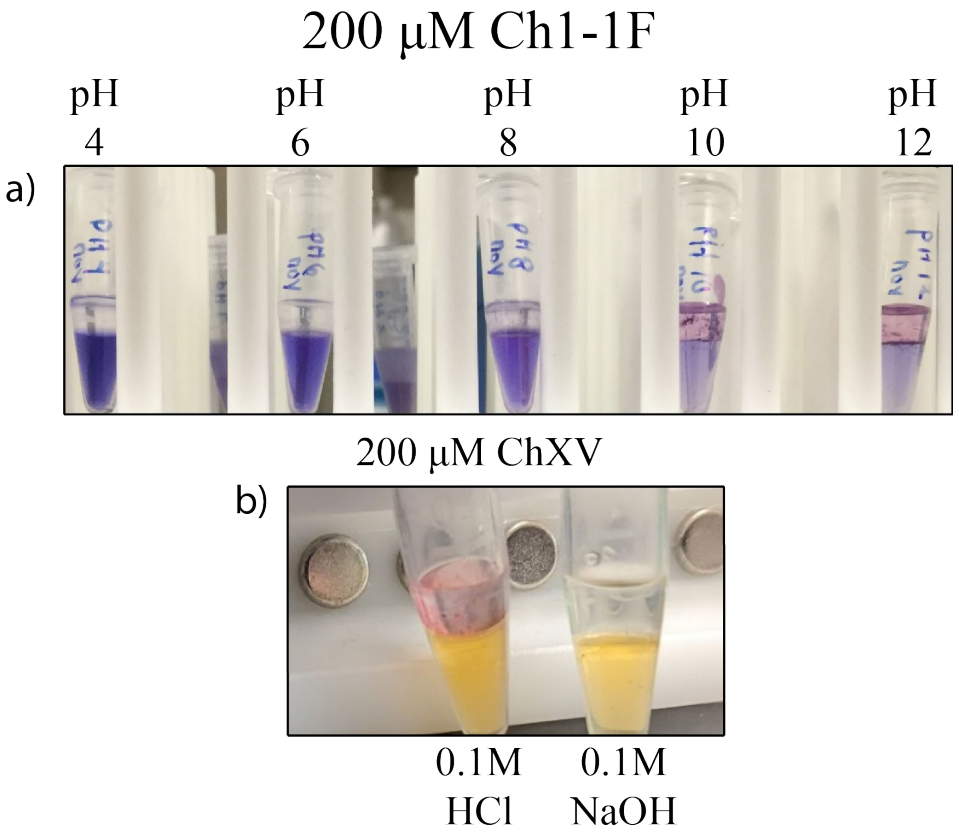

Figure 5.8. Testing pH stability of different chromoionophores in Novec oil. The appearance of precipitates in both cases suggest a breakdown of the chromoionophores due to pH changes. (a) Stability of 200 µM chromoionophore I-1F in Novec oil. Note the appearance of the purple-red precipitate around pH10. (b) Stability of 200 µM chromoionophore XV in Novec oil. Note the appearance of the red precipitate in acidic conditions.

To counteract this in future chromoionophore designs, a hydrocarbon spacer will be used in between the fluorocarbon tail and the rest of the molecule, hopefully improving stability by mitigating the electrophilicity. For Chromoionophore XV, by contrast, the reverse was true, where acidic conditions caused the breakdown of the chromoionophore while basic conditions led to stability (**Figure 5.8**). This suggests that the means of molecular breakdown between Chromoionophore XV and Chromoionophore I-F1 are different. It is likely that in Chromoionophore XV the acidic hydrogens cause a breakdown across the double bond, while in Chromoionophore I-F1 the breakdown occurs at the amide, as the electrophilic fluorinated tail would act as a good leaving group. Based on the methods of these breakdowns, it is hopeful that the fluorocarbon chain attached directly to the benzene ring in the core could maintain stability regardless of pH condition.

So far, we have yet to find a chromoionophore which maintains its stability in Novec 7500 across a variety of pHs. It is important to note that Chromoionophore I does not break down under either acidic or basic conditions and shows no leeching into the aqueous phase. Once an optimal dye is found, it will need to be tested for its pH responsiveness colorimetrically and fluorometrically before optimizing it for use in $PFOS^-$ droptodes. We have many chromoionophores left to characterize, which would be an excellent short-term project for a new lab member in the near future.

5.3.5 Preliminary Optode Detection of PFAS

Preliminary work, using similar sensing chemistries, has also been performed to create a dipstick test for $PFOS^-$, which could be used in a variety of situations where the microscopes needed for droptodes are inaccessible. Traditionally optodes are made by depositing a plasticizer alongside the chromoionophore and ionophores needed for sensing, on a solid-state matrix such as PVC. However, since the selectivity in our droptodes comes from the oil phase itself rather than an ionophore, such a solid-state matrix would need to be fluorinated. While it would be possible to fluorinate PVC, or to attach fluorinated reagents covalently to the solid-state matrix, a simpler solution would be to use Teflon as the solid-state matrix using standard optodic deposition techniques.

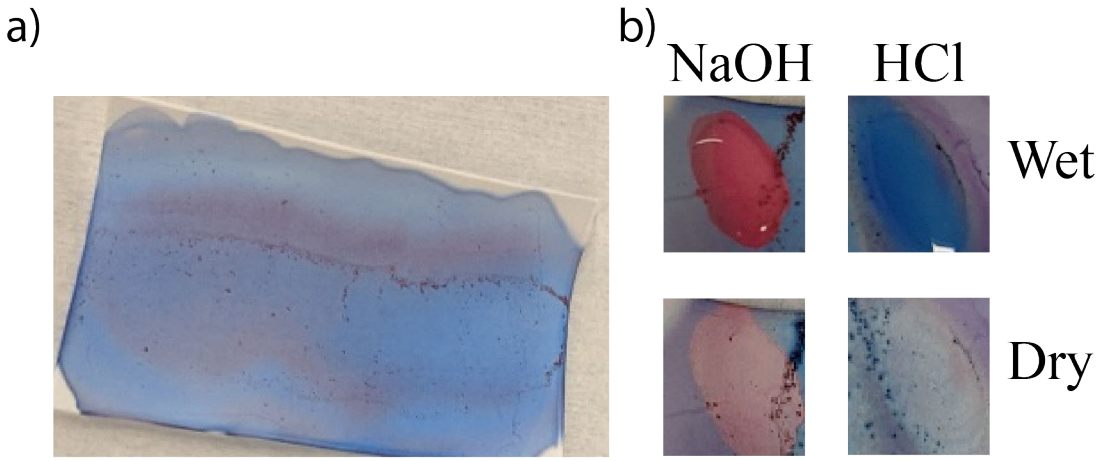

Figure 5.9. Development of Teflon optodes using Chromoionophore I. (a) A porous Teflon optode doped with 200 µM Chromoionophore I in perfluorooctanol after drying. (b) pH responsiveness of Teflon optode both 10 minutes after the sample is applied (top) and after the sample has dried (bottom).

Initially both Teflon tape and Teflon sheets of various thicknesses were explored to be the solid-state matrix of 200 µM chromoionophore I in perfluorooctanol. However, each ran into mechanical challenges; Teflon tape was too thin so upon drying the tape would shrivel leading to

inconsistent dye spread and challenges in imaging. The Teflon sheet, regardless of its thickness, did not have even partitioning of the chromoionophore leading to minimal signals.

In order to improve deposition ability of the chromoionophore, porous Teflon was also tested as a solid-state matrix. Porous Teflon had much better partitioning than Teflon Sheets (**Figure 5.9**), though deposition was still not optimized for complete even surface coverage. Even so, changes could be seen in the color of the sheet based upon pH in both wet and dry conditions (**Figure 5.9**). Based off this, preliminary tests were run to see if 10^{-3} M $PFOS^-$ could be differentiated from buffers at three different buffer conditions: pH 10 (carbonate buffer), pH 7 (phosphate buffer), and pH 3 (acetate buffer) (**Figure 5.10**). While "wet" conditions had minimal differentiation regardless of pH, "dry" conditions resuled in potential differences when using pH 7 and pH 10 buffers. This experiment would need to be repeated with a more uniform deposition

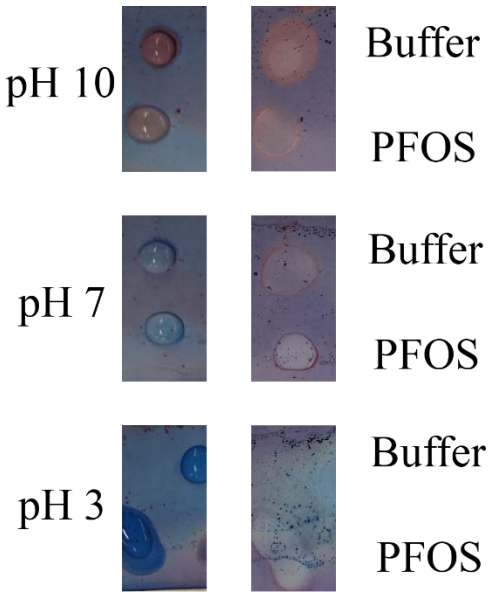

Figure 5.10. Application of Teflon optode towards PFOS detection. Buffer and 10^{-3}M PFOS were applied in 10 µL droplets to a porous Teflon sheet coated with 200 M chromoionophore I in perfluorooctanol. The left column was 10 minutes after droplet application. The right column was after droplets had dried. There may be differences at pH 7 and pH 10 but it is hard to discern if that was due to unequal deposition of the chromoionophore initially.

procedure to see if detection of $PFOS^-$ is replicable. Regardless, this represents the first use of Teflon as an optodic matrix, potentially broadening the matrix options for optode creation.

5.4 CONCLUSIONS AND FUTURE WORK:

This work demonstrated the potential for detection of perfluoroalkyl chains using both microfluidic droptodes and Teflon-based optodes. Limits of detection down to 10^{-6} M $PFOS^-$ in aqueous solution were found. The exploration of novel fluorinated chromoionophores will likely aid in this process, by allowing the use of Novec 7500, a more selective fluorinated oil. The ability to perform point-of-analysis PFAS detection could allow for more rapid testing of waterways for pollution, especially in low resource areas, thereby minimizing human PFAS exposure.

5.4.1 Future Work

Aside from continuing the exploration work outlined in this chapter, further work testing selectivity must also be performed for the ultimate volumes used in droptodes. There should be a variety of tests performed for PFAS contamination on the water used to make the buffers, the bottles that the $PFOS^-$ comes in and anything used in the process of diluting the $PFOS^-$ for samples. Additionally, Teflon-based optodes should continue to be characterized for optimal deposition and physical characteristics of performance.

There are a few theoretical characterizations of PFAS droptodes which would be interesting to conduct. For instance, how the length of the PFAS tail affects its characterization by the droptode. Or how the head group that the PFAS has affects its droptode response. There

also should be further selectivity assays run against non-PFAS fluorinated compounds such as chemotherapy drugs like capecitabine.[19]

Once PFAS detection in microfluidic droptodes is achieved at the appropriate EPA sensitivity range, the assays can be used for point-of-analysis detection in a variety of locations. One particular sample of interest would be detection of PFAS in human biological samples, including serum, blood, and urine. This detection would allow tracking of the influence of PFAS pollution in a variety of communities and could potentially highlight communities most effected by the pollution. Additionally, it would be interesting to tack PFAS pollution in remote environmental samples, such as in Artic ice. Fully developing optodes and/or droptodes for PFAS detection would allow these studies to proliferate, further informing PFAS pollution control.

5.5 ACKNOWLEDGMENTS

S.P.W.Q (DGE-1256260) acknowledges the National Science Foundation for support. Keenan Wright and Joshua Wolfe are acknowledged for their individual experiments and Dr Jennifer Reeves for her fluorinated chromoionophore synthesis. Prof Mark Meyerhoff is acknowledged for useful conversation and feedback. The authors would also like to acknowledge Nicolas Mesyngier, of the University of Michigan for providing the basis for the MATLAB analysis code.

5.6 REFERENCES

1. Basic Information on PFAS | Per- and Polyfluoroalkyl Substances (PFAS) | US EPA. https://www.epa.gov/pfas/basic-information-pfas.

2. Hu, X. C. *et al.* Detection of Poly- and Perfluoroalkyl Substances (PFASs) in U.S. Drinking Water Linked to Industrial Sites, Military Fire Training Areas, and Wastewater Treatment Plants. *Environ. Sci. Technol. Lett.* **3**, 344–350 (2016).

3. Maisonet, M. *et al.* Maternal Concentrations of Polyfluoroalkyl Compounds During Pregnancy and Fetal and Postnatal Growth in British Girls. *Environ. Health Perspect.* **120**, 1–26 (2012).

4. Andersen, C. S. *et al.* Prenatal Exposures to Perfluorinated Chemicals and Anthropometric Measures in Infancy. *Am. J. Epidemiol.* **172**, 1230–1237 (2010).

5. Shoaff, J. *et al.* Prenatal Exposure to Perfluoroalkyl Substances. *Environ. Epidemiol.* **2**, e010 (2018).

6. US EPA. *Drinking Water Health Advisories for PFOA and PFOS*. https://www.epa.gov/ground-water-and-drinking-water/drinking-water-health-advisories-pfoa-and-pfos (2019).

7. EPA Drinking Water Research Methods | Water Research | US EPA. https://www.epa.gov/water-research/epa-drinking-water-research-methods.

8. Third Unregulated Contaminant Monitoring Rule | Monitoring the Occurrence of Unregulated Drinking Water Contaminants | US EPA. https://www.epa.gov/dwucmr/third-unregulated-contaminant-monitoring-rule.

9. Jamari, N. L. A., Dohmann, J. F., Raab, A., Krupp, E. M. & Feldmann, J. Novel Non-Targeted Analysis of Perfluorinated Compounds Using Fluorine-Specific Detection Regardless of Their Ionisability (HPLC-ICPMS/MS-ESI-MS). *Anal. Chim. Acta* **1053**, 22–31 (2019).

10. Riedel, T. P., Lang, J. R., Strynar, M. J., Lindstrom, A. B. & Offenberg, J. H. Gas-Phase Detection of Fluorotelomer Alcohols and Other Oxygenated Per- and Polyfluoroalkyl Substances by Chemical Ionization Mass Spectrometry. *Environ. Sci. Technol. Lett.* **6**, 289–293 (2019).

11. Kazemi, R., Potts, E. I. & Dick, J. E. Quantifying Interferent Effects on Molecularly Imprinted Polymer Sensors for Per- A nd Polyfluoroalkyl Substances (PFAS). *Anal. Chem.* **92**, 10597–10605 (2020).

12. Cheng, Y. H. *et al.* Metal-Organic Framework-Based Microfluidic Impedance Sensor Platform for Ultrasensitive Detection of Perfluorooctanesulfonate. *ACS Appl. Mater. Interfaces* **12**, 10503–10514 (2020).

13. Viada, B. N., Yudi, L. M. & Arrigan, D. W. M. Detection of Perfluorooctane Sulfonate by Ion-Transfer Stripping Voltammetry at an Array of Microinterfaces Between Two Immiscible Electrolyte Solutions. *Analyst* **145**, 5776–5786 (2020).

14. Al Amin, M., Sobhani, Z., Chadalavada, S., Naidu, R. & Fang, C. Smartphone-Based / Fluoro-SPE for Selective Detection of PFAS at ppb Level. *Environ. Technol. Innov.* **18**, 100778 (2020).

15. Fang, C., Wu, J., Sobhani, Z., Amin, M. Al & Tang, Y. Aggregated-Fluorescent Detection of PFAS with a Simple Chip. *Anal. Methods* **11**, 163–170 (2019).

16. Wang, X. *et al.* Ionophore-Based Biphasic Chemical Sensing in Droplet Microfluidics. *Angew. Chemie Int. Ed.* **58**, 8092–8096 (2019).

17. Xia, Y. & Whitesides, G. M. Soft Lithography. *Angew. Chemie - Int. Ed.* **37**, 550–575 (1998).

18. Wetzler-Quevedo, S. P. & Bailey, R. C. Characterization of the Impact of Mixing and Volumes on the Behavior of Microfluidic Droptodes. *Submitted.* (2021).

19. Johnson, B. M., Shu, Y. Z., Zhuo, X. & Meanwell, N. A. Metabolic and Pharmaceutical Aspects of Fluorinated Compounds. *J. Med. Chem.* **63**, 6315–6386 (2020).

Chapter 6.

Contextualizing Undergraduate Analytical Chemistry Labs Through National Disasters: Enzyme Linked Immunosorbent Assays Through the Lens of COVID-19 Antibody Analysis

6.1 INTRODUCTION:

A major challenge in Science Technology Engineering and Math (STEM) fields is student retention, especially with respect to students not traditionally represented in STEM fields.[1] A variety of methods have been developed to provide additional student support, including active learning techniques, a focus on peer interactions with respect to the taught material and an emphasis on providing inclusive examples of scientists, both historical and modern.[1]

An alternative but complementary means of student support is to increase student interest in STEM material, potentially by making direct connections between the material taught and student life. Students have repeatedly expressed enjoyment in seeing real-world applications of the material learned in class, and cite relevance as a major factor in improving their experience in chemistry classes.[2] Not only do students enjoy courses with a focus on application; a focus on how chemistry can be used outside of class gives students more reason to be interested in the coursework, leading to better recall and comprehension of the information.[1,3–7] Contextualizing chemistry has been cited as being particularly useful for students with low success expectations, such as those from backgrounds not traditionally represented in STEM. Relevance-focused teaching was found to increase grades of students by as much as 2/3 of a letter grade, on average, compared to teaching focused on theoretical chemistry.[7]

There are a variety of methods shown to enhance student interest, including focusing on drugs, diseases, the environment, or common industrial processes,[2,3] taking advantage of the "human interest factor",[1] or simply by connecting the material to topics students study in other courses.[6] Students learn best when able to make personal, and potentially even emotional, connections, to the material.[1] Thus, labs should be designed around national or international events, not only to peak interest, but also to foster additional inclusivity in the laboratory environment.[1,4,5] Demonstrating how science has played a role in resolving crises can also encourage students to view themselves as vehicles of change through science, furthering student retention.[5,7] Much work has been done to improve the relevance of both chemistry lecture and lab material to non-chemistry applications, creating an opportunity for novel lab development.

6.1.1 Using Theory of Relevance to Create a Quantitative Enzyme Linked Immunosorbent Assay (ELISA) Lab

In attempting to create a relevant laboratory experience, the first question to address is the concept of relevance. There have been numerous reviews addressing the concept of relevance, specifically in secondary education,[8-10] but the same analyses can be applied to collegiate coursework. Relevance is an umbrella term incorporating many categories of motivation, as will be discussed briefly in this chapter. It is also important to note that relevance is not a yes/no question, but a spectrum, in which the relevance of a topic can change over time as well as being an intrinsic motivator for the student or a society or authority-imposed reason as to why a student should learn the material.[10]

Relevance can come in a variety of different categories, including personal relevance, technological relevance, vocational relevance, and societal relevance.[9,10] Personal relevance is

typically focused on students' interests and curiosity as motivators for learning material. This can include interest in big questions (such as how humans came to exist), excitement due to demonstrations, or observing relationships between the material and their daily lives. Technological relevance generally focuses on connecting the fundamental science to technological applications, explaining how everyday objects work or function. In this way, technological relevance is often seen as a subfield of personal relevance, but does not rely on the personal connection of each individual student. Vocational relevance is based upon providing skills and information that students will use in future careers. Vocational relevance is often portrayed as giving students "a leg up" when it comes to both applying to and succeeding in various jobs. Finally, societal relevance is typically focused around students developing into responsible and independent scientifically literate citizens. Societal relevance, currently often expressed as STS (Science Technology and Society) analyzes the way science and society are connected, enhancing students' abilities to contribute to scientific debates and make educated decisions on future scientific policies.

As this lab was developed to be a stand-alone lab in a separate bioanalytical curriculum, to be completed in one class period, focus was predominantly placed on developing an Applied Chemistry lab, where everyday life issues and applications of chemistry are used as an illustration of fundamental chemistry principles or techniques.[8] Questions of societal importance, which are often the focus in CTS [9]or Critical-Reflexive Chemistry curricula,[8] were incorporated in the lab as follow-up questions, hopefully fostering discussions about inequitable medical access and the importance of rolling out disease diagnostics to broader populations, if time allowed. Both intrinsic and extrinsic motivations were applied within the lab, as well as a focus on both present interests and future goals of the students.

Enzyme Linked Immunosorbent Assays (ELISAs) are the gold standard for specific protein and antibody quantitation. ELISAs are used in a variety of biomedical fields, including to run titer assays,[11] to determine vaccine effectiveness,[12] to diagnosis HIV,[13] tuberculosis,[14] or auto-immune diseases such as Lupus as part of an anti-nuclear antibody panel.[15] In what could be considered less of a biomedical application, ELISAs are also used to determine the presence of poisonous enterotoxins in food.[16] The importance of ELISAs in bioanalytical chemistry suggests that performing a quantitative ELISA in an undergraduate lab environment might be useful preparation for students' future in the field; providing a form of intrinsic vocational relevance based on future goals.

More immediate to most students, however, is the role that ELISAs have played in controlling the COVID-19 pandemic. ELISAs have been used to determine if someone has previously been exposed to COVID-19, allowing epidemiological tracking of the rate of community spread without concern over missing asymptomatic cases.[17] ELISAs were also a key aspect of the vaccine development workflow, as they were used to ensure that vaccines were causing COVID-19 antibody creation, and thus immunity.[18] Given the impact that COVID-19 has had on students, both on a personal and academic level, performing ELISAs with the context of COVID-19 detection might be able to contribute to situational and personal interest, hopefully improving knowledge retention through intrinsic present motivation.

Many students have been participants in COVID-19 tests over the past year and a half, of a variety of natures (i.e., rapid antigen, RNA testing, antibody). Performing an ELISA could thus invite students to compare and contrast diagnostic tests, allowing them to differentiate when each test would be appropriate and what assumptions are made with each form of test. Thus, students would be able to see how they, as a scientist, would fit into a COVID-19, or any pandemic,

workflow. Finally, understanding the methodology of detecting a history of COVID-19 could be an excellent gateway for studies analyzing the spread of COVID-19 in various locations, potentially leading to discussion about differential pandemic impacts based on societal factors.

6.1.2 Experimental Overview

In this undergraduate laboratory experiment for a Bioanalytical Chemistry lab, the idea of using ELISAs to detect antibodies for disease history, such as having COVID-19, was introduced. This lab's development was started prior to the COVID-19 pandemic, and thus the original focus of the lab was on detecting auto-antibodies as part of a Lupus Anti-Nuclear Antibody panel. In light of the pandemic, I readapted the lab to focus on COVID-19 as it was more likely to have an emotional impact and improve student retention. The flexibility of this laboratory design, focusing on an application rather than a fundamental concept, allows the lab to be updated easily to reflect current events.

The use of ELISAs in COVID-19 pandemic control was first discussed with students, and then students were asked to identify the concentration of antibodies in unknown samples using ELISAs. Using serial dilutions, students prepared protein standards, in order to make a calibration curve for the ELISA. Students then used their calibration curves to find the unknown concentration with error, as well as the assay's limit of detection and limit of quantitation. Students subsequently identified what could have impacted the limit of detection from their protocol, the impact of complex matrix effects and common troubleshooting issues in a multi-page lab report format.

6.1.3 Experimental Learning Goals

Students were expected to demonstrate their skills at serial dilution as part of this experiment, as well as identifying common causes of error in bioanalytical experiments. Students were also expected to gain familiarity with performing non-linear fitting in Excel and determining unknown concentrations, limit of detection (LoD) and limit of quantitation (LoQ) from sigmoidal calibration curves. By the end of the lab, students were expected to be familiar with the typical ELISA format, as well as its limit as a tool in results interpretation, preparing them for future biomedical lab work.

6.2 MATERIALS AND METHODS

This protocol will serve up to 10 teams of 2 students each, or 20 students total. This is a one period lab, taking a total of 2 hours for lab work and up to another hour, either at home or in lab, for data workup.

6.2.1 Reagents

The base ELISA kit was the ELISA Immuno Explorer Kit provided by Bio-Rad. This kit includes lyophilized stock autoantibody (hereafter the antigen), primary, and secondary antibodies as well as a 10x phosphate buffer saline (PBS) solution, 10% Tween 20, disposable plastic transfer pipets and microcentrifuge tubes. Instructors will need to provide 20-200 μL adjustable volume pipettes, pipet tips, paper towels, 96-well plates, and a microplate reader, as well as microcentrifuge tube racks.

6.2.2 Instructor Preparation

Following the protocol provided with the instruction manual for the kit, instructors should make 100 mL of 1x PBS and 900 mL of wash buffer (PBS + 0.5% Tween). The instructor should create a 50x antigen stock for storage by adding 0.5 mL of 1x PBS to the antigen vial.[19] Less than 24 hours before the lab period, the instructor should dilute the 50x stock into 10x stock using 1x PBS (final concentration of 5 μg/mL) and aliquot into 500 μL volumes for each student. The instructor should also prepare 1x primary antibody and secondary antibody solutions as detailed in the instruction manual; first dissolve the lyophilized primary and secondary antibody in 0.5 mL of 1x PBS to make a 50x stock solution, then diluting down to 1x using wash buffer (24.5 mL wash buffer, 0.5 mL 50x antibody stock).[16] The antibodies should be aliquoted into 1.5 mL volumes for student use. All antibodies should be stored at 4°C. Instructor preparation will not only save lab time, but also ensure that students' stock concentrations are accurate, keeping the focus on the ELISA technique. The TMB substrate (1.5 mL), wash buffer (mL) and PBS (500 μL) should also be aliquoted for each student. Finally, the instructor should prepare the stopping solution, 0.16M H_2SO_4, by dissolving concentrated H_2SO_4 in distilled water, and aliquot it into 1.5 mL volumes for each student.

Instructors should also make unknowns from which students should identify antibody concentrations based on their calibration curves. The unknowns need to have a concentration in the linear range of the calibration curve, approximately 10 ng/mL to 200 ng/mL, in order for students to do proper unknown identification. To increase the relevance and interest in the

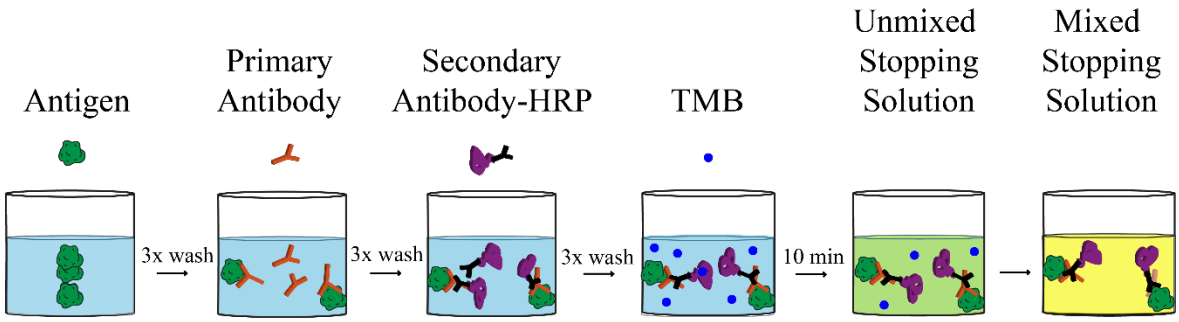

Figure 6.1. Schematic explaining ELISA procedure. Initially, the antigen is added to the well and captured by the walls. After washing to remove unbound antigen, the primary antibody is incubated in the well and binds to the antigen at the wall surface. After washing, a secondary antibody conjugated to HRP, is incubated and binds to the primary antibody. This is followed by another round of washing,and then the substrate for HRP, TMB, is added, turning the well blue. After incubation, a stopping solution of acid can be added to change the well's color to yellow, proportional to the amount of HRP. Students will then take the absorbance of the wells.

experiment, it would also be ideal to have several different unknowns to distribute to students, some in the "COVID-19 negative history" range (below 50 ng/mL) and some in the "COVID-19 positive history" range (~50-100 ng/mL).[20] The differences in results could potentially spark conversations among students, not only encouraging them to make connections but also to discuss why results differed with each other, further cementing learning.

6.2.3 Hazards

The stopping solution is composed of 0.16 M H_2SO_4 which is corrosive. All students should wear appropriate PPE including gloves and goggles. In case of a spill, stopping solution should be neutralized with sodium bicarbonate.

6.2.4 Student Methods

Students will be given a 5 µg/mL stock solution of antigen and asked to serially dilute the antigen to a variety of different concentrations. To simplify this process during lab-time, the pre-

lab will prompt students to fill in the needed volumes of stock and diluent on a table. Students will use the 6 standard dilutions they created, plus a buffer blank, to perform an ELISA calibration curve in duplicate. They will also test an unknown sample.

To perform the ELISA, students first incubate the antigen in the well plate for 20 minutes, allowing time for the antigen to stick to the glass walls (**Figure 6.1**). After three 250 µL washes using the wash buffer, designed to remove any antigen not specifically bound to the walls, students will add the primary and secondary antibodies solutions, respectively, again incubating each solution for 20 min and washing with three 250 µL in-between (**Figure 6.1**). After the final wash, students will add the TMB substrate, and gently mix by briefly swirling the plate (**Figure 6.1**). After 10 minutes of the plate resting, timed from the addition of the substrate to the first well, students will add 50 µL of stopping solution to each well. Students then will swirl the plate until the wells with the highest concentration appears yellow (**Figure 6.1**). The students will then determine the absorbance of each well at 450 nm using a plate reader. After data collection, students will neutralize the stopping solution with sodium bicarbonate and dispose of the waste.

Students will use the absorbance of each well to make a sigmoidal calibration curve by plotting the absorbance against the logarithm of the antigen concentration. For many students, this will be the first introduction to a sigmoidal calibration curve and performing a sigmoidal fit in Excel. To facilitate student learning, part of the pre-lab is a step-by-step fitting of a sigmoidal curve in Excel, using sample data provided. Students will then calculate the limit of detection (LoD) and limit of quantitation (LoQ) based on their calibration curves, and then use the calibration to calculate the concentrations of the unknown (**Figure 6.2**). Students then will

estimate the range of the 95% confidence interval based on the unknown replicates and draw conclusions about the potential diagnostic history of the individual.

6.2.5 Discussion of Relevance With Students

Students summarized their results in a report, providing a brief introduction of why the lab was important, addressing questions from the protocol as well as interpreting their data (Appendices). The questions from the protocol were the vehicle for ensuring the students saw the relevance of what they did in the laboratory by having them not only interpret their own results to determine whether or not an individual previously had COVID-19, but also results which were more ambiguous (provided in the question). The motivation behind students' interpreting results which are less clear as to whether an individual had COVID-19 is to encourage students to view the ELISA assay as not an end-all be-all, but a tool which should be used in light of other societal constructs, like risk factors based on race, age and weight. Such analysis will hopefully help students to see scientific assays for what they are, instruments not irrefutable theorems.

6.3 STUDENT RESULTS AND OUTCOMES

Students were asked to share their lab reports with me for analysis, resulting in five group lab reports with two student authors each. Students were successful in performing ELISAs and fitting a sigmoidal calibration curve which using Excel (**Figure 6.2**). Students' calibration curves were generally in the range of typical ELISAs (LoDs ~1 ng/mL). However, students' percentage difference between their calculated and the actual unknown value varied greatly (**Table 6.1**).

Table 6.1. A Sample of Student Results for Limit of Detection, Limit of Quantitation and the Percentage Difference Between their Calculated Unknowns and Actual Unknown Values

LoD/ng/mL	LoQ/ng/mL	% Diff (Calculated v Actual Unknown)
1	2.5	3%
0.6	0.8	32%
2.5	3.3	29%
0.2	0.3	65%
25*[2]	N/A	N/A

[2] Students had a high error in their blank making calculating the LoQ impossible. The concentration of the unknown also came in below the LoQ so they were unable to quantitate.

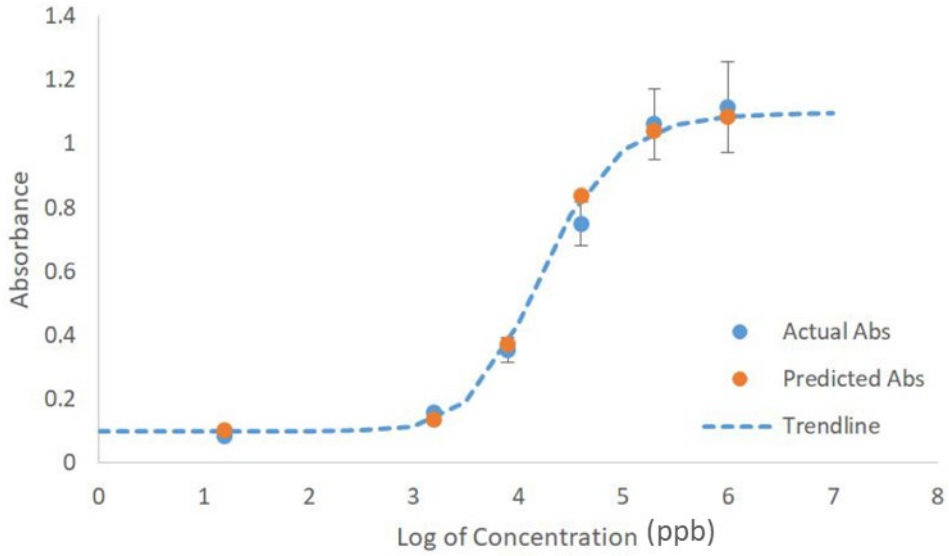

Figure 6.2. Sample data collected and plotted by a CHEM 246 student, taken directly from a student lab report. Absorbance data was taken from a plate reader and fit against the log of the concentration of the antigen in ppb. Error bars represent the standard deviation in the replicate measurements. Students could then use the calibration curve to calculate the value of unknowns.

There could be a few reasons for the variable accuracy on the unknown concentration, despite the good calibration curves. During the second class-period, one of the unknowns did not cause any signal, suggesting a stability issue. Additionally, students found the units of the sigmoidal fit to be challenging, often confusing whether the fit was based upon the logarithm of the concentration or the actual concentration. Students were also unclear if their calculations were in pg/mL, ng/mL, or in ppb. This could potentially be addressed by using consistent units throughout the course, and then asking for individual conversions as necessary.

Student feedback overall was positive, based on discussions had with the students while performing the lab. Within reports, students were able to demonstrate their understanding of the temperature dependent matrices of antibodies as well as identify common causes of user error during ELISAs. They also, despite not working with complex samples in this lab, were able to correctly predict how a complex sample matrix might impact the LoD and LoQ of the ELISA

assay. Students' responses to the questions in the lab also demonstrated points for clarification in learning, such as comprehension of least square error fitting. The interpretation of what a least square error fit is and how to define its quality, were consistent areas with questions within lab reports. Additionally, students demonstrated a lack of contextualization for error within real-world experiments. Students often stated that if the concentration found was even 0.01 ng/mL out of a given range for a disease, the person does not have the disease, rather than recognizing that as the concentration is close to the range, more studies are needed to confirm the value.

6.4 CONCLUSIONS AND FUTURE WORK

In conclusion, I developed a lab focused on quantitative enzyme linked immunosorbent assays (ELISAs), with the motivation of the lab focused around COVID-19 antibody detection. Students, during the lab period, were able to create an ELISA calibration curve, identify limits of detection and quantitation, and calculate concentrations of unknowns with 95% confidence intervals. Student feedback demonstrated the benefits of relevance for the lab, as well as identified informational weaknesses in student learning.

6.4.1 Future Work

Though my work at Michigan on this project is done, I hope to continue working on improving this lab at Virginia Military Institute, incorporating clearer units, more information on goodness of fit and encouraging students to question diagnostic ranges. I also hope to incorporate a larger sample size of students, surveys for more direct feedback, and questions on exams in order to directly address student learning. In light of the COVID-19 pandemic, I am also interested in adapting this lab for remote learning or low resource environments. Thus, I am in the process of

coding an ELISA lab for students to run at home on their computer, including randomized standard error and error in pipetting as part of the workflow. I have built the code skeleton and am in the process of building the graphical user interface, which will allow students to observe color changes etc. using LABVIEW.

I hope to also continue working towards improving lab relevance to everyday lives and cutting-edge science. I have started developing a lab with a focus on optode development for small molecule detection, such as water contaminants or pollutants, using paper microfluidics. I also plan to develop a lab focused on GC detection of opioid mimics in urine samples. Labs such as these will hopefully encourage students to see the relevance of chemistry in their daily lives, improve retention of information and improve retention of student interest, hopefully continuing to expand the diversification and knowledge base of chemistry in the process.

6.5 ACKNOWLEDGMENT

SPQ would like to acknowledge the Future Faculty GSI Program at University of Michigan Chemistry for sponsoring this project. This chapter was prepared based on data collected in Ryan C. Bailey's CHEM 246 Biomedical Analytical laboratory class in Fall 2019 as part of a Future Faculty GSI project. I would specifically like to acknowledge Likitha Nimmagadda whose sample data I am displaying in this chapter (and SI) and Ciara Witt and Hayley Lhotka who were the GSIs during this class period. I would also like to acknowledge Mou-chi Cheng for his help in procuring the ELISA kits.

6.6 REFERENCES

1. Sandoval, J. Teaching in Subject Matter Areas: Science. *Annu. Rev. Psychol.* **46**, 355–374 (1995).

2. Urban, S., Brkljača, R., Cockman, R. & Rook, T. Contextualizing Learning Chemistry in First-Year Undergraduate Programs: Engaging Industry-Based Videos with Real-Time Quizzing. *J. Chem. Educ.* **94**, 873–878 (2017).

3. Schwartz-Bloom, R. D., Halpin, M. J. & Reiter, J. P. Teaching High School Chemistry in the Context of Pharmacology Helps Both Teachers and Students Learn. *J. Chem. Educ.* **88**, 744–750 (2011).

4. Fensham, P. J. Real world contexts in PISA science: Implications for Context-Based Science Education. *J. Res. Sci. Teach.* **46**, 884–896 (2009).

5. Buckley, P. & Fahrenkrug, E. The Flint, Michigan Water Crisis as a Case Study to Introduce Concepts of Equity and Power into an Analytical Chemistry Curriculum. *J. Chem. Educ.* **97**, 1327–1335 (2020).

6. Singh, B. R. A First-Day Exercise on Relevance of Chemistry to Nonscience Majors Kindles Sustained Positive Student Response. *J. Chem. Educ.* **76**, 1219–1220 (1999).

7. Hulleman, C. S. & Harackiewicz, J. M. Promoting Interest and Performance in High School Science Classes. *Science.* **326**, 1410–1412 (2009).

8. Sjöström, J. & Talanquer, V. Humanizing Chemical Education: From Simple Contextualization to Multifaceted Problematization. *J. Chem. Educ.* **91**, 1125-1131 (2014).

9. Eilks, I., Rauch, F., Ralle, B. & Hofstein, A. "How to Allocate the Chemistry Curriculum Between Science and Society." *Teaching Chemistry- A Studybook: A Practical Guide and Textbook for Student Teachers, Teacher Trainees and Teachers.* Ed. Eilks, I. & Hofstein, A. Sense Publishers, 2013, 1-36.

10. Stuckey, M., Hofstein, A., Mamlok-Naaman, R. and Eilks, I. The meaning of 'relevance' in science education and its implication for the science curriculum. *Studies in Science Education*. **49**, 1-34 (2013).

11. Rabenau, H. F., Marianov, B., Wicker, S. & Allwinn, R. Comparison of the Neutralizing and ELISA Antibody Titres to Measles Virus in Human Sera and in Gamma Globulin Preparations. *Med. Microbiol. Immunol.* **196**, 151–155 (2007).

12. Miura, K. *et al.* Development and Characterization of a Standardized ELISA Including a Reference Serum on Each Plate to Detect Antibodies Induced by Experimental Malaria Vaccines. *Vaccine* **26**, 193–200 (2008).

13. Enzyme-Linked Immunosorbent Assay (ELISA) | Stanford Health Care. https://stanfordhealthcare.org/medical-conditions/sexual-and-reproductive-health/hiv-aids/diagnosis/elisa.html.

14. Veldsman, C. *et al.* QuantiFERON-TB GOLD ELISA assay for the Detection of *Mycobacterium tuberculosis* -Specific Antigens in Blood Specimens of HIV-Positive Patients in a High-Burden Country. *FEMS Immunol. Med. Microbiol.* **57**, 269–273 (2009).

15. Lupus Blood Tests : Johns Hopkins Lupus Center. https://www.hopkinslupus.org/lupus-tests/lupus-blood-tests/.

16. Freed, R. C., Evenson, M. L., Reiser, R. F. & Bergdoll, M. S. Enzyme-Linked Immunosorbent Assay for Detection of Staphylococcal Enterotoxins in Foods. *Appl. Environ. Microbiol.* **44**, 1349–1355 (1982).

17. Serology Testing for COVID-19 at CDC | CDC. https://www.cdc.gov/coronavirus/2019-ncov/lab/serology-testing.html.

18. Ewer, K. J. *et al.* T Cell and Antibody Responses Induced by a Single Dose of ChAdOx1 nCoV-19 (AZD1222) Vaccine in a Phase 1/2 Clinical Trial. *Nat. Med.* **27**, 270–278 (2020).

19. Rad-Bio. Biotechnology Explorer GMO. 1–84 (2012).

20. Zeng, W. *et al.* Characterization of SARS-CoV-2-Specific Antibodies in COVID-19 Patients Reveals Highly Potent Neutralizing IgA. *Signal Transduction and Targeted Therapy* vol. 6 1–3 (2021).

Chapter 7.
Conclusions and Future Directions

This chapter references research performed by Nicholas Glenn (heparin, PQ, perchlorate detection), Michaela Barber (hydrophilic coating of PDMS), Claire Cook (portable fluorescent light source development) and Nicolas Mesyinger (viscosity and refractive index determination) all students of Professor Ryan C. Bailey.

7.1 DISSERTATION SUMMARY

In this work, I have demonstrated the optimization of organic interfaces for enhanced selectivity and sensitivity in small molecule detection. In Chapter I, I discussed the advantages of using organic-aqueous interfaces in order to detect a variety of small molecules, including pollutants, metabolites and water (in the form of humidity). However, until this point, there have been few non-gaseous, multiplexable, point-of-analysis detection techniques across organic/aqueous interfaces. In Chapter II, I demonstrated how I expanded the use of organic-aqueous interfaces to liquid/solid interfaces by growing polymer brushes from the surface of silicon photonic microring resonators. I showed that the microring resonators were able to characterize a variety of interactions between polymer brushes and analytes, including comparative partition coefficients, diffusion coefficients and maximum partitioning thickness. Microring resonators were also able to characterize various aspects of the polymer brushes themselves, including pK_as for pH-sensitive polymer brushes and polymer brush thickness. However, the limitations of polymer brushes on microring resonators as an easily accessible

point of care technology pushed exploration of alternative technologies such as microfluidic droptodes.

In Chapter III, I expanded the utility of the droptode platform by demonstrating that the limit of detection and sensitivity of droptodes can be tuned simply by changing fluidic properties such as the flow rate and the size of the droplets. Thus, one droptode could be tuned to a variety of applications simply by using different syringe pump conditions. In Chapter IV, I demonstrated the ability to multiplex oil phases on droptodes, the first time that I am aware of that multiple oil phases have been continuously run on one device. Thus, I was able to perform multiplexed detection of various ions detected in blood panels, while minimizing reagent and sample waste. In Chapter V, I explored the potential for developing a microfluidic droptode for perfluoroalkyl chains (PFAS) and was able to detect PFAS at micromolar levels. I also discussed how I am testing novel fluorinated choromoionophores for future use in PFAS detection.

Finally, I performed education research in Chapter VI, where I discussed the development of a new lab experiment for an undergraduate bioanalytical class (CHEM 246). The goal of this lab was to better demonstrate relevance of analytical chemistry to everyday life, as well as to improve material's accessibility by making it more relevant to students' lives. The primary lab developed was an enzyme linked immunosorbent assay (ELISA) which was contextualized in terms of COVID-19 antibody detection. Work is ongoing to adapt this lab to a remote format, by creating an ELISA simulation in Labview.

While I have expanded the utility of organic interfaces for small molecule detection, there is still much work to be done. With a focus on droptode technology, due to its improved point of care characteristics compared to polymer brush coated microring resonators, I will discuss both

ideas for future work as well as preliminary results for some suggested droptode improvements below.

7.2 FUTURE WORK

7.2.1 Improving Droptodes Using Microfluidic Modifications

Optimizing the droptode interface for detection relies on both the improved transportation of reagents to the interface as well as interface stabilization. While transport to the surface can be enhanced by mixing, as discussed in Chapter III, lack of interfacial stability can lead to inconsistent droplet sizing, spacing or lack of selectivity. Traditionally in droplet microfluidic set-ups, interface stability is ensured by the use of surfactants, which stabilize the aqueous droplet in the carrier oil phase due to having both hydrophobic and hydrophilic ends. The use of surfactants in droplet microfluidics has allowed for droplets to be collected and reinjected into new devices,[1,2] be respaced on device,[2,3] and have solutions added, all while preserving the integrity of the droplet.[3]

Unfortunately, surfactants have been previously shown to be detrimental to detection limits on ion-selective electrodes, regardless of if the surfactants are ionic or non-ionic in nature.[4] Potentially, this might not apply to droptodes, as the impact of surfactants could be due to ISEs being an interface-sensitive technique, which is different than the bulk nature of droptodes. Additionally, mixing of both the oil and aqueous phase is promoted more in droptodes than in optodes, which may allow some compensation for interfacial transfer hinderance due to surfactants. Surfactants would allow us to perform more operations within droptodes, so the

extent of their impacts on droptodes' responses should be confirmed, starting with non-ionic surfactants like polyglyercol alky ethers.

If surfactants are able to be incorporated into droptodes, there is a whole new range of possibilities for droptode experimentation. For instance, expanding off of the work I performed in Chapter III, droplet size and spacing could actually be studied independently, by creating droplets of one size on one device and then respacing them differently on another device. This multiple device technique could also be a convenient way to multiplex samples by interfacing devices with different oil phases. While Chapter IV demonstrates the ability to multiplex on one device, the sample requirements for multiple device interfacing would be much lower, as the same droplet could be used for each measurement, being preferable for detection in highly precious samples.

Surfactants would also potentially allow for the development of techniques which promote temporary interface destabilization such as the use of electromagnetic fields. Electromagnetic stimulation is traditionally used to add reagents into the aqueous phase,[3] momentary electric fields temporarily break the droplet-oil interface allowing aqueous addition. The droplet reforms once the electromagnetic field is turned off. Electromagnetic stimulation could potentially be leveraged to improve droptodes' limits of detection, by making it easier for charged molecules to cross the aqueous-oil interface and interact with ionophores in the oil phase. The interface would then reform, potentially compensating for the lack of selective partitioning created during the electric pulse.

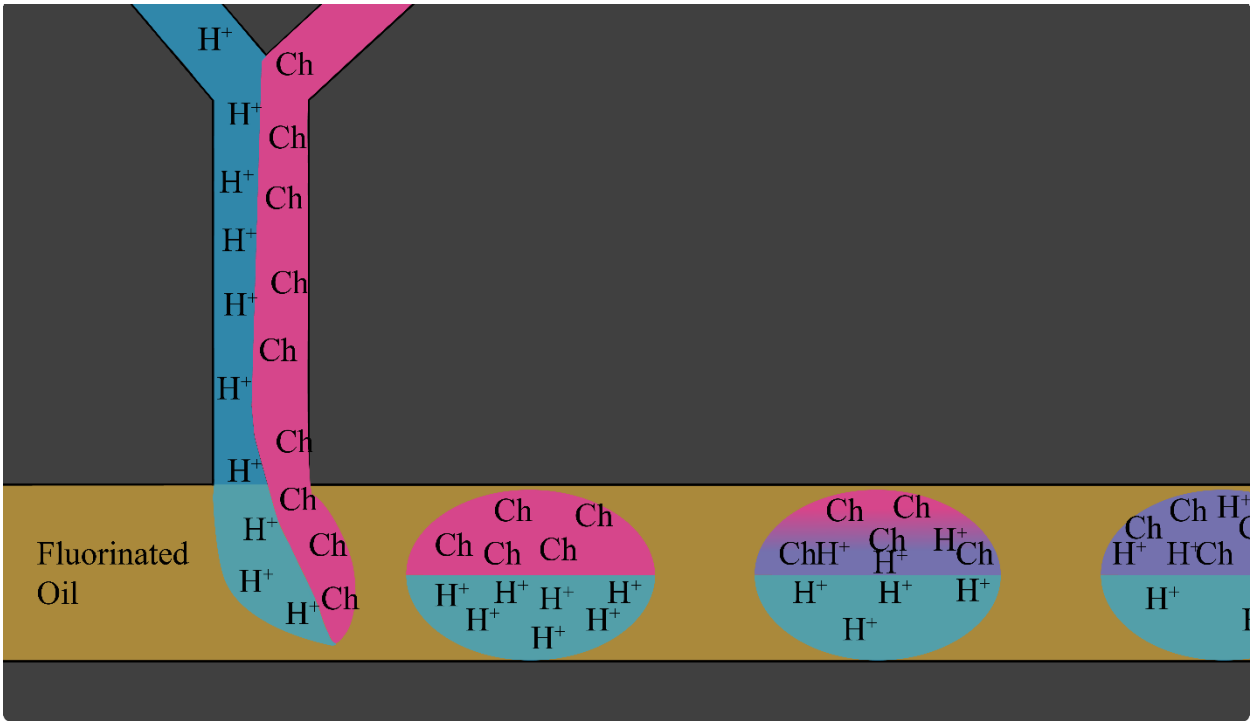

Figure 7.1. Microfluidic Janus Droptodes. The sample (blue) and sensing (pink) phase are combined into one droplet with a different carrier oil phase, allowing for better mixing. Image not drawn to scale.

Surfactants would also allow for the creation of Janus droplets (**Figure 7.1**). In a Janus droplet, the sample phase and sensing phase would be effectively combined into two faces of one droplet, suspend in an inert carrier phase, such as a fluorinated oil. Janus droplets previously have been used for controlled drug release, self-assembly and optical displays.[5] The potential benefits to Janus droptodes are two-fold: first, by placing both the sensing phase and sample phase into droplets, there is potentially better mixing within both phases, rather than the traditional improved mixing in only the sample phase. Additionally, by minimizing the volume of the sensing phase, background should be minimized as well, potentially allowing for lower limits of detection or better sensitivity. However, making Janus droplets is challenging due to the need to stabilize three flow fields. Additionally, imaging Janus droplets fluorescently may be

difficult depending upon the orientation of the droplets to the camera (i.e. seeing both oil and aqueous phases or only seeing aqueous or oil phase).

The final possibility for improving droptode detection limits that should be further explored is the use of the sensing phase in droplets with the sample phase as the carrier phase (**Figure 7.2**). The Bailey lab has successfully replicated coating PDMS with poly(vinyl alcohol) in order to make it hydrophilic.[6] Hydrophilic PDMS should cause the sample aqueous phase to behave as a carrier phase, allowing the oil sensing phase to be in droplets and experience the droplet mixing benefits. Additionally, oil droplets would maximize the surface area of oil phase in contact with the aqueous phase, potentially allowing for higher sensitivity and lower limits of detection.

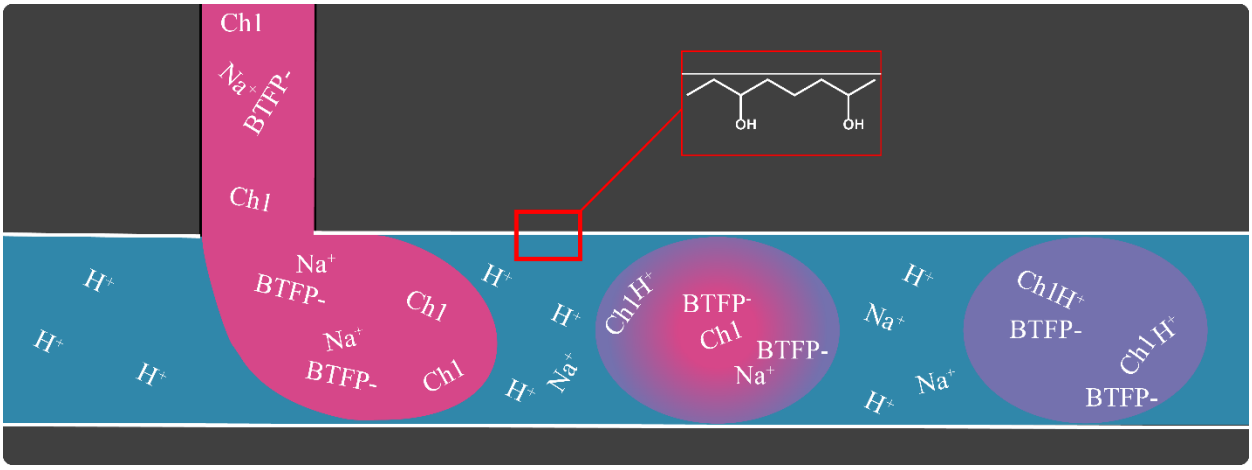

Figure 7.2.Use of hydrophilic coating to improve droptodes. Since the sensing phase will now be in the droplet, there is maximal interfacial interaction and mixing. Image not drawn to scale.

7.2.2 Expansion of Droptode Analytes

While my thesis has expanded the success of droptode detection to include divalent cations and anions, there are still many interesting analytes we can potentially detect. Work is ongoing in the Bailey lab towards detecting heparin, a standard polyvalent anion protein used in the blood coagulation cascade (*manuscript in progress*). There is currently interest in expanding this work to potentially performing separation based on number of charges in the molecule, effectively creating a polydispersity measurement. There is also research being done towards detecting various pollutants in local rivers, including perchlorate ions, industrial pollutants found in groundwater,[7,8] and polyquarternary ammonium salts (PQs) which come from cosmetic, water treatment and biomedical industries.[9–11]

Building off of the multiplexed droptode blood panel developed in Chapter IV, other blood panels could be developed. Specifically, the droptode provides an excellent model for a portable heavy metal ion panel, including metals such as copper, lead, aluminum and cadmium. Current heavy metal ion panel technologies rely on ICP/MS which requires a blood draw, thus

requiring a doctor's visit for testing. A droptode heavy metal ion panel thus could be a useful alternative, allowing more constant monitoring for heavy metal poisoning for people working with heavy metals at a variety of worksites or for miners who often work in remote locations. From a theoretical perspective, a heavy metal ion panel would also expand the droptode system to include both trivalent cations as well as ions which could have multiple charge states, which would be a new challenge.

While the variety of analytes to explore is exciting, the variety of detection matrices is also intriguing. The droptode technology is primed for working with small sample volumes, due to its use of microfluidics, as well as potentially more complex matrices due to its isolated sensing phase. Prior work has even shown the potential to perform detection in 50% diluted whole blood.[12] However, the droptode technology allows us to go a step further, potentially performing detection in neonatal blood, plasma or serum samples, which have to be small in order to allow maximal testing with minimal impact on the neonate.[13,14] Finally, detection should also be possible in organic matrices, as long as they are immiscible with the oil sensing phase, opening up many opportunities for droptode integration into industrial workflows as methods of detection for trace carcinogenic contaminants like perfluoroalkyl chains (PFAS) or bisphenol A (BPA), which can be leftover in products (from their use in earlier synthetic processes) and can leech out over time.

One of the challenges with exploring a variety of matrices, especially if switching over into organic matrices, is the material composition of the microfluidic devices. While PDMS is an excellent inert matrix for aqueous phases, in certain organic solvents such as methanol, PDMS will start to swell, disturbing the flow and channel dimensions, as well as potentially changing sample analyte concentrations. A common alternative to PDMS for droplet microfluidics, used

because of PDMS swelling, is thermoplastics.[15] Common thermoplastics include cyclic olefin copolymer (COC), poly(methyl methacrylate) (PMMA) and polycarbonate (PC), each of which have their own compatibility with various analytes and solvents, as well as surface chemistries which could be manipulated to promote mixing. However, as each of them is themselves an organic matrix, there is continued concern that even without swelling, small organic molecules will partition into the device matrix rather than the sensing phase. Thus, as the dimensions of the droptode device become optimized for each application, droptodes should move towards glass microfluidic devices, which should be inert to the majority of solvents, relatively air impermeable, as well as extremely reusable which would be ideal for low-resource settings.

7.2.3 Towards Miniaturization

One of the known benefits of droplet microfluidic technologies is its portability. The small footprint afforded by the microfluidic chip, with dimensions on the order of centimeters, as well as the ability to create pumps on device,[16–18] highlights the microfluidic point of care potential. Additionally, PDMS is low cost, allowing this technology to be used in low resource areas, which might not be able to afford a blood gas analyzer, or have electrical setups or training needed for instrumentation like ISEs.

While the current droptode set-up benefit from a small device size, it currently uses a high speed expensive camera for visualization, a large fluorescent lamp for excitation, and external syringe pumps to drive flow. I have done some preliminary work to improving the portability of the droptode system by switching our detection scheme from a high speed camera to a standard smartphone (**Figure 7.3**). Using flow rates on the order of 2 μL/min, we are able to see droplets both in brightfield (**Figure 7.3**) and fluorescent images (**Figure 7.3**) simply using

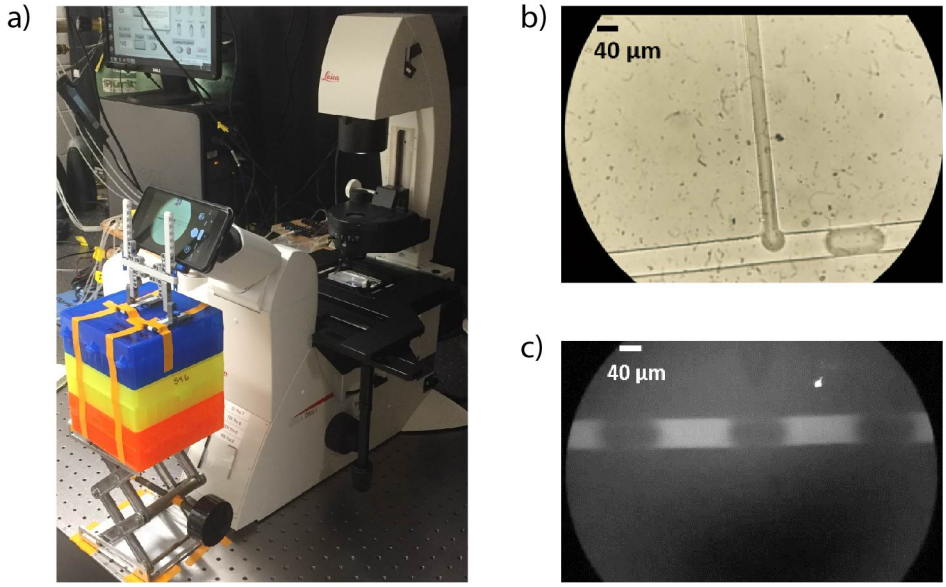

Figure 7.3. Using a smartphone for droptode measurements. (a) Set up of smartphone detection requiring only a microscope and a cell phone stand made from LEGOs. (b) Example of brightfield image taken by smartphone. (c) Example of fluorescent image taken by smartphone.

the microscope eyepiece, as well as perform a standard calibration (**Figure 7.4**). Work is

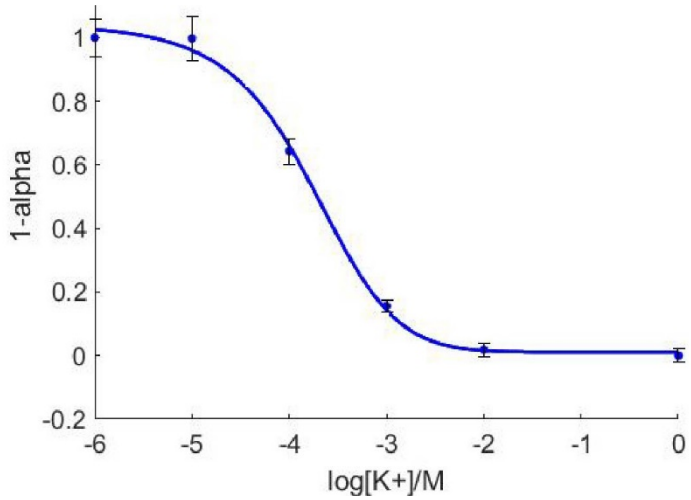

Figure 7.4 Sample calibration curve taken using a smartphone in place of a high-speed camera. Note that the limit of detection, sensitivity and goodness of fit rival that of the high-speed camera, demonstrating the potential for using a smartphone as a droptode camera.response will be measured at the location noted by the star.

ongoing in the Bailey lab to create a portable fluorescent light source, which would rely on light emitting diodes and filters to create the right wavelength of excitation light. The final aspect of portability to be addressed would be to create pumps on device that cause fluid flow at our

desired flow rates. Microfluidic pumps on chip have been created using a variety of principles including osmosis,[16] capillary flow[17] and piezoelectric pumping,[18] creating many areas of exploration for our lab to find a pump which suits our needs.

7.2.4 Assay Development

There are a variety of assays that we could consider developing using droptode technology. Many assays suffer from low selectivity of sensing phases or high limits of detection with low sample sizes, which is a prime technology gap for droptodes. For ease of reading, I have broken these down into four sub-categories of assays: optode optimization, protein concentration determination, bound ion concentration assays and biochemical assays.

7.2.4.1 Optode Optimization

A novel and exciting application of droptodes could be to improve optode optimization. Microfluidics allows for the quick mixing of reagents via the use of serpentine channels and juts in a design (Figure 5). Thus, I have designed a device, based off of a previous design used in our lab for optimizing nanodisc composition,[19] which would allow for the rapid testing of a variety of oil compositions over a short period of time. By varying the flow rates of each of the components of a droptode oil phase (i.e. chromoionophore, ionophore, ion-exchanger), each oil composition can be tuned to have the highest sensitivity at the estimated concentration of the sample of interest. With each novel oil composition, a full droptode experiment could be run with a fluorescent read-out, which would theoretically correspond to optode sensitivity.

As the chemistry is the same, just on a smaller time and volume scale, droptodes are expected to be a good stand-in for an optode. The optimal oil droptode composition and ratio of aqueous to organic phase should be equivalent to that of an optode. However, rather than making

10 different optodes with different percentages of ionophores, pre-conditioning them and then testing them, a process which could take 1-2 days and use copious reagents, the droptode device would be able to do similar testing in the matter of hours.

Preliminary results demonstrate that the device can modulate the composition of the oil phase, and that oil phase composition can be correlated to the droptode response (**Figure 7.5**). However, further characterization is needed to ensure that the mixing between all three components has come to completion, that the flow has returned to laminar flow before forming droplets and that there is high reproducibility. Additionally, it needs to be confirmed that the optimal oil phase suggested by the droptode gives the optimal response for optodes.

One of the big advantages of droptodes, that we have yet to fully take advantage of, is the difference between kinetic and thermodynamic measurements, as discussed in Chapter III. Droptodes do not require measurements at equilibrium in order to be reproducible, opening up not only potentially faster ways of detecting molecules of interest, but also possibly means of controlling selectivity based upon kinetic selection. This could come into play when looking at calcium ionophores, for example, which often have a strong cross-reactivity with magnesium due to the divalent nature and similar size of the two ions. While this cross-reactivity is true at equilibration, it is possible that before equilibration, calcium binds and partitions into the oil phase faster because of its smaller charge density. Thus, if calcium concentration was measured earlier on the device, kinetics could be used to ensure selectivity. What this also means is that one run on a device could measure multiple ions with the same less specific oil phase, a new form of multiplexing compared to that discussed in Chapter IV. Droptodes could be used to form an electronic tongue,[20–22] based upon changes in signal from a sample over time. Using kinetics could potentially allow for determination of common interferents like sodium while using a non-

sodium ionophore, measuring the interfering ion kinetically and the ion associated with the ionophore being measured thermodynamically at equilibrium.

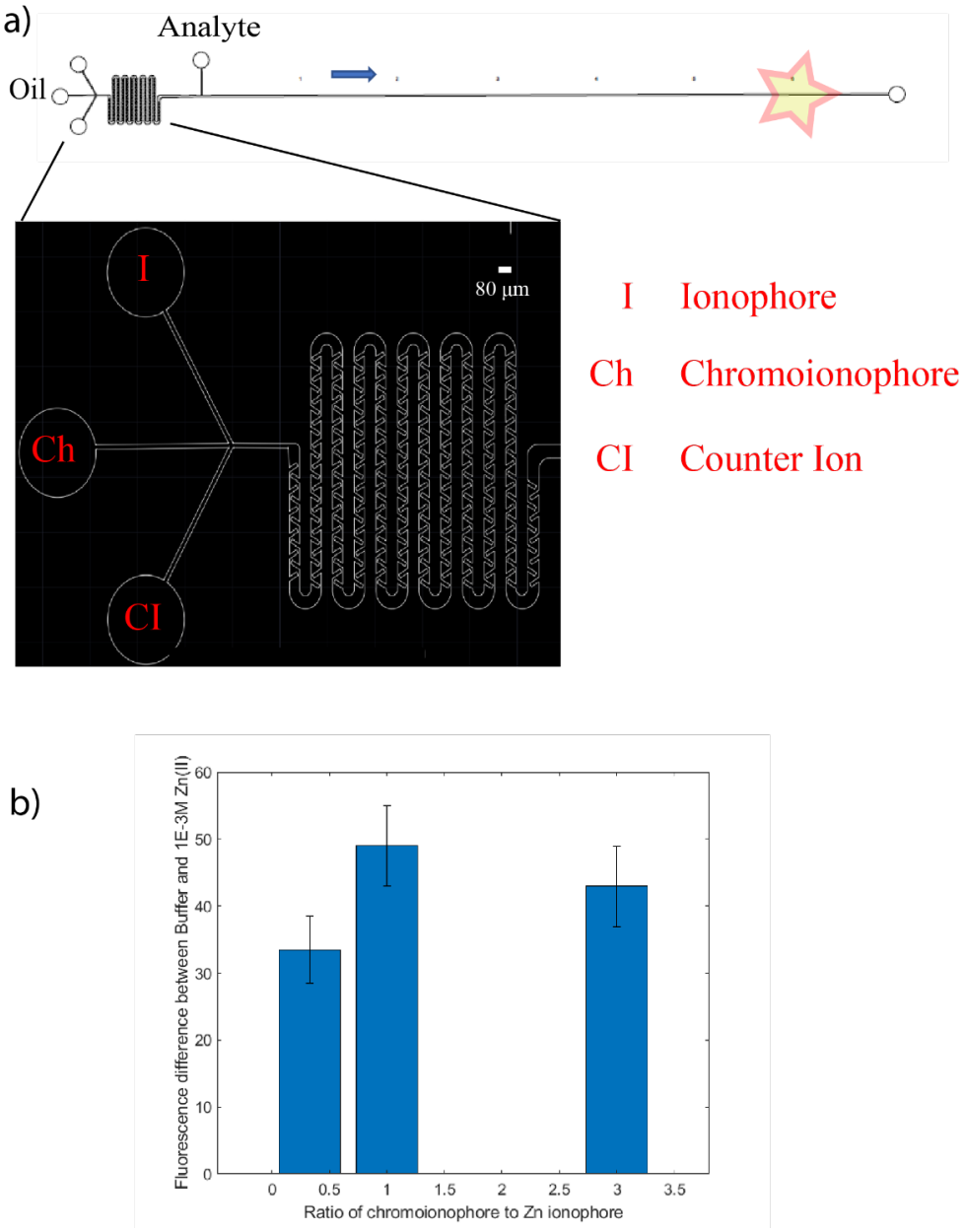

Figure 7.5 (a) Schematic in Autocad of the optode optimization microfluidic device design. Each component of the oil phase would be flowed at varying flow rates into its respective outlets, and then be mixed using the serpentine mixer. This mixed oil phase will then be used as the droptode oil phase as droplets form at the analyte junction and the droptode response will be measured at the location noted by the star. (b) Evidence of differing oil compositions on device modulating droptode response. By changing the ratio of two components the droptode responded differently to both the buffer and zinc concentration, and had variations in the differences between those responses, suggesting the utility of this device.

7.2.4.2 Biochemical

Droptodes potentially have utility in a biochemical space as well, both due to the small sampling volume and the ability of droplets to preserve cell viability.[28] Droptodes could be used to explore cell secretions, including hormones, proteins and antibodies. The ability of droplet microfluidics for single cell analysis also creates the possibility to explore cell heterogeneity within these assays, which would be particularly useful for cancer research.

A new possibility to explore with microfluidic droptodes is the use of enzymes in sample phases, which would allow the conversion of an analyte of interest into a small, charged molecule that droptodes could detect. The prime analyte for these examples would be proteins, as they are likely to misfold upon export into an oil phase. As a proof of concept, an assay to detect fibroblast growth factor receptor (FGFR) activity could be converted into droptode format. FGFR has been shown to be often mutated in cancers such as squamous non-small cell lung cancer.[29,30] The premise of this assay is that FGFR will phosphorylate a specific substrate by converting ATP to ADP. ADP will then undergo a reaction with a coupling phosphatase to produce AMP and an inorganic phosphate, which we should be able to detect using the droptode system. The benefit of doing this assay in droptodes rather than in bulk as performed currently is that the sensing phase in droptodes will be more isolated, so there is less need to worry about interferences from the complex biological matrix or any drugs used to test the FGFR response, potentially increasing sensitivity. Doing droptode assays could also allow for less volume of the sample protein to be used, allowing further concentration in the sample and increasing signal in the droptode.

Biochemical assays that could be performed in droptodes include cell death assays. Cell death assays, also known as cell viability assays, are generally used to determine effective

treatments for diseases such as cancer, where cell-to-cell variability is a prevalent issue. The basis for cell death assays is to give a drug to a cell and see if it dies. One of the most common cell viability assays is the lactase dehydrogenase assay. After cell death the membrane becomes more permeable, causing a release of lactase dehydrogenase into the surrounding cell media. This release is traditionally detected via the conversion of spiked lactate into pyruvate, electronically coupled by NADH to the formation of formazan, which has fluorescent properties, from a tetrazolium salt. This assay has a large number of potential analytes for droptode detection, potentially leading to improved sensitivity. While formazan is definitely a viable detection option, both lactate and pyruvate are charged organic molecules, so there is a potential for enhanced detection capabilities in organic sensing phases, without use of a tetrazolium salt. Using a droptode assay for cell death assays would have a two-fold purpose. First, enhancing detection capabilities down to smaller cell populations would be particularly important when performing analyses on rare cell populations, such as circulating tumor cells (CTCs). The limit of detection of the LDH technology is 1000 cells/mL, which translates to 50 cells/well of a 96 well plate. As the volume we would be using for each droplet is on the order of nanoliters, if the assay sensitivity is consistent we should be able to perform LDH detection on single cells. Thus, droptodes would open up the possibility to study cell-to-cell variation in drug response, which would be important for treating cancer.

7.2.5 Multiplexed Measurements

The compatibility of droptodes for both inline and concurrent measurements is also an advantage that cannot be ignored. Droptodes provide a quintessential separation technology, and thus could be coupled to a variety of different detection techniques in order to provide more

information about sensing and sample phase composition. Prior work by the Kennedy lab has demonstrated the ability to couple droplet microfluidics to mass spectrometry,[31] for which droptode techniques would provide a higher degree of selectivity for a molecule of interest. There also is a potential to couple droptodes to nuclear magnetic resonance imaging (NMR), as a way of understanding extraction efficiency of the sensing phase. By measuring analyte concentration in the aqueous phase via NMR, the process for optimizing oil phases could be greatly sped up. Studies are ongoing to determine a way of making a NMR on a chip, which would enhance the ability of droptodes further.[32] Finally, there is the potential to take advantage of capillary electrophoresis (CE) to improve droptodes, using electric fields to concentrate charged molecules of interest, rather than destabilize the interface. CE could improve the chance of binding of an ionophore to the analyte, or could separate out interfering ions using capillary zone electrophoresis with lateral flow charged based separation.[33] Droplet microfluidic work can also be combined with current work performed in the Bailey lab, focusing on detection of refractive index and viscosity changes based on droplet conditions changing a diffraction pattern. This is an ideal coupling to droptode technology because, as demonstrated in Chapter III, droptodes can work at a variety of shapes and sizes. Additionally, the diffraction pattern determination would be independent of the fluorescence measurement, potentially allowing the measurements to be taken concurrently.

7.2.6 Microfluidic Monitoring

The small volume, fast analysis speed and high selectivity of droptodes for molecules of interest make droptodes an ideal tool for microfluidic monitoring. Microfluidic monitoring not only provides the opportunity for automation and minimizing waste, but also could allow for

continuous monitoring using online detection systems. Continuous monitoring will allow for rapid feedback if something within a system has gone wrong while not requiring specialized staff.[34] Use of microfluidics for continuous monitoring has been used extensively for water quality monitoring[35] and monitoring of biochemical processes including enzyme reactions, molecule production and cellular sorting.[34] However, there are a variety of more industrial applications to which microfluidic monitoring, like seen in droptodes, could be applied.

For instance, during the distilling process, alcohol experts from a variety of different alcohol industries generally tap a distilling bottle and use about 1-5 mL every few days in order to determine amounts of important components of the alcohol like sugar or ethanol.[36] It would be ideal to have an automated measurement system which uses only μL of sample and is able to quickly quantify a variety of compounds of interest, including some which would be problematic to overall alcohol flavor or safety. Droptodes could provide that ability for detection through careful ionophore and enzymatic selection, potentially increasing the automatability of breweries.

Another microfluidic monitoring proof of concept is monitoring of shrimp tanks. The microbiome in a shrimp tank is extremely important to maintaining healthy shrimp. Generally, shrimp microbiomes are established by inoculating a new tank with a microbiome from a tank that has previously successfully grown shrimp. The importance of the environmental microbiome comes down to two different species of nitrifying bacteria: ammonia-oxidizing bacteria (AOB) and nitrite-oxidizing bacteria (NOB). Both species are crucial for the survival of a shrimp tank; ammonia, a natural byproduct of shrimp metabolism, is toxic to shrimp in high concentrations. In an ideal shrimp tank microbiome, ammonia from the shrimp is broken into nitrite by AOB, and the nitrite, also toxic at high levels, is then oxidized to nitrate by the NOB.

The nitrogen cycle provides multiple handles on this process, to determine the ratio of microbiome species, thus finding the optimal time for shrimp introduction into the tank (**Figure 7.6**). First, the shrimp tank water can be sampled and ammonia introduced on device (**Figure 7.6**). After an incubation period, if AOB is present, nitrite should be present, and if both NOB and AOB are present nitrate should be present (**Figure 7.6**). Thus, the ratio of AOB to NOB can be determined by quantifying the amount of ammonia left (**Figure 7.6**) (which would be inversely correlated to the amount of AOB) and either the amount of nitrite consumed or the amount of nitrate produced (**Figure 7.6**). Microfluidics would allow the quantitation to be done on the same chip in two spatially close channels in mere seconds, allowing real time observation of microbiome changes.

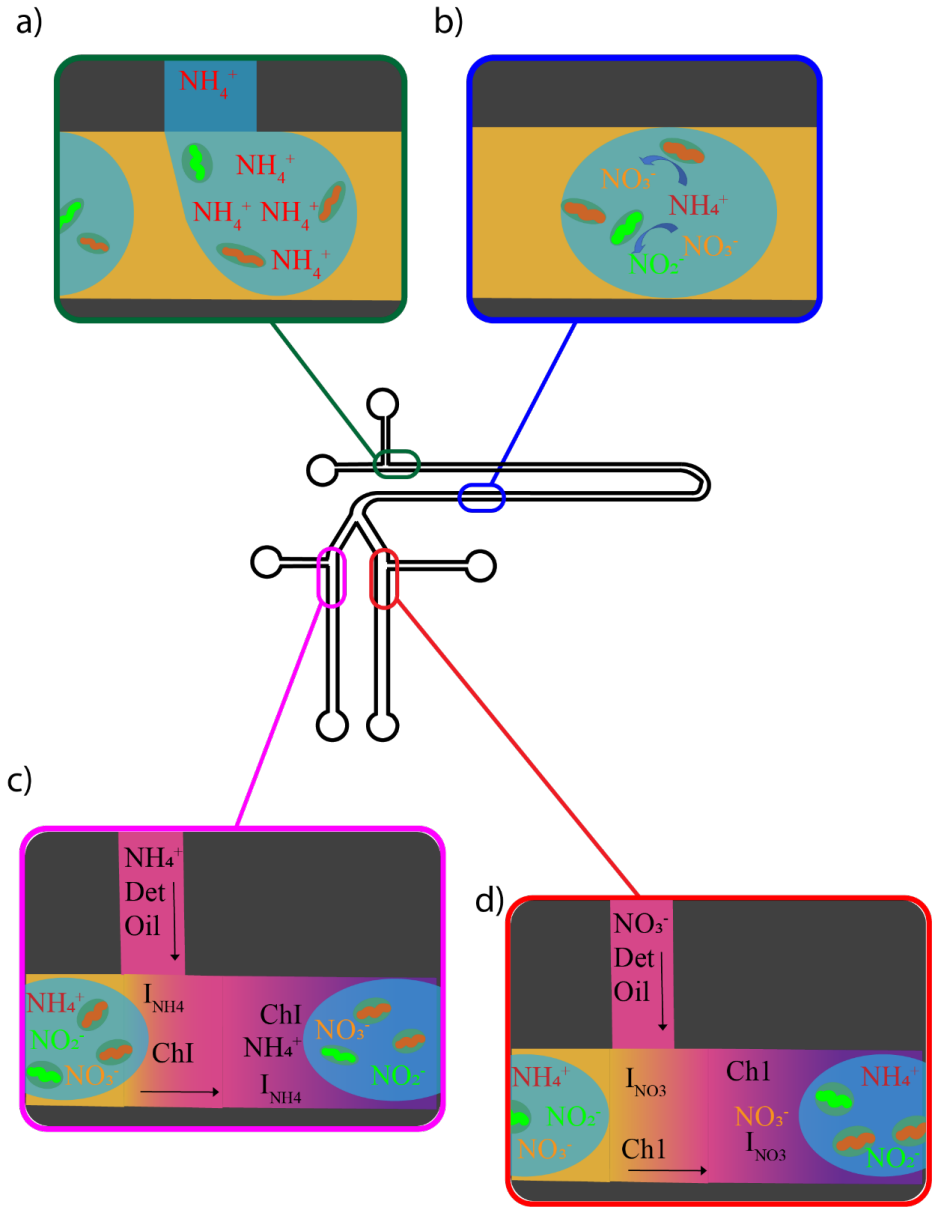

Figure 7.6. Microfluidic device for contiunous monitoring of shrimp envrionments. The schematic in the middle is the Autocad of the analysis device. (a) Samples are taken from the tank and spiked with NH_4+. The NH_4^+ is broken down into nitrate by the ammonia oxidizing bacteria (b, orange). The nitrite is then turned into nitrate by nitrite oxidizing bacteria. Both ammonia (c) and nitrate (d) can be measured in the sample to determine the ratio of bacterial species in the sample. Image not drawn to scale.

7.3 CONCLUDING REMARKS

In this thesis, I have contributed to the use of microfluidic organic phases to enhance small molecule detection. Using novel technologies such as silicon photonic microring resonators and droptodes, I have enhanced detection of a variety of pollutants and electrolytes, as well as optimizing platforms for further small molecule detection. Using microfluidic tools opens the gateway to real-time monitoring of various small molecules, both inside and outside the body, which could allow more personalized medicine, better pollution control and improved consumer safety. Droptodes, given their point-of-analysis nature as a detection platform, should be the focus of small molecule measurements moving forward (compared to microring resonators) and I am excited to see the continued work on droptodes and hopefully their development into a commercial technology with wide-ranging applications.

7.4 REFERENCES

1. Doonan, S. R., Lin, M., Lee, D., Lee, J. & Bailey, R. C. C3PE: Counter-Current Continuous Phase Extraction for Improved Precision of In-Droplet Chemical Reactions. *Microfluid. Nanofluidics* **24**, 1–11 (2020).

2. Xu, Y. *et al.* A Droplet Microfluidic Platform for Efficient Enzymatic Chromatin Digestion Enables Robust Determination of Nucleosome Positioning. *Lab Chip* **18**, 2583–2592 (2018).

3. Doonan, S. R. & Bailey, R. C. K-Channel: A Multifunctional Architecture for Dynamically Reconfigurable Sample Processing in Droplet Microfluidics. *Anal. Chem.* **89**, 4091–4099 (2017).

4. Malinowska, E. & Meyerhoff, M. E. Influence of Nonionic Surfactants on the Potentiometric Response of Ion-Selective Polymeric Membrane Electrodes Designed for Blood Electrolyte Measurements. *Anal. Chem.* **70**, 1477–1488 (1998).

5. Nisisako, T. Recent Advances in Microfluidic Production of Janus Droplets and Particles. *Curr. Opin. Colloid Interface Sci.* **25**, 1–12 (2016).

6. Trantidou, T., Elani, Y., Parsons, E. & Ces, O. Hydrophilic Surface Modification of PDMS for Droplet Microfluidics Using a Simple, Quick, and Robust Method Via PVA Deposition. *Microsystems Nanoeng.* **3**, (2017).

7. Todd, E. Perchlorate as an Environmental Contaminant. *Environ. Sci. Pollut. Res.* **9**, 187–192 (2002).

8. García, S., Albero, I., Ortuño, J. A., Sánchez-Pedreño, C. & Expósito, R. Flow-Through Bulk Optode for the Spectrophotometric Determination of Perchlorate. *Microchim. Acta* **143**, 59–63 (2003).

9. Ferguson, S. A. & Meyerhoff, M. E. Manual and Flow-Injection Detection/Quantification of Polyquaterniums via Fully Reversible Polyion-Sensitive Polymeric Membrane-Based Ion-Selective Electrodes. *ACS Sensors* **2**, 1505–1511 (2017).

10. Ferguson, S. A., Wang, X. & Meyerhoff, M. E. Detecting Levels of Polyquaternium-10 (PQ-10): Via Potentiometric Titration with Dextran Sulphate and Monitoring the Equivalence Point with a Polymeric Membrane-Based Polyion Sensor. *Anal. Methods* **8**, 5806–5811 (2016).

11. Ferguson, S. A., Wang, X., Mahoney, M. & Meyerhoff, M. E. Detection and quantification of polyquaterniums via polyion- sensitive ion-selective optodes inkjet printed on cellulose paper. *Anal. Sci.* **34**, 45–50 (2018).

12. Wang, X. *et al.* Ionophore-Based Biphasic Chemical Sensing in Droplet Microfluidics. *Angew. Chemie - Int. Ed.* **58**, 8092–8096 (2019).

13. WHO | Blood Sample Volumes in Child Health Research: Review of Safe Limits. *WHO* (2011).

14. Maximum Allowable Blood Draw From Infants - Seattle Children's Hospital. https://seattlechildrenslab.testcatalog.org/show/1000721-1.

15. Sahore, V., Doonan, S. R. & Bailey, R. C. Droplet Microfluidics in Thermoplastics: Device Fabrication, Droplet Generation, and Content Manipulation Using Integrated Electric and Magnetic Fields. *Anal. Methods* **10**, 4264–4274 (2018).

16. Xu, Z. R. *et al.* An Osmotic Micro-Pump Integrated on a Microfluidic Chip for Perfusion Cell Culture. *Talanta* **80**, 1088–1093 (2010).

17. Safavieh, R., Tamayol, A. & Juncker, D. Serpentine and leading-edge capillary pumps for microfluidic capillary systems. *Microfluid. Nanofluidics* **18**, 357–366 (2015).

18. Zhao, B. *et al.* A Controllable and Integrated Pump-enabled Microfluidic Chip and Its Application in Droplets Generating. *Sci. Rep.* **7**, 1–8 (2017).

19. Wade, J. H. *et al.* Microfluidic Platform for Efficient Nanodisc Assembly, Membrane Protein Incorporation, and Purification. *Lab Chip* **17**, 2951–2959 (2017).

20. Cetó, X., González-Calabuig, A., Capdevila, J., Puig-Pujol, A. & Del Valle, M. Instrumental Measurement of Wine Sensory Descriptors Using a Voltammetric Electronic Tongue. *Sensors Actuators, B Chem.* **207**, 1053–1059 (2015).

21. Chikukwa, M. T. R. *et al.* Assessment of Taste Masking of Captopril by Ion-Exchange Resins Using Electronic Gustatory System. *Pharm. Dev. Technol.* **25**, 281–289 (2020).

22. Heras, J. Y., Pallarola, D. & Battaglini, F. Electronic Tongue for Simultaneous Detection of Endotoxins and Other Contaminants of Microbiological Origin. *Biosens. Bioelectron.* **25**, 2470–2476 (2010).

23. Payne, R. B., Carver, M. E. & Morgan, D. B. Interpretation of Serum Total Calcium: Effects of Adjustment of Albumin Concentration on Frequency of Abnormal Values and on Detection of Change in the Individual. *J. Clin. Pathol.* **32**, 56–60 (1979).

24. Morton, A. R., Garland, J. S. & Holden, R. M. Is the Calcium Correct? Measuring Serum Calcium in Dialysis Patients. *Semin. Dial.* **23**, 283–289 (2010).

25. Ladenson, J. H., Lewis, J. W. & Boyd, J. C. Failure of Total Calcium Corrected for Protein, Albumin, and pH to Correctly Assess Free Calcium Status. *J. Clin. Endocrinol. Metab.* **46**, 986–993 (1978).

26. Hou, S. H. *et al.* Calcium and Phosphorus Fluxes During Hemodialysis With Low Calcium Dialysate. *Am. J. Kidney Dis.* **18**, 217–224 (1991).

27. Link, A. *et al.* Total-to-Ionized Calcium Ratio Predicts Mortality in Continuous Renal Replacement Therapy with Citrate Anticoagulation in Critically Ill Patients. *Crit. Care* **16**, R97 (2012).

28. Matuła, K., Rivello, F. & Huck, W. T. S. Single-Cell Analysis Using Droplet Microfluidics. *Adv. Biosyst.* **4**, (2020).

29. Krook, M. A. *et al.* Fibroblast Growth Factor Receptors in Cancer: Genetic Alterations, Diagnostics, Therapeutic Targets and Mechanisms of Resistance. *British Journal of Cancer* **124**, 880–892 (2020).

30. Hallinan, N. *et al.* Targeting the Fibroblast Growth factor receptor family in cancer. *Cancer Treatment Reviews* **46**, 51–62 (2016).

31. Holland-Moritz, D. A. *et al.* Mass Activated Droplet Sorting (MADS) Enables High-Throughput Screening of Enzymatic Reactions at Nanoliter Scale. *Angew. Chemie - Int. Ed.* **59**, 4470–4477 (2020).

32. Davoodi, H. *et al.* An NMR-Compatible Microfluidic Platform Enabling *in situ* Electrochemistry . *Lab Chip* **20**, 3202 (2020).

33. Cheng, L. J. & Chang, H. C. Switchable pH Actuators and 3D Integrated Salt Bridges as New Strategies for Reconfigurable Microfluidic Free-Flow Electrophoretic Separation. *Lab Chip* **14**, 979–987 (2014).

34. Karle, M., Vashist, S. K., Zengerle, R. & von Stetten, F. Microfluidic Solutions Enabling Continuous Processing and Monitoring of Biological Samples: A Review. *Anal. Chim. Acta* **929**, 1–22 (2016).

35. Jaywant, S. A. & Mahmood Arif, K. A Comprehensive Review of Microfluidic Water Quality Monitoring Sensors. *Sensors (Switzerland)* **19**, (2019).

36. Quality Control in the Brewery. https://www.probrewer.com/library/archives/quality-control-in-the-brewery/.

Appendices

Appendix A

Code For Analysis of Microring Resonator Data

Working Up Raw Ring Data

Included below is the code developed to analyze the microring resonators data. The initial code was developed by Dr James Wade (University of Michigan) and can be run using R (Code 1).

```
GetName <- function(){
  # get the filename from the current working directory
  directory <- basename(getwd())
  # directory naming from MRR: "CHIPNAME_gaskGASETTYPE_DATE"
  # extracts and returns GASKETTYPE from directory name
  name <- unlist(strsplit(directory, split = "_"))
  name <- name[2]
  # define name as global variable for use in other functions
  name <<- gsub('gask','',name) # removes "gask" from name
}
AggData <- function(loc = 'plots') {
  # load relevant libraries
  library(readr)
  # get working directory to reset at end of function
  directory <- getwd()
  # change this file name to use alternative ring or group labels
  filename <- "groupNames_allClusters.csv"
  # get information of chip layout from github repository
  if (!file.exists("groupNames_allClusters.csv")){
    url <- "https://raw.githubusercontent.com/jwade1221/XenograftProteinProfiling/master/groupNames_allClusters.csv"
    filename <- basename(url)
    download.file(url, filename)
  }
  # define recipe as global variable for use in other functions
  recipe <<- read_csv(filename, col_types = cols())
  targets <- recipe$Target
  # generate list of rings to analyze (gets all *.csv files)
  rings <- list.files(directory, pattern = ".csv", recursive = FALSE)
  idfile <- grepl("group", rings)
  removeFiles <- c("comments.csv", rings[idfile])
  rings <- rings[!rings %in% removeFiles]
  # create empty data frame to store data
  df <- data.frame()
```

```
  # add data to data frame corresponding for each ring in rings
  for (i in rings) {
    ring <- as.vector(i)
    dat <- read_csv(ring, col_types = cols(), col_names = FALSE)
    time_shift <- dat[ ,1]
    shift <- dat[ ,2]
    ringStr <- strsplit(i, "\\.")[[1]]
    ringNum <- as.numeric(ringStr[1])
    recipe.col <- which(recipe$Ring == ringNum)
    groupNum <- recipe$Group[recipe.col]
    ring <- rep(ringNum, nrow(dat))
    group <- rep(groupNum, nrow(dat))
    groupName <- as.character(recipe$Target[[recipe.col]])
    groupName <- rep(groupName, nrow(dat))
    channel <- recipe$Channel[[recipe.col]]
    channel <- rep(channel, nrow(dat))
    run <- rep(name, nrow(dat))
    time_point <- seq(1:nrow(dat))
    tmp <- data.frame(ring, group, time_shift, shift, groupName,
                      channel, run, time_point)
    df <- rbind(df, tmp)
  }
  # renames columns in df
  names(df) <- c("Ring", "Group", "Time", "Shift", "Target", "Channel",
                 "Experiment", "Time Point")
  # creates "plots" directory if one does not exist
  if (!file.exists(loc)){dir.create(loc)}
  # saves aggregated data with name_allRings.csv
  write_csv(df, paste(loc, '/', name, "_allRings.csv", sep=""))
  # returns working directory to top level
  setwd(directory)
}
SubtractControl <- function(loc = 'plots', ch, cntl){
  #load relevant libraries
  library(readr)
  library(dplyr)
  # get working directory to reset at end of function
  directory = getwd()
  # get ring data and filter by channel
  dat <- read_csv(paste0(loc, "/", name, "_", "allRings.csv"))
  if (ch != "U"){
    dat <- filter(dat, Channel == ch)
  }
  dat <- filter(dat, Target != "Ignore")
  # get thermal control averages
  controls <- filter(dat, Target == cntl)
  ringList <- unique(controls$Ring)
  # gets times from first thermal control
  times <- filter(controls, Ring == ringList[1]) %>% select(Time)
  df.controls <- data.frame(times)
  # create dataframe with all controls
  for (i in ringList){
    ringShift <- filter(controls, Ring == i) %>% select(Shift)
    names(ringShift) <- paste('Ring', i, sep='')
    df.controls <- cbind(df.controls, ringShift)
  }
  # averages thermal controls
  cols <- ncol(df.controls)
  if (length(unique(controls$Ring)) != 1) {
    df.controls$avgControls <- rowMeans(df.controls[,c(2:cols)])
```

```
  } else {
    df.controls$avgControls <- df.controls[,c(2:cols)]
  }
  avgControls <- as.vector(df.controls$avgControls)
  #subtracts thermal controls from each ring
  ringNames <- unique(dat$Ring)
  for(i in ringNames){
    ringDat <- filter(dat, Ring == i) %>% select(Shift)
    ringTC <- ringDat - avgControls
    dat[dat$Ring == i, 4] <- ringTC
  }
  write_csv(dat, paste(loc,"/", name, "_", cntl, "Control", "_ch", ch,
                       ".csv", sep = ''))
}
PlotRingData <- function(cntl, ch, loc = 'plots'){
  # loads relevant libraries
  library(ggplot2)
  library(readr)
  library(RColorBrewer)
  # get working directory to reset at end of function
  directory <- getwd()
  # use thermally controlled data if desired
  if (cntl != "raw"){
    dat <- read_csv(paste(loc, "/", name, "_", cntl, "Control",
                          "_ch", ch,".csv", sep=''), col_types = cols())
  } else if (cntl == "raw") {
    dat <- read_csv(paste(loc, "/", name, "_allRings.csv", sep=''),
                    col_types = cols())
  }
  #set colors for plot
  colorCount <- length(unique(dat$Target))
  getPalette <- colorRampPalette(brewer.pal(8, "Paired"))(colorCount)
  #configure plot and legend
  plots1 <-ggplot(dat, aes(Time, Shift, colour = Target)) +
    xlab("Time (min)") +
    ylab(expression(paste("Relative Shift (",Delta,"pm)"))) +
    scale_colour_manual(values = getPalette, name = 'Target') +
    theme_bw() + theme(panel.grid = element_blank(),
                       axis.title.x=element_blank()) +
    theme(legend.key = element_rect(colour = 'white',
    fill = 'white'), legend.key.size = unit(0.4, "cm")) +
    geom_vline(xintercept = c(5, 10), linetype = "longdash")
  plots <- ggplot(dat, aes(Time, Shift, colour = 'red')) +
    xlab("Time (min)") +
    ylab(expression(paste("Relative Shift (",Delta,"pm)"))) +
    #scale_colour_manual(values = getPalette, name = 'Target') +
    #theme_bw() + theme(panel.grid = element_blank(),
     #                  axis.title.x=element_blank()) +
    #theme(legend.key = element_rect(colour = 'white',
                                    #fill = 'white'), legend.key.size = unit(0.4, "cm")) +
    geom_vline(xintercept = c(5, 10), linetype = "longdash")
  if (cntl == "raw"){
    plots <- plots + geom_point(size = 1) + facet_grid(.~ Channel)#+xlim(94,105)
    plots1 <- plots1 + geom_point(size = 1) + facet_grid(.~ Channel)#+xlim(94,105)
  } else {plots <- plots + geom_point(size = 1)
  plots1 <- plots1 + geom_point(size = 1)}
  #plot figure, uncomment to plot
  #plots
  # alternative plot
  dat.2 <- dat %>% group_by("_ch", `Time Point`) %>% summarise_each(funs(mean, sd), c(Time, Shift))
```

```
 head(dat.2)
 g <- ggplot(dat.2, aes(Time_mean, Shift_mean, color = "red"))
 plot2 <- g + geom_line(size = 1) +
  geom_ribbon(aes(ymin = Shift_mean - Shift_sd,
                  ymax = Shift_mean + Shift_sd, linetype = NA),
              fill = "slategrey", alpha = 1/3) +
  theme_bw() + theme(panel.grid = element_blank()) +
  theme(legend.key = element_rect(colour = 'white', fill = 'white'),
        legend.key.size = unit(0.4, "cm")) +
  xlab("Time (min)") +
  ylab(expression(paste("Relative Shift (",Delta,"pm)")))
 #save plot, uncomment to save
 filename <- paste0(name, "_", cntl, "Control", "_ch", ch)
 filename2 <- paste0(name, "_", cntl, "Control", "_ch", ch, "_avg")
 setwd(loc)
 ggsave(plots, file = paste0(filename, ".png"), width = 8, height = 6)
 #ggsave(plots, file = paste0(filename, ".pdf"), width = 8, height = 6)
 ggsave(plots1, file = paste0(filename, ".png"), width = 8, height = 6)
 #ggsave(plots1, file = paste0(filename, ".pdf"), width = 8, height = 6)
 ggsave(plot2, file = paste0(filename2, ".png"), width = 8, height = 6)
 #ggsave(plot2, file = paste0(filename2, ".pdf"), width = 8, height = 6)
 setwd(directory)
}
GetNetShifts <- function(cntl, ch, loc = 'plots', time1, time2, step = 1){
 # load relevant libraries
 library(readr)
 library(dplyr)
 # get working directory to reset at end of function
 directory <- getwd()
 # use thermally controlled data if desired
 if (cntl != "raw"){
  dat <- read_csv(paste(loc, "/", name, "_", cntl, "Control",
                        "_ch", ch, ".csv", sep=""), col_types = cols())
 } else {
  dat <- read_csv(paste(loc, "/", name, "_", "allRings.csv",
                        sep=''), col_types = cols())
 }
 # generate list of rings and empty dataframe to store net shift data
 ringList <- unique(dat$Ring)
 dat.rings <- data.frame()
 # locations for each time is determined using which, min, and abs func
 for (i in ringList){
  dat.ring <- filter(dat, Ring == i)
  time1.loc <- which.min(abs(dat.ring$Time - time1))
  time1.val <- dat.ring$Shift[time1.loc]
  time2.loc <- which.min(abs(dat.ring$Time - time2))
  time2.val <- dat.ring$Shift[time2.loc]
  time.diff <-time1.loc-time2.loc
  ring <- i
  group <- unique(dat.ring$Group)
  target <- unique(dat.ring$Target)
  experiment <- unique(dat.ring$Experiment)
  channel <- unique(dat.ring$Channel)
  tmp <- data.frame(i, group, target, time1.val, time2.val,
                    experiment, channel, step)
  dat.rings <- rbind(dat.rings, tmp)
 }
 # renames dat.rings columns
 names(dat.rings) <- c("Ring", "Group", "Target", "Shift.1", "Shift.2",
                       "Experiment", "Channel", "Step")
```

```
  # calculate nat shift and create new column in dataframe
  dat.rings$`Net Shift` <- dat.rings$Shift.1 - dat.rings$Shift.2
  dat.rings$`Slope` <- dat.rings$`Net Shift`/time.diff
  # save net shift data
  setwd(loc)
  write_csv(dat.rings, paste0(name, "_netShifts_ch", ch, "step_", step, ".csv"))
  setwd(directory)
}
PlotNetShifts <- function(cntl, ch, loc = 'plots', step = 1){
  # load relevant libraries
  library(ggplot2)
  library(readr)
  library(dplyr)
  # get working directory to reset at end of function
  directory <- getwd()
  # get net shift data
  if (cntl != "raw"){
    dat <- read_csv(paste0(loc, "/", name, "_netShifts_ch", ch, "step_", step,
                           ".csv"), col_types = cols())
  } else {
    dat <- read_csv(paste(loc,"/", name, "_netShifts_chU.csv",
                          sep=""), col_types = cols())
  }
  # configure plot and legend
  dat.nothermal <- filter(dat, Target != "thermal")
  plots <- ggplot(dat.nothermal, aes(Target, `Net Shift`, color = Target)) +
    geom_boxplot() +ylim(-100,1000)+
    ylab(expression(paste("Net Shift ( ", Delta,"pm)"))) +
    theme_bw() + theme(panel.grid = element_blank(),
                       axis.title.x=element_blank()) +
    theme(axis.text.x = element_text(angle = 45, hjust = 1)) +
    theme(legend.key = element_rect(colour = 'white',
                                    fill = 'white'), legend.key.size = unit(0.3, "cm"))
  allRings <- ggplot(dat.nothermal, aes(factor(Ring), `Net Shift`, fill = Target)) +
    geom_bar(stat = "identity")+ylim(-100,1000)
  # save plot, uncomment to save
  filename <- paste0(name, "_NetShift_ch", ch, "_step", step, ".png", sep="")
  filename2 <- paste0("IndyRings_", filename)
  setwd(loc)
  ggsave(plots, file = filename, width = 10, height = 6)
  ggsave(allRings, file = filename2, width = 21, height = 9)
  setwd(directory)
}
AnalyzeData <- function() {
  GetName()
  AggData()
  SubtractControl(ch = 1, cntl = "thermal")
  SubtractControl(ch = 2, cntl = "thermal")
  SubtractControl(ch = "U", cntl = "thermal")
  PlotRingData(cntl = "thermal", ch = 1)
  PlotRingData(cntl = "thermal", ch = 2)
  PlotRingData(cntl = "thermal", ch = "U")
  PlotRingData(cntl = "raw", ch = "U")
   #GetNetShifts(cntl = "thermal", ch = 1, time1 = 23, time2 = 5, step = 1)
  #GetNetShifts(cntl = "thermal", ch = 1, time1 = 55, time2 = 38, step = 2)
}
```

The following codes for fitting were developed by me and run in R to fit the data to various curves.

Linear Fit:

```
nlsfit <- function() {
  library(dplyr)
  library(ggplot2)
  library(readr)
  # create dataframe for nls function to read from (have as tidy data only)
  dat <- read.csv(file="pdmaema_pH3_cal.csv", header=TRUE)
  # Cautionary thing, but read dat to ensure you have the correct columns and data
  head(dat)
  start1 = min(dat$Thickness)
  startAverage = min(dat$Average)
  datAdjusted <- mutate(dat, Average = Average- startAverage)
  print(datAdjusted)
  # Set paraeter start (these are examples)
  A_start <- (max(datAdjusted$Average)-min(datAdjusted$Average))/(max(dat$Thickness)-start1)
  D_start <- min(datAdjusted$Average)

  #print(A_start)
  #print(B_start)

  limits <-aes(ymax = datAdjusted$Average + datAdjusted$Error,
               ymin = datAdjusted$Average - datAdjusted$Error)
  hlimits <-aes(xmax = datAdjusted$Thickness + datAdjusted$Xerror,
                xmin = datAdjusted$Thickness - datAdjusted$Xerror)
  # Fit plot
  fitplot1 <- ggplot2::ggplot(datAdjusted,
                              ggplot2::aes(x = Thickness,
                                           y = Average)) +
    ggplot2::labs(x = "Dry Brush Thickness (nm)",
                  y = expression(paste("Relative Shift (",Delta,"pm)")),
                  color = "Target") +
    ggplot2::geom_point(size = 1) + ggplot2::geom_errorbar(limits)+ ggplot2::geom_errorbarh(hlimits)+
    theme_bw() + theme(panel.border = element_blank(), panel.grid.major = element_blank(),
                       panel.grid.minor = element_blank(), axis.line = element_line(colour = "black"),
axis.text=element_text(size=16, colour = "black"), text = element_text(size=18, colour = "black"))+
    ggplot2::geom_smooth(method = "nls",
                         # Insert formula for logistic regression here
                         formula = y ~ A*x+D,
                         size = 1,
                         method.args = list(algorithm = "port", start = list(A=A_start, D=D_start), lower = list(-5000,-5000), upper =
list(5000, 5000), nls.control(maxiter = 100000,tol = 1e-02, minFactor = 1e-08)),
                         se = FALSE)
  print(fitplot1)
  ggsave(fitplot1, file = paste0("pdmaema_pH3_cal.png"), width = 8, height = 6)
  # Get fit from plot
  fitoutput <- nls(Average ~ A*Thickness+D, datAdjusted, algorithm = "port", start =list(A=A_start,D=D_start),lower = list(-
5000,-5000), upper = list(5000, 5000), nls.control(maxiter = 10000,tol = 1e-02,minFactor = 1e-08))
  fitsum <- summary(fitoutput)
  # Create txt file
  capture.output(fitsum,file = "fitInfo_pdmaema_pH3_cal")
}
```

Logistic Fit

```
nlsfit <- function() {
  library(dplyr)
  library(ggplot2)
  library(readr)
  # create dataframe for nls function to read from (have as tidy data only)
  dat <- read.csv(file="pdmaema_7F_closeup_pH9.csv", header=TRUE)
  # Cautionary thing, but read dat to ensure you have the correct columns and data
  head(dat)
  start1 = min(dat$Base_pH)
  startShift = min(dat$Shift)
  datAdjusted <- mutate(dat, Base_pH = Base_pH - start1, Shift = Shift- startShift)
  print(datAdjusted)
  # Set paraeter start (these are examples)
  A_start <- 250
  B <- 1
  C_start <- 2
  D_start <- 4

  limits <-aes(ymax = datAdjusted$Shift + datAdjusted$Std_devy,
               ymin = datAdjusted$Shift - datAdjusted$Std_devy)
  datAdjusted$`Xerror` <-0.01
  hlimits <-aes(xmax = datAdjusted$Base_pH + datAdjusted$Xerror,
                xmin = datAdjusted$Base_pH - datAdjusted$Xerror)
  # Fit plot
  fitplot1 <- ggplot2::ggplot(datAdjusted,
                              ggplot2::aes(x = Base_pH,
                                           y = Shift)) +
    ggplot2::labs(x = "pH",
                  y = expression(paste("Contact Angle (",Delta,"degrees)")),
                  color = "Target") +
    ggplot2::geom_point(size = 1) + ggplot2::geom_errorbar(limits)+ ggplot2::geom_errorbarh(hlimits)+
    theme_bw() + theme(panel.border = element_blank(), panel.grid.major = element_blank(),
                       panel.grid.minor = element_blank(), axis.line = element_line(colour = "black"))+
    ggplot2::geom_smooth(method = "nls",
                         # Insert formula for logistic regression here
                         formula = y ~ A /(B+C*exp(-D*x)),
                         size = 1,
                         method.args = list(start = list(A=A_start, C=C_start,D=D_start), nls.control(maxiter = 1000,tol = 1e-02,
minFactor = 1e-08)),
                         se = FALSE)
  print(fitplot1)
  ggsave(fitplot1, file = paste0("pdmaema_7F_closeup_pH9.png"), width = 8, height = 6)
  # Get fit from plot
  fitoutput <- nls(Shift ~ A /(B+C*exp(-D*Base_pH)), datAdjusted, start =list(A=A_start, C=C_start,D=D_start),
nls.control(maxiter = 10000,tol = 1e-02,minFactor = 1e-08))
  print(fitoutput)
  # Create txt file
  capture.output(fitoutput,file = "fitInfo_pdmaema_7F_closeup")
}
```

Exponential Fits

```
nlsfit <- function() {
  library(dplyr)
  library(ggplot2)
  library(readr)
  # create dataframe for nls function to read from (have as tidy data only)
  dat <- read.csv(file="pdmaema_pH8_cal.csv", header=TRUE)
  # Cautionary thing, but read dat to ensure you have the correct columns and data
  head(dat)
  start1 = min(dat$Thickness)
  startAverage = min(dat$Average)
  datAdjusted <- mutate(dat, Average = Average- startAverage)
  print(datAdjusted)
  # Set paraeter start (these are examples)
  A_start <- max(datAdjusted$Average)
  B_start <- -0.02
  C_start <- min(datAdjusted$Average)

  #print(A_start)
  #print(B_start)

  limits <-aes(ymax = datAdjusted$Average + datAdjusted$Error,
               ymin = datAdjusted$Average - datAdjusted$Error)
  hlimits <-aes(xmax = datAdjusted$Thickness + datAdjusted$Xerror,
                xmin = datAdjusted$Thickness - datAdjusted$Xerror)
  # Fit plot
  fitplot1 <- ggplot2::ggplot(datAdjusted,
                              ggplot2::aes(x = Thickness,
                                           y = Average)) +
    ggplot2::labs(x = "Dry Brush Thickness (nm)",
                  y = expression(paste("Relative Shift (",Delta,"pm)")),
                  color = "Target") +
    ggplot2::geom_point(size = 1) + ggplot2::geom_errorbar(limits)+ ggplot2::geom_errorbarh(hlimits)+
    theme_bw() + theme(panel.border = element_blank(), panel.grid.major = element_blank(),
                       panel.grid.minor = element_blank(), axis.line = element_line(colour = "black"),
axis.text=element_text(size=16, colour = "black"), text = element_text(size=18, colour = "black"))+
    ggplot2::geom_smooth(method = "nls",
                         # Insert formula for logistic regression here
                         formula = y ~ A*exp(B*x)+C,
                         size = 1,
                         method.args = list(algorithm = "port", start = list(A=A_start, B=B_start, C=C_start), lower = list(-500,-500,-10),
upper = list(5000, 500, 10), nls.control(maxiter = 100000,tol = 1e-02, minFactor = 1e-08)),
                         se = FALSE)
  print(fitplot1)
  ggsave(fitplot1, file = paste0("pdmaema_pH8_cal.png"), width = 8, height = 6)
  # Get fit from plot
  fitoutput <- nls(Average ~ A*exp(B*Thickness)+C, datAdjusted, algorithm = "port", start =list(A=A_start,B=B_start,
C=C_start),lower = list(-500,-500,-10), upper = list(5000, 500, 10), nls.control(maxiter = 10000,tol = 1e-02,minFactor = 1e-08))
  fitsum <- summary(fitoutput)
  # Create txt file
  capture.output(fitsum,file = "fitInfo_pdmaema_pH8_cal
```

Appendix B

Process for ImageJ Analysis for Microfluidic Droptodes

This protocol was developed with help from Dr. Steven Doonan (Washington University), Nicolas Mesyinger (University of Michigan) and Nicholas Glenn (University of Michigan).

Combining Images Into One File

This code combines all of the individual videos into one file, so all contrast changes can be applied evenly. This code runs in ImageJ (NIH) using AVI images. The AVI images must all be in one folder. The code produces 1 .tiff image with the same number of columns as number of samples being measured and the same number of rows as number of measurement points per sample.

```
macro "Combine [0]"{
path = getDirectory("Choose a data folder");
setBatchMode(true);
list = getFileList(path);
for (i = 0; i < list.length; i++)
      open(list[i]);
x = getNumber("Number of samples being measured please",8);
y = getNumber("Number of measurement points per sample please",2);
for(i=1;i<=y;i++)
{
            title = getString("What do you want this to be called", "Booger");
            for(j=1; j<x; j++)
            {
                  run("Combine...");
            }
```

```
            saveAs("tiff",path+title);
}
title2 =  getString("What do you want this to be called", "Booger");
for(k=1; k<y; k++)
{
run("Combine...");
}
saveAs("tiff",path+title2);
}
```

Measuring Fluorescence of Each Image

This code measures the fluorescence in an area defined by the user across all frames of the combined video. In order to run the code, the combined .tiff file must be open in ImageJ. The code starts by enhancing the contrast of the image to 0.3% saturation. The code asks the user how many separate samples to measure, as well as the size of the area to measure the fluorescence over. The code then asks the user for the coordinates of the upper left side of the measurement square. Each video had two measurement spots: one in the middle of the channel and one outside of the channel (for background). The code will output a CSV file combining an area's fluorescence in each frame. These CSVs will all be saved in a single folder defined by the user at the start of the run.

```
macro "Time Point [b]"{
title = getTitle();
path = getDirectory("Where do you want to save enhanced image")
path2 = getDirectory("Choose where to put logs")
selectWindow("" + title +"");
run("Enhance Contrast...", "saturated=0.3 process_all");
saveAs("gif",path+title);
z = getNumber("Number of samples please",6);
A = getNumber("What rectangle width do you want",100);
B = getNumber("What rectangle height do you want", 25);
for(j=1; j<=z; j++)
{
name = getString("How do you want to name the sample", "T");
setSlice(1);
x = getNumber("What is the x value?",100);
y = getNumber("What is the y value?",25);
makeRectangle(x, y, A, B);
for(i=1; i<=nSlices(); i++)
{
run("Measure");
run("Next Slice [>]");}
  headings = split(String.getResultsHeadings);
  i=1;
  for (row=0; row<nResults; row++) {
     line = "";
     for (col=1; col<lengthOf(headings); col++)
     line = line + getResult(headings[col],row) + "  ";
     print(line);
  }
 saveAs("Text", path2+name+"Log.csv");
 IJ.deleteRows(0,nResults);
 print("\\Clear");
}
close();
```

Appendix C

MATLAB Peak Analysis for Microfluidic Droptodes

Raw Data Analysis

The code for the analysis of the fluorescent CSV codes was modified from code written by Nicolas Mesyinger. The code was modified to measure both the maximum fluorescence (oil phase) and the minimum fluorescence (aqueous phase).

```
close all
clear all
%xl=860;    %lowest x position for second order peak
%xh=890;    %highest x position for second order peak
dir1='C:\Users\swetzler\Desktop\PFOS Logs\Logs'
cd 'C:\Users\swetzler\Desktop\PFOS Logs\Logs'
files = dir('*.csv');
N = length(files);   % total number of files
mkdir New;
SumEnd=[   ];
SumT=[   ];
SumMid=[   ];
SumPB=[    ];
SumFin=[    ];
SumEnd1=[   ];
SumT1=[   ];
SumMid1=[   ];
% loop for each files
for i = 1:N
   thisfile = files(i).name
   if strlength(thisfile)>4
      str=strcat(dir1,'\',thisfile);
      filename = erase(string(thisfile),".csv");
      %open file
      fid = fopen(str,'rt');
      %figure out how many columns are there
      firstline = fgetl(fid);
      ncol = 4;
   %reset to beginning of file
      fseek(fid,0,0);
   %read data
      indata = textscan(fid,repmat('%f%*n',1,ncol),'Delimiter',',','CollectOutput',1);
      V = [size(indata{1}), 1]; V(find(V == 1, 1)) = numel(indata);
      A = reshape(horzcat(indata{:}), V);
      nrow=size(A,1);
      for(i=1:nrow)
```

```
        A(i,4)=i;
    end
    n=1;
    k=[];
    for(i=1:nrow)
        if(A(i,1)==0)||i>200
            k(n)=i;
            n=n+1;
        end
    end
    for(j=size(k,2):-1:1)
      A(k(j),:)=[];
    end
    CondA=A(:,[1 4]);    %close file
    fclose(fid);
    D=CondA;
    D(:,2)=CondA(:,1);
    D(:,1) = CondA(:,2);

    writematrix(D,dir1+"\New\new"+thisfile);

    B=D;
    r=size(B);
    c=r(2);
    r=r(1);
    skipped=0;


  %identify locations of largest peak in each spectrum
    [Z,z] = max(D,[],1);
    highest=(B(z(:),1));
    ordered=sort(highest);
    Tallest=unique(ordered);
    T=size(Tallest,1);
    counter=zeros(T);
    check=0;
    plus=0;
    minus=0;
%   text(locs+.02,pks,num2str(locs));
%   [N,I] = max(pks,[],1);
    LDE=0;
    RDE=0;
    Ld=0;
    Rd=0;
    Peaks=0;
    Location=0;
    plot(B(1:r-1, 1), CondA(2:r,1),'DisplayName', 'average');
    [pks, locs] = findpeaks(B(:,2),'MinPeakDistance',1,'MinPeakHeight',0.9*max(B(:,2)));
    filename = erase(filename,"Log");
    filename1 = string(filename);
    xlabel('Frame')
    ylabel('Fluorescence Changes')
    saveas(gcf,dir1+"\New\cal"+filename1+".png");
  %drops
    B2=-D;
    r1=size(B2);
    c=r1(2);
    r1=r1(1);
    skipped=0;
```

```
%identify locations of largest peak in each spectrum
    [Z,z] = max(-D,[],1);
    highest1=(B2(z(:),1));
    ordered1=sort(highest1);
    Tallest1=unique(ordered1);
    T1=size(Tallest1,1);
    counter1=zeros(T1);
    check1=0;
    plus1=0;
    minus1=0;
    LDE1=0;
    RDE1=0;
    Ld1=0;
    Rd1=0;
    Peaks1=0;
    Location1=0;
    C2=-CondA(2:r1,1);
    plot(B2(1:r1-1, 1), C2,'DisplayName', 'average');
    [pks2, locs2] = findpeaks(B2(:,2),'MinPeakDistance',1,'MinPeakHeight',1.1*max(B2(:,2)));
%    s=size(locs);
%    d=ones(s(1)-1,1);
%    for i=1:s(1)-1
%        d(i)=locs(i+1)-locs(i);
%    end
%    d;
    text(locs2+.02,pks2,num2str(locs2));
    diff = mean(pks)-abs(mean(pks2));
    diffstdv=sqrt(std(pks)^2+std(pks2)^2);
    filename = erase(filename,"Log");
    filename1 = string(filename);
    saveas(gcf,dir1+"\New\cal"+filename1+"drops.png");
%pks;
    if contains(filename1,"T")
        filename = erase(filename,"T");
        measurement=[filename mean(pks) std(pks) abs(mean(pks2)) std(pks2) diff diffstdv];
        SumT=[SumT;measurement];
    %measurement1=[filename mean(minima) std(minima)];
    %SumT1=[SumT1;measurement1];
    elseif contains(filename1,"Mid")
        filename = erase(filename,"Mid");
        measurement=[filename mean(pks) std(pks) abs(mean(pks2)) std(pks2) diff diffstdv];
        SumMid=[SumMid;measurement];
      %measurement1=[filename mean(minima) std(minima)];
    %SumMid1=[SumMid1;measurement1];
    elseif contains(filename1,"PB")
        filename = erase(filename,"PB");
        measurement=[filename mean(pks) std(pks) abs(mean(pks2)) std(pks2) diff diffstdv];
        SumPB=[SumPB;measurement];
    elseif contains(filename1,"End")
        filename = erase(filename,"End");
        measurement=[filename mean(pks) std(pks) abs(mean(pks2)) std(pks2) diff diffstdv];
        SumEnd=[SumEnd;measurement];
    %measurement1=[filename mean(minima) std(minima)];
    %SumEnd1=[SumEnd1;measurement1];
    else
        filename = erase(filename,"Fin");
        measurement=[filename mean(pks) std(pks) abs(mean(pks2)) std(pks2) diff diffstdv];
        SumFin=[SumFin;measurement];
    end
```

```
    end
end
writematrix(SumEnd,cd+"\New\Endcal.csv")
%writematrix(SumT,cd+"\New\Tcal.csv")
writematrix(SumMid,cd+"\New\Midcal.csv")
% writematrix(SumPB,cd+"\New_05022020\PBcal.csv")
writematrix(SumFin,cd+"\New\Fincal.csv")
%writematrix(SumEnd1,cd+"\New_Diff\Endcal_drops.csv")
%writematrix(SumT1,cd+"\New_Diff\Tcal_drops.csv")
%writematrix(SumMid1,cd+"\New_Diff\Midcal_drops.csv")
x=str2double(SumEnd(:,1));
y=str2double(SumEnd(:,6));
stddev=str2double(SumEnd(:,7));
errorbar(x,y,stddev, 'bx')
x=str2double(SumEnd(:,1));
y=str2double(SumEnd(:,2));
stddev=str2double(SumEnd(:,3));
errorbar(x,y,stddev, 'bo','MarkerFaceColor','b')
xlabel('log(CO32-)/[M]')
ylabel('Fluorescnce')
saveas(gcf,dir1+"\New\cal_fig.png")
% xT=str2double(SumT(:,1));
% yT=str2double(SumT(:,6));
% stddevT=str2double(SumT(:,7));
% hold on
% errorbar(xT,yT,stddevT,'rx')
% saveas(gcf,dir1+"\New\cal.png")
hold on
xM=str2double(SumMid(:,1));
yM=str2double(SumMid(:,2));
stddevM=str2double(SumMid(:,3));
errorbar(xM,yM,stddevM,'mx')
saveas(gcf,dir1+"\New\cal_fig.png")
% hold on
% xP=str2double(SumPB(:,1));
% yP=str2double(SumPB(:,6));
% stddevP=str2double(SumPB(:,7));
% errorbar(xP,yP,stddevP,'yx')
hold on
xF=str2double(SumFin(:,1));
yF=str2double(SumFin(:,2));
stddevF=str2double(SumFin(:,3));
errorbar(xF,yF,stddevF,'gx')
saveas(gcf,dir1+"\New\cal_fig.png")
```

Normalization of Data To Background

I wrote this code to subtract out the background of each run, in order to control for any dye partitioning or leaking. This code needs to be run after the raw background code using the combined dataset from inside all of the channels (here labeled as “End”) and the combined dataset from the background (here labeled as “Mid”). The code will output the difference between inside and outside the channel for each frame, labeled as “Fin.”

```
dir='C:\Users\swetzler\Desktop\02242021\Analytes\pH2\Logs'
dir1='C:\Users\swetzler\Desktop\02242021\Analytes\pH2\Logs\New'
cd 'C:\Users\swetzler\Desktop\02242021\Analytes\pH2\Logs\New'
num="-1.62"; %User types
endfile=dir1+"\new"+num+"EndLog.csv"
midfile=dir1+"\new"+num+"MidLog.csv"
%read in End file
fid1=fopen(endfile,'rt');
%figure out how many columns are there
 firstline1 = fgetl(fid1);
 ncol1 = 2;
 %reset to beginning of file
fseek(fid1,0,0);
%read data
indata1 = textscan(fid1,repmat('%*n%f',1,ncol1),'Delimiter',',','CollectOutput',1);
V1 = [size(indata1{1}), 1]; V1(find(V1 == 1, 1)) = numel(indata1);
A1 = reshape(horzcat(indata1{:}), V1);
nrow=size(A1,1);
for(i=1:nrow)
    A1(i,2)=i;
 end
%close file
 fclose(fid1);
%Read in Mid file
fid2=fopen(midfile,'rt');
%figure out how many columns are there
 firstline2 = fgetl(fid2);
 ncol2 = 2;
 %reset to beginning of file
fseek(fid2,0,0);
%read data
indata2 = textscan(fid2,repmat('%*n%f',1,ncol2),'Delimiter',',','CollectOutput',1);
V2 = [size(indata2{1}), 1]; V2(find(V2 == 1, 1)) = numel(indata2);
A2 = reshape(horzcat(indata2{:}), V2);
nrow2=size(A2,1);
for(j=1:nrow2)
    A2(j,2)=j;
 end
%close file
 fclose(fid2);
%Array subtract
A3=zeros(nrow2,1);
for(k=1:nrow2)
 A3(k,1)=A1(k,1)-A2(k,1);
```

```
end
%output fin
writematrix(A3,dir+"\"+num+"FinLog.csv");
```

Sigmoidal Fits in MATLAB

This code was used to perform all sigmoidal fits to the normalized dataset.

```
clear all
%data loading section
X2=[-1 -1.14 -1.4 -0.91 -0.7 0]; %Cl Cal
Y2=[1.08 .99 1.03 0.89 0.29 0];
Y2error=[0.05 0.05 0.02 0.1 0.001 0.1];
% X6=[-8 -6 -4 -2 0 ]; %Na Cal
% Y6=[1 0.88 0.53 0.15 0];
% Y6error=[0.08 0.08 0.05 0.05 0.05];

%fit defining section
fo = fitoptions('Method','NonlinearLeastSquares',...
            'Lower',[-5,0,-10,-30],...
            'Upper',[Inf,Inf, 0.1, 10],...
            'StartPoint',[0 1 -3 -15]);
ft = fittype('((B-A)/(1+(x/C)^D))+A','independent',{'x'},'dependent',{'y'},'coefficients',{'A','B','C','D'},'options',fo);
% fo = fitoptions('Method','NonlinearLeastSquares',...
%             'Lower',[-5,-5],...
%             'Upper',[5,5],...
%             'StartPoint',[-1 -1]);
% ft = fittype('M*x+B','independent',{'x'},'dependent',{'y'},'coefficients',{'M','B'},'options',fo);
%fitting section
myfit2=fit(X2',Y2',ft)
%myfit6=fit(X6',Y6',ft)
% myfit16=fit(X16',Y16',ft)

%plotting section
hold on
scatter(X2,Y2,24,[1 0 0],'filled')
%scatter(X6,Y6,24,[0,0,1],'filled','d')



f2=plot(myfit2,'r',X2,Y2)
%f6=plot(myfit6,'b',X6,Y6)

errorbar(X2, Y2, Y2error,'Color','k', 'LineStyle','none');
%errorbar(X6, Y6, Y6error,'Color','k', 'LineStyle','none');
%legend('Potassium','Sodium')
xlabel('log[Cl]/M')
ylabel('Relative Fluorescence')
```

Linear Fits in MATLAB

This code was used to perform all linear fits of the normalized fluorescence.

```
clear all
%data loading section
X2=[-2 -0.85 -0.83 -0.7 -0.89 0]; %Ca Cal
Y2=[1 0.29 0.23 0.27 0.32 0];
Y2error=[0.01 0.02 0.01 0.005 0.06 0.1];
% X6=[-8 -6 -4 -2 0 ]; %Na Cal
% Y6=[1 0.88 0.53 0.15 0];
% Y6error=[0.08 0.08 0.05 0.05 0.05];

%fit defining section
fo = fitoptions('Method','NonlinearLeastSquares',...
            'Lower',[-5,-5],...
            'Upper',[5,5],...
            'StartPoint',[-1 -1]);
ft = fittype('M*x+B','independent',{'x'},'dependent',{'y'},'coefficients',{'M','B'},'options',fo);

%fitting section
myfit2=fit(X2',Y2',ft)
%myfit6=fit(X6',Y6',ft)
% myfit16=fit(X16',Y16',ft)

%plotting section
hold on
scatter(X2,Y2,24,[1 0 0],'filled')
%scatter(X6,Y6,24,[0,0,1],'filled','d')



f2=plot(myfit2,'r',X2,Y2)
%f6=plot(myfit6,'b',X6,Y6)

errorbar(X2, Y2, Y2error,'Color','k', 'LineStyle','none');
%errorbar(X6, Y6, Y6error,'Color','k', 'LineStyle','none');
%legend('Potassium','Sodium')
xlabel('log[Na]/M')
ylabel('Relative Fluorescence')
```

Appendix D

Lab Protocol for COVID-ELISA Lab

Lab Protocol for ELISA Lab

Experiment 6 – CHEM 246/247

Using ELISAs to determine the concentration of a protein biomarker

Introduction

The aim of this experiment is to understand the function, operation, and application of Enzyme-Linked Immunosorbent Assays (ELISAs), which are the clinical gold standard for the detection of many protein biomarkers. Specifically, you will use an ELISA assay to make a calibration curve for a representative protein biomarker—an antibody—and then utilize this calibration relationship to measure the concentration of the biomarker within a provided unknown sample.

Background

Given their central role in normal biological function, altered levels of specific proteins can be utilized as biomarkers for a range of disease conditions. Specifically, protein biomarkers are commonly used in the clinical diagnosis of many diseases, including cancer. A specific class of biomarkers known as antibodies are currently utilized as biomarkers that enable the individualized confirmation that a patient has immunity against a particular disease. Such classification is important, not only to ensure that someone will not become ill due to exposure to

a disease, but also to monitor the extent of pandemics, such as COVID-19. Measuring antibodies was a frequent method used to determine community spread of COVID-19 and was even used by some countries, against the recommendation of the World Health Organization, to allow travel for people who had already had COVID-19 and therefore were less likely to recontract it (1-5). Measuring COVID-19 antibodies was also the main way of determining the effectiveness of a vaccine, by monitoring the immune response of the trial participants who got it during its experimental phase (Phase 1, 2 and 3).

In order to create an appropriate assay for a given protein biomarker, including antibodies, a few different factors need to be considered. For instance, protein concentration is generally measured in blood, a matrix which contains many other proteins and small molecules. Thus, any assay chosen for protein detection must have good specificity towards the biomarker of interest over the many other proteins found in the blood. Additionally, assays must have the necessary sensitivity, limits of detection (LoD), and limits of quantitation (LoQ) that correspond to both normal and "disease" levels of the biomarker.

The most common protein biomarker detection method used in research and clinical laboratories is the Enzyme-Linked Immunosorbent Assay, which is commonly referred to as an ELISA. ELISAs utilize antibodies as target capture agents that deliver high levels of specificity over other proteins present in a sample. Antibodies are naturally produced by the immune system for the recognition of foreign proteins; however, for biotechnology applications antibodies can be generated in other species (e.g. rabbit, mice, chicken, goat, etc.) and then applied to the detection of human protein biomarker associated with disease. The biomarker towards which an antibody has specificity is referred to as the target or antigen of the assay. Antibodies are utilized in conjunction with enzymatic reagents that generate a colorimetric signal that is proportional to the

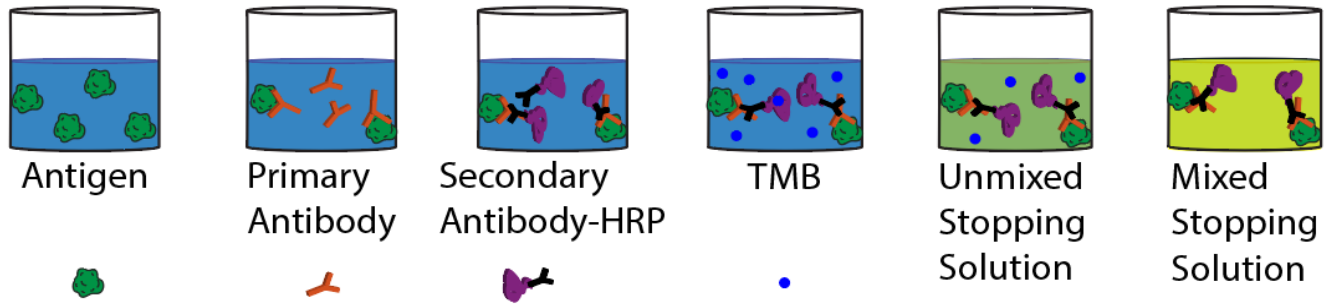

Figure A.1. Schematic for procedure for ELISA. Initially the antigen is added to the well and captured by the walls. After washing the primary antibody binds to the antigen. After another incubation and washing a secondary antibody, conjugated to HRP, binds to the primary antibody. After another round of incubation and washing, the substrate for HRP, TMB, is added, turning the well blue. After some incubation time, a stopping solution of acid can be added to change the well's color to yellow.

concentration of the target biomarker in the original biological specimen. More details information on the entire ELISA process can be found at: https://www.bioconcept.ch/KundenUpload/pdf/KPL%20ELISA%20Technical%20Guide.pdf. The basic procedure for an ELISA, which is traditionally performed in a 96-well plate, involves a series of incubation and washing steps that are shown in **Figure A.1**.

First, a well plate is modified so that it can bind the target biomarker. After incubation of a sample in the well, the antigen is bound to the bottom of the well plate. After washing to remove any loosely bound (non-specific/non-targeted) proteins, a primary antibody is introduced that specifically recognizes the captured antigen. After another round of washing, a secondary antibody, which has specificity for the primary antibody, and has been pre-tethered to an enzyme (e.g., horseradish peroxidase) is introduced. The enzyme can then react with an oxidant (i.e., H_2O_2) and a colorless reagent (i.e. TMB; 3,3',5,5'-Tetramethylbenzidine) to generate a colored product (blue in color). To further increase the sensitivity, the solution is acidified to yield a stable yellow product that can be sensitively detected by its absorption band at 450 nm (λ_{max}) (Figure 1). The

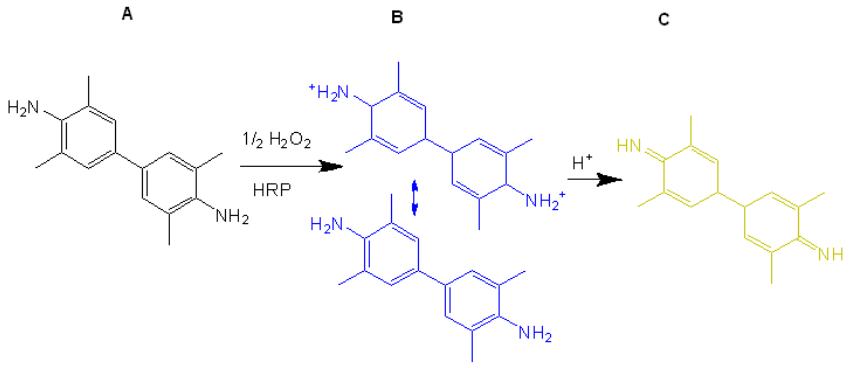

Figure A.2 The TMB substrate (A) is enzymatically oxidized to the charge-transfer equilibrium species (B), and then protonated to yield the yellow product (C), which is detected by its absorption at 450 nm.

chemical reactions carried out by the enzyme and subsequent acidification are show in **Figure A.2** (6).

At this point in the semester, you are familiar with the generation and utilization of linear calibration curves for unknown determination. However, the nature of the antibody-antigen interactions in ELISA assays results in a non-linear calibration relationship. More specifically, ELISA calibration curves are typically sigmoidal and are fit with logistic functions of the following form:

$$y = B + \frac{A-B}{1+(\frac{x}{x_0})^d} \qquad [8.1]$$

where y is the absorbance signal, x is the analyte concentration, A is the lower asymptote (essentially the minimal signal), B is the upper asymptote (essentially the maximum signal), x_0 is the midpoint of the linear range (defined by the upper and lower asymptotes) and d is the slope of the linear range at the midpoint (**Figure A.3**).

In addition to the calibration relationship, which is needed to determine unknown concentrations,

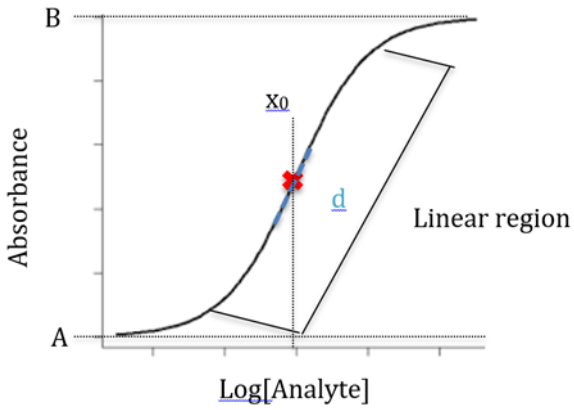

Figure A.3. Example of a sigmoidal curve like found in the calibration curve for ELISAs. The four variables in the logistic fit (*A*, *B*, x_0, and *d*) are marked off on the curve's diagram.

other useful analytical metrics such as LoD and LoQ can also be determined from the logistic fit parameters. Formally, LoD is defined as the concentration of antigen at which the signal can be statistically differentiated from the blank, which can also be stated as the concentration equivalent to the signal of the blank plus three times the standard deviation of the blank (σ_b— from the replicate blank measurements). The LoQ is the minimum concentration that can be clearly quantified (not just detected, indicating a confidence in the added precision of the value), which is defined as the concentration equivalent to blank signal plus ten times σ_b. Mathematically, LoD and LoQ can be determined from the logistic parameters following:

$$LoD = x_0 \left(\frac{A-B}{Blank+3\sigma_b-B} - 1\right)^{\frac{1}{d}} \qquad [8.2]$$

and

$$LoQ = x_0 \left(\frac{A-B}{Blank+10\sigma_b-B} - 1\right)^{\frac{1}{d}} \qquad [8.3]$$

where *Blank* is the signal of the blank, σ_b is the standard deviation of the blank, and *A* and *B* are the logistic fit parameters as described above.

Objectives

In this lab you will perform an ELISA to determine an unknown concentration of a protein biomarker (an antibody) in an aqueous sample. This will involve running two calibration curves, in order to determine the absorbance to protein concentration relation, the error associated with each measurement, as well as blank measurements in the unknown sample matrix. From the overall calibration curve you will be able to determine the unknown concentration of the protein biomarker as well as the LoD and LoQ, which will be included in your report.

Procedure

Required Apparatus

1. Well plates (each plate will be split between two groups—each group gets half)
2. 100 µL pipette
3. 20-200 µL pipette tips
4. Disposable pipettes
5. Aluminum foil
6. Timer
7. Plate reader

Reagents

1. Stock chicken autoantibody solution (5 µg/mL hGH in 1x PBS)
2. Phosphate buffer saline solution (1x PBS)
3. Wash buffer (1x PBS + 0.05% Tween-20)
4. Primary Antibody solution (100 µg/mL polyclonal Mouse anti-chicken in 1xPBS + 0.05% Tween-20)
5. Secondary Antibody-HRP solution (100 µg/mL anti-mouse rabbit-HRP in 1xPBS + 0.05% Tween-20, already in lab)
6. Substrate solution (3,3',5,5'-Tetramethylbenzidine (TMB), already in lab)
7. Stopping solution (0.16 M H_2SO_4, already in lab)

General Procedure

1. You will start with a 5 µg/mL solution of protein (provided) and then make a set of five standards via serial dilution. Each standard will have a volume of 500 µL, as described in

the table below.

Table A.1. Serial Dilutions for ELISA Experiment

Standard solution	Dilution "recipe"
1 µg/mL	___ µL 5 µg/mL *(stock)* into ___ µL 1x PBS
200 ng/mL	___ µL 1 µg/mL into ___ µL 1x PBS
40 ng/mL	___ µL 200 ng/mL into ___ µL 1x PBS
8 ng/mL	___ µL 40 ng/mL into ___ µL 1x PBS
1.6 ng/mL	___ µL 8 ng/mL into ___ µL 1x PBS

2. Obtain an unknown sample (1 x 200 µL sample) from your GSI and record the unknown ID number.

3. Add 50 µL of each standard to a well in your half of the well plate. Each standard should appear 2x in your well plate. In two of the remaining wells, add 50 µL of PBS buffer. In two remaining wells, add 50 µL of your unknown. Gently swirl/tap until bottom of well completely covered with liquid. Cover well strip with foil. Let incubate for 20 minutes.

4. Dump out all liquid in wells as demonstrated at the start of lab, being careful to make sure the wells do not splash into one another. Refill all the wells with wash buffer (approximately 250 µL each). Dump wash buffer out and repeat the washing step one more time.

5. Add 50 µL of primary antibody to each well. Cover with foil and let incubate for 20 minutes. Dump and wash two times (as in step 4).

6. Add 50 µL of secondary antibody-HRP to each well. Cover with foil and let incubate for

20 minutes. Dump and wash three times.

7. Add 50 µL of the substrate to each well. Cover with foil and incubate for 10 minutes. Start timing when the substrate is added to the first well. As time passes your wells should turn increasingly dark blue in color—the higher standard concentrations being the most highly colored.

8. After 10 minutes add 50 µL of stopping solution to each well, at which point the wells should turn yellow. If wells look green, the stopping solution is not fully mixed so gently swirl your plate to fully mix.

9. Determine the absorbance of each well in your plate at 450 nm using the plate reader in lab. To clean up, use sodium bicarbonate to neutralize the stopping solution and dispose of properly.

Data Analysis

1. Plot the average of the absorbances of each standard vs the log of the concentration of the protein standards in ng/mL (i.e., calibration curves). (Note: Treat the blank as having a concentration one log lower than your lowest concentration.). Error bars will be the standard deviation in the measurements. Fit to a logistic fit and obtain the equation and statistics for the fit (i.e. the least squared error). A more detailed set of instructions on how to fit a logistic fit is found in the Appendix (at the end of this protocol).

2. Based on the logistic fit equation and error observed between your two calibration curves, report the LoD and LoQ for your ELISA assay.

3. Determine the protein concentration in the unknown and estimate the range associated with

the 95% confidence interval (use your n=2 replicate unknown measurements and associated standard deviation).

Lab Report

1. Show your calibration curve (the plot of the absorbance vs log concentration) for the protein standards. Report the equation of the logistic fit along with the relevant statistics and units. Also report the limit of detection and limit of quantitation. How do the limit of detection and limit of quantitation compare to typical ELISA values? What might be the cause for the difference between them? How do you think the LoQ and LoD would change if we used a complex sample (i.e., plasma) instead for our calibration? Why?

2. Report in a summary table the concentration of protein found for the unknown sample (in ng/mL), with standard deviation and 95% confidence interval. Make sure you clearly indicate the i.d. # of your sample. Does it appear that the unknown individual has COVID (literature values suggest that long term antibody levels for COVID-19 range between 50 and 100 ng/mL after undergoing a 1000-fold dilution (7))?

3. What could be reasons why your individual was higher than this range? Lower but non-zero?

4. If someone is within the COVID-19 antibody range, are they actively contagious? Why or why not? How would you test for contagious COVID-19?

References

1. Okba, N. M. A. *et al.* Severe Acute Respiratory Syndrome Coronavirus 2-Specific Antibody Responses in Coronavirus Disease Patients. *Emerg. Infect. Dis.* **26**, 1478–1488 (2020).
2. Zhao, J. *et al.* Antibody Responses to SARS-CoV-2 in Patients with Novel Coronavirus Disease 2019. *Clin. Infect. Dis.* **71**, 2027–2034 (2020).
3. Liu, W. *et al.* Evaluation of nucleocapsid and spike protein-based ELISAs for detecting antibodies against SARS-CoV-2. *medRxiv* (2020) doi:10.1101/2020.03.16.20035014.
4. Ying, L. *et al.* Diagnostic indexes of a rapid IgG/IgM combined antibody test for SARS-CoV-2. *medRxiv* (2020) doi:10.1101/2020.03.26.20044883.
5. 'Immunity passports' in the context of COVID-19. https://www.who.int/news-room/commentaries/detail/immunity-passports-in-the-context-of-covid-19.
6. Josephy PD, Eling T, Mason RP. The horseradish peroxidase-catalyzed oxidation of 3,5,3',5'-tetramethylbenzidine. Free radical and charge-transfer complex intermediates. Journal of Biological Chemistry. 1982;257(7):3669-75.
7. Zeng, W. *et al.* Characterization of SARS-CoV-2-specific antibodies in COVID-19 patients reveals highly potent neutralizing IgA. *Signal Transduction and Targeted Therapy* vol. 6 1–3 (2021).

How to Fit a Sigmoidal Curve in Excel

It is important to note that the data provided here is in no way representative of the data you will get in this lab in terms of order of magnitude. This is just to practice the process of curve fitting.

1. Install the Solver Add-in to Excel if you haven't already (More detailed instructions at https://support.office.com/en-us/article/load-the-solver-add-in-in-excel-612926fc-d53b-46b4-872c-e24772f078ca)

2. Make a table with your log of your concentrations in the leftmost column and your average absorbance in the right column. (Note the errors from the measurements are also in the table so they do not get lost.)

	A	B	C
1	Conc	Absorb	Absorb Err
2	6.9	340	25
3	5.9	330	28
4	2.9	295	18
5	1.9	200	9
6	1.8	205	8
7	1.6	190	5
8	2	215	9
9	1.7	200	3
10	1	90	3
11	0.9	65	14
12	0.5	45	3
13	0.3	0	3

Figure A.4. Table of log of concentrations, absorbance and errors in Excel

3. Create cells for *A*, *B*, x_0 and *d* in Excel. Input your initial guesses for each of those variables (i.e. for A, what you think the upper asymptote might be, etc.).

	A	B	C
1	Conc	Absorb	Absorb Err
2	6.9	340	25
3	5.9	330	28
4	2.9	295	18
5	1.9	200	9
6	1.8	205	8
7	1.6	190	5
8	2	215	9
9	1.7	200	3
10	1	90	3
11	0.9	65	14
12	0.5	45	3
13	0.3	0	3
14			
15			
16			
17			
18	A	0	
19	B	340	
20	x0	2	
21	d	2	

Figure A.5. Creating Cells for *A*,*B*, x_0 and *D* in Excel.

4. In the column next to the absorbances, make a column of predicted absorbances, where A, B, x0 and d are plugged in to the expected sigmoidal fit for all of the possible x values. (In this case the red boxed cell would have '=$B$19-($B$18-$B$19)/(1+(A2/$B$20)^$B$21)'

	A	B	C	D	E
1	Conc	Absorb	Absorb Err		Pred Abs
2	6.9	340	25		313.6485
3	5.9	330	28		304.9575
4	2.9	295	18		230.411
5	1.9	200	9		161.2878
6	1.8	205	8		152.1547
7	1.6	190	5		132.6829
8	2	215	9		170
9	1.7	200	3		142.6125
10	1	90	3		68
11	0.9	65	14		57.25572
12	0.5	45	3		20
13	0.3	0	3		7.481663
14					
15					
16					
17					
18	A	0			
19	B	340			
20	x0	2			
21	d	2			

Figure A.6. Making a column of predicted absorbances which are calculated based on A, B, x_0 and D.

5. In a new column, find the difference between the actual data and the predicted value and square the difference. Do this for all data points. (In this case the red boxed cell would have in it '=(E2-B2)^2

	A	B	C	D	E	F
1	Conc	Absorb	Absorb Err		Pred Abs	Sq Diff
2	6.9	340	25		313.6485	694.4006
3	5.9	330	28		304.9575	627.1275
4	2.9	295	18		230.411	4171.744
5	1.9	200	9		161.2878	1498.636
6	1.8	205	8		152.1547	2792.626
7	1.6	190	5		132.6829	3285.247
8	2	215	9		170	2025
9	1.7	200	3		142.6125	3293.327
10	1	90	3		68	484
11	0.9	65	14		57.25572	59.97392
12	0.5	45	3		20	625
13	0.3	0	3		7.481663	55.97528
14						
15						
16						
17						
18	A	0				
19	B	340				
20	x0	2				
21	d	2				

Figure A.7. Finding the difference between the predicted and actual absorbance values using Excel. This is represented as a squared value so sign does not matter.

6. In a new cell find the sum of all of the squared differences.

	A	B	C	D	E	F
1	Conc	Absorb	Absorb Err		Pred Abs	Sq Diff
2	6.9	340	25		313.6485	694.4006
3	5.9	330	28		304.9575	627.1275
4	2.9	295	18		230.411	4171.744
5	1.9	200	9		161.2878	1498.636
6	1.8	205	8		152.1547	2792.626
7	1.6	190	5		132.6829	3285.247
8	2	215	9		170	2025
9	1.7	200	3		142.6125	3293.327
10	1	90	3		68	484
11	0.9	65	14		57.25572	59.97392
12	0.5	45	3		20	625
13	0.3	0	3		7.481663	55.97528
14						
15						
16						
17						
18	A	0				
19	B	340				
20	x0	2				
21	d	2				
22						
23						
24						
25						19613.06

Figure A.8. Calculating the sum of squared differences in Excel. The red boxed cell would be '=SUM(F2:F13)'

7. Click on Tools >> Solver. (Note this might also be under Data>>Analyze>>Solver depending on your Excel version). Set the Objective cell as the one where you have the sum of the squared differences. Set the Objective cell as "Min." Set the range of Changing Cells to include the estimated values of A, B, x_0 and d.

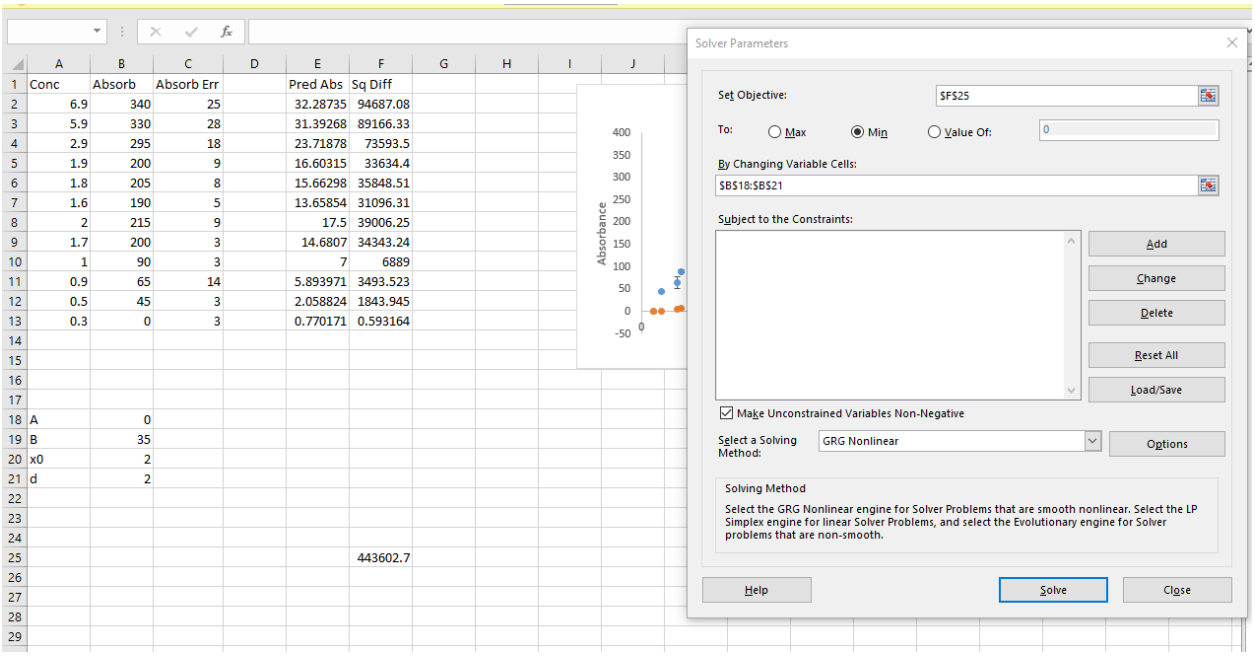

	A	B	C	D	E	F
1	Conc	Absorb	Absorb Err		Pred Abs	Sq Diff
2	6.9	340	25		32.28735	94687.08
3	5.9	330	28		31.39268	89166.33
4	2.9	295	18		23.71878	73593.5
5	1.9	200	9		16.60315	33634.4
6	1.8	205	8		15.66298	35848.51
7	1.6	190	5		13.65854	31096.31
8	2	215	9		17.5	39006.25
9	1.7	200	3		14.6807	34343.24
10	1	90	3		7	6889
11	0.9	65	14		5.893971	3493.523
12	0.5	45	3		2.058824	1843.945
13	0.3	0	3		0.770171	0.593164
18	A	0				
19	B	35				
20	x0	2				
21	d	2				
25						443602.7

Figure A.9. Sample of what variables will be seen when setting up the Solver tool to optimize the fit parameters.

8. Click Solve. Excel will minimize the difference between the actual absorbance and the predicted absorbance by changing the value of A, B, x_0, and d.

9. Plot the concentration against the actual and predicted absorbances. Make sure the curves align closely.

	A	B	C	D	E	F
1	Conc	Absorb	Absorb Err		Pred Abs	Sq Diff
2	6.9	340	25		338.7517	1.558163
3	5.9	330	28		334.6384	21.51441
4	2.9	295	18		284.2959	114.5771
5	1.9	200	9		214.4394	208.4969
6	1.8	205	8		203.5874	1.995319
7	1.6	190	5		179.2996	114.4994
8	2	215	9		224.4521	89.34221
9	1.7	200	3		191.8744	66.02483
10	1	90	3		90.41445	0.17177
11	0.9	65	14		75.22625	104.5761
12	0.5	45	3		25.80615	368.4038
13	0.3	0	3		12.21382	149.1773
14						
15						
16						
17						
18	A	6.380464				
19	B	347.9705				
20	x0	1.583745				
21	d	2.435918				
22						
23						
24						
25						1240.337

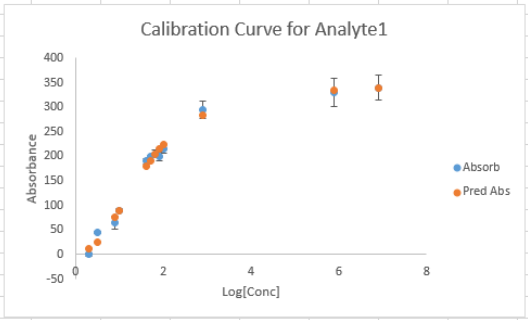

Figure A.10. Plotting actual absorbance against predicted absorbance. There is good agreement between the two curves as the data points almost always overlap.

10. If the curves do not align closely: this suggests that the initial values for A, B, x_0 and d were not close enough to the actual values. Modify the guessed values until you get good agreement.

Hints About Finding Close Enough Values for Fitting Variables

For A and B start with your max and min signal points

For x_0 look in approximately the middle of your linear range of your curve when just plotting the raw concentration vs. absorbance data

For d, guess in the region of 1-10. Depending on what you see, either make the slope more or less to fit your data better.

Sample Pre-Lab for ELISA COVID Lab

1. For practice: Find the sigmoidal fit for the following data:

Log(Conc)	Absorbance	Error
-10	0.001	0.0001
-8	0.05	0.05
-7.5	0.27	0.07
-7	0.44	0.05
-6.5	0.64	0.02
-6	0.76	0.05
-5.5	0.84	0.07
-5	1	0.07
-4	1	0.07

2. Fill in the necessary serial dilutions.

Standard solution	Dilution "recipe"
1 µg/mL	___ µL *5 µg/mL (stock)* into ___ µL 1x PBS
200 ng/mL	___ µL *1 µg/mL* into ___ µL 1x PBS
40 ng/mL	___ µL 200 ng/mL into ___ µL 1x PBS
8 ng/mL	___ µL 40 ng/mL into ___ µL 1x PBS
1.6 ng/mL	___ µL 8 ng/mL into ___ µL 1x PBS

Answers for Instructors:

1. For the practice data, the results should approximately look like:

A = 0.995

B = -0.0496

x_0 = -6.855

d = 10.403

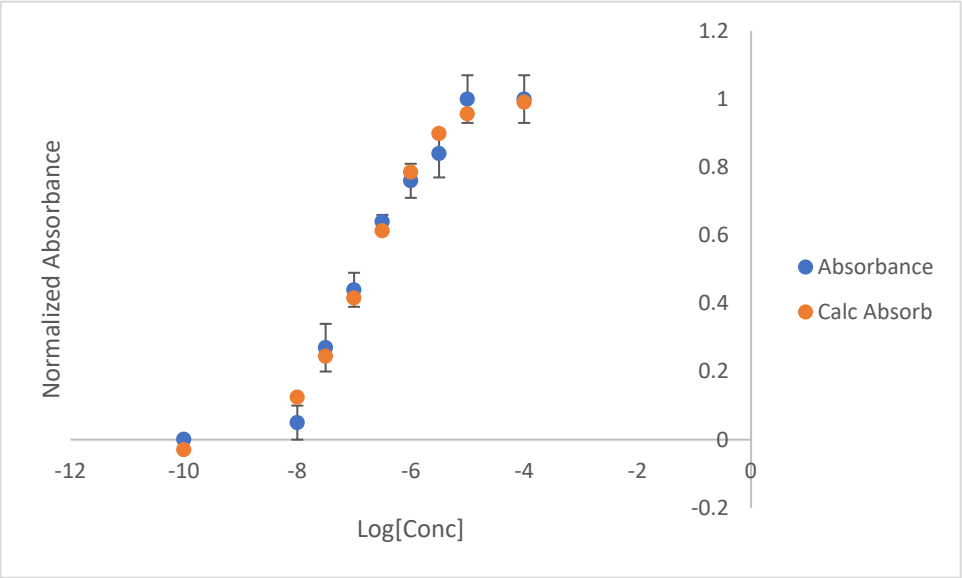

2.

Standard solution	Dilution "recipe"
1 µg/mL	100 µL *5 µg/mL (stock)* into 400 µL 1x PBS
200 ng/mL	100 µL *1 µg/mL* into 400 µL 1x PBS
40 ng/mL	100 µL 200 ng/mL into 400 µL 1x PBS
8 ng/mL	100 µL 40 ng/mL into 400 µL 1x PBS
1.6 ng/mL	100 µL 8 ng/mL into 400 µL 1x PBS

Sample Student Lab Report

Experiment 8

Introduction

The purpose of this experiment was to determine the concentration of a protein biomarker in unknown sample #13 through the use of an Enzyme-Linked Immunosorbent Assay (ELISA). An ELISA is run by adhering an antigen to the wells of a well plate. Then, a primary antibody is added to the wells which bind to the antigen. Next, a secondary antibody is added to the wells which bind to the primary antibodies. The wells are then reacted with an oxidant and TMB to result in a colored product which is stabilized by the addition of an acid. The absorbance of each well is measured and then correlated to a protein concentration. In this experiment, known amounts of protein are added to separate wells of a 96 well plate. The assay is run on the standards to create a calibration curve with a logistic fit line of best fit, which will then be used to calculate the concentration of protein in unknown sample #13. In addition, the LoD, the concentration of protein at which the signal can be differentiated from the blank with statistical significance, and the LoQ, the smallest concentration of protein which can be quantified, are calculated using the following equations (Eqn 8.2, Eqn 8.3).

$$LoD = x_0\left(\frac{A-B}{Blank+3\sigma_b-B}-1\right)^{\frac{1}{d}} \qquad \text{(Equation 8.2)}$$

$$LoD = x_0\left(\frac{A-B}{Blank+10\sigma_b-B}-1\right)^{\frac{1}{d}} \qquad \text{(Equation 8.3)}$$

where *Blank* is the absorbance of the blank, σ_b is the standard deviation of the absorbances of the blank, and x_0, A, B, a nd d are from the logistic fit equation shown below (Eqn 8.1).

$$y = B + \frac{A-B}{1+\left(\frac{x}{x_0}\right)^d} \qquad \text{(Equation 8.1)}$$

where x is the concentration of the protein and y is the absorbance at that concentration. ELISAs are important tools in analytical chemistry and in wet lab research due to their ability to

determine a wide range of biomarker concentrations to a relatively high degree of sensitivity without the high costs associated with other analytical techniques. In addition, ELISAs are commonly used in the pharmaceutical industry for drug discovery purposes, making experience with ELISAs a highly valuable quality for students looking either into higher education or industry.

Procedure

The procedure was followed as was listed on the course website. No deviations were made.

Results

A logistic fit was conducted on the data in the previous figure to generate the following equation for the line of best fit which can also be seen in the figure as a dashed line (**Figure A.11**).

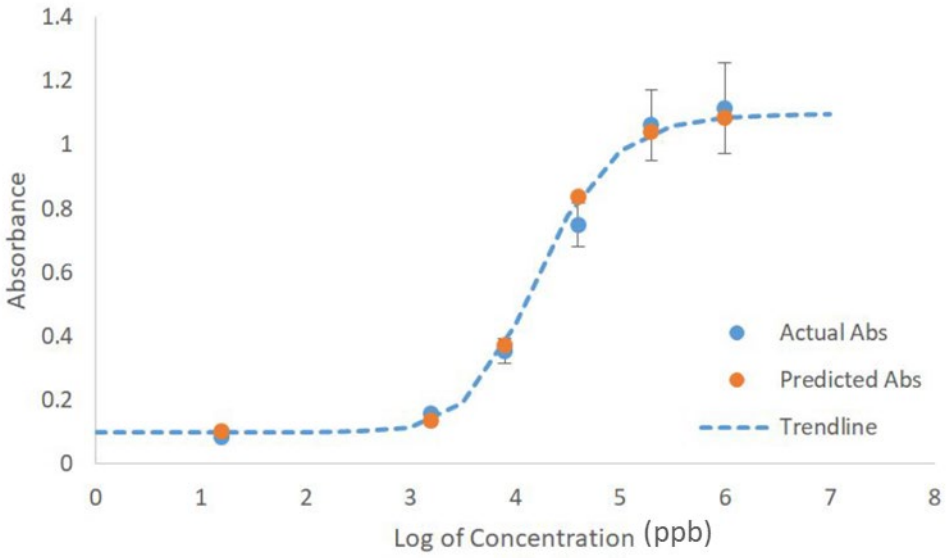

Figure A.11. Calibration curve for protein biomarker generated using standards with concentrations of 1.6 ppb, 8 ppb, 40 ppb, 200 ppb and 1000 ppb protein.

$$y = 1.097701 + \frac{0.100018 - 1.097701}{1 + (\frac{x}{4.230995})^{12.20189}} \qquad \text{(Equation 8.4)}$$

The aforementioned regression line was used to calculate the concentration of protein in unknown sample #13, and the results are summarized in the table below (**Table A.2**).

Table A.2. Protein concentration present in unknown sample #6 with statistical significance.

Protein Concentration (ppb)	**Standard Deviation (ppb)**	**95% Confidence Interval (ppb)**	**LoD (ppb)**	**LoQ (ppb)**
14.3 ppb	$\pm$ 0.2 ppb	14.3 $\pm$ 2.0 ppb	2.5 ppb	3.3 ppb

The results (**Table 0.2**) indicate that there was a rather high degree of precision in the results indicated by the low standard deviation and narrow confidence interval. If a complex sample was used to run the standards, the LoD and LoQ would likely increase because it would be more difficult to detect the protein due to the other molecules in the solution causing background absorbance.

Conclusion

The overall conclusion of this experiment is that the concentration of protein in unknown sample #13 was 14.3 ± 0.2 ppb with a 95% confidence interval of 14.3 ± 2.0 ppb, and it was able to be determined through the use of the logistic fit regression equation from a calibration curve generated from standards with known concentrations of protein. In addition, the final concentration of protein in the unknown sample has a narrow standard deviation and 95% confidence interval, indicating that the measurement has a high degree of precision, but the accuracy is yet to be determined.

There were numerous sources of error in this experiment. First, it is definitely possible that the calibration curve is not accurate, as can be seen by some of the data points being above or below the regression equation. As such, even though the regression equation seems to be a

good fit for the data, it is possible that the equation is simply inaccurate when used to calculate the protein concentration based on just an absorbance value. This would have resulted in a variable error in the final protein concentration in the unknown sample. In addition, protein is light sensitive, so it is possible that while the protein standards were waiting to be neutralized, some of the protein was degraded by light resulting in a regression equation that would result in a concentration of protein in the unknown sample that is less than what it should be.